Prospect studies for Higgs boson pair production to $b\bar{b}\gamma\gamma$ final state at the HL-LHC with the ATLAS detector

*Thesis submitted for the degree of
Doctor of Philosophy*

Daniel Lawrence Briglin

Particle Physics Group
School of Physics and Astronomy
University of Birmingham
February 2020

ABSTRACT

$\mathfrak{B}$y the end of the HL-LHC era, before 2040, the ATLAS experiment aims to increase the size of the dataset from $\sim$300fb^{-1}, acquired at the end of LHC running, up to $\sim$3000fb^{-1} The large dataset expected after HL-LHC operation increases the likelihood of seeing rare processes such as the $H \rightarrow HH \rightarrow b\bar{b}\gamma\gamma$ decay channel. This channel is one of the most promising for measuring the Higgs boson self-coupling. To mimic the expected ATLAS detector response to various physics objects at the HL-LHC, upgrade performance functions are constantly developed and updated. A recent update to these functions included the addition of a considerably more realistic estimate of the expected material budget of the ITk, as well as dedicated functions for both the $50\times50\mu$m^2 and $25\times100\mu$m^2 pixel sensor geometries. A BDT method was applied to the $H \rightarrow HH \rightarrow b\bar{b}\gamma\gamma$ channel to determine the effects of these changes. It was shown that the more realistic material budget and dedicated $50\times50\mu$m^2 functions results in a $\sqrt{q_0, A}$ significance for observing this channel of 3.10$\pm$0.13. Comparable results are obtained when using either a pixel sensor geometry of $25\times100\mu$m^2 or reducing the radius of the innermost pixel layer.

Declaration of Author's Contribution

𝕿he contents of this thesis represent the work I have undertaken and contributed to over the course of my post-graduate studies. The work outlined here is the result of input from many parties, specifically those in the HL-LHC ATLAS community. I was fortunate to contribute to both the hardware for the HL-LHC and an analysis on its prospects for measuring $H \to HH \to b\bar{b}\gamma\gamma$. All the results published by the ATLAS collaboration are dependant on the efforts of thousands of people who contributed to the construction and running of the ATLAS detector and who contribute still to its upgrades. I contributed to the outreach of ATLAS by taking several groups into the cavern to see the ATLAS detector up close during my time as a tour guide.

Chapter 1 begins the thesis with a summary of the theoretical background, starting with the standard model of particle physics and leading to the importance of di-Higgs measurements. The LHC and ATLAS detector are described in Chapter 2 which also details the design and performance expected of the ATLAS detector upgraded for HL-LHC operation.

Chapter 3 described my contributions to the irradiations for ATLAS using the University of Birmingham Medical Physics Cyclotron and its commissioning as an AIDA-2020 transnational access radiation facility. I performed tests on several HL-LHC technologies to determine if they could maintain sufficient performance after receiving similar radiation doses to those expected during HL-LHC operation.

Chapter 4 outlines the production of Monte Carlo samples for the $H \to HH \to b\bar{b}\gamma\gamma$ channel, I was not involved with this however it is important to include in this thesis. The topologies of these samples are detailed in Chapter 5 as well as an introduction to the analysis techniques that are used. Chapter 6 updates previously published results which are shown to be unrealistic and further optimises the signal capturing capabilities through a boosted decision tree method.

In all chapters any work which is not my own is referenced.

Acknowledgements

$\mathfrak{I}$ would like to start by thanking three people without whom I would not have been able to complete my PhD. Firstly my primary supervisor Phil Allport for his endless support throughout and especially for translating my English into actual English. Secondly, Nansi Andari who was always happy to help and an absolute pleasure to work with. I feel lucky to have been supervised by her and wish her all the best for the future. Thirdly, James "Jamés" Broughton, who was always extremely helpful at all hours, as well as being a pleasure to live with.

I would like to thank all those who helped me during my main analysis project, most notably: Ben Smart, Stephane Jezequel, Nathan Readioff and Monika Wielers. Much of my analysis work has been dependent on their contributions. For my qualification task I had the pleasure of working with the team at the cyclotron here at Birmingham. They were always happy to help and great company during the many long irratiation sessions. During this time I received a huge amount of help from Laura Gonella, Juergen Thomas and John Wilson. A special thank you must go to Laura and Phil for not giving up on me though the difficult midterm writing stage. Also thanks to Mark Slater for maintaining the Birmingham batch system allowing me to clock up an impressive 240,000 weighted hours.

I can not pass up this opportunity to mention some of the great times I have had with the students of Birmingham over the years. Matt Baca (Mac Baccar) without whom the cure for sadness would not have been brewed. Also for my personalised batarangs. Again Jamés for our brief time together in Geneva where we completed SWBF (no easy task) and who taught me how to snowboard and code in C++. James Kendrick for many great times while living together for an entire year in Geneva and for encouraging me to try the (to date) worst "food" I have ever eaten. Also for organising our tour of Vietnam which was truly amazing. Jack "but why?!" Lindon who is a constant source of entertainment and a great guy to be around. Always up for a meal out and a R1 lunch, where we had (to date) one of the greatest meals ever, truffle oil pasta. Also to Jack and Ryan for lending me their sofa bed on more than one occasion (even after destroying Jacks actual bed). My fellow occupants of the basement (Den), Govind "Gov" Virdee, Daniel Lewis and Nandish Gorasia whom I wish I could have shared an office with for longer. They made the last stretch of the PhD not only bearable but enjoyable as well as being great company both in and out of the office. Also to Elliot Reynolds who introduced me to climbing and with whom I scaled the Jura and Salève. I wish him all the best in this postDoc at Birmingham. Also to Russell Turner and Robert Vallance for accompanying me on skiing/snowboarding trips. And to Alasdair Winter, Jamés and Andy Foster who welcomed me to the office so warmly with beer and a video of a Gorilla Vs a Leopard. All of you made the office the greatest it has ever been. Finally to you all for many great memories (and indeed missing memories) from all the conference dinners and times outside the office. A special mention to Gordon

Ramsay whose shouting and swearing I found to be oddly soothing as a background while working, cooking and eating.

Lastly, but most importantly, I would like to thank my Mum, Dad, Sister and Brother-in-law (and of course Sam, Smudge and Eleven). All of you have supported me throughout the PhD and throughout my life prior for which I will be forever grateful and will do my best to repay. And to nanny Chris who passed away during this PhD, to know her was to love her.

I will cherish all the great memories from my time as a PhD student and look forward to whatever the future will bring. Exploring the unknown.

I'd rather try something new and not enjoy it than not try it at all

Contents

List of Tables

List of Figures

DEFINITIONS OF ACRONYMS

ABC ATLAS Binary Chip

ABC130 ATLAS Binary Chip with 130nm Technology

ALiBaVa Liverpool Barcelona Valencia

ALICE A Large Ion Collider Experiment

ASICs Application Specific Integrated Circuits

ATLAS A Toroidal Lhc ApparatuS

BDT Boosted Decision Tree

BEH Brout-Englert-Higgs

CERN Conseil Europen pour la Recherche Nuclaire

CMS Compact Muon Solenoid

CMOS Complimentary MOS both n and p type

EMCal Electromagnetic Calorimeter

ggF gluon-gluon Fusion

HCC Hybrid Control Chip

HCC130 Hybrid Control Chip with 130nm Technology

HGTD High Granularity Timing Detector

HL-LHC High Luminosity LHC

IBL Insertable B-Layer

ID Inner Detector

ITk Inner Tracker

LAr Liquid Argon

LHC Large Hadron Collider

LHCb LHC-beauty

LO Leading Order

MC Monte Carlo

MOSFET Metal Oxide Semiconductor Field Effect Transistor

NMOS N(negative)-type Metal Oxide Semiconductor

NNLO Next-to-next-to-leading Order

NLO Next-to-leading Order

PDF Probability Density Function

QCD Quantum Chromodynamics

QFT Quantum Field Theory

RINCE Radiation Induced Narrow Channel Effects

SM Standard Model

STI Shallow Trench Isolation

TID Total Ionising Dose

TMVA Toolkit for Multivariate Data Analysis

TRT Transition Radiation Tracker

UPF Upgrade Performace Functions

VBF Vector Boson Fusion

CHAPTER 1

THEORY

$\mathfrak{P}$hysics is the mathematical description of a universe and this description is currently dependent on the length scales under investigation. At very large scales, astrophysics and cosmology give a description of how the universe is unfolding and how structures from asteroids to super-massive black holes form. At very small scales, where an atom is considered relatively large, particle physics attempts to explain the nature and interactions of the universe's fundamental constituents. Probing the internal structure of particles is complicated as it depends on the energy scale (resolution) of the probe. High energies are required for two reasons, to probe small structures and to produce new massive particles through exploiting Einstein's equation $E = mc^2$.

1.1 The Standard Model of Particle Physics

The current and most complete understanding of particle physics is encompassed in the Standard Model (SM) [1–6]. The SM describes fundamental particles and their interactions and is often represented by a single Lagrangian. Since its inception in the 1960s and 1970s the model accurately explained all that was known about subatomic particles at the time, as well as predicting the existence of other particles summarised in Table 1.1. The Higgs boson was the last of these predicted particles to be discovered in 2012 by the ATLAS [7] and CMS [8] experiments at CERN and is described in detail in Section 1.4. The SM is comprised of twelve fundamental particles with spin 1/2 called fermions [1]. The fermions are split into six leptons and six quarks and grouped into three generations of matter. The first generation of fermions, electrons, up and down quarks comprise the majority of the visible matter in the universe. They do not decay, unlike charged particles in the second and third generations. These fundamental fermions are considered to be point-like particles; depending on their type, their interactions may include the strong, weak and electromagnetic forces. These forces all have a corresponding coupling strength which is related to the *charge* of each force. Every fermion has an identical counterpart known as its antiparticle which has identical mass but differs by inverted signs of all internal quantum numbers such as electric charge. All twelve elementary particles experience the weak force and all except the neutrinos (which are electrically neutral) participate in electromagnetic interactions. The quarks carry an additional colour charge which is the Quantum Chromodynamics (QCD) equivalent of electric charge and therefore they are the only fermions to experience the strong force [2,3]. Each of the forces are mediated by spin-1 gauge bosons with interactions described within the framework of Quantum Field Theory (QFT). For electromagnetism this is the theory of Quantum Electro-Dynamics (QED) where the massless photon mediates interactions between charged particles. The strong force is described by QCD and interactions take place through the exchange of massless gluons (which form a group of eight distinct particles). The weak force is mediated by the massive Z and $W^{\pm}$ bosons responsible for neutral-current and charged-current interactions

Table 1.1: Summary of all the elementary particles of the SM, composed of quarks and leptons divided into three generations of matter and the force carrying bosons. The electric charge is in units of the electron charge. All masses taken from [9]

Type	Generation	Name	Symbol	Mass[GeV]	Charge	Spin
Quark	I	up	u	0.002	$+2/3$	$1/2$
		down	d	0.005	$-1/3$	$1/2$
	II	charm	c	1.3	$+2/3$	$1/2$
		strange	s	0.09	$-1/3$	$1/2$
	III	top	t	172.9	$+2/3$	$1/2$
		bottom	b	4.2	$-1/3$	$1/2$
Lepton	I	electron	e	0.0005	-1	$1/2$
		electron-neutrino	ν_e	$<10^{-9}$	0	$1/2$
	II	muon	μ	0.106	-1	$1/2$
		muon-neutrino	ν_μ	$<10^{-9}$	0	$1/2$
	III	tau	τ	1.78	-1	$1/2$
		tau-neutrino	ν_τ	$<10^{-9}$	0	$1/2$
Boson	Vector	gluon	g	0	0	1
		photon	γ	0	0	1
		Z boson	Z	91.2	0	1
		W boson	$W^{\pm}$	80.4	± 1	1
	Scalar	Higgs boson		125.1	0	0

respectively.

Interactions between the fundamental forces and elementary particles of the Standard Model are derived via the application of a $SU(3)_C \otimes SU(2)_L \otimes U(1)_Y$ local gauge symmetry. The $SU(3)_C$ group represents transformations of the colour state of a system (see Section 1.2) and the $SU(2)_L \otimes U(1)_Y$ symmetry represents a unified description of the weak and electromagnetic interactions (see Section 1.3).

However even with all the triumphs of the SM it is not considered a complete theory as there are several phenomena which remain unexplained. The matter in the SM accounts for only 4.9% of the universe [10]. It does not give a description of dark matter which, through various astrophysical and cosmological observations, constitutes 26.8% of the universe, nor does it explain the scale of asymmetry between observed matter and anti-matter. In collider experiments an asymmetry between the interactions of matter and anti-matter can be observed but not on a scale large

enough to account for a universe dominated by matter [11]. The SM also does not accommodate gravity♠ and does not explain why neutrinos have mass or the actual mass values of any of the fundamental fermions.

1.2 Quantum Chromodynamics

QCD is the section of the SM which explains the interactions between the quarks and the gluons. Unlike the electric charge which only has two possible values $(+,-)$, the strong charge can take six values or colours $(R, G, B, \bar{R}, \bar{G}, \bar{B})$ [2,3]. The observed particles in QCD can only manifest as colour singlets, therefore the partons (quarks and gluons) comprising these particles must combine to produce a net colour charge of zero (hadrons). Colour neutral states can be comprised in two ways, firstly pairs of colour and anti-colour $(R\bar{R}, G\bar{G}, B\bar{B})$ called mesons or as triplets of all three colours $(RGB, \bar{R}\bar{G}\bar{B})$ called baryons. Unlike photons, which do not carry the electromagnetic charge, the gluon also carries a colour charge which allows it to self-interact. Unlike the other forces, the strong force gets weaker the closer two objects become and stronger at increased distances. As a consequence of the increasing force with separation, a quark formed in a high energy experiment will produce many other hadrons in a process called *hadronisation*. As the field strength increases it becomes high enough to produce additional quark/anti-quark pairs. Hadronisation produces collimated cones of hadrons around the original quark or gluon directions which are knows as jets. Advanced algorithms called *flavour taggers* are used to study the properties of the jets to match them to the most likely original parton, see e.g. [12]. Flavour taggers are vital as many analyses at the Large Hadron Collider contain jets as a common signal or as background.

The majority of visible matter in the universe takes the form of protons and neutrons which consist of up and down quarks. However their masses are much greater than the sum of the three valence quarks which constitute only approximately 1% of

---

♠ Although as it is roughly 10^{-37} times weaker than the strong force at 1fm it therefore has a negligible impact on subatomic interactions

their total masses. As previously mentioned the strong force gets weaker at small distances so that it asymptotically approaches zero. In the case of a proton the two up quarks and the down quark are asymptotically free [13] and move at near the speed of light. The energy density associated with the strong force binding the quarks produces additional mass, which manifests itself as a *sea* of quark/anti-quark pairs and gluons collectively known as the QCD binding energy. Therefore the structure of a baryon is more accurately described in Figure 1.1 where approximately 1% of its mass is due to the three valence quarks and the other 99% is due to the QCD binding energy. Considering that the majority of the mass of an atom is concentrated in the nucleus (protons and neutrons), 99% of the matter in the universe is, in fact, QCD binding energy.
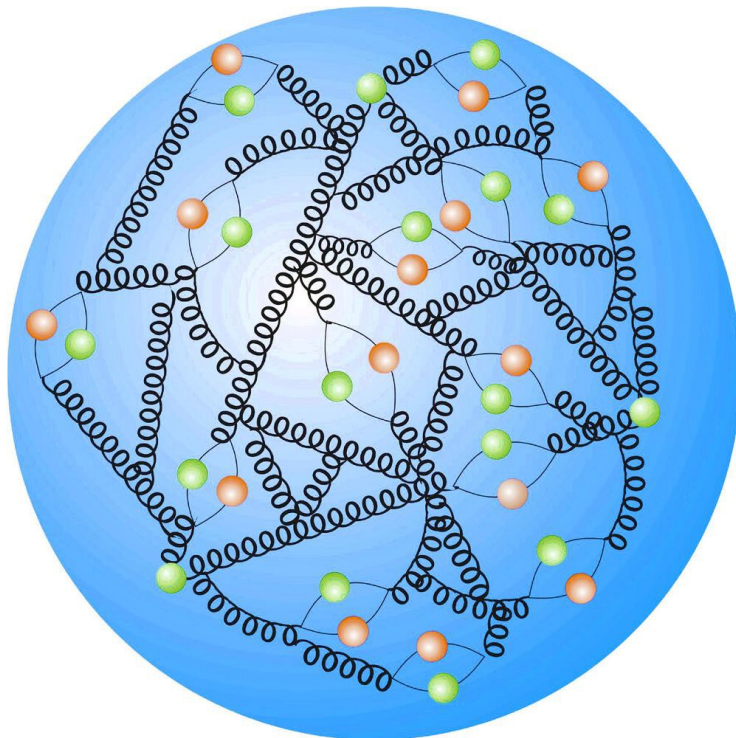
Figure 1.1: An artists impression of the structure of a baryon, showing the three valence quarks (green), additional quark/anti-quark (green/red) and the force carrying gluons [14]

1.3   Electroweak Theory

At sufficiently high energies the electromagnetic and weak forces can be described as two aspects of the same electroweak force [4–6]. The electroweak sector of the SM is described by the gauge group $SU(2)_L \otimes U(1)_Y$ where Y is defined as the weak hypercharge and L denotes left-handed fermions. In this description, fermions can be thought of as consisting of left and right handed fields, where the left handed components transform as doublets under $SU(2)$ transformations while the right handed components only transform as singlets. This results in weak interactions only acting on left handed field components. Hence the weak force only couples to left handed particles and to right handed antiparticles.

In quantum field theory, particles are considered as fields and fermions can be described by a Dirac field with a Lagrangian of the form:

$$\mathcal{L} = i\bar{\psi}(x)\gamma^\mu\partial_\mu\psi(x) - m\bar{\psi}(x)\psi(x) \tag{1.1}$$

Applying a global phase transition,

$$\psi(x) \to \psi'(x) = e^{iQ\alpha}\psi(x) \tag{1.2}$$

will leave the Lagrangian unchanged as $e^{i\alpha}\psi e^{-i\alpha}\psi = 1$. However, in the case of local gauge transformations the global phase transformation is replaced by a local one where $\alpha \to \alpha(x)$ i.e. the phase has a local space-time dependence, then Equation 1.1 is no longer invariant as:

$$\partial_\mu\psi(x) \to e^{iQ\alpha(x)}(\partial_\mu + iQ\partial_\mu\alpha(x))\psi(x) \tag{1.3}$$

In order to restore invariance, the derivative ∂_μ must be replaced with the covariant

derivative D_μ which is of the form:

$$D_\mu = \partial_\mu + ieA_\mu \tag{1.4}$$

where A_μ is a gauge field which transforms as:

$$A_\mu \to A'_\mu = A_\mu - \frac{1}{e}\partial_\mu\alpha(x) \tag{1.5}$$

The $SU(2)$ and $U(1)$ groups give rise to a weak isovector W_μ^a and a weak isoscalar B_μ respectively each with a corresponding coupling constant. These four fields combine through the weak mixing angle, θ_ω, to give the photon (A_μ), $W^\pm$ and Z^0 bosons as shown below:

$$\begin{aligned}
W_\mu^\pm &\equiv \frac{1}{\sqrt{2}}\left(W_\mu^1 \mp W_\mu^2\right)^2 & (W^\pm \text{ Bosons}) \\
Z_\mu &\equiv \cos\theta_w W_\mu^3 - \sin\theta_w B_\mu & (Z^0 \text{ Boson}) \\
A_\mu &\equiv \sin\theta_w W_\mu^3 + \cos\theta_w B_\mu & (\text{Photon})
\end{aligned} \tag{1.6}$$

The interesting result of this is the prediction that the bosons associated with these fields and the fermions they interact with, should be massless however, as shown in Table 1.1, the $W^\pm$ and Z bosons are in fact massive. This shortcoming is overcome by considering the final addition to the SM, the Higgs boson.

1.4   The Higgs Boson

An issue with original electroweak theory is that it does not provide a mechanism for the Z and W bosons to acquire their masses. To account for the Z and W masses a simple mass term cannot be added to the SM Lagrangian as this would not preserve the $SU(2)_L \otimes U(1)_Y$ symmetry. This motivated the formulation of the

Brout-Englert-Higgs (BEH) mechanism [15–17], through which the W and Z bosons generate mass and the photon remains massless. The BEH mechanism introduces a new doublet of complex scalar fields with a potential that breaks the invariance of the vacuum whilst maintaining the invariance of the Lagrangian under the electroweak symmetry. This is known as spontaneous symmetry breaking.

The complex doublet takes the form [6]:

$$\phi = \begin{pmatrix} \phi^+ \\ \phi^0 \end{pmatrix} = \frac{1}{\sqrt{2}} \begin{pmatrix} \phi_1 + i\phi_2 \\ \phi_3 + i\phi_4 \end{pmatrix} \tag{1.7}$$

where ϕ_i are real scalar fields.

The Lagrangian for this scalar field is given by:

$$\mathcal{L}_\phi = (D_\mu \phi)^\dagger (D_\mu \phi) - V(\phi) \tag{1.8}$$

where D_μ is the covariant derivative referring to the left handed fermions and the field's potential, $V(\phi)$ is given by:

$$V(\phi) = \mu^2 \phi^\dagger \phi + \lambda (\phi^\dagger \phi)^2 \tag{1.9}$$

where λ is the coupling constant and is greater than zero to ensure minima exist in the potential. To ensure a broken symmetry, μ must be chosen such that $\mu^2 < 0$, this results in a characteristic *Mexican Hat* potential shown in Figure 1.2. The potential is symmetric however the ground state is not and the minimum of this potential is not at the origin but is instead located at the vacuum expectation value, ν given by:

$$\phi^\dagger \phi = \frac{\mu^2}{\lambda} \equiv \nu^2 \tag{1.10}$$
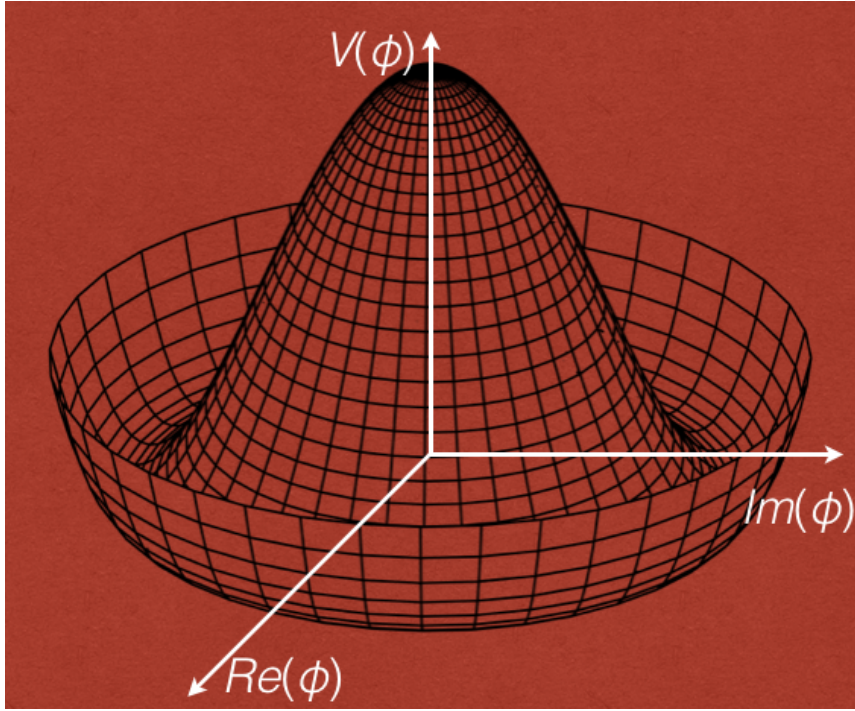
Figure 1.2: The Higgs field potential, $V(\phi)$

This spontaneous symmetry breaking results in infinite degenerate ground states. This degeneracy must be removed so the gauge $\phi_1 = \phi_2 = \phi_4 = 0$, $\phi_3 = \nu$ is chosen resulting in the ground state:

$$\phi_0 = \frac{1}{\sqrt{2}} \begin{pmatrix} 0 \\ \nu \end{pmatrix} \tag{1.11}$$

and Equation 1.7 becomes:

$$\phi = \frac{1}{\sqrt{2}} \begin{pmatrix} 0 \\ \nu + h \end{pmatrix} \tag{1.12}$$

where h represents radial perturbations around ν manifesting in the real scalar Higgs field. This choice of gauge results in spontaneous symmetry breaking of three of the four generators, known as the unphysical Goldstone bosons, which correspond to four degrees of freedom of $SU(2)_L \otimes U(1)_Y$. The $W^\pm$ and Z bosons absorb these Goldstone bosons and become massive as a result. The final unbroken generator

is the massless photon and the scalar doublet introduces an additional degree of freedom corresponding to the scalar Higgs Boson.

Expanding the potential of equation 1.9 about the minimum $V(\phi) \rightarrow \frac{1}{\sqrt{2}}V(\nu + h)$ and enforcing $\mu^2 < 0$ gives:

$$V(\nu + h) = -\frac{\lambda\nu^4}{4} + \lambda\nu^2 h^2 + \lambda\nu h^3 + \frac{\lambda}{4}h^4 \qquad (1.13)$$

Where the potential is now in terms of the vacuum expectation value and the Higgs field. $\frac{\lambda\nu^4}{4}$ is a constant with no physical consequences, and the terms proportional to h^3 and h^4 are the triple and quartic Higgs self-interaction terms, which are responsible for the HH and HHH couplings respectively. Measuring these self-interaction terms probes the shape of the Higgs potential. By comparing the potential of equation 1.13 to the Lagrangian of a massive scalar field, it can be shown that the h^2 term can be interpreted as the Higgs boson mass given by:

$$m_H = \sqrt{2\lambda}\nu \qquad (1.14)$$

Since λ is a free parameter in the SM, the Higgs boson mass is not predicted and therefore has to be measured experimentally.

This mechanism explains how the $W^\pm$ and Z bosons become massive however does not give an explanation for the origin of fermion masses. The solution to this problem is the insertion of gauge invariant fermion mass terms into the Lagrangian. The fermions then gain mass through their Yukawa interactions with the Higgs field when the vacuum expectation value is non-zero. The strength of this interaction arises from the coupling between a fermion's field and the Higgs field proportional to that fermion's mass. The coupling strength between the vector bosons and the Higgs boson can also be calculated and is dependant on the vector boson mass squared. The Higgs boson can only couple to the massless photon and gluons indirectly

through quantum loops.

1.5   Higgs Boson Production and Decays at the LHC

Hadron colliders, such as the Large Hadron Collider (LHC) (described in detail in Chapter 2), can produce a Higgs boson through four main mechanisms [18] shown in Figure 1.3. The dominant production mode is gluon-gluon fusion, where a Higgs boson is produced through a triangular quark loop, which is dominated by top quarks, and to a lesser extent also b quarks, shown in Figure 1.3a. This production mechanism results in a final state comprised of only the Higgs boson's decay products. The Higgs boson can also be produced by the fusion of massive particles. As shown in Section 1.4, the Higgs boson couples to mass and therefore W's, Z's and top quarks are the most likely to fuse to produce a Higgs boson through mechanisms called Vector Boson Fusion (VBF) and $t\bar{t}$ fusion respectively. In VBF, shown in Figure 1.3b, two quarks, one from each incoming proton, both emit either a W or a Z boson which then fuse, producing a Higgs boson. This results in a final state containing two jets, originating from the recoiling quarks which are likely to propagate at small angles, as well as the Higgs boson's decay products. Figure 1.3d shows how two gluons both produce a pair of top quarks where one from each pair fuse to produce a Higgs boson. The decay products, along with the remaining top quarks, make up the final state. The final mechanism produces a Higgs boson in association with either a W or a Z boson shown in Figure 1.3c. In this mode, an off-shell W or Z emits a Higgs boson resulting in a real W or Z. The final state will therefore contain the decay products of the two bosons.

Measuring the properties of the Higgs boson is one of the main goals of the LHC. To date, A Toroidal Lhc ApparatuS (ATLAS) [19] has measured the total production cross section of a Higgs boson to be $57.0^{+0.6}_{-5.9}(stat.)^{+4.0}_{-3.3}(syst.)$pb with 36.1fb^{-1} [20] of data at a centre of mass energy of $\sqrt{(s)} = 13$ TeV, which is consistent with SM predictions (where fb^{-1} is a measure of the number of collisions and amount
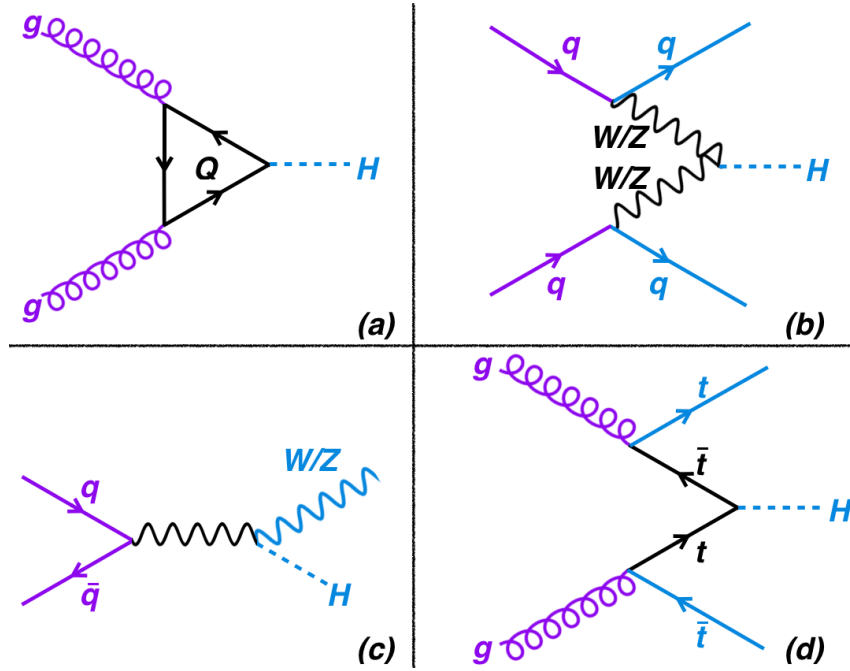
Figure 1.3: Feynman diagrams of the dominant Higgs production mechanisms. (a) Gluon-Gluon fusion, (b) Vector boson fusion, (c) Vector boson associated production and (d) $t\bar{t}$ fusion. The colours emphasise initial and final states for each process

of collected data, with 1fb^{-1} corresponding to $\sim 10^{12}$ proton-proton collisions). The mass of the Higgs boson has also been accurately measured through the $H \rightarrow ZZ^* \rightarrow 4\ell$ and $H \rightarrow \gamma\gamma$ channels with the ATLAS [21] and Compact Muon Solenoid (CMS) [22] [23] detectors. Combining these results gives a Higgs boson mass of $m_H = 125.09 \pm 0.21(stat.) \pm 0.11(syst.)\text{GeV}$ [24]. Due to its small cross section, a Higgs boson is only produced once in every billion collisions making detection very difficult. This is exacerbated by the many different decay modes of the Higgs boson to final states that have common backgrounds. Figure 1.4 shows some of the most common Higgs boson decays.

The increased luminosity of the High Luminosity LHC (HL-LHC) makes it possible, not only, to better measure these single Higgs boson decays but also to possibly observe the production and decays of di-Higgs events, which result predominantly through the mechanisms shown in Figure 1.5.

Figure 1.5a shows the main production mechanism, where an offshell Higgs boson
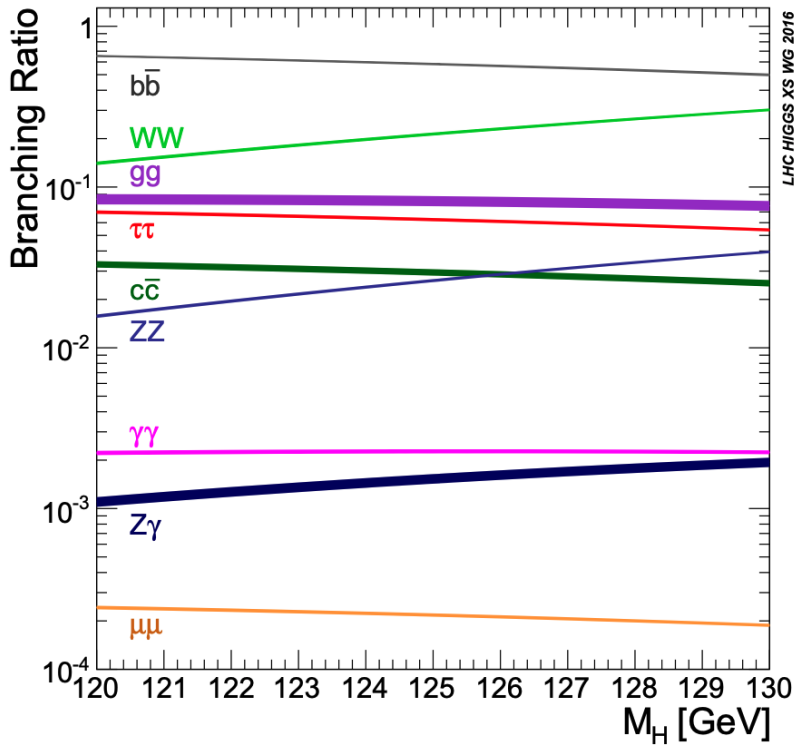
Figure 1.4: The branching ratios of the most common Higgs boson decays and their predicted uncertainties, shown as the thickness of each band, around a mass range of 125GeV [25]
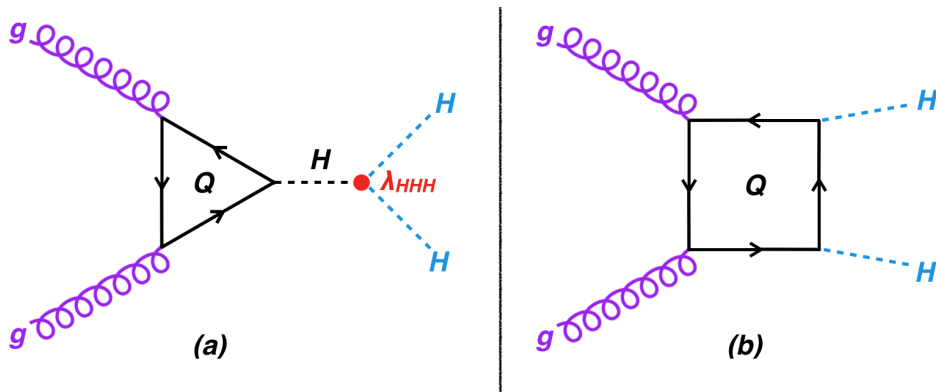
Figure 1.5: Feynman diagrams of the leading di-Higgs production mechanisms. (a) Higgs self-coupling and (b) Box diagram

decays to two real Higgs bosons. Measurements of di-Higgs production through this mechanism is the only way to access the Higgs boson trilinear coupling at the LHC and to probe the shape of the Higgs field potential shown in Figure 1.2. However this is a challenging measurement, even for the HL-LHC, as the box diagram, shown in

Figure 1.5b, interferes destructively, reducing the total cross section which is already relatively small and there are also large backgrounds from single H production. Each of the two Higgs bosons decay through one of the channels shown in Figure 1.4 to produce one of the final states shown in Figure 1.6.

	bb	WW	ττ	ZZ	γγ
bb	33% 40,000				
WW	25% 31,000	4.6%			
ττ	7.4% 8,900	2.5% 3,300	0.39%		
ZZ	3.1% 3,800	1.2% 1,300	0.34%	0.076%	
γγ	0.26% 320	0.10%	0.029%	0.013%	0.0053% 1.2

Figure 1.6: Branching ratio of di-Higgs decays and the expected total number of events assuming 3000fb^{-1}

To date ATLAS has published prospects studies on only a few of these potential channels such as $HH \to b\bar{b}b\bar{b}$, $HH \to b\bar{b}\tau^+\tau^-$ and $HH \to b\bar{b}\gamma\gamma$ summarised in [26] and also studies of different HH production mechanisms such as $t\bar{t}HH$ [27]. The $HH \to b\bar{b}b\bar{b}$ channel benefits from the largest branching fraction of HH decays, however four jets is a common background and therefore advanced techniques are required to identify the di-Higgs signal. The $HH \to b\bar{b}\tau^+\tau^-$ also has a relatively large branching fraction but suffers from the large number of jets expected in HL-LHC events, however this is offset by the more distinctive $\tau^+\tau^-$. Finally the $HH \to b\bar{b}\gamma\gamma$ benefits from both the reasonably large branching fraction of the $H \to b\bar{b}$ decay and the clear signature of the $H \to \gamma\gamma$ channel which, with its narrow mass peak, was used for the original Higgs boson discovery [7].

The results of [26] suggest an expected signal significance in the $HH \to b\bar{b}\gamma\gamma$ of 2.0σ with 3000fb^{-1} of data, however after a re-evaluation of the material in the tracking

volume (explained in Section 2.5.6) this significance is found to be an overestimation. As this is an important channel for the HL-LHC program it is important to see how the significance has been affected by this new re-evaluation. This re-evaluation and additional techniques are therefore discussed in more detail in Chapter 6.

CHAPTER 2

THE LARGE HADRON COLLIDER

𝕿he LHC is located 100m underground near the Conseil Europen pour la Recherche Nuclaire (CERN) particle physics laboratory on the Swiss French border and is 26.7km in circumference. It is the highest energy particle accelerator ever built, capable of both proton-proton as well as heavy ion collisions. There are four collision points around the ring where the experiments are located, these are two general purpose detectors ATLAS and the CMS and two specialised detectors LHC-beauty (LHCb) and A Large Ion Collider Experiment (ALICE) see Figure 2.1. The accelerator superconducting magnet system has an operating temperature of 2K. The design of the LHC allows for each proton beam to be accelerated to 7TeV creating a centre of mass energy at the collision points of $\sqrt{s} = 14$TeV. For a peak design luminosity of $10^{34}cm^{-2}s^{-1}$ there are 2808 bunches each containing 10^{11} protons, set to collide every 25ns. For each beam crossing, the average pile up is defined as the number of inelastic proton-proton collisions per beam crossing. During Run-2 the centre of mass energy was set to $\sqrt{s} = 13$TeV, as it would have taken longer to retrain

the LHCs magnet system to achieve $\sqrt{s} = 14$TeV, taking time away from physics research [28]. Figure 2.2 shows a summary of the data taken for all 13TeV data over Run-2 for the ATLAS experiment. Figure 2.2 shows, to-date, ATLAS has recorded a total of 147fb^{-1} of data at $\sqrt{s} = 13$TeV.
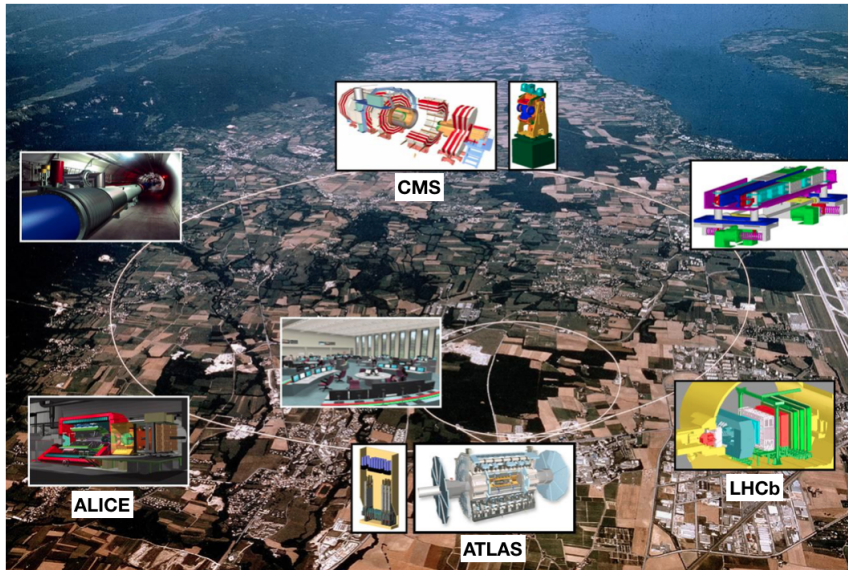
Figure 2.1: A map of the LHC and the general position of the main experiments CMS, LHCb, ATLAS, ALICE [29]
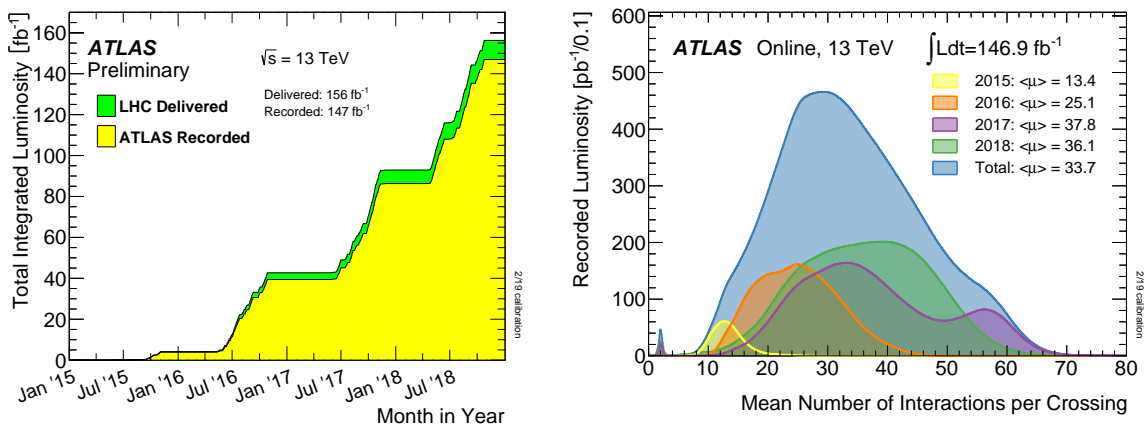
Figure 2.2: The total integrated luminosity (left) and the luminosity-weighted distribution of the mean number of interactions per crossing (right) for all 13TeV data from 2015-2018 [30].

2.1 CERN Accelerator Complex

The CERN Accelerator complex (illustrated in Figure 2.3) enables the colliding protons at the LHC to be accelerated to almost the speed of light. For Run-2 hydrogen atoms were fed into the source chamber of Linear Accelerator 2 (Linac2) where the electrons were stripped to leave the Hydrogen nuclei, a proton. The linear accelerator uses Radio Frequency cavities to apply a charge to cylindrical conductors alternating between positive and negative causing the protons to accelerate. The protons leave Linac2 in packets of 10^{11} at one third the speed of light with an energy of 50MeV, however linear acceleration is no longer practical at this point, so the packets then enter the circular Proton Synchrotron Booster. A pulsed electric field then accelerates the protons to 91.6% of the speed of light, they then pass into the Proton Synchrotron for 1.2s; here the energy added by the pulsing electric field mostly translates into an increase in mass. The protons leave the Proton Synchrotron with an energy of 25GeV, now 25 times heavier than at rest, and enter the Super Proton Synchrotron where they are further accelerated to 450GeV. Finally they enter the LHC where they enter one of two vacuum pipes for counter rotating beams. Kickers are used to precisely synchronise incoming packets and to accelerate those already circulating. To reach a target energy of 6.5TeV, 12,000A are applied to the LHC magnets in order to keep the protons on a circular path. This is achieved by making the magnets superconducting with a temperature of 2K. After roughly 20 minutes the packets are travelling 3ms^{-1} slower than the speed of light and complete 11,000 orbits of the LHC every second. The paths of the packets are then precisely altered and set to collide within the experiments around the LHC.
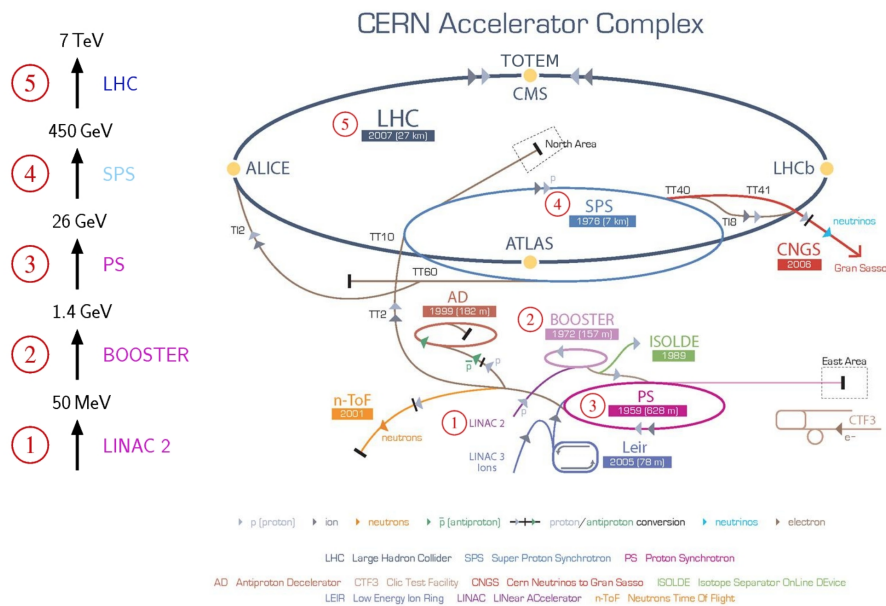
Figure 2.3: The current CERN Accelerator Complex from Hydrogen gas bottle to LHC injection showing the total energy at each stage. Taken from [31].

2.2   The LHC Upgrade Schedule

Figure 2.4 shows the upgrade time line for the LHC, it recently stopped taking data to allow for upgrades to both accelerators and experiments, thus ending Run-2 and starting LongShutdown 2 (LS2). At the end of 2024 there will be a further 30 month shut down, LS3, of the LHC to install improvements. The upgrade will allow a factor seven increase in luminosity, corresponding to HL-LHC operation. The increase in luminosity will increase pileup to $\langle \mu \rangle = 200$. The goal is to increase the dataset by over an order of magnitude and to achieve this in a reasonable time scale the luminosity of the colliding beams must be greatly increased. After LS2 the energy of the each colliding beam will be increased to 7TeV, which will be maintained for HL-LHC operation but will considerably increase radiation levels which the detectors will need to be able to withstand. The increase in the data available will greatly reduce statistical uncertainties and aid precision measurements [32]. The increased data set also increases the chance for rare processes to be observed, for example the Higgs boson self-coupling.
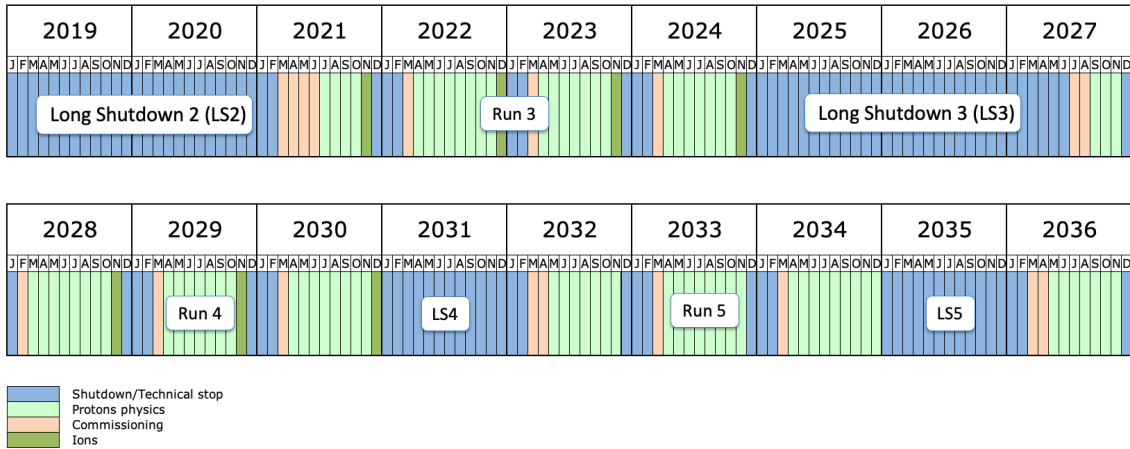
Figure 2.4: The time line for the operation of the LHC and upgrade to the HL-LHC after LS3 (Long Shutdown) [33]

2.3 LHC Experiments

The following describes the main detectors at the LHC and a brief overview of their physics motivations. As the analysis in this thesis was undertaken using the ATLAS detector, it will be described in detail in Section 2.4.

- The general purpose CMS [34] detector is used to collect data for a large array of different analyses and operates in conjunction with the ATLAS detector. The CMS detector has a compact design where tracking and calorimetry are encased within a single large solenoid magnet and surrounded by alternating layers of muon chambers and iron return yoke. It has an entirely silicon based inner tracker and the large solenoid magnet generates a field of 4T. CMS weighs a total of around 14,000 tonnes and with a radius of 7.5m and a length of 21m it is over ten times more dense than ATLAS.

- The 5600-tonne LHCb detector [35] is primarily designed to measure Charge-Parity violation, focusing on physics processes involving the bottom quark and it's rare decays. One aim is to make measurements which explain the matter-antimatter asymmetry of the universe. *b*-quarks are predominantly produced at small angles to the beam pipe and therefore LHCb adopts a *forward*, cone-

like, detector design where the first subdetector is mounted close to the collision point, with the others following, one behind the other, over a length of 21m [36].

- The ALICE detector [37] is optimised to operate during lead-lead collisions, where the high energy density creates a quark-gluon plasma with comparable conditions to one millionth of a second after the big bang. The ALICE collaboration studies this quark-gluon plasma as it expands and cools, observing how it progressively gives rise to the particles that constitute the matter of our universe today [38]. The detector weighs 10,000 tonnes and has dimensions 26m×16m×16m (length×height×width).

2.4 ATLAS

ATLAS is a general purpose detector which played a major role in the discovery of the Higgs Boson in 2012 [7]. The detector itself is 44m long and has a radius of 12.5m, weighing over 7000 tonnes [19]. ATLAS is constructed of several sub-detectors each sensitive to different aspects of the collision products. Figure 2.5 shows a cut-away view of the ATLAS detector with all sub-detectors and magnet systems. Figure 2.6 shows the signatures of various particles as they pass through the detector volume.
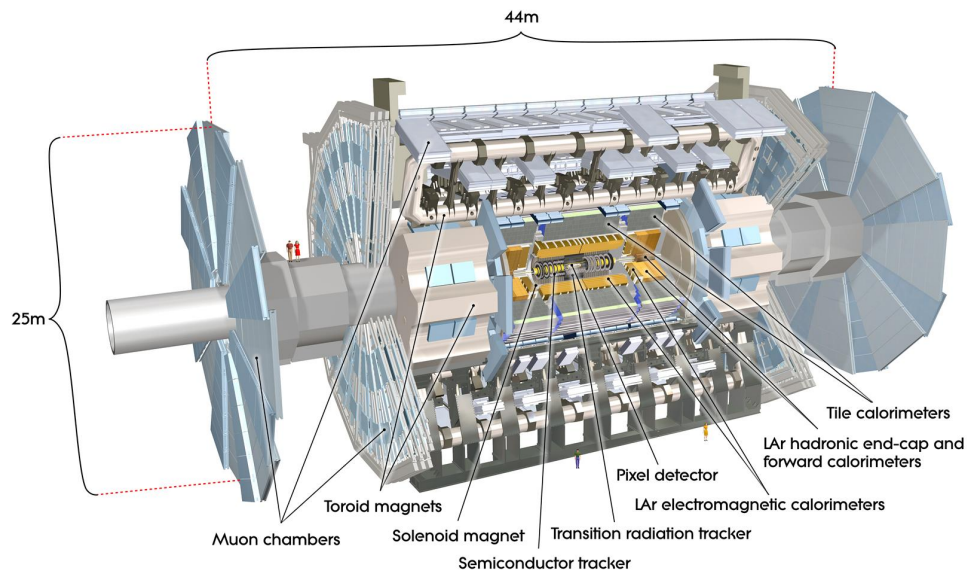
Figure 2.5: The design layout of the ATLAS detector currently installed at CERN [39]

2.4.1 Coordinate System and Quantity Definitions

The z-axis is defined as along the beam pipe, ϕ is the azimuthal angle around the beam pipe and θ is the angle from the beam pipe. The x-axis points from the z origin to the centre of the LHC and the y-axis is vertical towards the surface. The sub-detectors of ATLAS are arranged to be symmetric about the z axis in both x and y planes [39].

As the momentum distribution among the constituent partons of the hadron is
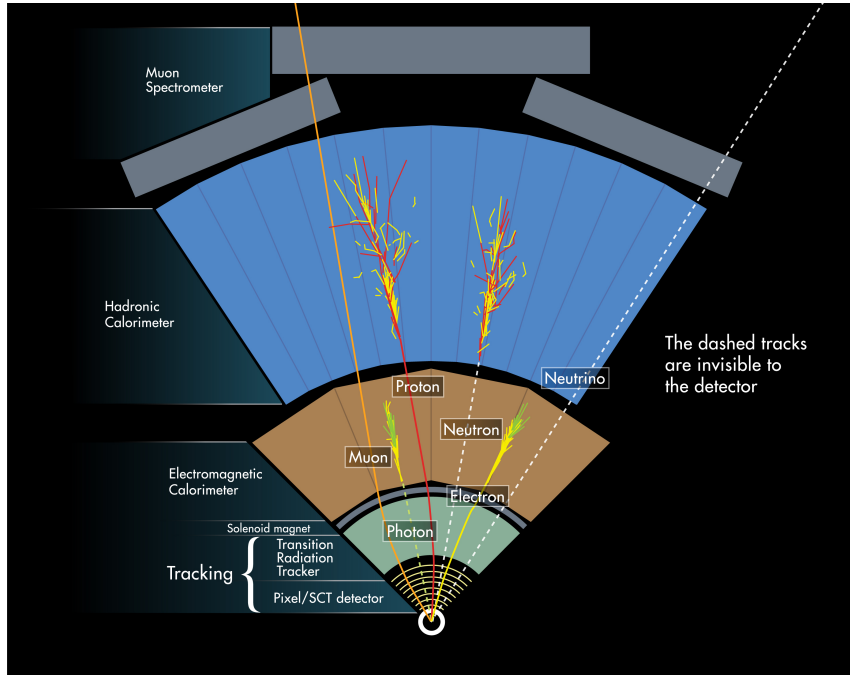
Figure 2.6: A graphical representation of particle detection within ATLAS [40]

unknown, parton collisions at the LHC are frequently boosted along the z-axis. This occurs even when the colliding beam energies are symmetrical. It is therefore useful to introduce a parameter called pseudorapidity which is defined as:

$$\eta = -\ln\tan\left(\frac{\theta}{2}\right) \tag{2.1}$$

The difference in η between two particles is Lorentz invariant which makes it a useful parameter for describing a particle's trajectory. Also particle production across units of pseudorapidity is roughly constant. The angular separation ΔR within the symmetrical detector between two particles is best described in terms of both η and ϕ space and is defined as:

$$\Delta R = \sqrt{\Delta\eta^2 + \Delta\phi^2} \tag{2.2}$$

A fixed ΔR around an object defines a cone in detector space which becomes a

useful tool for identifying characteristics of physics objects e.g. jets.

In hadron collider experiments it is not possible to exploit momentum conservation along the beam axis as the initial momentum of the colliding partons is unknown. This is overcome by applying momentum conservation to the transverse plane where the initial momentum is zero. Quantities such as transverse momentum, p_T, and transverse energy, E_T, are therefore used in many analyses.

2.4.2 Inner Detector

The Inner Detector (ID) is closest to the beam pipe and measures the trajectory of charged particles [41]. The many layers of sensors in the ID allow for excellent momentum and spatial resolution with fine detector granularity. The ID is enclosed within an axial, roughly uniform, 2T magnetic field produced by the solenoid magnet. Charged particles are therefore curved in this field and the transverse momentum (p_T) can then be measured. The ID has three detector types adopting two different technologies; silicon sensors in the two innermost sub-detectors and straw drift tubes in the outermost. Hits in the three sub-detectors give charged particle tracks which can be extrapolated back to the primary vertex. Tracks slightly missing the primary vertex can be used to identify secondary vertices as well. Figure 2.7 shows the layout of the ID. The ID can be split into three regions, concentric cylinders around the beam axis form the barrel region and disks covering the direction closer to the beam axis form the two endcap regions.

2.4.2.1 Pixel Layer

The innermost section of ATLAS, made of a pixel detector, gives a high track granularity close to the interaction point. The pixel sensors are arranged into four barrel layers and two endcaps with three disk layers each. The innermost barrel layer (the Insertable B-Layer (IBL) [43], added in 2014 and not shown in Figure 2.7) contains pixels with an area $50{\times}250\mu\text{m}^2$ whilst the outer three barrels and the endcaps are
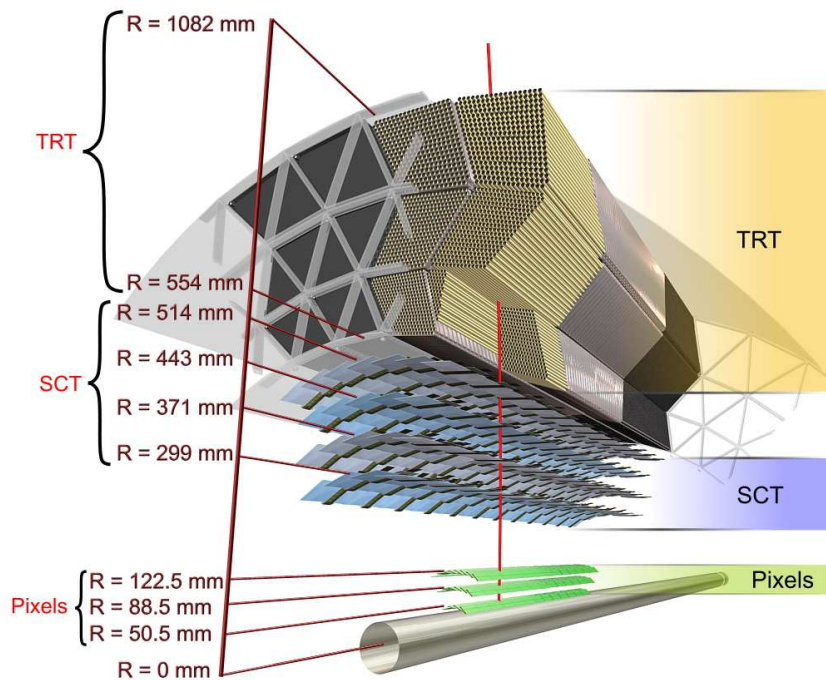
Figure 2.7: A breakdown of a section of the original ATLAS Inner Detector [42]

made of sensors with $50{\times}400\mu\mathrm{m}^2$. The sensor thickness is approximately $250\mu\mathrm{m}$. The pixel layers provide excellent spatial resolution for vertex finding. This is very important for analyses involving b-quarks, for example $H \to b\bar{b}$, as identifying the primary vertex where the collision occurred and any secondary vertices caused by short lived particles are key parameters in b-quark identification algorithms.

2.4.2.2   Silicon Tracker

The Silicon Tracker encloses the pixel layer with a further set of four barrel layers of silicon strips and a further nine endcap disks on each side. In total there are 15,912 silicon p-in-n strip sensors roughly $300\mu\mathrm{m}$ thick with a strip pitch of $80\mu\mathrm{m}$ [44]. These are daisy chained together (roughly 6cm$\times$6cm) in pairs giving modules of 12cm length measuring the ϕ coordinate at a given radius (barrel) or z position (endcap). Each double layer has their axes rotated with respect to one another by a small (40mrad) stereo angle, which results in a pair of measurements which also

derives a hit position in z for the barrel and r for the endcaps. Both the Pixel Layer and Silicon Tracker collect charge in the same way as will be discussed in Section 2.5.2.1.

2.4.2.3   Transition Radiation Tracker

The Transition Radiation Tracker is made entirely of straw drift tubes (roughly 300,000) which makes it the largest of the three ID sub-detectors. Each tube is 1.44m long and 4mm in diameter and filled with a mixture of gases. Any charged particle which traverses a drift tube will ionize the gas contained within the straw. An applied electron field causes the liberated electrons to drift towards to a central wire where the position is recorded. A typical particle produced from a collision at the LHC will traverse roughly 36 tubes. From these many recorded positions, precision momentum measurements can be made. Transition radiation is emitted when a charged particle passes through the boundary of media with different dielectric constants [45] and as an electron radiates more photons (transition radiation) compared to, for example, a pion, the Transition Radiation Tracker provides an additional capability for electron identification.

2.4.3   Calorimeter System

Sensitive to both neutral and charged particles, the calorimeters within ATLAS are designed to measure the energy of photons, hadrons and electrons. These particles shower as a result of interacting with the calorimeter material. The energy deposited by these showered particles is then summed to give an accurate measure of the energy of the initial particle. An overview of ATLAS calorimeter systems is shown in Figure 2.8. Electromagnetic showers are predominately comprised through bremsstrahlung, where photons are emitted through the deflection of charged particles interacting with the intense electric field near nuclei and pair production from photons. Nuclear interactions are responsible for hadronic showers. Two useful

parameters for describing a calorimeter's ability to cause showers are measured in terms of radiation lengths X_0 for the Electromagnetic calorimeter and interaction lengths λ for the Hadronic calorimeter. Here X_0 is defined as the mean distance over which an electron or photon looses a factor e of it's original energy; λ is the mean distance over which a hadron's energy is reduced by a factor e through strong interaction processes.
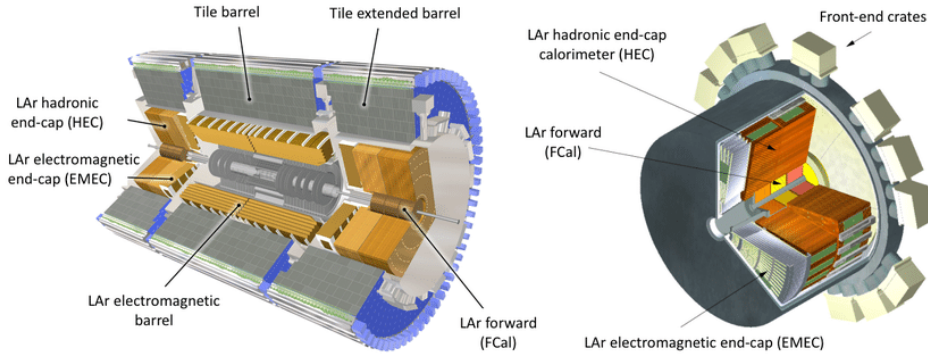
Figure 2.8: A diagram of the ATLAS Calorimetry systems [44].

2.4.3.1   Electromagnetic Calorimeter

The innermost calorimeter layer, the Electromagnetic Calorimeter (EMCal), measures electrons and photons which produce electromagnetic showers. The EMCal is constructed in alternating layers of Lead ($X_0 = 0.561$cm [46]) as the absorber material and liquid Argon as the active material. It adopts an accordion structure which ensures uninterrupted azimuthal coverage as shown in Figure 2.9. This design also ensures that across all active η regions the amount of material a particle traverses is approximately constant. The EMCal is split between barrel and endcap sections with the barrel covering $|\eta| = 1.475$ and the endcaps $1.375 < |\eta| < 3.2$. The EMCal has a depth of >22 radiation lengths in the barrel and >24 in the endcaps [39]. The EMCal is designed to have a depth sufficient to stop particles that interact electromagnetically. The fractional electromagnetic shower energy resolution is $\frac{\Delta E}{E} = \frac{10\%}{\sqrt{E}} \oplus 0.7\%$.

Electromagnetic objects can be identified by looking at the longitudinal and transverse shower shapes in the calorimeter and also various isolation variables [47]. Elec-

trons are also required to be associated with tracks in the ID, matching in both position and energy. Photons are required not to match with tracks in the ID.
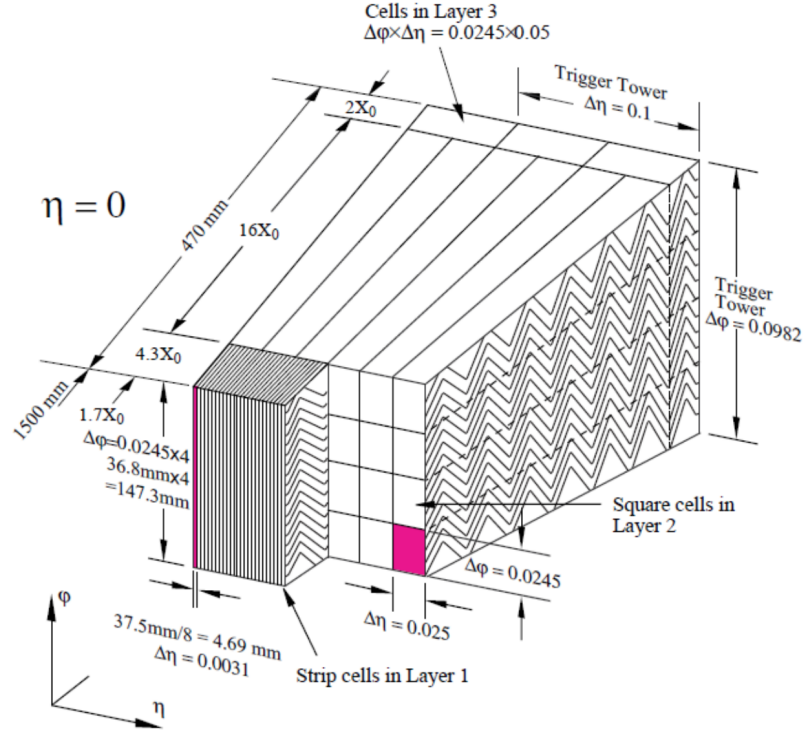
Figure 2.9: Schematic of the ATLAS EMCal showing the accordion geometry and the spatial resolution of each layer. [48].

2.4.3.2 Hadronic Calorimeter

The outer layers are formed of concentric tile calorimeters in the barrel and Liquid Argon (LAr) calorimeters in the endcaps which measure the energy of hadrons. The barrel calorimeter is split into a central region covering $|\eta| < 1$ and two extended barrel regions covering $0.8 < |\eta| < 1.7$. The tile calorimeters use 500,000 plastic scintillator tiles as the active material and steel for the absorbing layers. The hadronic endcap calorimeters are situated between $1.5 < |\eta| < 3.2$ and consist of Copper and LAr. Copper and Lead have nuclear interaction lengths of 15.32cm and 17.59cm respectively [39], which allows the hadronic endcap calorimeter to be compactly constructed. The hadronic calorimeter, combined with the electromagnetic

calorimeter, is designed to have a depth of >10 interaction lengths hermetically. This is sufficient to accurately measure all the energy of particles in jets, with the exception of muons which escape to the final layer of ATLAS. The fractional hadronic shower energy resolution is $\frac{\Delta E}{E} = \frac{50\%}{\sqrt{E}} \oplus 3\%$.

2.4.3.3   Forward Calorimeter

The Forward Calorimeter is exposed to a very high particle flux as it covers the high η region $3.1 < |\eta| < 4.9$. It is a LAr calorimeter used for both electromagnetic and hadronic measurements. It is divided into three sections, the first is constructed with copper and is used for electromagnetic interactions, the other two sections consist of tungsten and are used for hadronic measurements. The Forward Calorimeter has a total of 10 interaction lengths throughout and provides an energy resolution of $\frac{\Delta E}{E} = \frac{100\%}{\sqrt{E}} \oplus 10\%$ [39].

2.4.4   Muon Spectrometer

The Muon Spectrometer operates within a toroidal magnetic field and is the outermost part of the ATLAS detector which surrounds the calorimeter systems. The Muon Spectrometer will detect any charged particles that have a long lifetime and escape the calorimeter systems. Muons are particles that interact only through the electromagnetic and weak forces and have relatively high mass compared to electrons. Figure 2.10 shows the various muon systems. The Muon Spectrometer measures the momentum of particles in the region $|\eta| < 2.7$ and can be used to trigger on particles within $|\eta| < 2.4$ [49].

2.4.5   Magnet System

The ATLAS magnet system is comprised of three sections. Figure 2.11 shows the magnetic field, produced by the three sections, which covers a total of 12,000m^3.
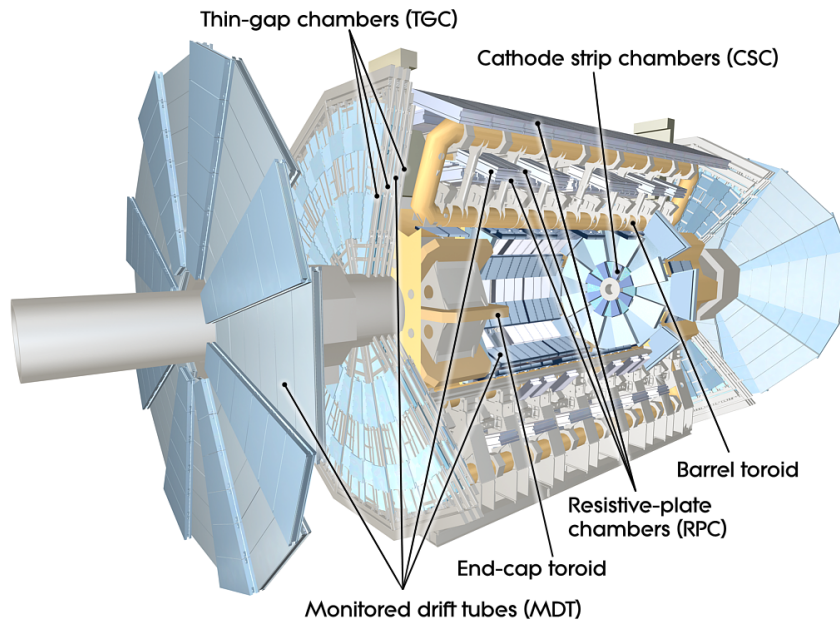
Figure 2.10: An overview of the ATLAS muon systems [44].

The innermost is the central solenoid magnet which surrounds the ID. It provides an axial magnetic field of 2T and has a total mass of 5.7 tonnes [50]. The remaining three magnets are the barrel and two endcap toroids which give ATLAS both its name and distinctive appearance. The barrel toroid consists of eight separate coils and contains 100km of superconducting wire. The toroid systems produce an average 0.8T field in the barrel and 1.3T in the endcaps [51].

2.4.6 Trigger System

The one billion per second proton-proton interactions, within ATLAS, require a sophisticated trigger system to record only information from interesting collisions. At present the read out and recording technologies are not sufficient to record all of the data from every collision. The ATLAS trigger system, shown in Figure 2.12, uses both a hardware-based first level trigger (Level-1) which uses coarse data from the calorimeters and muon detectors to make a first pass selection. This first trigger gives a fast read out in 2.5μs and reduces the event rate from roughly 40MHz to
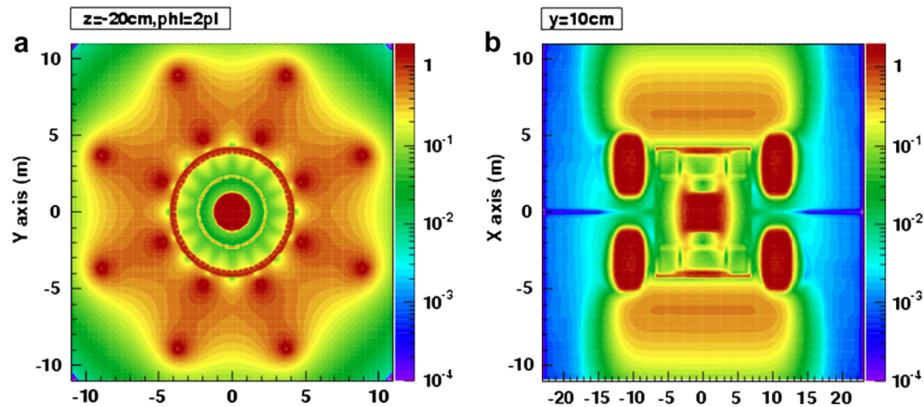
Figure 2.11: The configuration of the magnetic field in the ATLAS detector. The left plot shows the transverse cross section in the centre of the magnet system and therefore the field produced by the Endcap Toroids are not shown. While the right plot shows the longitudinal section [51]

100kHz rejecting over 99% of all events [52]. It also identifies Regions of Interest where features interesting for analyses at the next trigger level have been located. The next stage is known as the High Level Trigger. The Regions of Interest from Level-1 are analysed with the High Level Trigger and with full granularity to further reduce the event rate to 3.5kHz. Finally events are processed by the Event Filter which reconstructs the entire event and decides if the event should be recorded. This results in a final rate of approximately 1500Hz [53] which is a manageable amount of data to be recorded with available technologies.
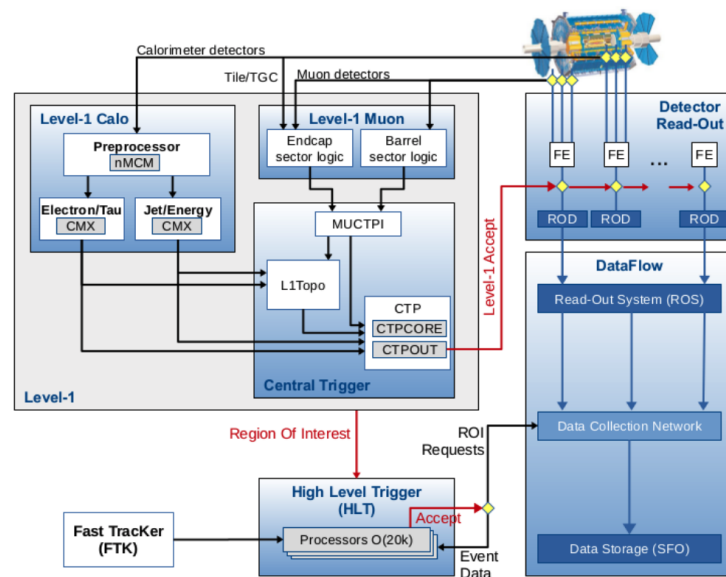
Figure 2.12: A schematic of the ATLAS trigger and data acquisition system [52].

2.5   The ATLAS Phase II Upgrade

The aim of the HL-LHC is to expand the dataset from $\sim$300fb^{-1}, acquired at the end of LHC running, up to $\sim$3000fb^{-1} by the end of the HL-LHC era before 2040. The HL-LHC will produce considerably higher radiation levels which the current detector could not cope with, this is discussed in detail in Section 3.1. Also the current granularity and readout of the ATLAS detector is not sufficient to deal with these high collision rates having $\langle\mu\rangle$, the average number of proton-proton collisions, as high as 200. Therefore most parts of the ATLAS detector, particularly electronics and triggering, will need to undergo significant upgrades. The largest upgrade required for the detector to cope with these conditions is the replacement of the currently installed ID with an entirely silicon tracker called the ITk [54], the ITk will be discussed in detail in Section 2.5.1. The calorimeter and trigger systems will also be affected by HL-LHC operation and will therefore need to be upgraded which will be discussed in Section 2.5.4. To reduce the impact of the $\langle\mu\rangle = 200$ pileup a new timing detector, the High Granularity Timing Detector (HGTD), will be added at high η, this will differentiate between tracks close in space but well separated in time. The HGTD was recently confirmed as part of the Phase II upgrade and its effects on many physics channels has not been explored. The effects of the HGTD on the $HH \to b\bar{b}\gamma\gamma$ will be discussed in this thesis and therefore it will be described in more detail in Section 2.5.3.

2.5.1   Inner Tracker

At the levels of pileup expected from the HL-LHC, the Transition Radiation Tracker (TRT) would significantly lose tracking efficiency, the ID will also not survive the increase in particle rates and integrated doses from HL-LHC running. Both will be replaced by an entirely silicon ITk. A sketch of the sensor layout of the ITk is shown in Figure 2.13. There will be a sub-detector of silicon pixels [55] closest to the interaction point and then silicon strips [56] at larger radii.
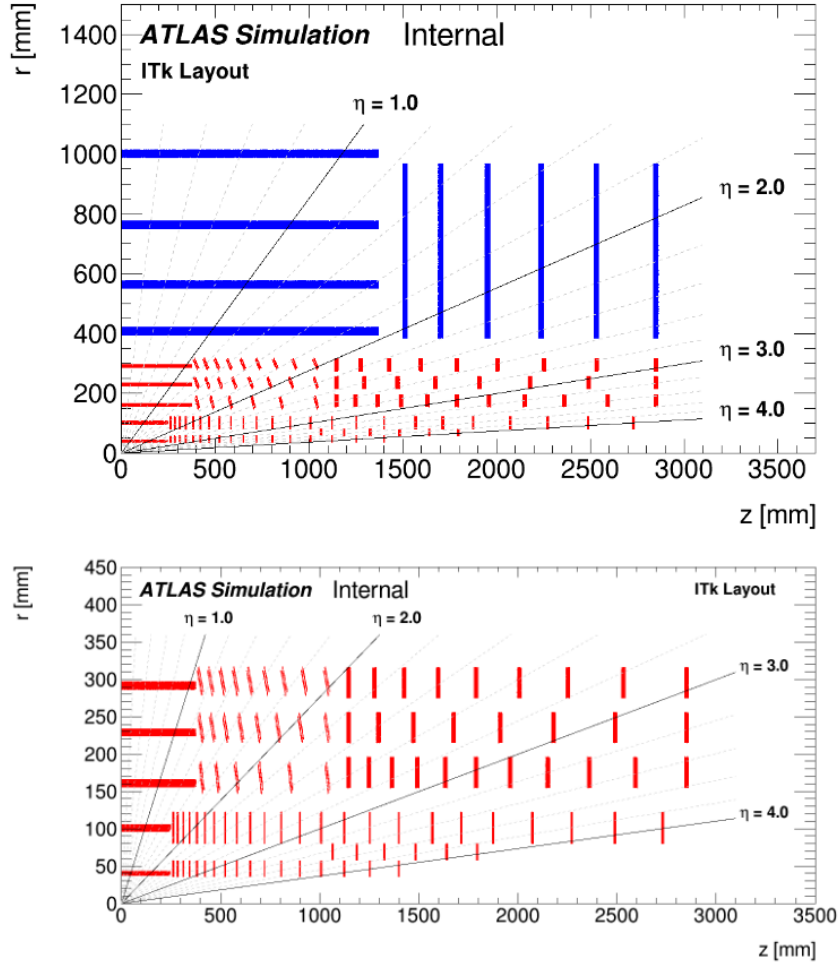
Figure 2.13: The layout of an upper quarter of the active area of the ITk detector. The layout is symmetrical about $R = 0$ and $\eta = 0$ with the interaction point at the origin. The top image shows the layout of both pixels (red) and strips (blue) while the bottom image is a zoomed-in view of the pixel detector only [57].

The pixel system will be extended in z covering the region $|\eta| < 4$ and also cover larger radii with a total coverage of 12.7m^2 and $\sim 5 \times 10^9$ channels. The geometry of the pixels will be different between the innermost layer (L0) and outer layers as well as between the barrel region and endcap regions. The current recommendation is to have L0 pixels in the barrel with a $25 \times 100 \mu$m^2 geometry and $50 \times 50 \mu$m^2 in the L0 endcaps and the outer layers. Both the $50 \times 50 \mu$m^2 and $25 \times 100 \mu$m^2 geometries will be considered in this thesis. In both cases the smaller pixel sizes, compared to the ID pixels of $50 \times 400 \mu$m^2, and the increase in the number of channels in the ITk will provide a considerable increase in detector granularity in regions of dense tracks.

The pixel system will consist of five barrel layers and five layers of rings covering large $|\eta|$. The innermost barrel layer will be positioned at a radius of 33mm, this was a relatively new decision and there are no detailed performance functions that consider L0 at 33m as yet. The latest functions are based on simulations assuming a L0 radius of 39mm, however it is possible to estimate the effects of smaller radii, which will be discussed in section 2.5.5 and the performance of three radii steps 39mm, 36mm and 33mm are considered in this thesis.

The rings are aligned either vertically or at a slight angle towards the interaction point. This design reduces the required area of pixel detectors needed, compared to an earlier proposed layout where the innermost barrel layers had a larger z coverage than the outer layers. This layout also benefits from both needing less service material and from reducing the material a forward particle has to traverse; leading to an improved extrapolated resolution at the vertex.

The silicon strip detector will have an active silicon area of approximately 165m^2, utilising two lengths of silicon strips in the barrel layers. Four barrel layers will enclose the interaction point each extending to $z = \pm1.4$m for a total length of 2.8m. Twelve vertically aligned endcap disks extend from $z = \pm(1.5{\to}3.0)$m separated equally in forward and backward regions. The barrel layers are split between 24.1mm and 48.2mm strip lengths for the inner two and the outer two barrel layers respectively. Layers of strip detectors with a small stereo angle between them are used to give both ϕ and z coordinates in the barrel or ϕ and r coordinates in the endcaps.

The ITk is designed to provide a minimum of nine precision measurements per track for any charged particle within $|\eta| < 4$ and with $p_T > 1$GeV and a minimum of 13 hits for $|\eta| > 2.7$.

2.5.2   Strip Modules

Figure 2.14 shows the assembly of a module for the ITk barrel combining both silicon sensors and Application Specific Integrated Circuits (ASICs). The sensors detect particles that pass through them and generate a signal. The signal is detected via implanted diode strips, capacitively coupled to the aluminium strips on the sensors, which are then connected via wirebonds to the front-end electronics chips, ATLAS Binary Chip (ABC) [56], these are attached to a hybrid flex circuit. Two hybrids with 10 readout chips (with each chip addressing 256 sensor strips) are glued onto the barrel strip sensors creating a module. 14 such modules are placed on either side of a low mass carbon core structure with embedded cooling called a stave. Figure 2.15 bottom shows a stave of 14 modules. The staves are the basic components from which the barrel is made. The communication between each module and the end of stave electronics is controlled by the Hybrid Control Chip (HCC) which handles data to and from the ABCs on the module [56]. Other features on the hybrid include the power distribution and monitoring circuits through the Autonomous Monitor and Control Chip (AMAC) (not shown in Figure 2.14). The production chips for the ITk strip modules will be the ABC* and HCC* [58]. The prototypes reported in this work are the ABC130 and HCC130.
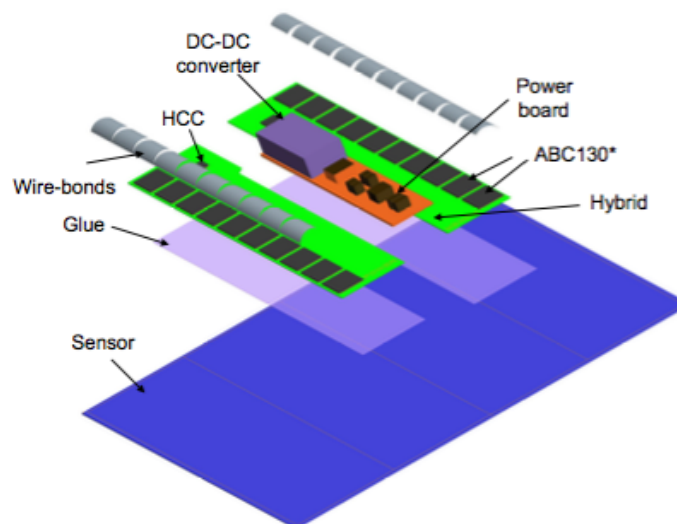
Figure 2.14: Breakdown of all the components of a strip barrel module [56]
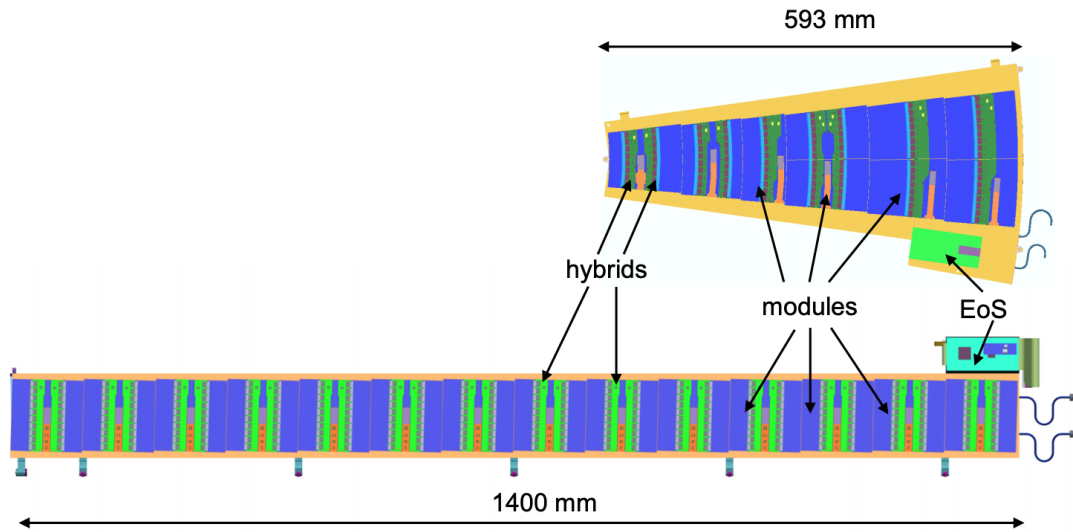
Figure 2.15:   Both endcap petal (top) and barrel stave (bottom) components overview [56]

2.5.2.1   Silicon Strip Sensors

Silicon can easily be doped with acceptors and donors to create respectively p- and n-type doped regions which makes it ideal for use in semiconductor technologies. An advantage is that different n-type and p-type regions can be created in the same silicon substrate. At the interface between p and n type regions any extra electrons or extra holes recombine to leave a depletion region of no net charge creating a pn diode junction. Silicon strip sensors are based on pn-junctions and can be seen as simple segmented diodes.

For the case of the silicon pixel and strip detectors the signal is determined by the charge generated by an incoming charged particle traversing the detector. Charged particles create electron-hole pairs as they ionise the depleted silicon substrate as shown in Figure 2.16. An applied bias voltage supplies an electric field which fully depletes the junction of charges. Any charges created in this region will drift, electrons to the n^+ strips and holes to the p^+ backplane. The signal induced at either end of the junction can be readout using amplification electronics. As shown in Figure 2.16 one side of the junction can be segmented into strips to provide spatial

hit information. The metal strips are connected to the readout electronics via wire-bonds and the signal is read by the front-end electronics (FEE) through capacitive AC coupling.
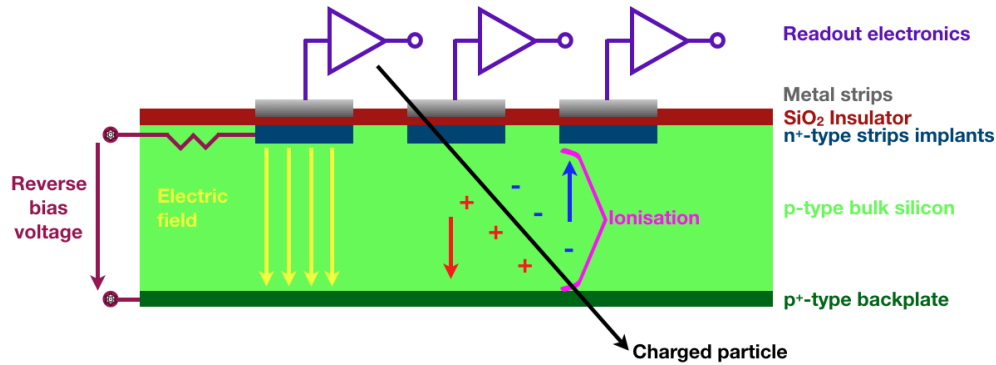
Figure 2.16: A schematic of a silicon strip sensor looking end on, showing three strips

2.5.2.2 On-Detector Readout

The basic block diagram for the readout of the front-end electronics of a single silicon strip sensor is shown in Figure 2.17. The current created by the separation of electron-hole pairs created by an ionising charged particle is collected and then readout as a charge. This charge is then integrated and amplified by the preamplifier creating a signal pulse. A pulse shaping circuit is then used to define the return to baseline of the signal. A discriminator with threshold is used to digitise the signal. In binary readout chips, only hit/no hit information is provided. The system registers 1 to indicate if the signal exceeds a predetermined threshold.

The ABC [59] is an ASICs made in a CMOS 130nm technology providing binary readout for 256 silicon strips. If the signal is above the threshold within a 25ns interval the hit is stored in the chip together with the time at which it occurred, until a trigger is given to release the hit information. The chip inputs the bunch crossing clock and control signals, these control signals include triggering and general commands [60]. They are received by the HCC and sent to the addressed ABCs. The HCC also receives the data from the ABCs and formats them before sending data to

the end of stave electronics.
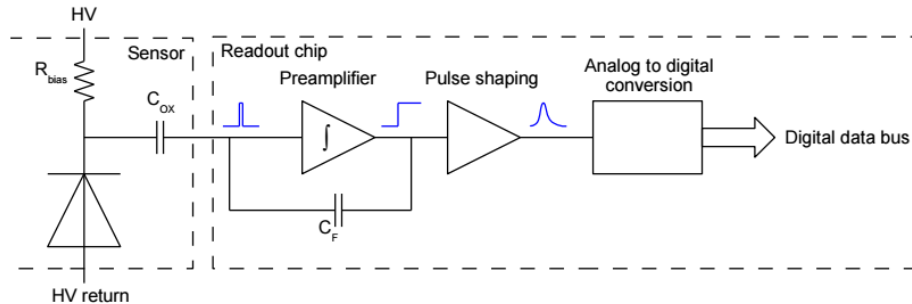
Figure 2.17: Box diagram of the front-end electronics for a silicon strip sensor [61]

2.5.3   HGTD - High Granularity Timing Detector

The HGTD will precisely measure the timings of charged particles to reduce background pileup from jets, as the increased pileup expected during HL-LHC running will require additional mitigation strategies [62]. It will cover the region $2.4 < |\eta| < 4.0$ where, despite the greatly enhanced pixel system, tracking ambiguity due to the high track density is greatest. It will have an active area of 6.4m^2 covering a radius between 120mm and 640mm at $z = \pm 3.5$m, in between the ITk and the endcap of the forward calorimeters. An overview of the original TDR version of the HGTD layout is shown in Figure 2.18, where the two double sided silicon layers are rotated in opposite directions by 15° to maximise hit efficiency [63], as shown in Figure 2.19. The sensors on each side of the layers are overlapped as shown in Figure 2.20 so that the number of hits is larger than the number of disks. As well as increasing the number of hits per track, the HGTD crucially also provides timing information. With the temporal spread of pileup collisions expected in the range 175ps to 260ps and the design track resolution of the HGTD between 30ps and 50ps (start to end of life respectively), a factor of $\frac{Average(175,260)}{30 \rightarrow 50} \approx 7.3 \rightarrow 4.4$ pileup suppression is achievable (start $\rightarrow$ end of life). The main tracking and timing parameters are shown in Table 2.1 [63].

In [63] it is assumed that the harsh radiation environment at high $|\eta|$ will re-

Table 2.1: The main tracking and timing parameters of the HGTD

Average number of hits per track	
$2.4 < \|\eta\| < 3.1$	$\simeq 2$
$3.1 < \|\eta\| < 4.0$	$\simeq 3$
Average time resolution per hit (start and end of lifetime)	
$2.4 < \|\eta\| < 3.1$	$\simeq$ 40ps (start) $\simeq$ 70ps (end)
$3.1 < \|\eta\| < 4.0$	$\simeq$ 40ps (start) $\simeq$ 85ps (end)
Average time resolution per track (start and end of lifetime)	$\simeq$ 30ps (start) $\simeq$ 50ps (end)

quire the innermost ring of the HGTD to withstand a Total Ionising Dose (TID) of $10.2 \times 10^{15} \mathrm{n}_{eq} \mathrm{cm}^{-2}$ and a total dose of 9.5MGy. These levels of radiation damage will necessitate the replacement of at least the lowest radius $(3.1 < |\eta| < 4.0)$ sensors and electronics at least once during the HL-LHC program. To fulfil the spatial and timing resolutions required for the HGTD, ATLAS have begun a broad research and development program into Low Gain Avalanche Detectors (LGADs) [64].
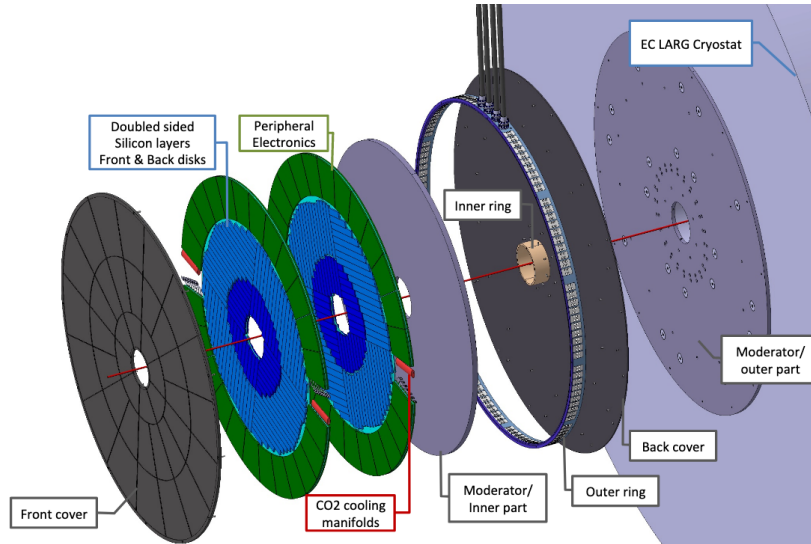
Figure 2.18: Global view of the HGTD to be installed on each of two calorimeter extended barrels. The various components are shown: hermetic vessel (front and rear covers, inner and outer rings), two instrumented double sided layers (mounted in two cooling disks), two moderator pieces placed inside and outside the hermetic vessel [63].

(a) First layer   (b) Last layer
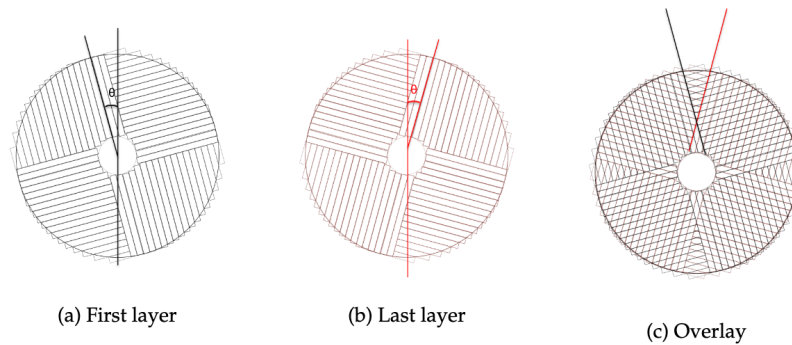
(c) Overlay

Figure 2.19: The orientation of the readout rows for the HGTD first and last layer separately, and overlay of both. Each layer is rotated in opposite directions by 15° [63].
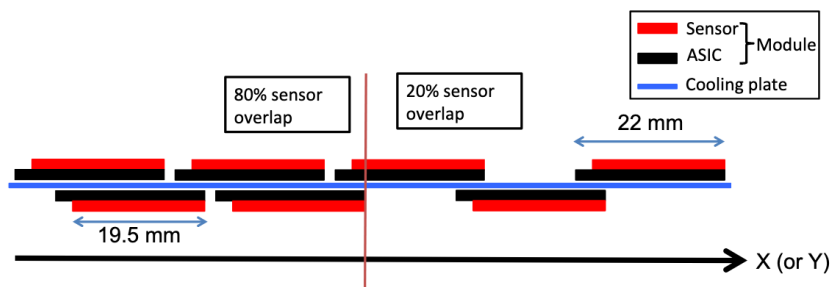
Figure 2.20: The schematic drawing shows the overlap between the modules on the front and back of a cooling disk. There is a sensor overlap of 20% for $r > 320$mm, and for $r < 320$mm an overlap of 80% between sensors [63].

2.5.4   Other ATLAS Phase II upgrades

As well as the major changes to the ATLAS detector with the replacement of the ID with the ITk and the inclusion of the HGTD there are also many other upgrades foreseen during the Phase II upgrade.

Both the LAr and Tile Calorimeters are expected to operate reliably throughout the HL-LHC phase, however the LAr readout electronics and the low-voltage powering system will be replaced due to the limited radiation tolerance of certain currently installed front-end components [65]. The trigger system will also need to be upgraded to account for the increase in instantaneous luminosity and pileup. The new Phase II trigger system will require the currently installed LAr readout electronics to

be replaced. Neither this system nor the current Tile Calorimeter readout electronics will survive the expected HL-LHC radiation doses [66]. The Phase II calorimeter readout electronics will allow for full LAr calorimeter granularity and longitudinal shower information to be available to the lowest level trigger processors. They will also allow the Tile Calorimeter to provide faster and more precise measurements.

By the start of Phase II operation the New Small Wheels should be installed and commissioned while the trigger and readout chain of the RPC and TGC trigger towers of the Muon Spectrometer will be completely redesigned for improved performance using modern technologies. Additional chambers will also be installed in the inner barrel layer. All the data from each bunch crossing from the TGC and RPC detectors will be available for trigger processing [67]. The Level-0 trigger system will take information from the LAr and Tile calorimeters and Muon Spectrometer at a rate of 40MHz. Followed by the Event Filter, where data is permanently stored at a rate of 10kHz [68].

2.5.5 Upgrade Physics Performance

Even with the much higher event rates, the Phase II upgrade of ATLAS is designed to produce similar or better physics performance compared to the current detector. A significant contribution to this is due to the ITk which will deliver superior b-tagging efficiencies over a larger η range.

2.5.5.1 Impact Parameter and Momentum Resolution

The impact parameter is a measure of the distance between the primary vertex and the point of closest approach of a track. The transverse impact parameter, d_0, is the distance in the x,y plane and the longitudinal impact parameter, z_0, is the z-coordinate of this point as shown in Figure 2.21. The precise measurement of the z_0 and d_0 in the ITk are essential to discriminate between heavy flavour jets originating from b- and c-quarks and those originating from light quarks and gluons.
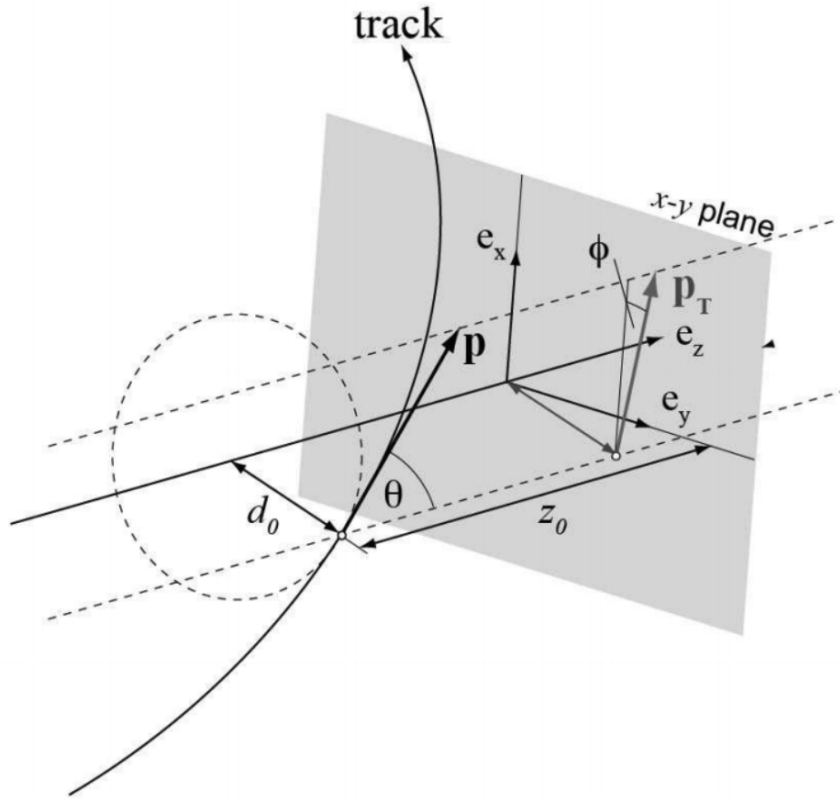
Figure 2.21: Diagram showing the transverse and longitudinal impact parameters [69]

Figure 2.22 shows the changes expected to the resolution of both the longitudinal and transverse impact parameters for simulated muons with $p_T = 1\text{GeV}$ and $p_T = 100\text{GeV}$.

The d_0 resolution of high p_T muons (top right) for the $50{\times}50\mu\text{m}^2$ pixel pitch gives similar performance to the Run-2 ATLAS detector as the IBL utilises a pixel pitch of $50{\times}250\mu\text{m}^2$ [70]. The improvement seen with the $25{\times}100\mu\text{m}^2$ pixel pitch by a factor two, compared to the IBL and $50{\times}50\mu\text{m}^2$ designs is due to the improved resolution in the ϕ coordinate, however for low momentum particles (top left) the resolution of both ITk pixel geometries deteriorates compared to Run-2. This is due to the difference in radii of the innermost pixel layers, 33mm for the IBL [70] and 39mm for the ITk. Investigations are ongoing into the feasibility of reducing the radius of the innermost ITk pixel layer to regain some of the lost resolution. The effect

of reducing this radius and of the different pixel geometries will be studied for the HH→$b\bar{b}\gamma\gamma$ channel in this thesis.

The resolution in z_0 for high p_T (bottom right) is improved for both ITk pixel geometries due to the relatively large IBL longitudinal pixel size. For both high and low p_T the $50\times50\mu$m^2 pixels outperform the $25\times100\mu$m^2 pixels in the extreme high and low $|\eta|$ regions.

The ITk silicon strip sensors will replace the IDs TRT straw tubes, where the superior resolution of the strips allows for a more precise measure of the sagitta♠ in the bending direction. As a result, the p_T resolutions for both ITk pixel geometries and at both momentum values under study, improve compared to that of the current detector as shown in Figure 2.23. For low p_T objects (left) there is relatively little difference between the performance of the two ITk pixel geometries and the resolution here is dominated by multiple scattering. For high p_T objects (right) the resolution of the $25\times100\mu$m^2 pixel pitch outperforms that of the $50\times50\mu$m^2 pitch at high η by a factor greater than two. This is because all the hits on a track at high η will be within pixels and therefore the resolution will be only affected by the choice of pixel pitch. At low η there are also hits in the strip sensors at lager radii, therefore the choice of pixel geometries does not greatly effect the resolution.

2.5.5.2   Pileup Jet Rejection

It is important that the ITk track reconstruction can discriminate between jets from the hard scatter vertex and those from pileup vertices especially with an expected pileup of $\langle\mu\rangle = 200$. Pileup jet rejection is based on the discriminant R_{pT} which is detailed in Refs [71] and [72] and is defined as the sum of the p_T of tracks that are associated with the jet originating from the hard scatter vertex divided by the fully calibrated jet p_T. This discriminant therefore peaks at 0 and falls sharply for pileup jets where there is relatively little p_T from the hard scatter vertex. Figure

---

♠ How much an arc deviates from a straight line is known as the sagitta of the arc. In high energy physics experiments it is used to measure the radius of curvature of tracks.
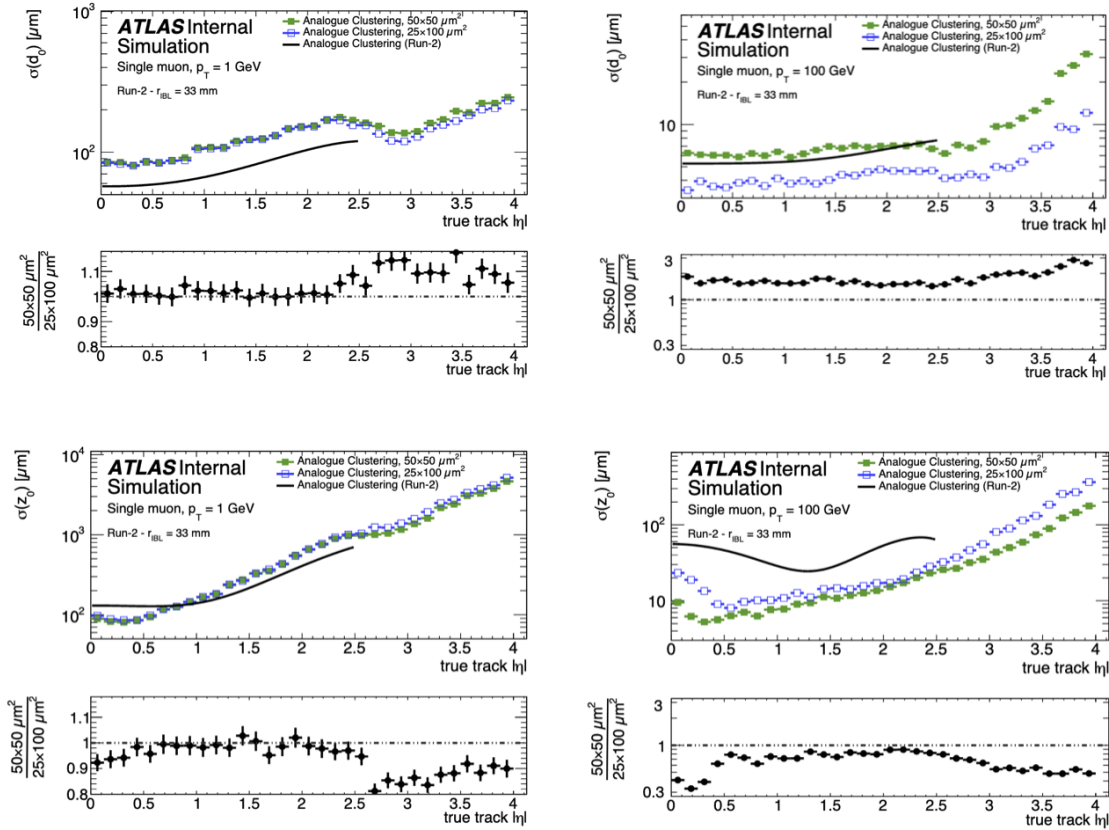
Figure 2.22: The transverse (top) and longitudinal (bottom) impact parameter resolutions of the ITk as a function of pseudorapidity for muons with $p_T = 1$Gev (left) and $p_T = 100$GeV (right) and $\langle \mu \rangle = 0$. Comparison to the Run-2 performance is also shown. The ratio plots are obtained from the resolutions using $50 \times 50 \mu m^2$ pixels over the resolutions using $25 \times 100 \mu m^2$ pixels [57]

2.24 shows the pileup rejection as a function of signal jet efficiency for di-jet and $t\bar{t}$ events, with an average of 200 pileup interactions superimposed using $50 \times 50 \mu m^2$ or $25 \times 100 \mu m^2$. Compared are the results for different η ranges and for two samples in jet p_T. Jets in the p_T interval between 20GeV and 40GeV yield more low-p_T particles and hence the multiple scattering in the detector material is expected to dominate in the performance comparison. For jets at p_T above 40GeV the impact resolution for charged particles is driven by the choice of pixel pitch. As can be seen in the Figure 2.24, both choices of pixel pitch yield very similar signal jet efficiencies at a typical rejection working point of 50 against pileup jets, independent of the jet p_T range. In the forward region, a gain of less than 1% in efficiency is observed,
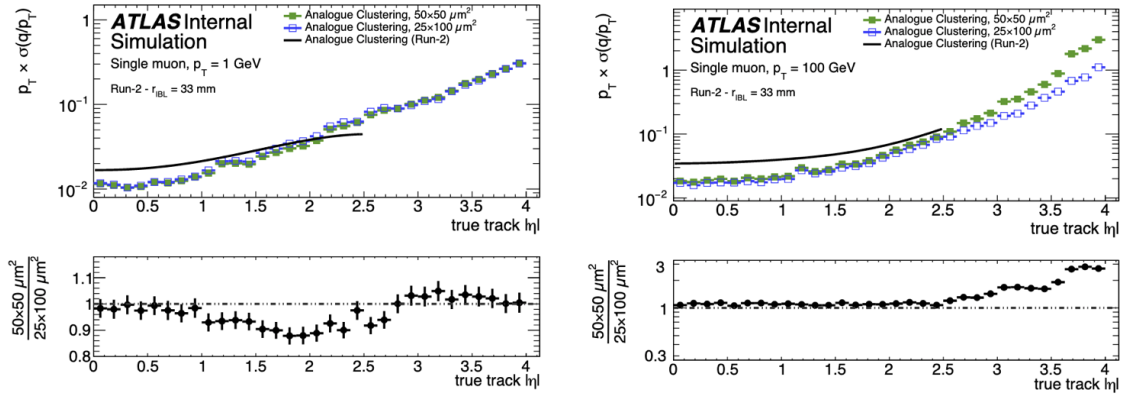
Figure 2.23: The relative track p_T resolution of the ITk as a function of pseudo-rapidity for muons with $p_T = 1\text{GeV}$ (left) and $p_T = 100\text{GeV}$ (right) and $\langle \mu \rangle = 0$. Comparison to the Run-2 performance is also shown. The ratio plots are obtained from the resolutions using $50 \times 50 \mu\text{m}^2$ pixels over the resolutions using $25 \times 100 \mu\text{m}^2$ pixels [57]

despite the improved impact parameter resolution in this region [73].
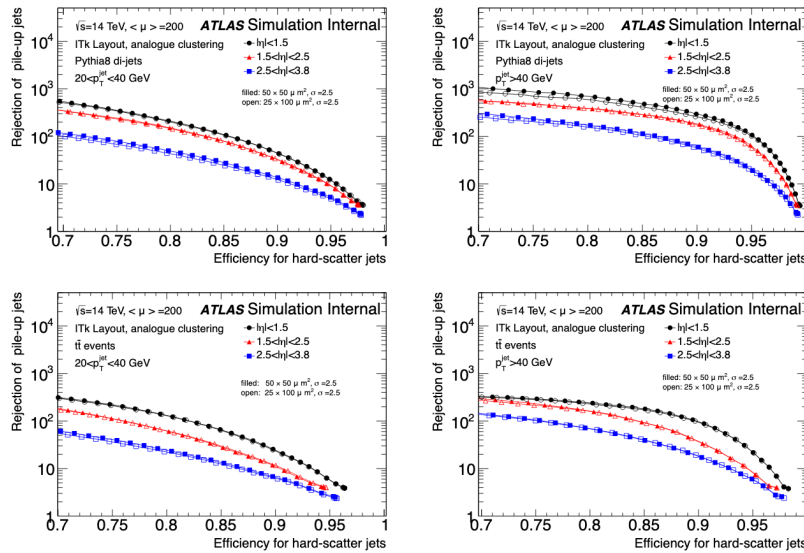
Figure 2.24: The rejection of pileup jets as a function of the efficiency for hard-scatter jets with $20 < p_T < 40\text{GeV}$ (left) and $p_T > 40\text{GeV}$ (right) using the R_{pT} discriminant. Shown are results for di-jet events (top) and $t\bar{t}$ events (bottom), with an average of 200 pileup events using $50 \times 50 \mu\text{m}^2$ or $25 \times 100 \mu\text{m}^2$ [73]

The expected resolution in the z-coordinate as a function of local pileup density of successfully reconstructed vertex candidates for two different processes is shown in

Figure 2.25. The resolution is not expected to be greatly affected by pileup for both cases. A pixel pitch of $50{\times}50\mu$m^2 would result in a slight improvement in resolution as a result of the track z_0 resolution [57]. For $t\bar{t}$ and $H \rightarrow \nu\nu\nu\nu$, the z coordinate resolution is expected to both greatly improve and also become considerably more robust against pileup with respect to the Run-2 detector.
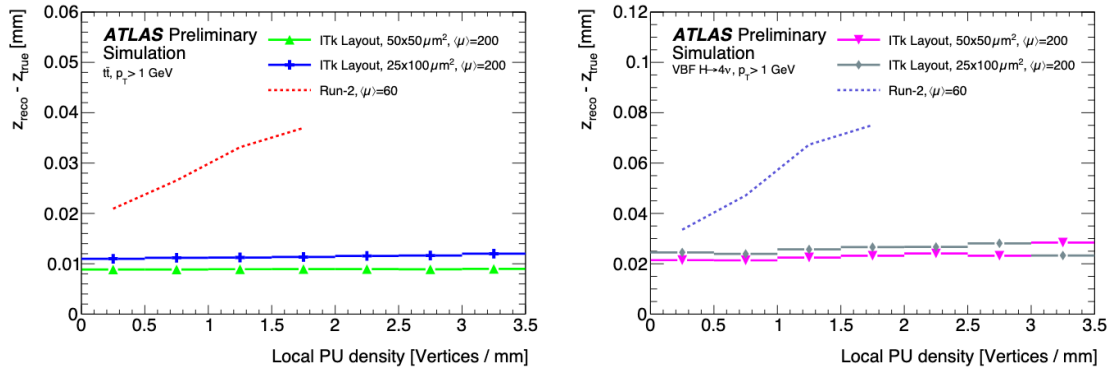
Figure 2.25: The resolution of the z coordinate of the reconstructed primary vertex for $t\bar{t}$ (left) and vector boson fusion $H \rightarrow \nu\nu\nu\nu$ (right) events as a function of local pileup density in events with $\langle\mu\rangle = 200$. Results use pixel sizes of $50{\times}50\mu$m^2 and $25{\times}100\mu$m^2 for the ITk. The primary vertex candidate is identified as the vertex with the highest Σp_T^2 of associated tracks [57]

2.5.6   Upgrade Performance Functions

To allow analyses to be performed for the HL-LHC, Upgrade Performace Functions (UPF) are calculated [74] [75]. These functions take the final state truth information of an object from Monte Carlo (MC) data samples as input. The UPFs are used to smear the p_T values and η position of a final state object as well as various reconstruction efficiencies to mimic the expected detector response. This thesis is focussed on looking for b-quarks and photons, therefore only the UPFs related to these objects and other potential backgrounds will be discussed in detail. The UPFs are constantly updated as more decisions are made on the layout of the HL-LHC ATLAS detector and more accurate material budget estimates are produced resulting in more realistic simulated detector responses. As the previously published studies used now outdated functions, the performance differences between the dif-

ferent versions of the UPFs are compared and detailed below. Figure 2.26 shows the difference in radiation length as a function of η, between a previous layout (left) and the updated Layout 3.0 (right) which has a more realistic material budget. The previous layout was found to contain several mistakes, most noticeable is the Support Structure differences where the inner barrel support weight was set as 272g instead of 1466g and important contributions, such as pixel module flex cables are missing entirely. As the latest published HL-LHC results for the $HH \rightarrow b\bar{b}\gamma\gamma$ channel [26] utilises the previous layouts material budget it is therefore inaccurate.
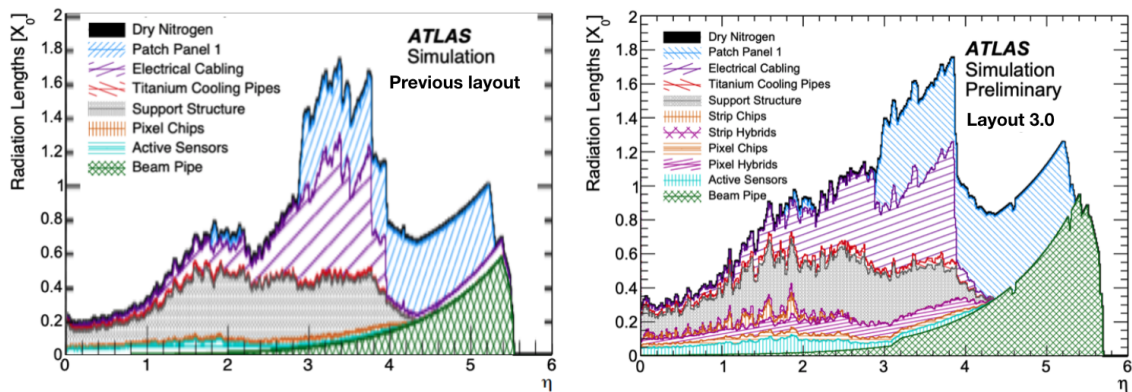
Figure 2.26: Radiation length X_0 verses η for a previously adopted ITk model (left) [56] and the Layout 3.0 model (right) [76]. The figures show only positive η since the material distribution is symmetric about $\eta = 0$

2.5.6.1 Photon Performance

The photon efficiency and fake rates are computed using simulations based on the detector layout presented in Ref. [75]. The efficiency for identifying photons as a function of p_T is shown in Figure 2.27 which plateaus at 85% above 150GeV. The probability of an electron faking a photon is assumed to be 2% in the barrel region and 5% in the endcap regions. The probability that a jet emerging from the primary interaction is mis-identified as a photon is $<5\times10^{-4}$.
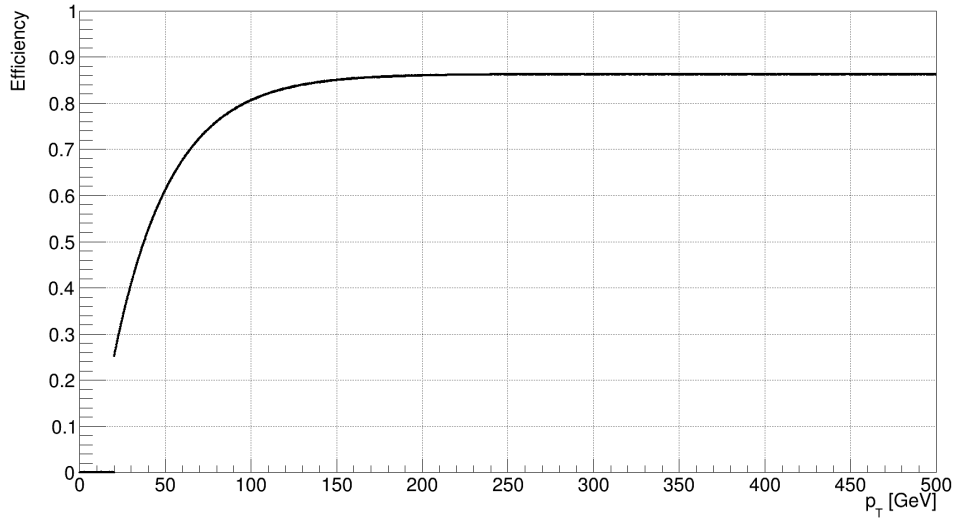
Figure 2.27: Expected photon reconstruction efficiency as a function of p_T
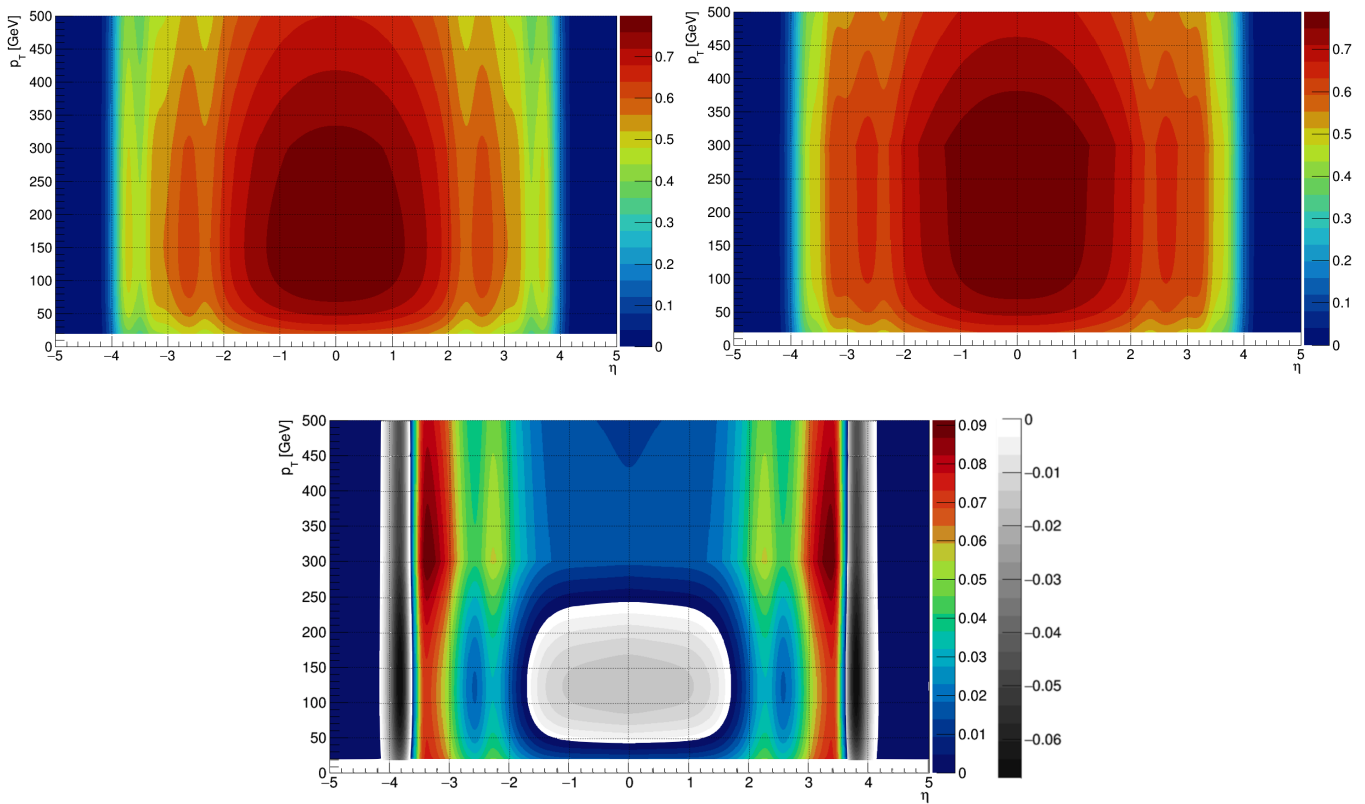
Figure 2.28: b-tagging efficiency for the MV2c10 tagging algorithm for a previous layout (top left), Layout 3.0 (top right) and the difference in performance (Layout 3.0 - previous layout) (bottom) in p_T-η space
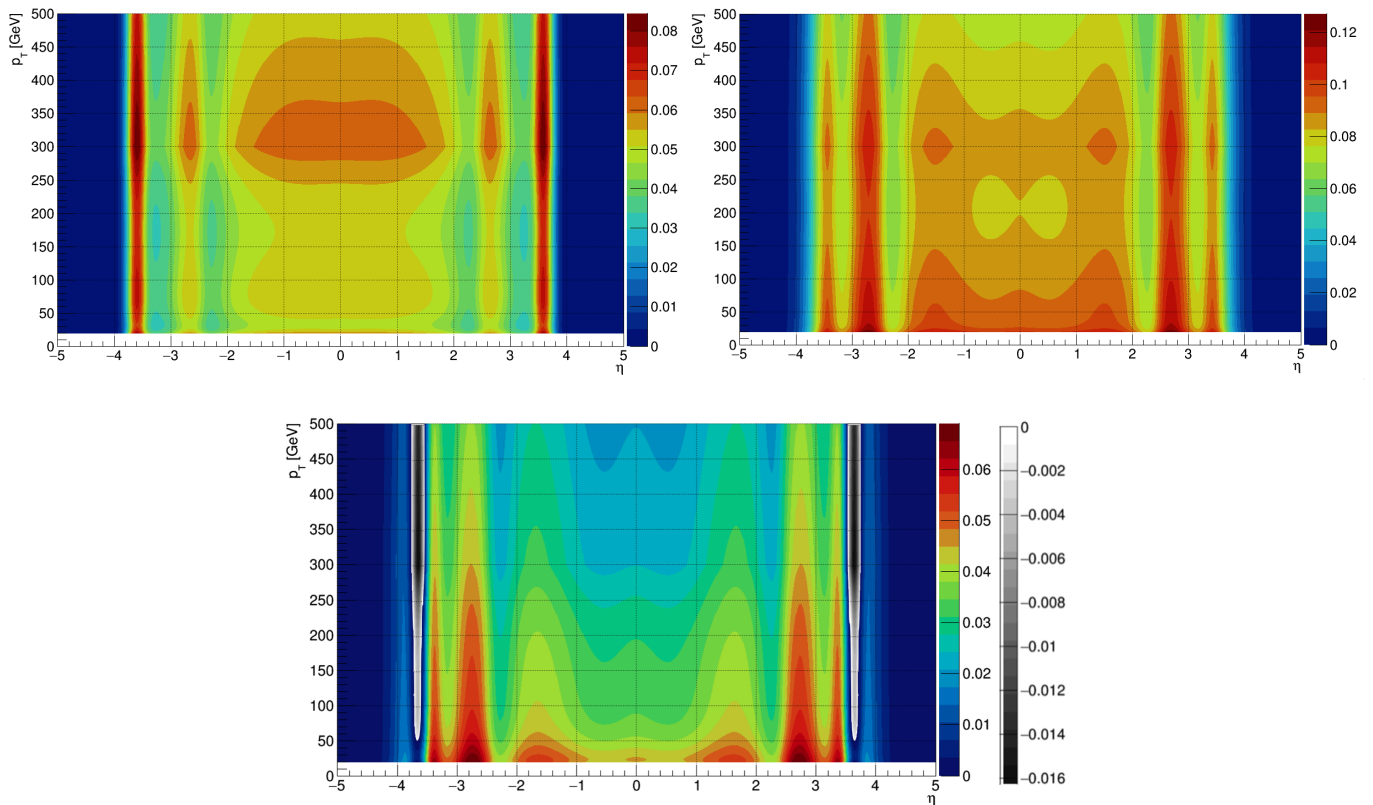
Figure 2.29: *c*-tagging efficiency for the MV2c10 tagging algorithm for a previous layout (top left), Layout 3.0 (top right) and the difference in performance (Layout 3.0 - previous layout) (bottom) in p_T-η space

2.5.6.2   b-tagging Algorithms

The *b*-tagging algorithms used in ATLAS exploit the long lifetime of hadrons containing *b*-quarks and they are either based on the track impact parameters (IP3D [77]) or on the properties of displaced vertices reconstructed inside the jet. For secondary vertex reconstruction, the algorithms used are the iterative vertex finder SV1 [78] and the JetFitter algorithm [79] (the latter goes beyond the secondary vertex and also searches for tertiary vertices).

The MV2c10 algorithm [77] is a Boosted Decision Tree (BDT) algorithm that combines the input of the IP3D, SV1 and JetFitter algorithms. The input variables for the MV2c10 algorithm are shown in Ref. [80]. The jet p_T and η are included
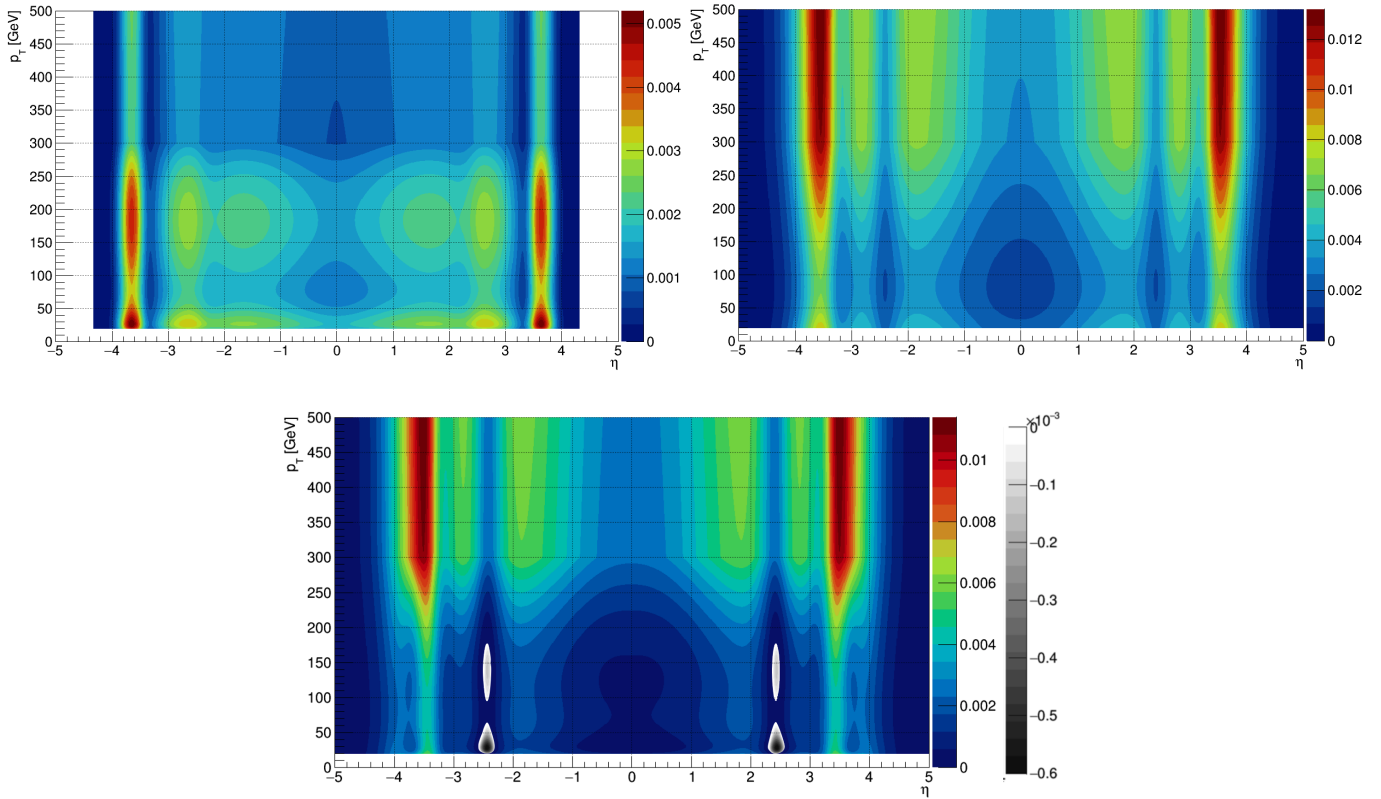
Figure 2.30: *l*-tagging efficiency for the MV2c10 tagging algorithm for a previous layout (top left), Layout 3.0 (top right) and the difference in performance (Layout 3.0 - previous layout) (bottom) in p_T-η space

in the training variables in order to exploit the correlations with other variables. The MV2c10 algorithm was trained on a subset of events from a simulated $t\bar{t}$ sample which includes all the $t\bar{t}$ decay channels. The fraction of jets originating from *c*-quarks used in the training phase of the MV2c10 algorithm is 7%, such that the training is performed assigning *b*-jets as signal and a mixture of 93% jets originating from light quarks and 7% *c*-jets as background.

The latest published HL-LHC results for the $HH \rightarrow b\bar{b}\gamma\gamma$ channel [26] utilises the MV2c10 *b*-tagging algorithm which is based on a detector model that overestimates the performance of the detector. Figure 2.28 shows the *b*-tagging performance for the MV2c10 tagging algorithm for a previous layout (top left), Layout 3.0 (top right) and the performance difference (bottom) (performance of Layout 3.0 - performance
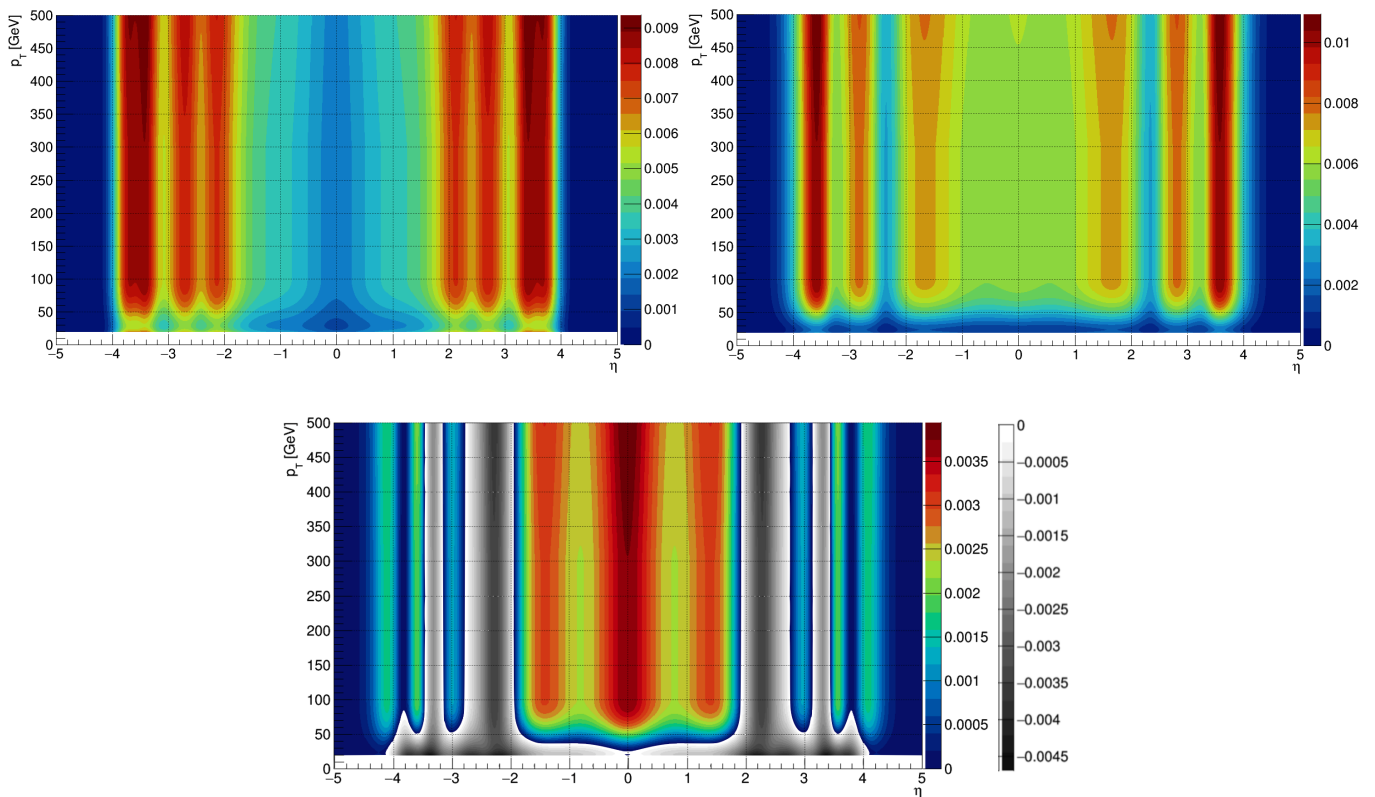
Figure 2.31: Pileup-tagging efficiency for the MV2c10 tagging algorithm for a previous layout (top left), Layout 3.0 (top right) and the difference in performance (Layout 3.0 - previous layout) (bottom) in p_T-η space

of previous layout) in p_T-η space. Figure 2.28 (bottom) has two separate scales; one positive showing the improvement possible from Layout 3.0 and one negative showing regions where performance decreases due to the more realistic material budget. The Layout 3.0 MV2c10 algorithm is based on a pixel sensor pitch of $50{\times}50\mu\mathrm{m}^2$ and as well as giving the probability a b-jet is correctly b-tagged, it also provides the likelihood of other physics objects being incorrectly b-tagged. Figures 2.29, 2.30 and 2.31 show the performance differences between the previous layout and Layout 3.0 for a c-jet, l-jet and a pileup jet to be reconstructed as a b-jet respectively. Note that for these plots a positive increase means that physics object is more likely to be falsely reconstructed with Layout 3.0.
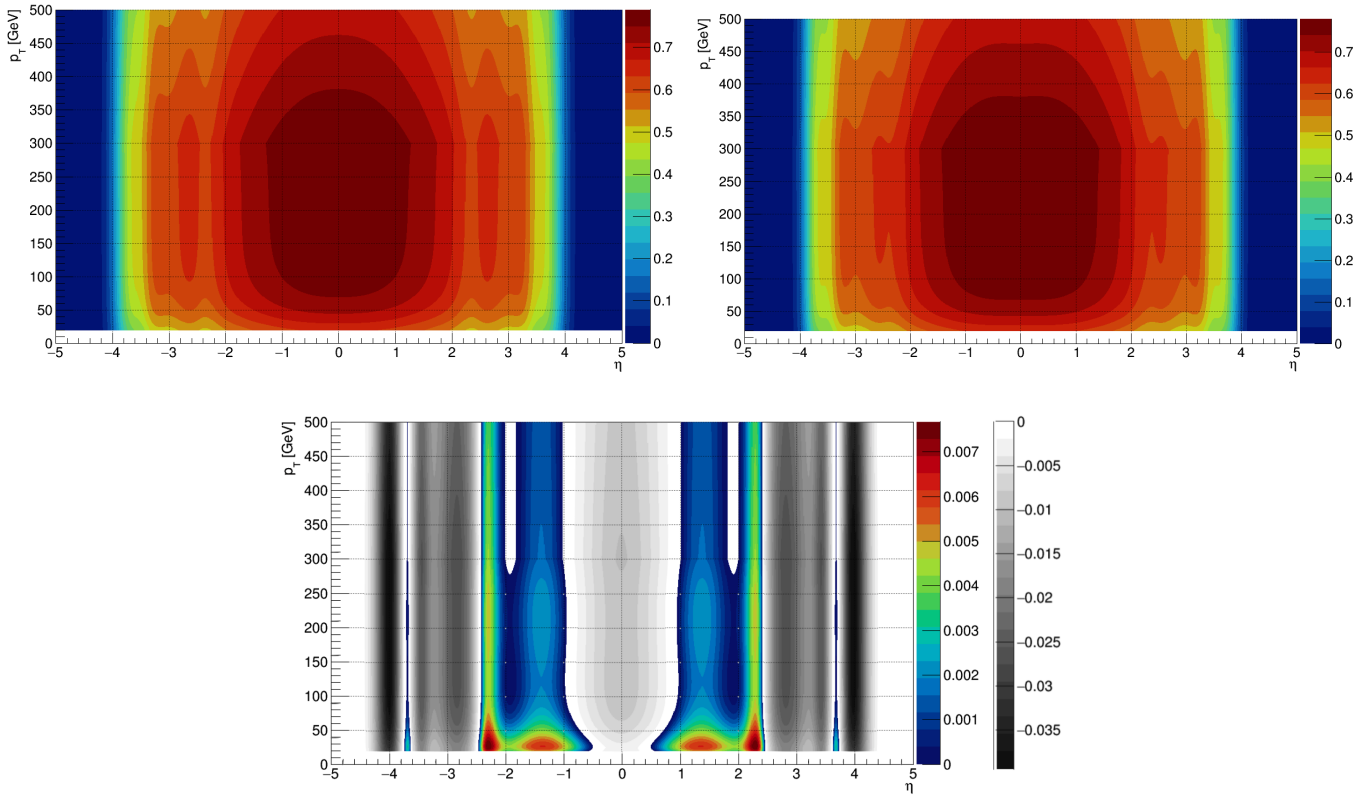
Figure 2.32: b-tagging efficiency for the MV2c10 tagging algorithm for pixel sensor geometries $50{\times}50\mu\mathrm{m}^2$ (top left), $25{\times}100\mu\mathrm{m}^2$ (top right) and the difference in performance ($25{\times}100\mu\mathrm{m}^2$ - $50{\times}50\mu\mathrm{m}^2$) (bottom) in p_T-η space

The MV2c10 algorithm has also been trained using the expected performance of pixel sensors with a pitch of $25{\times}100\mu\mathrm{m}^2$. Figure 2.32 shows the b-tagging performance for the MV2c10 tagging algorithm with a pixel sensor pitch of $50{\times}50\mu\mathrm{m}^2$ (top left), $25{\times}100\mu\mathrm{m}^2$ (top right) and the difference in performance (bottom) (performance of $25{\times}100\mu\mathrm{m}^2$ - performance of $50{\times}50\mu\mathrm{m}^2$) in p_T-η space. As before, Figures 2.33, 2.34 and 2.35 show the performance differences between the two pixel sensor geometries for a c-jet, l-jet and a pileup jet to be reconstructed as a b-jet respectively. The effects of these changes on the expected performance of the $HH \rightarrow b\bar{b}\gamma\gamma$ channel will be investigated in Chapter 6.

At the time of this thesis, dedicated upgrade performance functions were not avail-
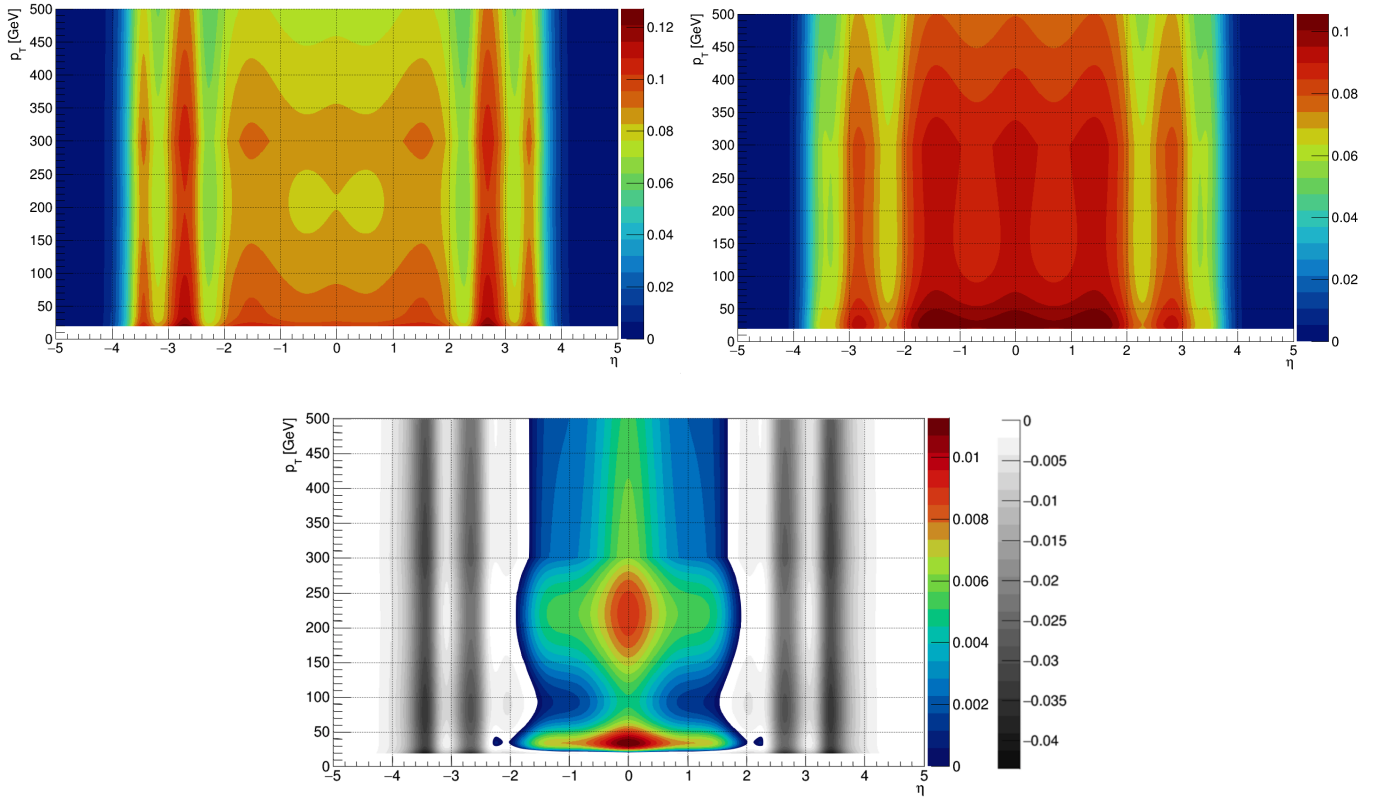
Figure 2.33: *c*-tagging efficiency for the MV2c10 tagging algorithm for pixel sensor geometries $50{\times}50\mu\text{m}^2$ (top left), $25{\times}100\mu\text{m}^2$ (top right) and the difference in performance ($25{\times}100\mu\text{m}^2$ - $50{\times}50\mu\text{m}^2$) (bottom) in p_T-η space

able for studies into reducing the radius of the innermost ITk layer. However, as shown in Figures 2.36 and 2.37 the expected light jet rejection factors for radii of 39mm, 36mm and 33mm in different η and p_T ranges can be extracted for both $50{\times}50\mu\text{m}^2$ and $25{\times}100\mu\text{m}^2$ pixel geometries respectively. This will also be investigated in Chapter 6.
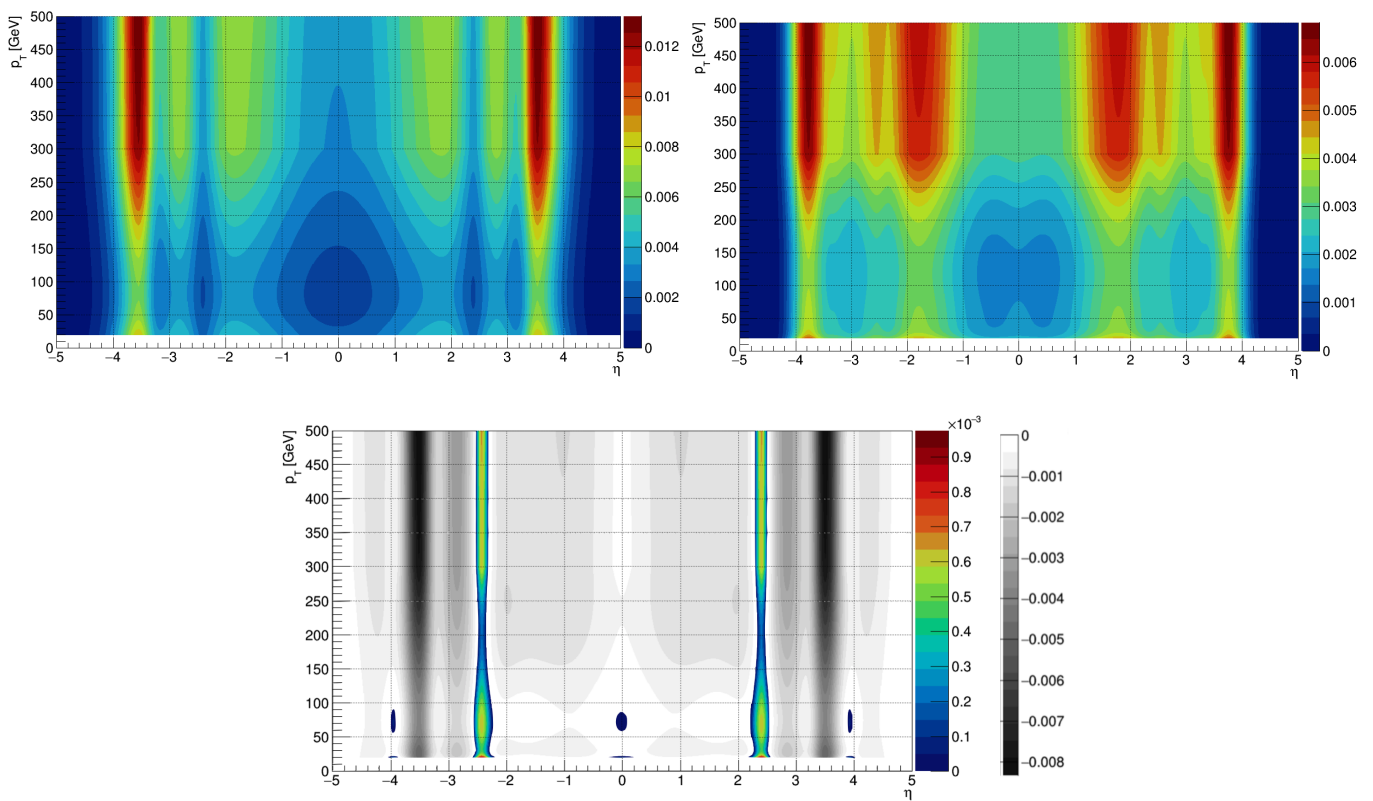
Figure 2.34: *l*-tagging efficiency for the MV2c10 tagging algorithm for pixel sensor geometries $50{\times}50\mu\mathrm{m}^2$ (top left), $25{\times}100\mu\mathrm{m}^2$ (top right) and the difference in performance ($25{\times}100\mu\mathrm{m}^2$ - $50{\times}50\mu\mathrm{m}^2$) (bottom) in p_T-η space
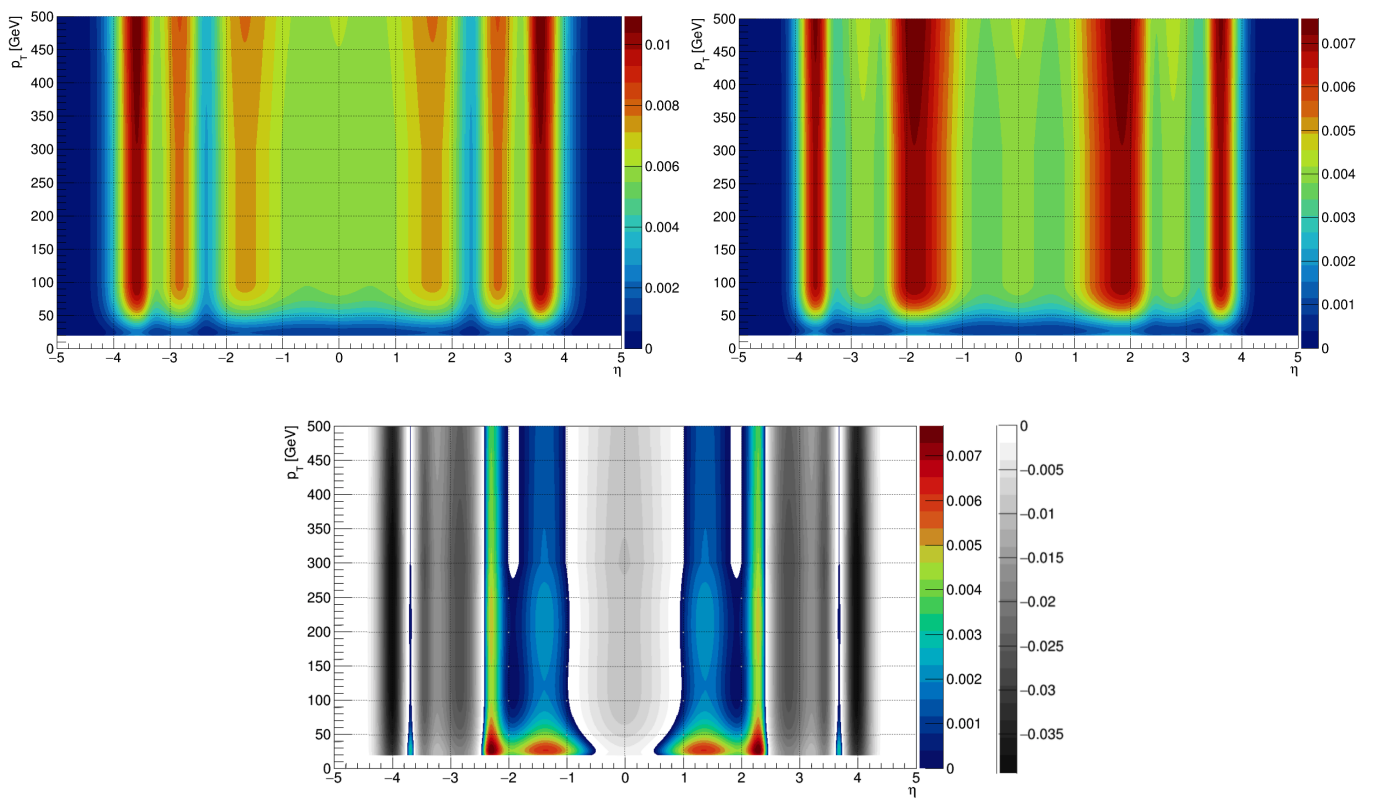
Figure 2.35: Pileup-tagging efficiency for the MV2c10 tagging algorithm for pixel sensor geometries $50{\times}50\mu\text{m}^2$ (top left), $25{\times}100\mu\text{m}^2$ (top right) and the difference in performance ($25{\times}100\mu\text{m}^2$ - $50{\times}50\mu\text{m}^2$) (bottom) in p_T-η space
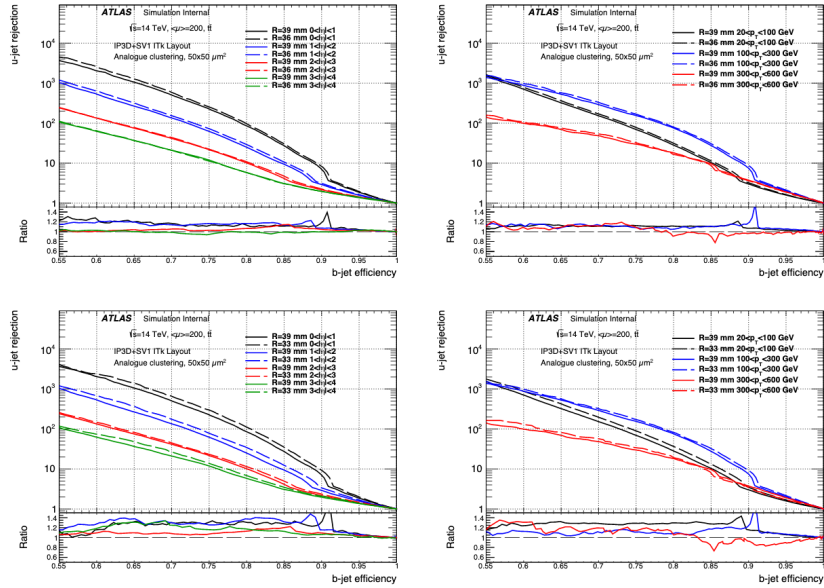
Figure 2.36: Light jet rejection as a function of b-tagging efficiency using the combined IP3D+SV1 algorithm and a pixel sensor geometry of $50\times50\mu\mathrm{m}^2$ at different radii (39mm vs 36mm (top) and 39mm vs 33mm (bottom)) for the innermost ITk layer. The effects are also shown in several η regions (left) and several p_T regions (right) [73]
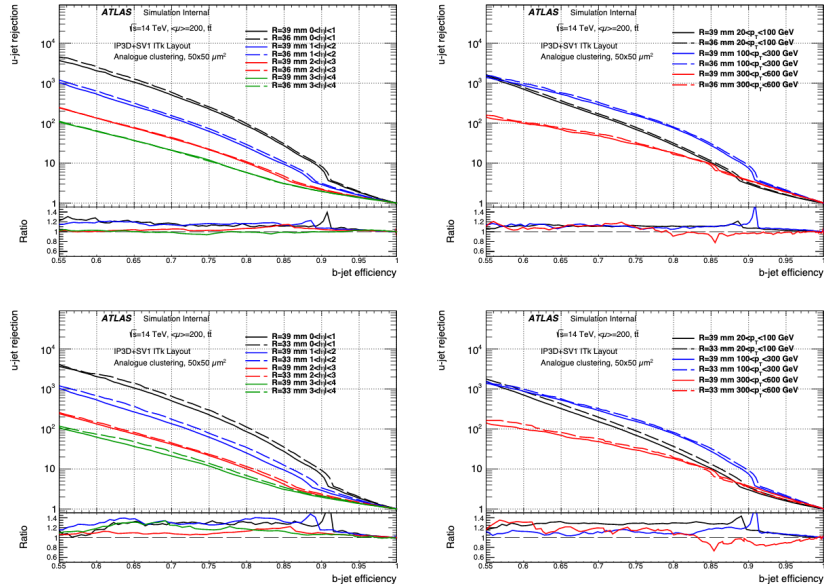
Figure 2.37: Light jet rejection as a function of b-tagging efficiency using the combined IP3D+SV1 algorithm and a pixel sensor geometry of $25\times100\mu\mathrm{m}^2$ at different radii (39mm vs 36mm (top) and 39mm vs 33mm (bottom)) for the innermost ITk layer. The effects are also shown in several η regions (left) and several p_T regions (right) [73]

CHAPTER 3

IRRADIATIONS

Prototype silicon strip sensors and readout electronics have been exposed to doses equivalent to those that are expected in the ITk by the end of the HL-LHC era. The University of Birmingham Medical Physics Cyclotron [81] is one of several facilities capable of delivering these doses, see Section 3.2.1.

3.1   Radiation Effects in Silicon

The two main types of radiation damage are firstly a single event effect due to the energy deposited by a single particle and secondly cumulative effects, principally displacement damage where protons or neutrons cause lattice defects [82]. These effects produce damage that can be roughly separated into bulk damage and surface damage, where bulk damage has the predominant effect on silicon sensors.

Incoming radiation, with energy roughly 15eV [83], can displace an atom (or several atoms, dependant on sufficient energy by a knock-on effect) from its original lattice position resulting in vacancies in the lattice [82]. At room temperatures these defects, both the displaced atoms, known as interstitial atoms, and the vacancies, become mobile and can form defect clusters in the silicon. The defects result in changes to the electric properties of the silicon by an increase in both leakage current and the trapping of produced charges, both culminate in a reduction to the recorded signal. The defects also alter the effective doping concentration which requires an increase in bias voltage to keep the bulk depleted of charge carriers.

Surface effects occur at the interfaces, where liberated electrons and holes get trapped. These effects include charge trapping in the oxides and at the SiO_2/Si interface. In deep submicron CMOS technologies, such as the one used for the ITk on-detector electronics, the oxide affected by radiation is the Shallow Trench Isolation (STI) oxide and its interface to the silicon. The gate oxide is too thin (few nm) to make a significant contribution as its thickness permits fast recombination of trapped holes with electrons from the gate or silicon bulk [84]. However the STI is a thick oxide at the edge of the transistor used for isolation. Radiation passing through the oxide creates electron-hole pairs. These electron-hole pairs typically recombine, but some of the more mobile electrons can escape the SiO_2, under the influence of electric fields, leaving behind the less mobile ions which migrate to the interface resulting in a layer of fixed positive charge [85]. This results in radiation induced interface states. Figure 3.1 shows an energy band schematic of the process that leads to these radiation induced interface states. The trapped positive charges, which accumulate with prolonged irradiation [86], and interface states change the leakage current and threshold properties of the transistor.

The narrower the transistor, the larger the effects of the irradiation, if the channel is wide the positive charge in the STI only effects the periphery and the main transistor is not greatly influenced. This effect, typical of submicron technologies, is called Radiation Induced Narrow Channel Effects (RINCE) [87]. The effect of RINCE on the leakage current of N(negative)-type Metal Oxide Semiconductor (NMOS) transistors

is discussed here as it is relevant to the work described in this chapters.
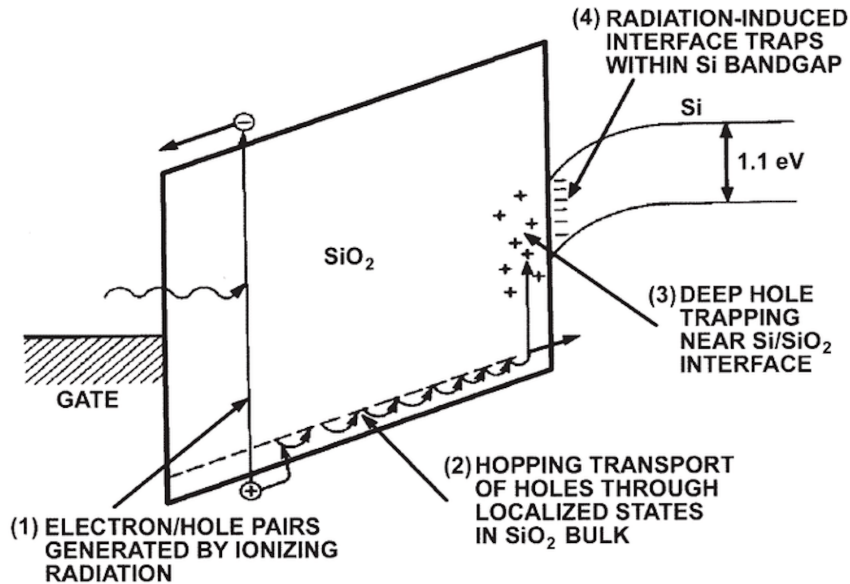
Figure 3.1: Energy band schematic showing the generation of radiation induced interface states [88]

Figure 3.2 shows the charges which accumulate in and around the STI of a MOSFET during irradiation. When irradiation begins, trapped positive charges in the bulk of the oxides rapidly accumulate increasing the leakage current (a). Further irradiation continues to increase the leakage but at a lesser rate, this is due to a gradual build up of negative interface states which begin to compensate for the positive trapped charges (b). After a certain dose the leakage current peaks and begins to decrease. This is due to the saturation of available states for trapping positive charges in the STI oxide, while the negative interface states continue to build (c). The dose has now reached a point where the negative interface states are more efficiently created than the trapped positive charges causing a decrease in the leakage current (d). Further irradiation would continue to decrease the leakage current to close to the original pre-irradiation value. However if the irradiation stops, there is no longer a build up of negative or positive charges. The thermal energy begins to pull away the trapped positive charges much more efficiently than the negative charges, this rapidly decreases the leakage current (e). When irradiation restarts, positive
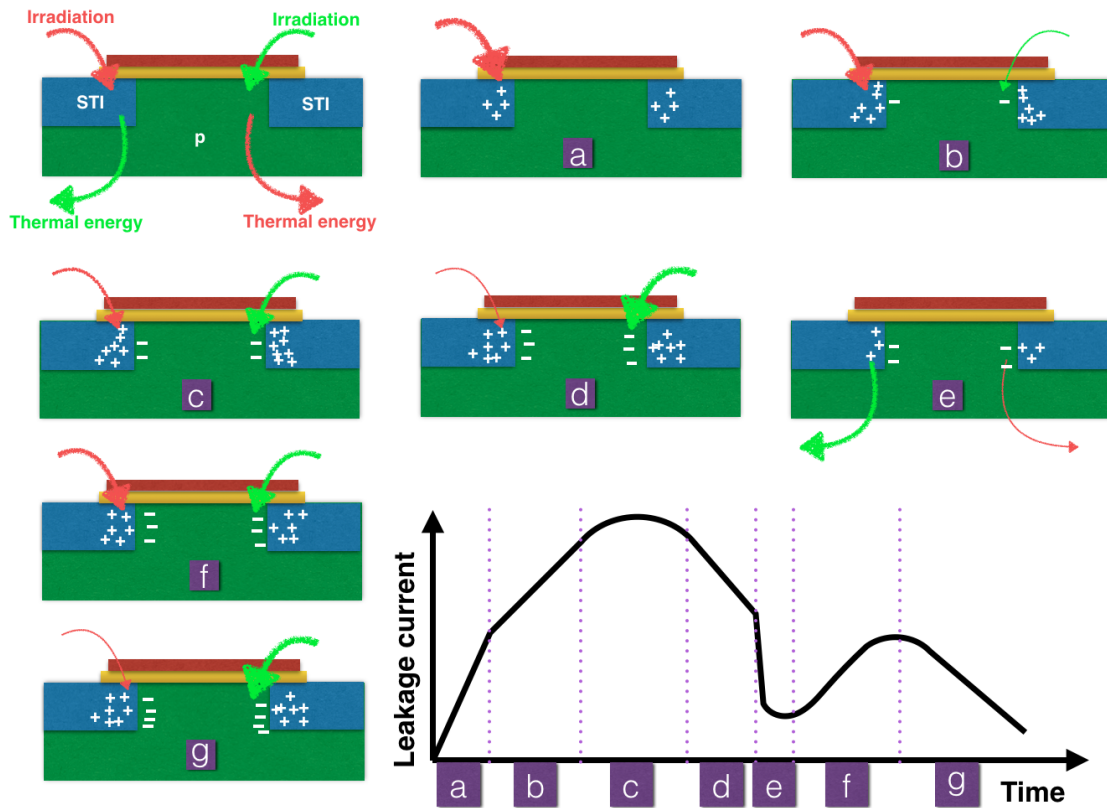
Figure 3.2: A series of diagrams showing the RINCE on the leakage current of a MOSFET caused by trapped charges in the STI. Red arrows indicate processes leading to an increase in leakage current and green arrows processes leading to a decrease

charges become trapped again however the residual negative interface states prevent the leakage current from peaking higher than before (f). Further irradiation will saturate the trapping states, as in (c), while the negative interface states continue to compensate, eventually returning to the pre-irradiation leakage current (g). Due to inconsistent irradiation in the LHC experiments♠, a behaviour as shown in Figure 3.2 bottom right is observed. This effect is heavily dose rate and temperature dependant as shown later in this chapter.

♠ There are many periods throughout LHC operation where there are no collisions e.g. during the particle acceleration, after a beam dump or Christmas holidays and therefore the dose rate is not constant

Table 3.1: Table of maximum doses expected for each layer of the ITk including a safety factor of 1.5 [56]

Strip Layer	Maximal Fluence [$n_{eq}cm^{-2}$]	Maximal Dose [kGy]	Maximal Dose [MRad]
Long Strips	3.8×10^{14}	98	9.8
Short Strips	7.2×10^{14}	325	32.5
Endcap	1.2×10^{15}	504	50.4

3.1.1   Radiation Levels in the ITk

The bulk damage occurring to a device is usually normalised to a 1MeV equivalent neutron fluence which would result in the deposition of the same non-ionising energy causing equivalent damage to the material. Both the expected 1MeV equivalent neutron fluence and TID for the ITk are shown in Figure 3.3. As shown in Table 3.1 the ITk strip detector is expected to experience fluences up to $1.2\times10^{15}n_{eq}cm^{-2}$ and doses up to 504kGy. Every detector component needs to be tested up to and beyond these levels. In this work the ABC130 and HCC130 have been irradiated to assess their radiation hardness. Radiation issues within silicon have been discussed further in Section 3.1.
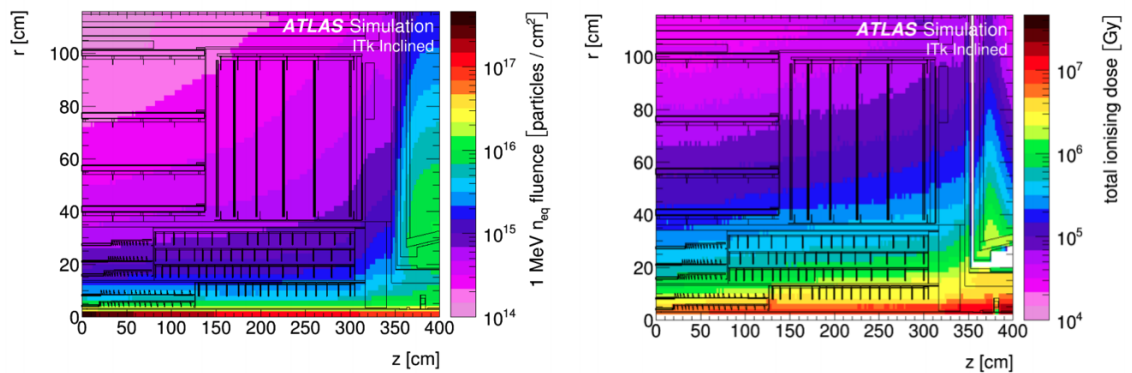
Figure 3.3: Simulation of the 1MeV equivalent neutron fluence (a) and TID (b) distribution through the ITk geometry [56]

3.2   Facilities and Setups

All components of the ITk need to be tested in high radiation environments to ensure they can survive the increased doses and particle rates produced by the HL-LHC. The results presented in this Chapter aided in commissioning the Birmingham medical physics cyclotron as an AIDA-2020 transnational access radiation facility [89]. The facility is intensively used to irradiate silicon sensors (both strip and pixel), microelectronics and integrated circuits, optical fibres, hybrid circuits, mechanical structures for the LHC upgrade program and many more [90].

3.2.1   Birmingham Medical Physics Cyclotron

HL-LHC doses can be delivered at the Birmingham medical cyclotron within minutes to several hours [89]. The standard beam energy is 27MeV with a maximum achievable of 36MeV. A variable beam current of 0.1-2000nA allows for precision irradiation to a wide range of total ionising doses and fluences. At the cyclotron, detectors are mounted in the box shown in Figure 3.4 which can be scanned in the beam and are cooled using the boil-off of liquid Nitrogen. Temperatures down to $-50°$C are easily achievable, the usual operating temperature is $-25°$. Samples are kept cool to reduce annealing effects and leakage current. The box is mounted on a x-y scanning system which allows for either fixed (*point*) or scanned irradiations depending on the area of the sample. A small Nickel foil is added to each sample to measure the fluence received offline. A gamma spectrum of the foil shows several decay peaks, the size of the peak at 1337KeV can be used to determine the fluence as a neutron equivalent dose to $\pm10\%$.

It was found that a thin 300μm Aluminium absorber is needed in front of the samples during irradiation in order to filter out low energy protons and give consistent results in agreement with other facilities. These low energy protons are possibly caused by

Figure 3.4: Photograph of the particle physics setup at the Birmingham medical physics cyclotron

the interaction of the beam with the collimator♠.

Studies with Gafchromic film showed that the 1cm×1cm beam spot does not give a uniform dose over this area similar to that shown in Figure 3.5 (left). Therefore during *point* irradiations some sections of the object being irradiated received a considerably larger dose than others, Figure 3.5 (middle). Further studies with the film showed that it was possible to considerably reduce this effect by scanning the object through the beam. During *scan* irradiations the box follows a right,down,left,down,repeat path, Figure 3.5 (right). The down movements are set smaller than the beam spot height which means the beam spot overlaps with previ-

---

♠ A 3MeV proton has a range of 107±5mm in air with a density of 0.00163gcm^{-3} (ICRU-104 material). Protons must have energy more than this to traverse 10cm of air between collimator and sample. A 7MeV proton loses around 1MeV in 10cm of air. A 6.5MeV proton has a range of $296 \pm 13 \mu m$ in pure Al so would be stopped. Values taken from SRIM [91]
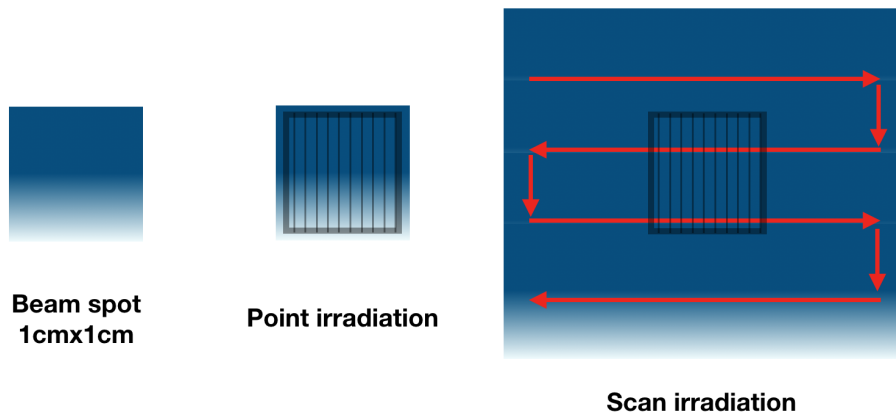
Figure 3.5: A simplified drawing showing the non-uniform dose of the beam spot (left), the sensor position during a *point* irradiation (middle) and how a *scan* irradiation can reduce the effects of the non-uniformities in the beam (right). The effective path of the beam spot is shown with red arrows

ously irradiated sections of the object resulting in a more uniform total dose.

3.2.2   ALiBaVa

The Liverpool Barcelona Valencia (ALiBaVa) is a test system which is used to characterise sensors before and after irradiation. It is a commercially available test system which is the standard for the CERN RD50 collaboration. The irradiated sensors are wire bonded with 128 channels to the LHCb analogue readout electronics. This is mounted onto a daughter board which is then mounted in a metal box to maintain a constant position. A 3D design drawing of the setup is shown in Figure 3.6. A Sr-90 Beta source is placed above the box where PMTs and scintillators provide a trigger which the ALiBaVa system uses to get a channel by channel readout of the sensor. The ALiBaVa software displays the signal, hitmap, noise and temperature. The system can then be used to measure collected charge with increasing voltage before and after irradiation and annealing. During the first year of the project several improvements were made to the ALiBaVa setup at Birmingham. These include the design of a new box which houses an upgraded board capable of taking the silicon sensors to

1000V bias voltage (500V max previously). This does allow for results to be more comprehensibly compared. The new box also has a reduced volume, scintillators at right angles and is more airtight. This allows N_2 to be continually pumped throughout the cooling and warming up phases of testing. If the box warms too quickly and without N_2 there would be considerable condensation on the sensor which can easily damage wire bonds as well as the sensor itself. Previously the freezer would need to have been switched off and allowed to warm up before the sensor could be safely removed. Any time the sensor spends close to room temperature, annealing takes place much more rapidly, which will start to alter the effects from the irradiation as discussed in Section 3.1. The new box allows for a considerably quicker warm up time while still maintaining N_2 flow at a safe level for the sensor. Offline, data from the ALiBaVa system is then analysed.
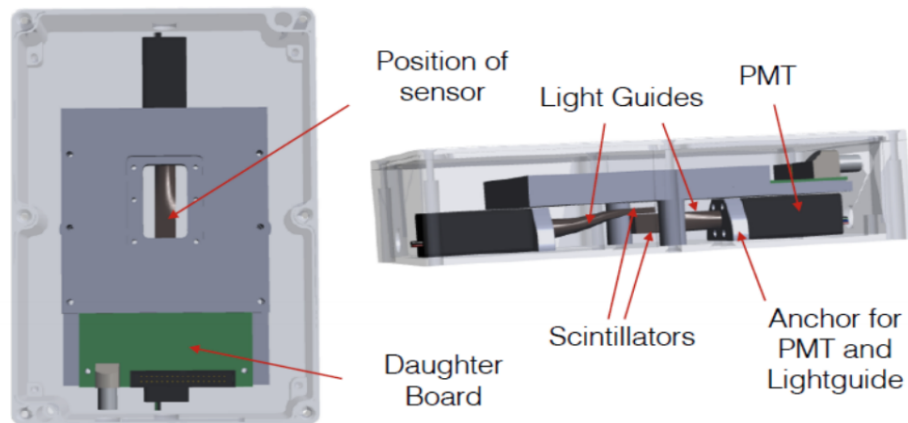
Figure 3.6: A 3D rendered drawing of the box containing the AliBaVa daughter card and scintillator triggers. The position of the sensor is aligned with the scintillators and source [92]

Figure 3.7 shows a Landau fit to the data taken by ALiBaVa. A Landau convolved with a Gaussian distribution is used to fit the data. The most probable value of the fitted data is then plotted for each voltage setting. A comparison between differently irradiated sensors can then be made easily.
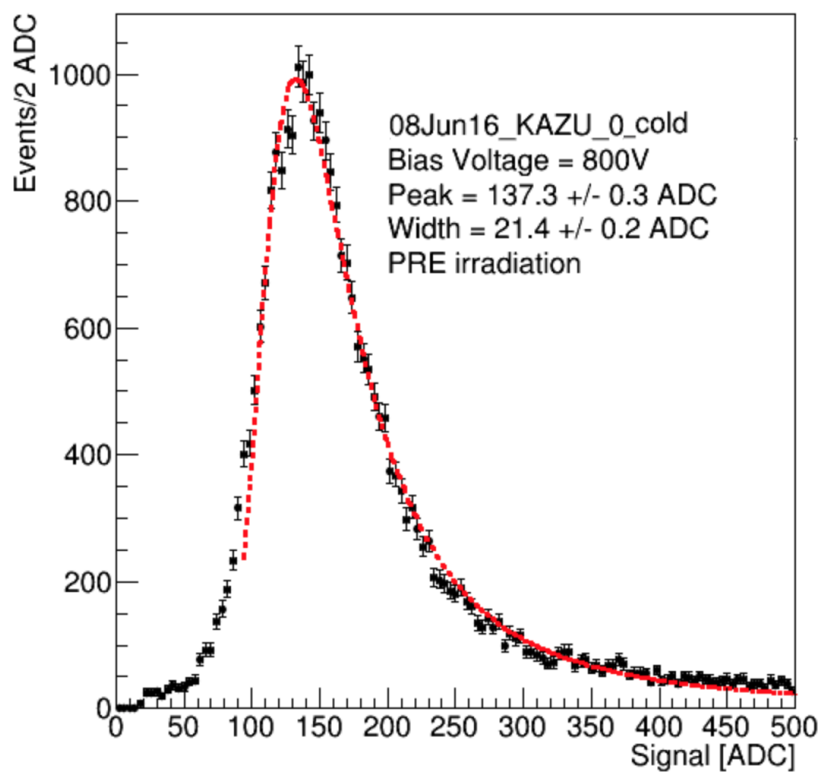
Figure 3.7: An example of a typical Landau fit to an unirradiated sensor biased at 800V

3.3   Sensor Irradiation Results

Issues arising from the radiation damage to ATLAS12 mini sensors were discussed at length in [92]. The main issue is a reduced signal at a given voltage when sensors are tested after irradiation. A signal consistent with other facilities can be achieved as discussed in 3.2.1.
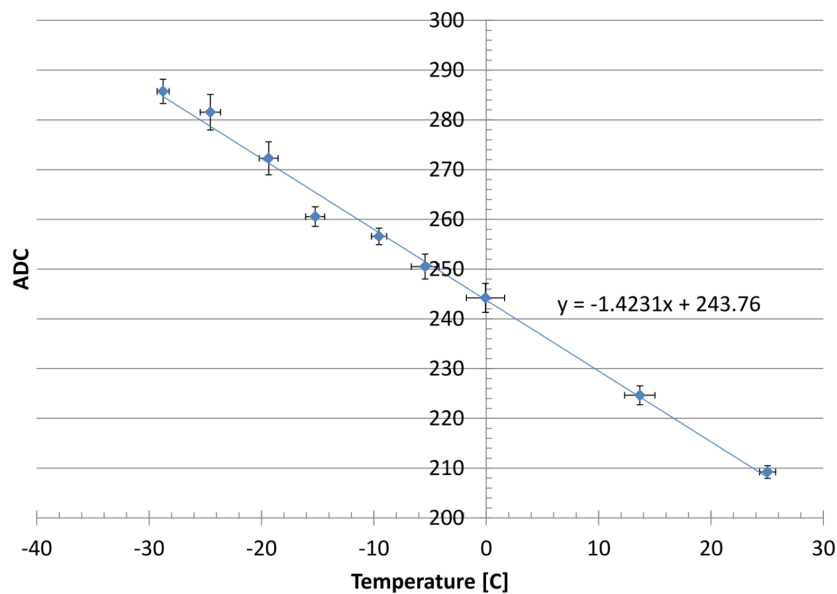
Figure 3.8: ALiBaVa output (in ADC counts) showing the temperature dependence of a daughter board [93]

The ATLAS12 mini sensors irradiated at the cyclotron are tested after irradiation using the ALiBaVa test system. The most probable signal is extracted from a fit to the data at each voltage step as described in Section 3.2.2 and Figure 3.7. The temperature dependence of the electronics gain shown in Figure 3.8 is corrected for. A test of the correction on an unirradiated sensor is shown in Figure 3.9 showing the same data before and after the temperature correction has been applied. The unirradiated sensor was tested at $+17°C$, $-25°C$ and $-30°C$ and thus the three datasets show different output signals measured in ADC counts (Figure 3.9 (left)). However once the temperature correction and an ADC to collected charge conversion♠ have

---

♠ A calibration for converting from an ADC to a Ke is found by noting that a fully depleted $300\mu m$ silicon sensor will produce approximately 23,000 electron-hole pairs from a passing MIP. This calibration is a constant and applies equally to all datasets and therefore the temperature correction is solely responsible for the relative changes between datasets
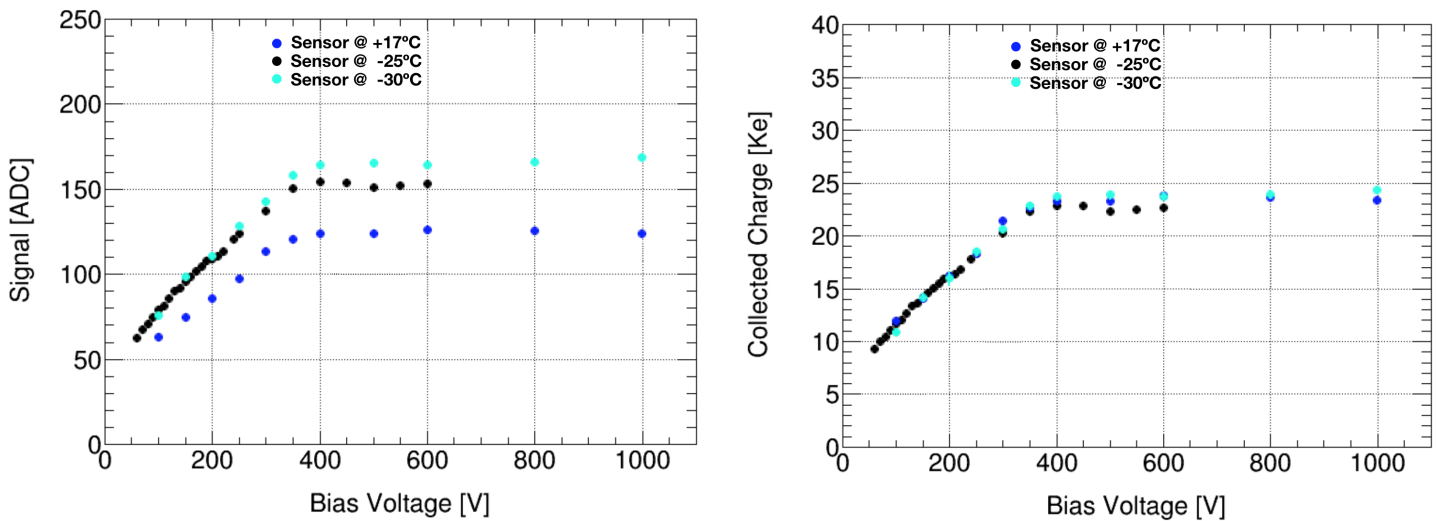
Figure 3.9: Signal (in ADC counts) of an unirradiated sensor measured with the ALiBaVa test system at several different temperatures (left). The same results are also shown after a temperature correction (Figure 3.8) is applied (right). The units of collected charge, Ke, correspond to one thousand times the charge of an electron, i.e. 1.6×10^{-16} Coulombs. This is found by calibrating the measurements to convert from an ADC to a Ke

been applied, all three datasets show consistent charge collection capabilities (Figure 3.9 (right)) .

Figure 3.10 shows the most probable signal values for several sensors, pre- and post-annealed, irradiated in February 2016. Sensors 2 and 3 were scanned through the beam (*scan*) whereas sensor 1 was fixed in place (*point*). All were irradiated to a target fluence of $1\times10^{15}n_{eq}cm^{-2}$. However, the relatively low fluence measured for sensor 1 has been attributed to non-uniformities within the beam, this issue is reduced when a sample is scanned through the beam as shown in Figure 3.5. Circles represent pre-annealed data and squares annealed data i.e. after 80mins at 60°C. As shown in Figure 3.11, annealing the sensors for this time and at this temperature improves the signal by reversing the radiation induced changes to the effective doping concentration. As expected there is an increase in the collected charge after annealing for all three sensors, however the relatively high signal in the
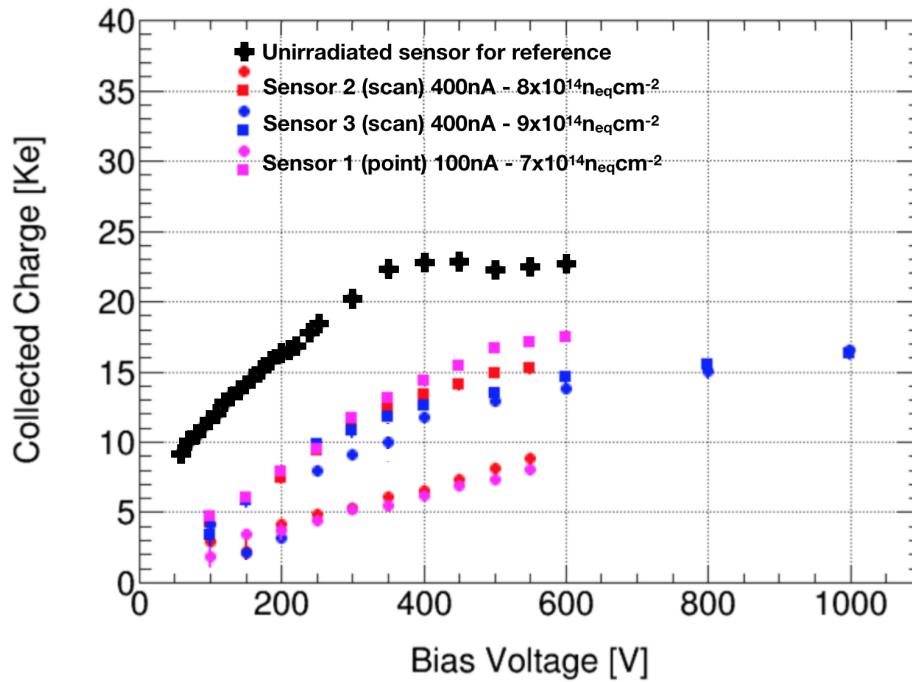
Figure 3.10: Radiation and annealing effects on the charge collecting abilities of several sensors. The black crosses show the collected charge for an unirradiated sensor for reference. For the three sensors, circles represent irradiated sensors and squares represent the same sensors tested again after the process of annealing. The fluence, measured from the Ni foils, of each sensor is shown and *scan* and *point* refer to the irradiation setup described in Figure 3.5

pre-annealed data for sensor 3 is not unexpected. The reason for comparison after annealing is because, in practice sensors will have annealed by varying amounts during and after irradiation. After 80mins at 60°C (equivalent to two weeks at room temperature) the evolution of signal with time, changes only slowly, making comparisons easier. As expected the three annealed datasets show that the higher the fluence the lower the collected charge for a given voltage.

The annealed results can then be compared to other radiation facilities with different beam energies and sources shown in Figure 3.12. The three sensors follow the trends of charge collection verses fluence of the other facilities.
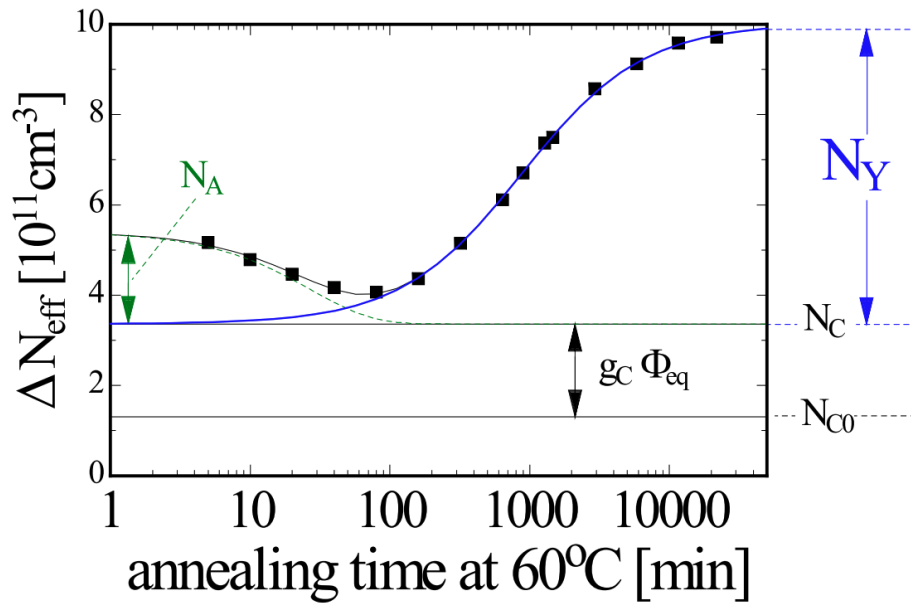
Figure 3.11: Evolution of the doping concentration as a function of annealing time for an irradiated sample of silicon. N_C is not dependent on annealing and is therefore called the *stable damage* component. The radiation induced changes to the effective doping concentration can be slightly reversed by *beneficial* annealing for a short time which is described by N_A, the sum of several exponentials. The effect is minimised after around 80mins at 60°C, although this is a relatively soft upper limit as the time scale is logarithmic, meaning that the effects remain minimised for many tens of minutes after 80mins. However after considerably long annealing times a *reverse* annealing effect occurs, this is parametrised by N_Y. N_C, N_A and N_Y are discussed at length in [94]
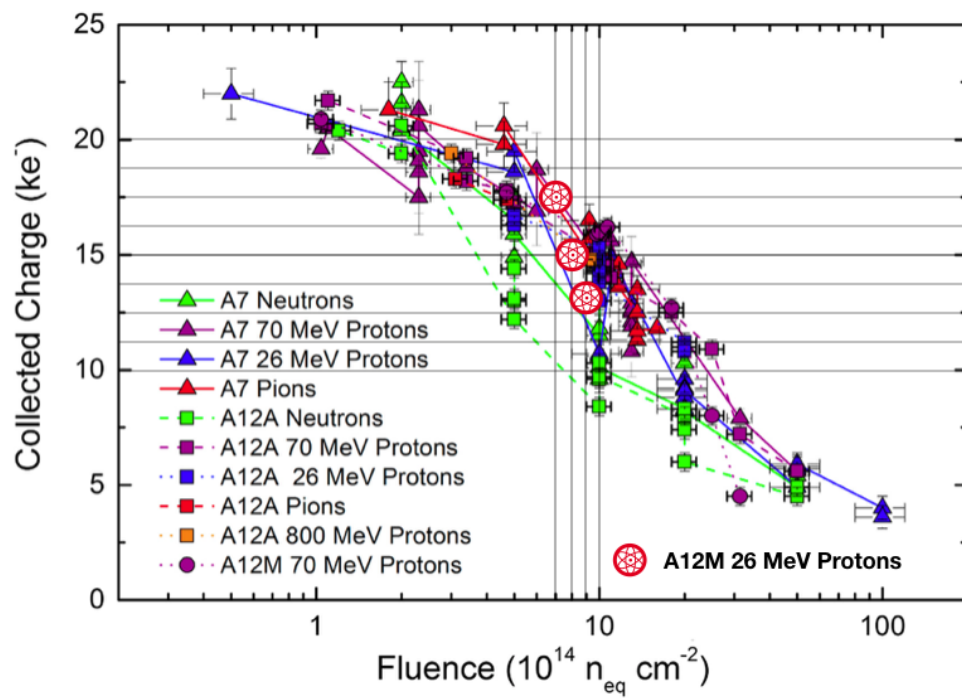
Figure 3.12: Collected charge at 500V vs fluence for three different sensor prototypes, A7, A12A and A12M (short for ATLAS12 mini). Results are shown separately for various irradiation sources after annealing [95]. The results for the three annealed A12M sensors at 500V from Figure 3.10 have been added by hand to the original figure

3.4   ASIC Irradiation Results

The ABC130 and HCC130 have both been irradiated at the Birmingham Medical
Physics Cyclotron with protons. During irradiation both ABC130 and HCC130 had
their current, gain and noise monitored. The ABC130 and HCC130 were irradi-
ated with a dose rate of 1.20MRad/hr and 1.25MRad/hr respectively both kept at
$-25°C$. The cyclotron cannot be operated overnight, therefore to reduce the impact
of annealing the ABC130 and HCC130 are left powered and cold during the night
with no beam.

3.4.1   ABC130 Irradiation Results

By using a low beam current the ABC130 was irradiated slowly to 10MRad over
three days. During the irradiation the current was monitored along with several
tests to determine the gain and input noise. Figure 3.13 shows the characteristics
of the Radiation Induced Narrow Channel Effects (RINCE) on the current drawn
by the ABC130 discussed in section 3.1. The vertical lines separate the days and
at the end of each irradiation period the chip was kept cooled overnight. In the
region of 0-2MRad the leakage current peaked at 1MRad. For these dose rate and
temperature conditions the maximum current increased by a factor of approximately
ten compared to the unirradiated current value.

Several irradiations using X-rays of the ABC130 have been performed at other fa-
cilities with different dose rates and at different temperatures. A table of all irradi-
ated ABC130s peak current increases and the facilities used is shown in Table 3.2
from [56]. Table 3.2 shows that the current increases of the ABC130 are dependent
on both temperature and dose rate. By comparing results at the same temperature
it can be seen that the higher the dose rate the larger the current increase. Also, by
comparing results at the same dose rate, the lower the temperature the greater the
effect. The Birmingham results, where the TID is provided by protons, are consistent
with these findings. More results with the same dose rate (or same dose rate and
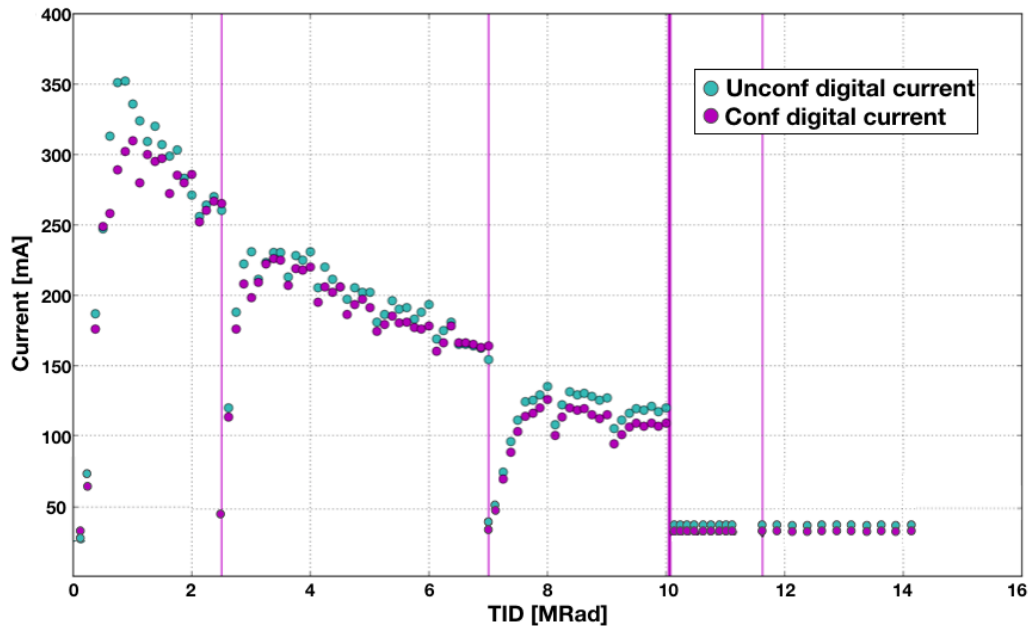
Figure 3.13: Digital current changes with TID for an ABC130 irradiated with a dose rate of 1.20MRad/hr at −25°C. The irradiation took place over three days (indicated by purple vertical lines), the ABC130 was then left annealing at room temp for several months before irradiating again (indicated by the thick purple vertical line after 10.125MRad). *Unconf* and *Conf* relate to the current before and after all DAQs have been setup

same temperature) would be needed before conclusions could be made about how the radiation source affects the current increase.

The gain and input noise of two ABC130s were taken at 1.5fC and plotted in terms of a percentage increase from the unirradiated value. Both were operated at −25°C with an average dose rate of 2.20MRad/hr. The gain was calculated using software from the ITkDAQ [96] and the input noise is then calculated from the gain. Figure 3.14 shows a gain decrease before reaching a plateau around −12% of the unirradiated value. Although there are large fluctuations in the percentage gain increase, the general trend can easily be seen. Irradiations with different dose rates and temperatures at different facilities all measured gain decreases less than those seen at Birmingham as shown in Figure 3.15 where the gain decreases by about 10% before recovering to the unirradiated value [56].

Table 3.2: Table showing the current increase of irradiated ABC130s with three source types and at different dose rates and temperatures. The factor the maximum current is above the unirradiated current gives the current increase. e.g. the $p\ Birmingham$ data here is taken from Figure 3.13 ($Conf$ data) where the unirradiated current is 32mA and peaks at 310mA giving a current increase of 9.7 [56]

Source	Temperature [°C]	Dose Rate [MRad/hr]	Current Increase
	−25	0.0023	2.5
Co-60 CERN	−10	0.0023	1.9
	−10	0.0006	1.3
p Birmingham	−25	1.25	9.7
	−15	0.062	3.9
X-ray CERN	−15	2.25	13.6
	+20	2.25	5.2
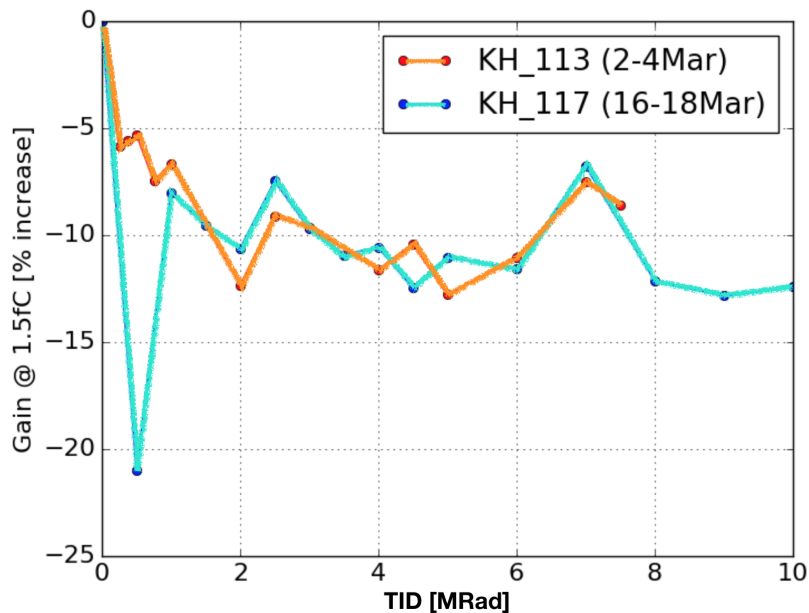
Figure 3.14: Percentage increase in gain for two irradiated ABC130s at −25°C with an average dose rate of 2.20MRad/hr

The irradiation has a considerably large effect on the input noise. Figure 3.16 shows a continued increase in the input noise up to 42% by 10MRad.

Figure 3.17 shows the percentage increase of the input noise measured at other facilities, which also reaches a plateau around 40-50% higher with no sign of decrease with continued irradiation. Such an input noise increase would significantly reduce
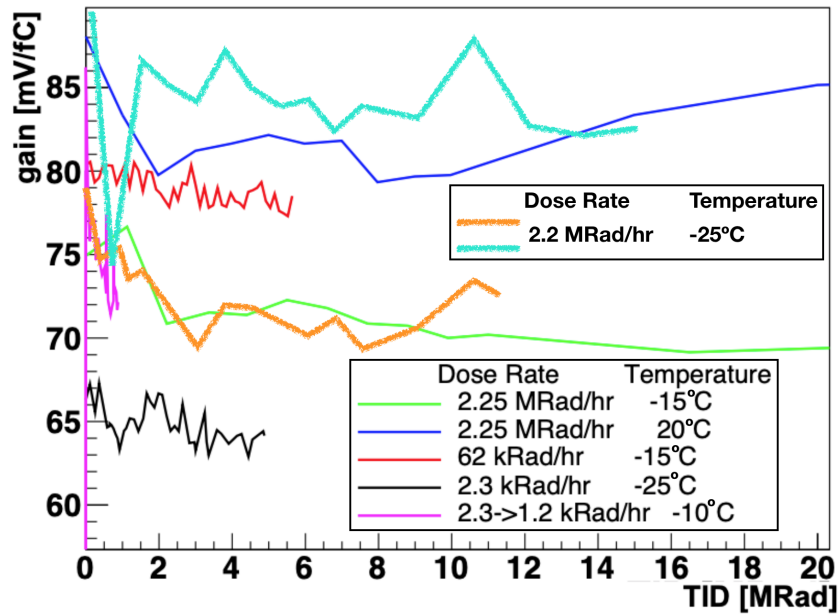
Figure 3.15: Gain in the ABC130 as a function of TID, for different dose rates and temperatures. The data from Figure 3.14 has been added to the original figure [56]
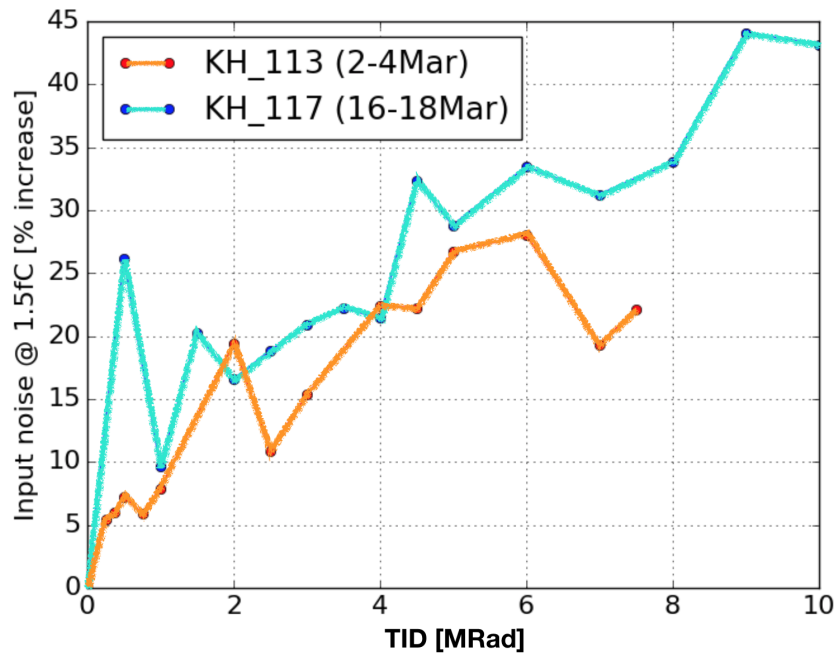
Figure 3.16: Percentage increase in the input noise for two irradiated ABC130s at $-25°$C with an average dose rate of 2.20MRad/hr

detector performance.
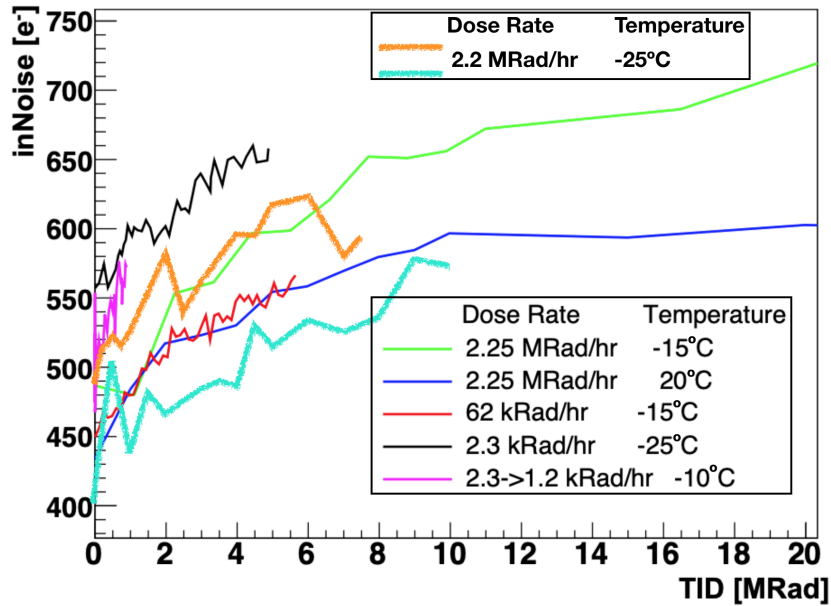
Figure 3.17: Increase of input noise in the ABC130 as a function of TID, for different dose rates and temperatures. The data from Figure 3.16 has been added to the original figure [56]

3.4.2   HCC Irradiation Results

A Hybrid Control Chip with 130nm Technology (HCC130) has also been irradiated at Birmingham. The HCC130 is also subject to Radiation Induced Narrow Channel Effects shown in Figure 3.18. The current increases by a factor of 2 at 0.5MRad. The difference in this increase, compared to the ABC130, is expected because of the differences in design, with a lower fraction of transistors in the HCC130 being so narrow as to be highly susceptible to RINCE.
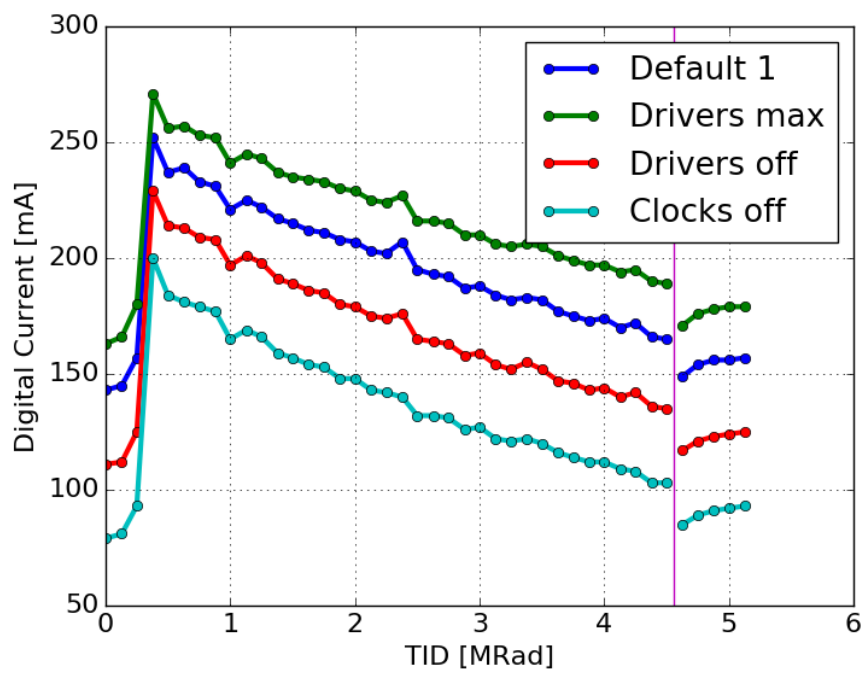
Figure 3.18: Digital current increase and decrease due to radiation induced effects from the irradiation of a HCC. Dose rate = 1.25MRad/hr T=−25°C

CHAPTER 4

$$H \to HH \to b\bar{b}\gamma\gamma$$

4.1 Introduction

One of the most promising channels to measure the Higgs self-coupling through the decay $H \to HH$ is the $b\bar{b}\gamma\gamma$ final state. This channel benefits from both the large branching fraction of the $H \to b\bar{b}$ decay and the narrow mass peak from the $H \to \gamma\gamma$ decay resulting in a clear di-Higgs signal. The following analyses are performed in the context of the HL-LHC.

The following studies are carried out with $\sqrt{s} = 14\text{TeV}$ Monte Carlo (MC) simulations. To mimic the detector response, the final-state particles are smeared at truth level according to the expected detector resolutions. Truth level here includes final state particles, after hadronisation and simulation hits, which are detectable but without the effects of finite detector resolution and acceptance. A pileup scenario with 200 overlapping events ($\langle \mu \rangle = 200$) is assumed.

4.2 Background and Signal Simulations

The background and signal samples used in this thesis are identical to those explained in [97] with the exception of Table 4.1 which has been updated with the latest cross-section calculations and Table 4.2 which has been added to help explain this analysis.

The signal and background processes are modelled in different MC samples. The main backgrounds arise from processes with multiple jets and photons that are reconstructed to a final state including two photons and two b-jets. These backgrounds can be separated into three categories. Firstly those containing a single Higgs boson which are $ggH(\to \gamma\gamma)$, $ZH(\to \gamma\gamma)$, $b\bar{b}H(\to \gamma\gamma)$, $t\bar{t}H(\to \gamma\gamma)$. Secondly reducible backgrounds that contain multiple jet and photon productions which are $b\bar{b}\gamma\gamma$, $c\bar{c}\gamma\gamma$, $jj\gamma\gamma$, $b\bar{b}j\gamma$, $c\bar{c}j\gamma$ and $b\bar{b}jj$ events. Finally other contributing backgrounds include $\gamma\gamma Z(\to b\bar{b})$, $t\bar{t}$ and $t\bar{t}\gamma$. A list of signal and background samples considered is displayed in Table 4.1. For each sample pileup jets$^\spadesuit$ are overlayed to events which have the possibility to be identified as a b-tagged jet, light jet or photon. Pileup jets are required to have a $p_T > 30\text{GeV}$.

To avoid overlap between events in different MC samples it is necessary to implement a veto, at truth level, which discards events which are already considered in a different SM sample. For example, in the $jj\gamma\gamma$ sample events with two truth level b-jets or two truth level c-jets are vetoed as these are already considered in the samples $b\bar{b}\gamma\gamma$ and $c\bar{c}\gamma\gamma$ respectively. If overlap was not taken into account duplicate events between samples would be considered twice and then the cross-sections used for weighting the samples would no longer be accurate. All overlap removals are shown in Table 4.2.

$^\spadesuit$ An independent sample of pileup jets exists. For each event, a number of these pileup jets are randomly selected and added as physics objects. The mean number of such pileup jets with $p_T > 30\text{GeV}$ and $|\eta| < 2.5$ is 5.5 ($\langle\mu\rangle = 200$) per event

Table 4.1: List of MC samples produced for this analysis including the generators used for the matrix element generation and the parton showering. In addition, the cross-section times branching ratio and the order in QCD of the cross-section calculation used for each sample are given

Process	Generator	$\sigma \cdot BR$ [fb]	Order QCD
$H(\to b\bar{b})H(\to \gamma\gamma)$	MadGraph5/Pythia8	0.105	NNLO
$ggH(\to \gamma\gamma)$	Powheg-Box/Pythia6	100.14	NNNLO
$t\bar{t}H(\to \gamma\gamma)$	Pythia8	1.40	NLO
$ZH(\to \gamma\gamma)$	Pythia8	2.24	NLO
$b\bar{b}H(\to \gamma\gamma)$	Pythia8	1.26	NLO
$b\bar{b}\gamma\gamma$	MadGraph5/Pythia8	141.93	LO
$c\bar{c}\gamma\gamma$	MadGraph5/Pythia8	1132.4	LO
$jj\gamma\gamma$	MadGraph5/Pythia8	16052	LO
$b\bar{b}j\gamma$	MadGraph5/Pythia8	380590	LO
$c\bar{c}j\gamma$	MadGraph5/Pythia8	1093100	LO
$b\bar{b}jj$	MadGraph5/Pythia8	466940000	LO
$\gamma\gamma Z(\to b\bar{b})$	MadGraph5/Pythia8	5.0682	LO
$t\bar{t}$	Powheg-Box/Pythia6	530000	NNLO
$t\bar{t}\gamma$	MadGraph5/Pythia8	5000	NLO

Table 4.2: Table showing the objects in an event which would cause that event to be vetoed from a sample. Also shown is the sample which would be overlapped if there were no veto applied. The main background from $t\bar{t}$ production comes from the production with one photon in the final state, therefore a $t\bar{t}\gamma$ sample was also produced. Events with one truth level photon are therefore removed from the $t\bar{t}$ sample to avoid overlap with the dedicated $t\bar{t}\gamma$ sample

Overlap applied to sample	If event contains the following truth object(s)	To avoid overlap with sample
$jj\gamma\gamma$	2 b-jets or 2 c-jets	$b\bar{b}\gamma\gamma$, $c\bar{c}\gamma\gamma$
$b\bar{b}j\gamma$	2 photons	$b\bar{b}\gamma\gamma$
$c\bar{c}j\gamma$	2 photons	$c\bar{c}\gamma\gamma$
$c\bar{c}\gamma\gamma$	2 b-jets	$b\bar{b}\gamma\gamma$
$bbjj$	1 photon	$bbj\gamma$
$t\bar{t}$	1 photon	$t\bar{t}\gamma$

4.2.1 Signal

For the signal process $HH \to b\bar{b}\gamma\gamma$ only the dominant gluon-gluon fusion production mode is generated using MadGraph5_aMC@NLO [98–100] at Leading Order (LO) (with finite top mass) with Pythia 8 [101] to model parton showering and hadronisation. The A14 tune [102] is used together with the NNPDF2.3LO Probability Density Function (PDF) set [103]. The event yields are normalised to the Next-to-next-to-leading Order (NNLO) cross-sections of Ref. [104] and [105] (using the infinite top mass approximation).

4.2.2 Single Higgs

The background from single Higgs boson production via gluon-gluon fusion is generated using PowhegBox [106]. This process uses the CT10 PDF set [107] and is interfaced to Pythia 6 [108] for parton showering and hadronisation. The cross section is normalised to next-to-next-to-next-leading order in QCD predictions [25]. The associated Higgs production modes $ZH(\to \gamma\gamma)$, $t\bar{t}H(\to \gamma\gamma)$ and $b\bar{b}H(\to \gamma\gamma)$ samples are generated using Pythia 8. The $ZH(\to \gamma\gamma)$ process is normalised to cross-sections calculated to NNLO in QCD [109] with Next-to-leading Order (NLO) Electroweak corrections [110]. The $t\bar{t}H(\to \gamma\gamma)$ process is normalised to a calculation at NLO in QCD [111–114] and the $b\bar{b}H(\to \gamma\gamma)$ process is normalised to a calculation at NNLO in QCD with Next-next-to-leading-log accuracy [115].

4.2.3 Reducible Backgrounds

The non-resonant $\gamma\gamma$ backgrounds arise from the processes $b\bar{b}\gamma\gamma$, $c\bar{c}\gamma\gamma$, $jj\gamma\gamma$, $b\bar{b}j\gamma$, $c\bar{c}j\gamma$ and $b\bar{b}jj$, where the jets in the last process come from both light quarks and gluons. In the $jj\gamma\gamma$ sample, the jets arise either both from light quarks or $bj\gamma\gamma$, $cj\gamma\gamma$ or $bc\gamma\gamma$. These processes are produced with MadGraph5_aMC@NLO interfaced with Pythia 8 for the showering and hadronisation. The CTEQ6L1 PDF [116] set

is used. These samples were generated inclusively (e.g. an additional jet in the tree-level matrix element is allowed). The jets and photons produced in the hard process are required to have $p_T > 20\text{GeV}$ and 25GeV respectively and the photon rapidity is limited to $|\eta| < 2.7$. The invariant mass of two jets has to exceed 25GeV. In addition, for processes with two photons produced in the hard process, the di-photon invariant mass is restricted to $60 < m_{\gamma\gamma} < 200\text{GeV}$ and for processes with two b-quarks, the invariant mass of the $b\bar{b}$ system has to exceed 45GeV.

4.2.4   Others

The $\gamma\gamma Z(\to b\bar{b})$ process is produced in the same fashion as the reducible backgrounds. Backgrounds from $t\bar{t}$ production are estimated at NLO in QCD using POWHEG-BOX, which is interfaced to PYTHIA 6 for parton showering and hadronisation. The CT10 PDF set [107] is used for this process. The events are filtered to contain at least one lepton with $p_T > 20\text{GeV}$ in the final state. The cross-section is calculated with the TOP++2.0 program to NNLO in QCD, including soft-gluon resummation to NNLO (see Ref. [117] and references therein) and assuming a top-quark mass $m_{top} = 172.5\text{GeV}$. The main background from $t\bar{t}$ production comes from the production with one photon in the final state. Therefore, a $t\bar{t}\gamma$ sample was also produced in LO, using MADGRAPH5_aMC@NLO interfaced with PYTHIA 8 for the showering and hadronisation and the CTEQ6L1 PDF set. The cross-section is normalised to the NLO predictions [118].

CHAPTER 5

HL-LHC $H \to HH \to b\bar{b}\gamma\gamma$ ANALYSIS STRATEGIES

$\mathfrak{T}$o best capture the small number of expected events (roughly 315 in 3000fb^{-1}) the prospects for observing the $HH \to b\bar{b}\gamma\gamma$ channel at the HL-LHC have been studied with various analysis methods. Each method builds on the previous method to enhance the signal acceptance. For the purpose of this thesis the selection criteria are only explained in detail before the first method, see Section 5.2 and thereafter only the variations are described.

Initial results were published with a cuts based analysis [97], called the Legacy method. In this method Monte Carlo events are either kept or rejected completely, which is a problem for backgrounds with small sample sizes. Given limited Monte Carlo statistics and to reduce the reliance on random numbers, an additional cuts based approach was later developed to improve the performance by using the weight

of each object in an event [119]. This method is referred to as the weighted cuts based approach, however neither of these approaches make optimal use of all the data available; a Boosted Decision Tree (BDT) method was subsequently implemented [26]. This allows for all the information about each simulated event to be more efficiently utilised by assigning the probability that the event is either a HH candidate or a background process.

As the results reported in Chapter 6 are based on the Legacy method, the weighted cuts based approach and the Boosted Decision Tree method, they are all discussed in detail in this chapter.

5.1   Sample Topologies

This section shows the distributions of some of the most important discriminating variables considered in all of the following analyses to best differentiate $HH \to b\bar{b}\gamma\gamma$ events from those due to background processes. These distributions motivate the choice of selection cuts used.

In each case the samples are normalised with respect to the correct cross-sections before they are summed into their respective categories. The following figures in this chapter show each of these categories then normalised to 1, unless explicitly stated otherwise. Each of the following variables are shown for the samples; $HH \to b\bar{b}\gamma\gamma$ (red); $b\bar{b}\gamma\gamma$ (cyan); reducible backgrounds (pink) consisting of $b\bar{b}j\gamma$, $b\bar{b}jj$, $c\bar{c}\gamma\gamma$, $c\bar{c}j\gamma$ and $jj\gamma\gamma$ (referred to as *Reducibles* in figures); single Higgs (blue) which includes ZH, $t\bar{t}H$, $b\bar{b}H$ and ggH; and finally others backgrounds (green) containing $\gamma\gamma Z(\to b\bar{b})$, $t\bar{t}\gamma$ and $t\bar{t}$. It is useful to plot the $b\bar{b}\gamma\gamma$ sample separately to the reducible backgrounds as it will be shown to be the dominant background.

Figure 5.1 shows the number of truth photons with $p_T > 20$GeV per event. Both reducible and other backgrounds have predominately zero photons per event and so these backgrounds must be due to other physics objects being wrongly reconstructed
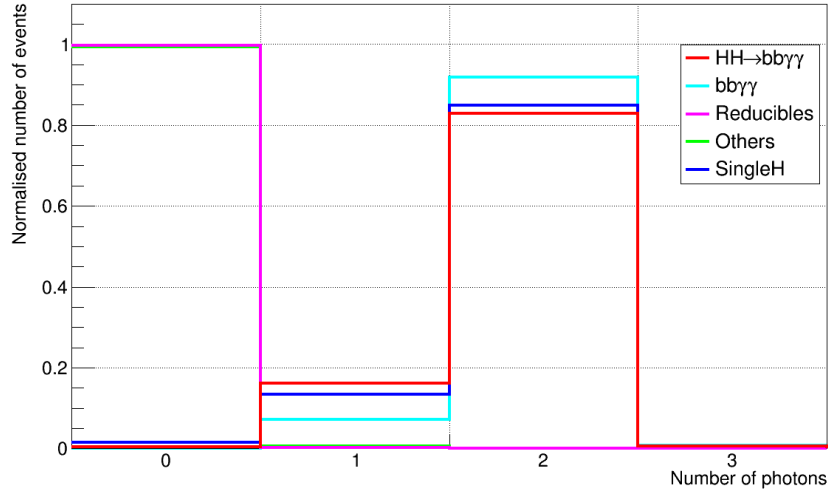
Figure 5.1: Normalised number of photons per event. $Reducibles[b\bar{b}j\gamma,\ b\bar{b}jj,\ c\bar{c}\gamma\gamma,$ $c\bar{c}j\gamma,\ jj\gamma\gamma],\ Others[\gamma\gamma Z(\to b\bar{b}),\ t\bar{t}\gamma,\ t\bar{t}],\ SingleH[ZH,\ t\bar{t}H,\ b\bar{b}H,\ ggH]$
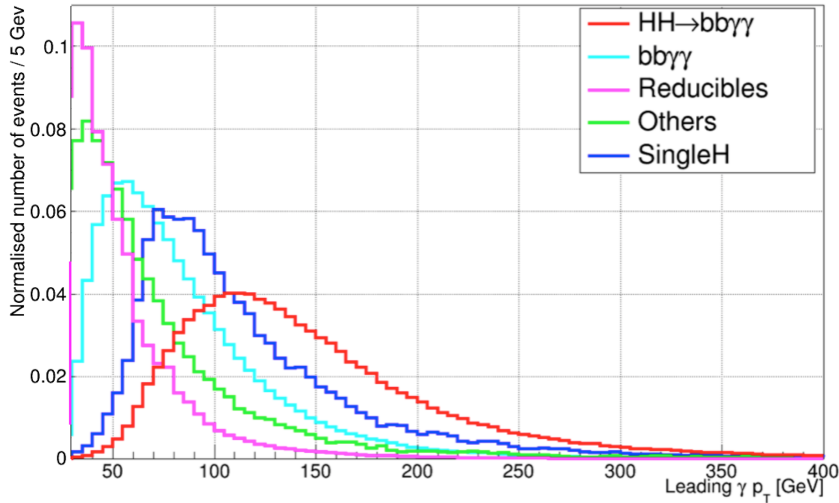
Figure 5.2: Normalised p_T distribution of the leading photon. $Reducibles[b\bar{b}j\gamma,\ b\bar{b}jj,$ $c\bar{c}\gamma\gamma,\ c\bar{c}j\gamma,\ jj\gamma\gamma],\ Others[\gamma\gamma Z(\to b\bar{b}),\ t\bar{t}\gamma,\ t\bar{t}],\ SingleH[ZH,\ t\bar{t}H,\ b\bar{b}H,\ ggH]$

as photons. Figures 5.2 and 5.3 show the p_T distributions of the leading and sub-leading photons (respectively) with $p_T > 20$GeV for each event. They also show the signal photons are most distributed at higher p_T values compared to the remaining categories which is due to the boost from the decaying Higgs bosons. This is also why the photons in the single Higgs backgrounds have high p_T.

Figure 5.4 shows the total number of truth jets from all sources per event with 20
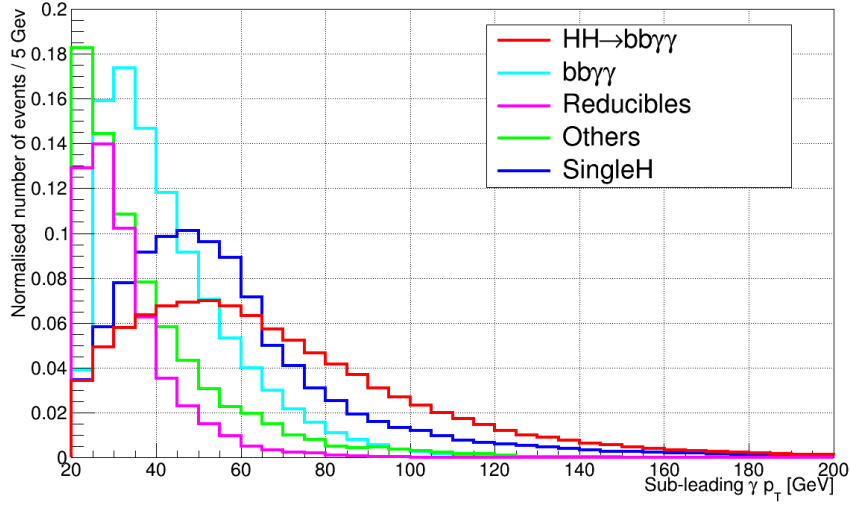
Figure 5.3: Normalised p_T distribution of the sub-leading photon, note the tighter $p_T < 200$GeV distribution compared to Figure 5.2. $Reducibles[b\bar{b}j\gamma, b\bar{b}jj, c\bar{c}\gamma\gamma, c\bar{c}j\gamma, jj\gamma\gamma], Others[\gamma\gamma Z(\rightarrow b\bar{b}), t\bar{t}\gamma, t\bar{t}], SingleH[ZH, t\bar{t}H, b\bar{b}H, ggH]$
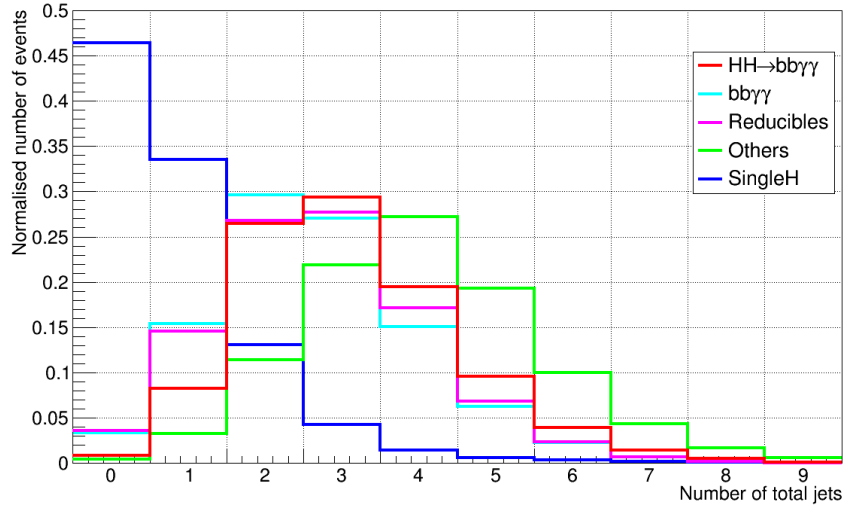
Figure 5.4: Normalised number of total jets per event. $Reducibles[b\bar{b}j\gamma, b\bar{b}jj, c\bar{c}\gamma\gamma, c\bar{c}j\gamma, jj\gamma\gamma], Others[\gamma\gamma Z(\rightarrow b\bar{b}), t\bar{t}\gamma, t\bar{t}], SingleH[ZH, t\bar{t}H, b\bar{b}H, ggH]$

$< p_T < 1500$GeV and $|\eta| < 2.5$ and Figure 5.5 shows the number of truth b-jets per event which satisfy the same requirements. Most categories peak between two and four jets and either one or two b-tagged jets, except for the single Higgs backgrounds which peak at zero jets in both cases due to the ggH background being dominant in this group.
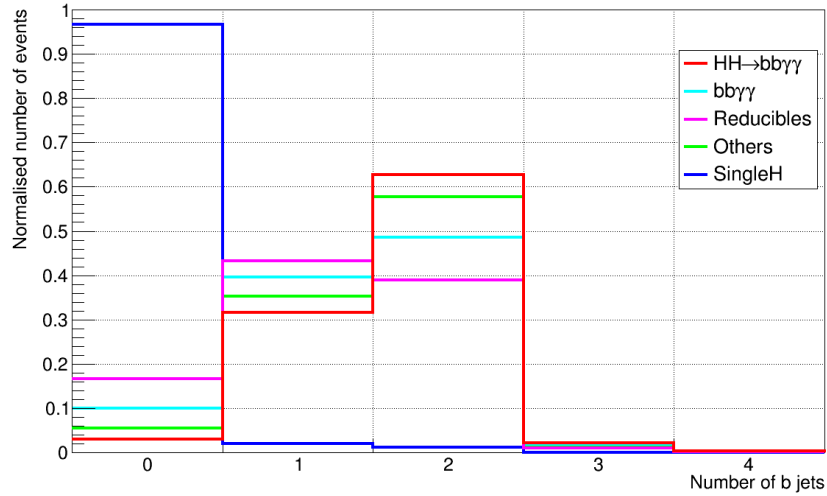
Figure 5.5: Normalised number of truth b-jets per event. $Reducibles[b\bar{b}j\gamma, b\bar{b}jj, c\bar{c}\gamma\gamma, c\bar{c}j\gamma, jj\gamma\gamma], Others[\gamma\gamma Z(\to b\bar{b}), t\bar{t}\gamma, t\bar{t}], SingleH[ZH, t\bar{t}H, b\bar{b}H, ggH]$
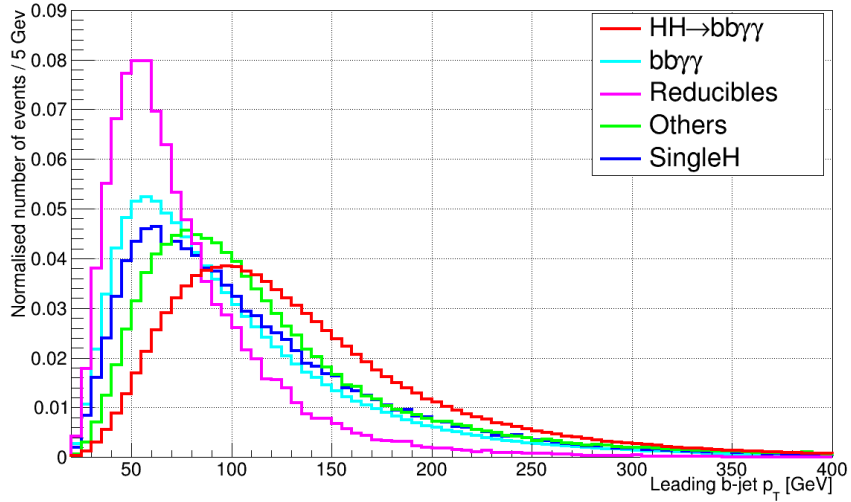
Figure 5.6: Normalised p_T distribution of the leading b-tagged jet. $Reducibles[b\bar{b}j\gamma, b\bar{b}jj, c\bar{c}\gamma\gamma, c\bar{c}j\gamma, jj\gamma\gamma], Others[\gamma\gamma Z(\to b\bar{b}), t\bar{t}\gamma, t\bar{t}], SingleH[ZH, t\bar{t}H, b\bar{b}H, ggH]$

Figures 5.6 and 5.7 show the p_T distributions of the leading and sub-leading b-tagged jets (respectively) with $p_T > 20\text{GeV}$ for each event. As shown for the photon p_T distribution, the signal b-tagged jets are also produced with a high p_T.

The ΔR separation between the leading and sub-leading photon is shown in Figure 5.8 and between the leading and sub-leading b-tagged jet in Figure 5.9. These two variables show good discrimination between signal and backgrounds thanks to
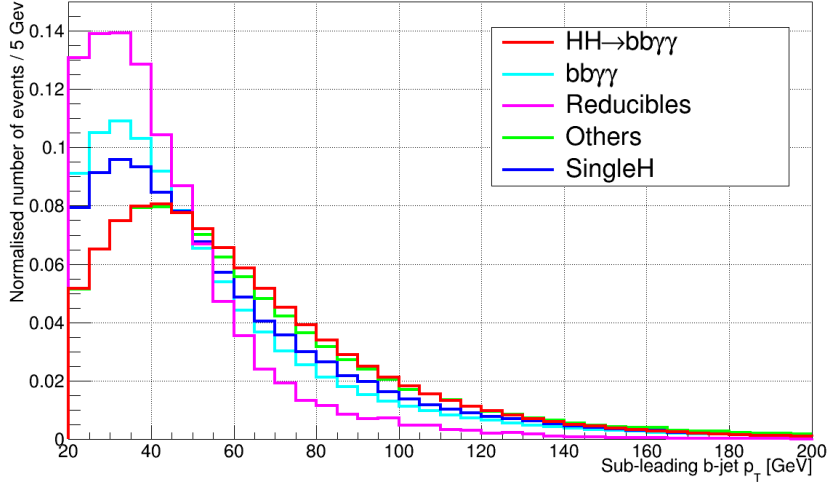
Figure 5.7:   Normalised p_T distribution of the sub-leading b-tagged jet. $Reducibles[b\bar{b}j\gamma,\ b\bar{b}jj,\ c\bar{c}\gamma\gamma,\ c\bar{c}j\gamma,\ jj\gamma\gamma],\ Others[\gamma\gamma Z(\to b\bar{b}),\ t\bar{t}\gamma,\ t\bar{t}],\ SingleH[ZH,\ t\bar{t}H,\ b\bar{b}H,\ ggH]$
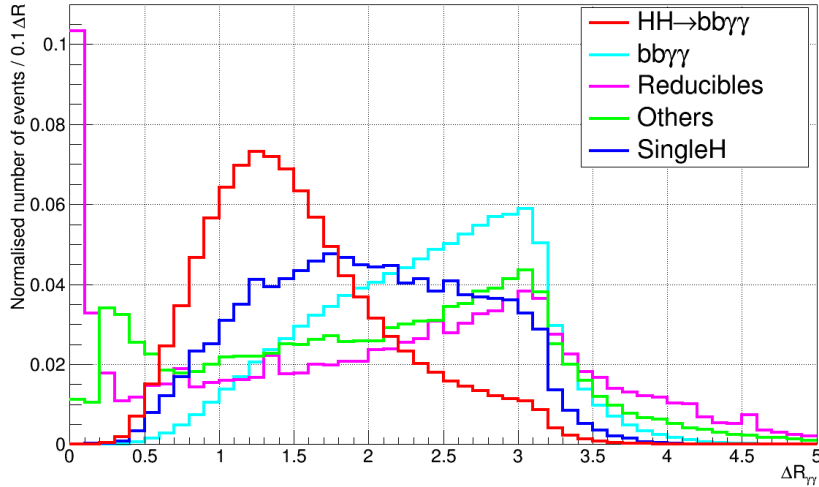
Figure 5.8: Normalised ΔR distribution of the two photons. $Reducibles[b\bar{b}j\gamma,\ b\bar{b}jj,\ c\bar{c}\gamma\gamma,\ c\bar{c}j\gamma,\ jj\gamma\gamma],\ Others[\gamma\gamma Z(\to b\bar{b}),\ t\bar{t}\gamma,\ t\bar{t}],\ SingleH[ZH,\ t\bar{t}H,\ b\bar{b}H,\ ggH]$

a boost from the decaying Higgs bosons. The boost results in a small angular separation. Figure 5.10 also shows the ΔR separation between each of the two photon and each of the two b-tagged jets. Here the discrimination is not as clear, however the region $\Delta R_{\gamma b} < 0.4$ includes relatively little signal compared to all other background processes.

The following variable distributions are no longer normalised to 1 but instead by
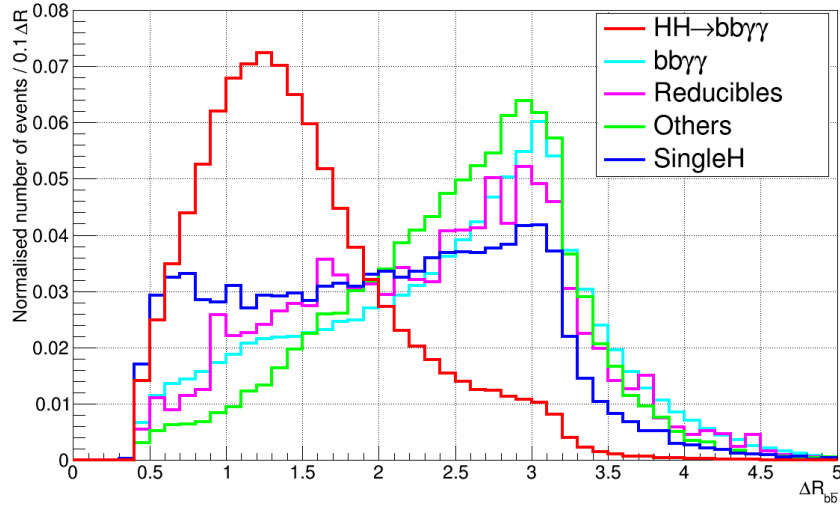
Figure 5.9: Normalised ΔR distribution of the two b-tagged jets. $Reducibles[b\bar{b}j\gamma,$ $b\bar{b}jj,\ c\bar{c}\gamma\gamma,\ c\bar{c}j\gamma,\ jj\gamma\gamma],\ Others[\gamma\gamma Z(\to b\bar{b}),\ t\bar{t}\gamma,\ t\bar{t}],\ SingleH[ZH,\ t\bar{t}H,\ b\bar{b}H,\ ggH]$
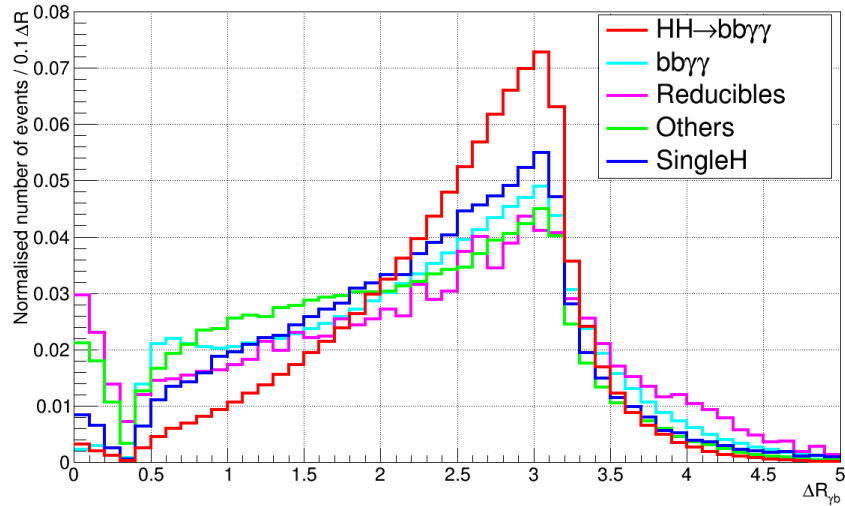
Figure 5.10: Normalised ΔR distribution of each photon and each b-tagged jet. i.e. $\Delta R_{\gamma 1b1},\ \Delta R_{\gamma 1b2},\ \Delta R_{\gamma 2b1}$ and $\Delta R_{\gamma 2b2}$. $Reducibles[b\bar{b}j\gamma,\ b\bar{b}jj,\ c\bar{c}\gamma\gamma,\ c\bar{c}j\gamma,\ jj\gamma\gamma],$ $Others[\gamma\gamma Z(\to b\bar{b}),\ t\bar{t}\gamma,\ t\bar{t}],\ SingleH[ZH,\ t\bar{t}H,\ b\bar{b}H,\ ggH]$

the expected cross-sections only. Each category is the sum of the previously plotted categories which allows for both the distributions to be clearly seen as well as the potential number of events which could be cut.

Figure 5.11 shows the mass distribution of the two photon system in terms of the number of expected events with 3000fb^{-1} of integrated data at HL-LHC. Between $120 < M_{\gamma\gamma} < 130\text{GeV}$ the distinctive mass peak of the Higgs can clearly be seen

as a combination of the signal and a significant contribution from the single Higgs backgrounds. The very large number of background events in the region $M_{\gamma\gamma} < 100$GeV shows why $M_{\gamma\gamma}$ is one of the best discriminating variables to focus on when considering any channel containing $H \to \gamma\gamma$. The mass distribution of the two b-tagged jet system is shown in Figure 5.12, with the signal considerably more spread about the Higgs mass.
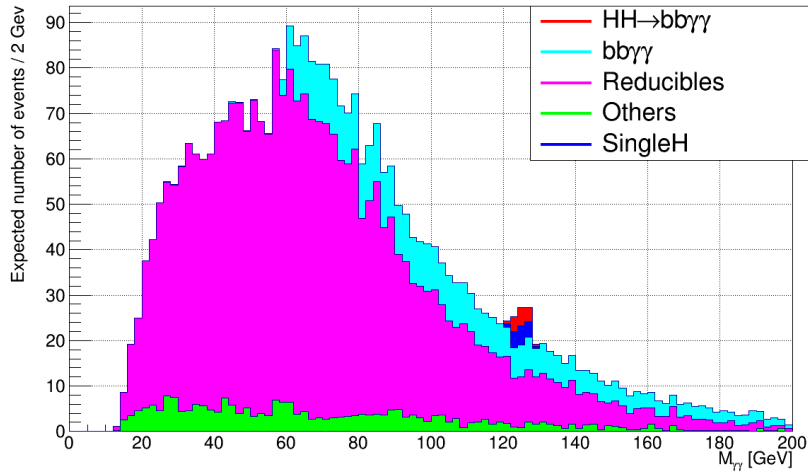
Figure 5.11: Mass distribution of the two selected photons, after a $H \to b\bar{b}$ candidate has been selected, in terms of the number of expected events with 3000fb^{-1} of integrated data. $Reducibles[b\bar{b}j\gamma, b\bar{b}jj, c\bar{c}\gamma\gamma, c\bar{c}j\gamma, jj\gamma\gamma]$, $Others[\gamma\gamma Z(\to b\bar{b}), t\bar{t}\gamma, t\bar{t}]$, $SingleH[ZH, t\bar{t}H, b\bar{b}H, ggH]$
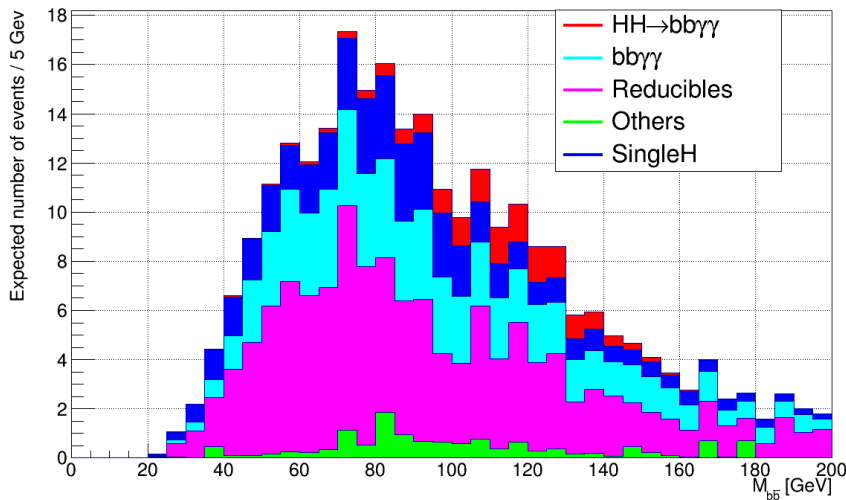
Figure 5.12: Mass distribution of the two selected b-tagged jets, after a $H \to \gamma\gamma$ candidate has been selected, in terms of the number of expected events with 3000fb^{-1} of integrated data. $Reducibles[b\bar{b}j\gamma, b\bar{b}jj, c\bar{c}\gamma\gamma, c\bar{c}j\gamma, jj\gamma\gamma]$, $Others[\gamma\gamma Z(\to b\bar{b}), t\bar{t}\gamma, t\bar{t}]$, $SingleH[ZH, t\bar{t}H, b\bar{b}H, ggH]$
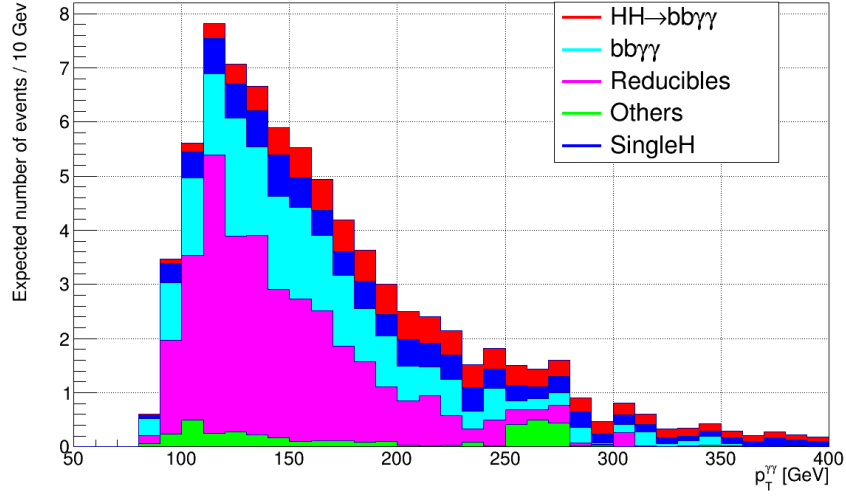
Figure 5.13: p_T distribution of the two selected photons in terms of the number of expected events with 3000fb^{-1} of integrated data. $Reducibles[b\bar{b}j\gamma,\ b\bar{b}jj,\ c\bar{c}\gamma\gamma,\ c\bar{c}j\gamma,\ jj\gamma\gamma],\ Others[\gamma\gamma Z(\to b\bar{b}),\ t\bar{t}\gamma,\ t\bar{t}],\ SingleH[ZH,\ t\bar{t}H,\ b\bar{b}H,\ ggH]$
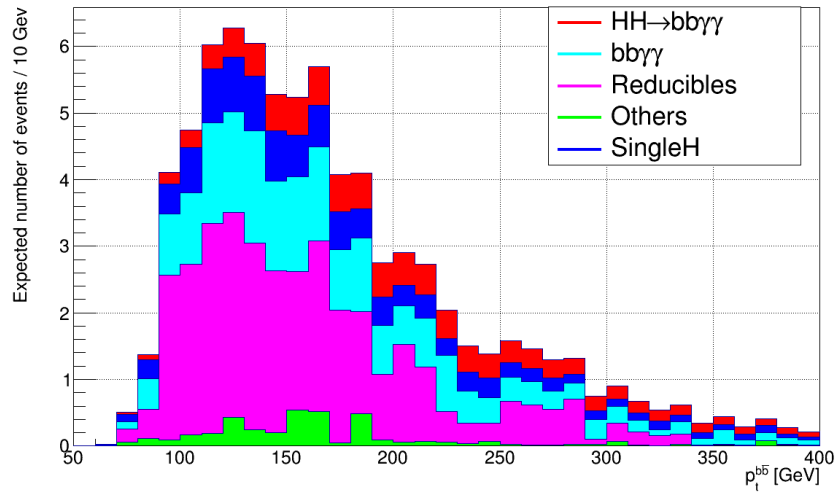
Figure 5.14: p_T distribution of the two selected b-tagged jets in terms of the number of expected events with 3000fb^{-1} of integrated data. $Reducibles[b\bar{b}j\gamma,\ b\bar{b}jj,\ c\bar{c}\gamma\gamma,\ c\bar{c}j\gamma,\ jj\gamma\gamma],\ Others[\gamma\gamma Z(\to b\bar{b}),\ t\bar{t}\gamma,\ t\bar{t}],\ SingleH[ZH,\ t\bar{t}H,\ b\bar{b}H,\ ggH]$

The p_T distributions of the photon and b-tagged jet systems are shown in Figures 5.13 and 5.14 respectively. Both show how a large proportion of the backgrounds could be removed by applying a cut on high values of $p_T^{\gamma\gamma/b\bar{b}}$.

Table 5.1: Event selection criteria for $HH \to b\bar{b}\gamma\gamma$ events

Event Selection Criteria
Trigger: ≥ 2 isolated photons, with $p_T > 25$GeV, $\|\eta\| < 1.37$ or $1.52 < \|\eta\| < 2.4$
≥ 2 isolated photons, with $p_T > 30$GeV, $\|\eta\| < 1.37$ or $1.52 < \|\eta\| < 2.37$
≥ 2 jets identified as b-jets with leading/subleading $p_T > 40/30$GeV, $\|\eta\| < 2.5$
< 6 jets with $p_T > 30$, $\|\eta\| < 2.5$
No isolated leptons with $p_T > 25$, $\|\eta\| < 2.5$
$0.4 < \Delta R_{b\bar{b}} < 2.0$, $0.4 < \Delta R_{\gamma\gamma} < 2.0$, $0.4 < \Delta R_{\gamma jet}$
$122 < m_{\gamma\gamma} < 128$GeV, $100 < m_{b\bar{b}} < 150$GeV
$p_T^{\gamma\gamma}, p_T^{bb} > 80$GeV

5.2   Event Selection Criteria

To select the $HH \to b\bar{b}\gamma\gamma$ events, the following event selection cuts, summarised in Table 5.1, are applied. These selection cuts were optimised by eye from the figures of the previous section. Only events accepted by the simulated di-photon trigger, which requires each photon to have a p_T greater than 25GeV within $|\eta| < 2.5$, are considered. In the offline reconstruction, the two photons should have $p_T > 30$GeV and be within the acceptance of the EMCal excluding the region between the barrel and endcap calorimeter, in which the performance is poor (i.e. select $|\eta| < 1.37$ or $1.52 < |\eta| < 2.37$). To ensure the photons are isolated, each photon is required to be separated by $\Delta R_{\gamma\gamma} > 0.4$ and by $\Delta R_{\gamma jet} > 0.4$ from the jets found in the event. Furthermore $\Delta R_{\gamma\gamma}$ has to be below 2.0 due to the boost of the photons from the Higgs boson. The two-photon system should fulfil $p_T > 80$GeV and have an invariant mass within $122 < m_{\gamma\gamma} < 128$GeV. In addition, events including isolated electrons and muons with $p_T > 25$GeV within $|\eta| < 2.5$ are rejected.

Events are required to contain no more than five jets with $p_T > 30$GeV and $|\eta| < 2.5$. At least two of these jets must be b-tagged within $|\eta| < 2.4$. The leading b-jet is required to have $p_T > 40$GeV and the subleading jet p_T has to exceed 30GeV. The $b\bar{b}$ system must have $p_T > 80$GeV, $100 < m_{b\bar{b}} < 150$GeV and is required to fulfil $0.4 < \Delta R_{b\bar{b}} < 2.0$.

The sources of *b*-tagged jets and reconstructed photons are shown in Figure 5.15 for all background samples ♠.
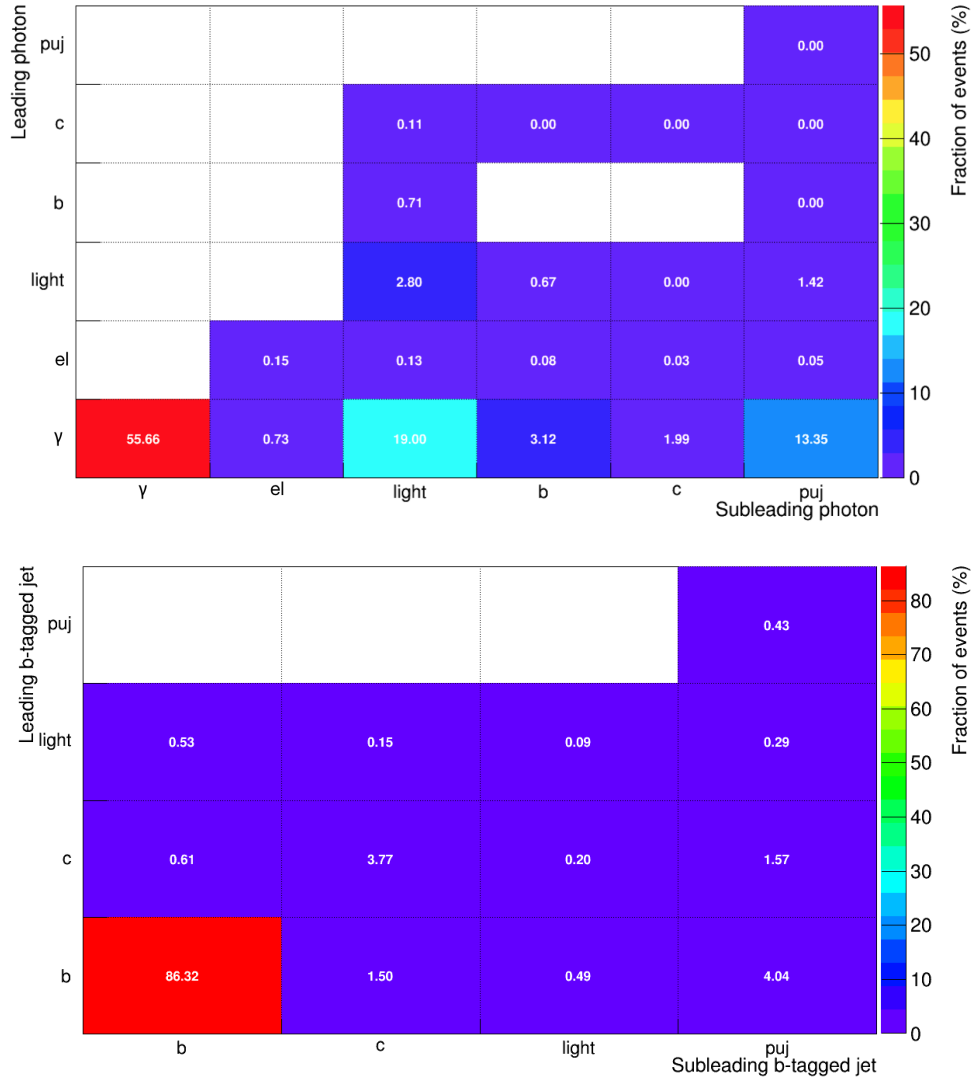
Figure 5.15: Source of photons (top) and *b*-tagged jets (bottom) combining all background channels. The sources considered are *b*-jets (b), *c*-jets (c), jets arising from light quarks (light) or from pileup jets (puj). Photon fakes can arise from fake jets and misidentified electrons (el)

♠ The sources of *b*-tagged jets and reconstructed photons for the $HH \rightarrow b\bar{b}\gamma\gamma$ sample are shown in Appendix A.3

5.3   Material Common To All Analysis Modes

Analyses with the Legacy, weights based and Boosted Decision Tree (BDT) methods are all based on the Upgrade Performance Functions [75] (discussed in Section 2.5.6) which smear MC samples to mimic the expected detector response. Some functions use a random seed which applies a predetermined amount of smearing. The initial seed is a single user set number, with each call of the related function the previous seed is used to seed the next random number which also has a predetermined amount of smearing. This is beneficial as different seeds apply different amounts of smearing and the same seed can be used for reproducibility and testing.

For each MC event, a set of truth objects are available, corresponding to truth jets, truth photons, etc. These truth objects can be reconstructed as various jet types, photons, electrons and so on, collectively known as *physics objects* in this thesis.

The upgrade performance functions are used to determine the probability p_{ij} for a given truth object t_i to be reconstructed as a given physics object $r_j \cdot p_i = f_{ij}(t_i)$, where $f_{ij}()$ is one of the upgrade performance functions, for a truth object i to be reconstructed as a physics object j.

The probability $p_{ij} = p_X$ for a given truth object not to be reconstructed is given by the product $p_X = \Pi_j(1 - p_{ij})$, however special note should be taken of the case where p_{ij} refers to a reconstructed jet.

Two separate functions are used for reconstructed jets; firstly, a function is used to determine the probability of a given truth object to be reconstructed as a jet♠, p_{jet} and secondly, a separate function is used to determine the probability of that truth object to be b-tagged $p_{b\text{-}tag}$. The probability for a truth object to be reconstructed as a b-jet is therefore $p_{b\text{-}jet} = p_{jet}p_{b\text{-}tag}$. The probability for a truth object to be reconstructed as a light-jet is $p_{l\text{-}jet} = p_{jet}(1 - p_{b\text{-}tag})$. The probability for a truth object not to be reconstructed as a jet is then $p_{\times\text{-}jet} = 1 - p_{jet}$. In this way, light jet

---

♠ Objects considered to be reconstructed as jets are shown in Figure 5.15 (bottom), i.e. b-jets, c-jets, jets arising from light quarks or from pileup jets

and b-jet are by construction mutually exclusive categories.

For each truth object t_i, the sum $s_i = \Sigma_j p_{ij}$ must equal 1. This is checked for each truth object, and where $s_i \neq 1$ the sum s_i is normalised by multiplying the probabilities p_{ij} by the scale factor $1/s_i$. In cases where $s_i = 1 + \epsilon$ where $\epsilon \neq 0$, ϵ is typically found to be very small, consistent with rounding/float-precision errors.

For all the following results a b-tagging efficiency of 70% is adopted.

5.4 Legacy Method

The Legacy method was first applied to $HH \rightarrow b\bar{b}\gamma\gamma$ in the study [120] after an initial study of HH event topologies was undertaken [121].

In this method, each truth object is either reconstructed as one physics object or is not reconstructed. For each truth object t_i, the probabilities p_{ij} are computed and normalised as described above. A random number between 0 and 1 is generated, and used with the probabilities p_{ij} to determine what physics object r_j, the truth object t_j will be considered as. In this way, each MC event results in one final state being analysed. This is problematic for channels which both give large backgrounds and where, even though the cuts result in large rejection, the remaining number of signal candidates is still significant. This limitation can be somewhat reduced by running on the same events with different random seeds. Where the different seeds apply different amounts of smearing to each truth object in an event. In this way it becomes more likely that backgrounds with large rejection will pass the cuts. The number of events and number of different seeds considered is accounted for in a luminosity normalisation calculation.

5.5   A Weighted Cuts Based Approach

For the weights based method the cuts applied to each object are the same as in the Legacy method however the treatment of physics objects is different. To reduce the dependence on random numbers and improve the performance of limited MC statistics the weights based analysis was developed, in this method physics objects are not kept or discarded based on a comparison to a random number. A weight of between 0 and 1 is passed to the cut flow instead of the discrete 0 or 1 as in the Legacy method. This weight is calculated based on the requirements of the cut. For the trigger cut, two photons are required to pass the pseudorapidity and p_T criteria as shown in Table 5.1, the weight for this cut is first calculated by considering the efficiencies of every object in each event to be reconstructed as a photon. If one of the objects does not pass the trigger cut criteria it is given a weight of zero but only for this particular cut. For example, a truth b-jet may fall in the region $1.37 < |\eta| < 1.52$ and would carry a weight of zero to be reconstructed as a photon however its likelihood to be reconstructed as any other kind of physics object is unaffected. To hasten computation of all combinations only the cases of zero and one photon reconstructed needs to be considered, $W_0^{\gamma trig}$ and $W_1^{\gamma trig}$. $W_0^{\gamma trig}$ is the probability that none of the objects in an event are reconstructed as a photon and thus is given by $W_0^{\gamma trig} = \prod_i (1 - \varepsilon_i^{\gamma trig})$ where $\varepsilon^{\gamma trig}$ is the photon efficiency for each object♠ . $W_1^{\gamma trig}$ is the probability for only one photon from all the objects in an event to be reconstructed as a photon and is given by $W_1^{\gamma trig} = \sum_i \varepsilon_i^{\gamma trig} \prod_{j \neq i}(1 - \varepsilon_j^{\gamma trig})$. Then the probability for an event to have two or more reconstructed photons is given by $W_{2+}^{\gamma trig} = 1 - (W_0^{\gamma trig} + W_1^{\gamma trig})$. The above is also applied, with the respective efficiencies, for the tighter photon, two jet and two b-jet cuts. For the less than six jet cut, the probability of zero to five reconstructed jets is calculated and summed, i.e. $W_{<6}^{jet} = \sum_i^6 W_i^{jet}$ where, for example, $W_4^{jet} = \sum_{i \neq j \neq k \neq l} \varepsilon_i^{jet} \varepsilon_j^{jet} \varepsilon_k^{jet} \varepsilon_l^{jet} \prod_{m \neq i,j,k,l}(1 - \varepsilon_m^{jet})$. For the lepton veto the only case which needs to be considered is of zero electrons reconstructed, which is identical in method to how $W_0^{\gamma trig}$ was calculated

---

♠Note that $\varepsilon^{\gamma trig} \not\equiv \varepsilon^{\gamma \geq 2}$ as an object that does not pass the greater than two photon cut can pass the trigger cut. Thus it is possible to have $\varepsilon^{\gamma trig} > 0$ and $\varepsilon^{\gamma \geq 2} = 0$

above but with $\varepsilon^{\gamma_{trig}} \Rightarrow \varepsilon^{lveto}$. For each cut the weight of each previous cut is multiplied to give the final value applied to the cut flow, so the value applied to lepton veto cut flow is given by $W^{total} = W_{2+}^{\gamma_{trig}} W_{2+}^{\gamma \geq 2} W_{2+}^{jet} W_{2+}^{bjet} W_{<6}^{jet} W_0^{lveto}$.

For the cuts on ΔR, $m_{\gamma\gamma}$, $m_{b\bar{b}}$ and Hp_T it becomes necessary to define two photons and two b-tagged jets. Every combination of making these four objects is considered, ensuring an object is not reconstructed more than once per combination. A weight is calculated for each combination from the product of the four respective object efficiencies. The combination of the four objects which produce the highest weight are used in the subsequent cuts. The ΔR, $m_{\gamma\gamma}$, $m_{b\bar{b}}$ and Hp_T of this four object system is calculated and then passed through the same cuts as described in the Legacy method above. However, the W^{total} is summed to the cut flow rather than unity.

Therefore in this method, cut flows up to the lepton veto cut are always passed with a value greater than zero, however small. After this cut the cut flows are passed as either 0 or the W^{total} for that event.

5.6   Boosted Decision Tree

A Boosted Decision Tree (BDT) was developed after the success of the weights based approach [119] because it became necessary to develop the analysis to enable the optimisation of many parameters simultaneously to focus on the topology of the $HH \to b\bar{b}\gamma\gamma$ events. To that end, a Boosted Decision Tree approach was adopted, which will be described in detail in this section.

The first step to a decision tree is to find the variable and associated cut value which best separates signal (s) and background (b) events. This is found by minimising an impurity function, which for this analysis is the Gini Index [122], G, defined in Equation 5.1:

$$G = 1 - \Sigma_{i=s,b}p_i^2 = 2p(1-p) = \frac{2sb}{(s+b)^2} \tag{5.1}$$

Where p is the signal purity resulting from a cut. This function peaks at 0.5 which indicates a cut equally separating signal and background and which would be no better than guessing. The function is minimised at both high and low values of p, making it equally beneficial to identify cuts which result in a high signal purity as well as in a high background purity. The Gini Index is calculated for each variable at many different cut values, both for events which pass the cut and also for events which do not pass the cut. A weighted average of these two Gini indices is then calculated. The combination of variable and cut that minimises the weighted G is selected as the first cut in the decision tree. The two sets of events, those that pass the cut and those that do not, then repeat the first step independently, to again separate signal and background events. This splitting process continues until one of the following conditions has been met; the user-specified maximum number of repeats has been reached (*depth*); a cut results in pure signal or pure background events remaining; a cut leaves a number of events less than the user-specified minimum number of events, often a percentage of the total sample; or a cut results in a worse Gini Index than the previous cut. Sub-samples of events which do not have subsequent cuts are called *leaves*. As this method is unlike the previous cuts based analyses where the events which do not pass a particular cut are discarded, a considerably improved signal selection is possible.

The above only describes how a single decision tree is trained, a BDT uses these techniques but many times creating many trees, up to thousands. A user specified number of individual decision trees are trained sequentially, with a boosting process in between each training. Boosting consists of adjusting the weights of individual events according to whether the previously trained tree classified them correctly. The boosting algorithm used for this analysis is the AdaBoost [123] described in detail below.

In the first trained tree all events, i, are given the same weight $w_i = \frac{1}{N}$, where N

is the total number of events. Each event is then passed through the tree, however if a background event ends in a leaf that is signal dominated (or vice versa) then that event has been incorrectly classified. A function, I_i, is defined as 1 if an event has been incorrectly classified and 0 otherwise. The error rate for a particular tree is then defined as:

$$E_r = \frac{\Sigma_i w_i I_i}{\Sigma_i w_i} \qquad (5.2)$$

The boost factor α for the tree is then given by:

$$\alpha = \frac{1}{2}\ln\left(\frac{1 - E_r}{E_r}\right) \qquad (5.3)$$

The initial event weights are then *boosted* as follows:

$$w_i \xrightarrow{\text{boost}} w_i e^{\alpha \cdot I_i} \qquad (5.4)$$

The updated weights are then renormalised such that $\Sigma_i w_i = 1$. Each event weight is then cumulatively summed such that each event falls in a bin between 0 and 1 of width w_i. A random number between 0 and 1 is then generated and whichever event falls in the equivalent bin is selected for the next training tree. Therefore events from the previous tree which were misidentified have a higher chance to be selected to be trained again. The same event can be selected more than once to appear in the next sample, making it more likely to be correctly classified during the next training tree. This is repeated until the new sample size is the same as the initial number of events for the initial tree, N. A second decision tree is then trained on the new sample following all the same steps outlined above. This is repeated until a user-specified number of trees, m, is reached. Every event is then given a score, S_i, called the BDT response, based on how well each tree classifies it, which is defined as:

$$S_i = \frac{\Sigma_m \alpha_m (p_i)_m}{\Sigma_m \alpha_m} \tag{5.5}$$

where $(p_i)_m$ is the purity of the leaf, from tree m, that each event i falls into. A frequency plot of the BDT response is then produced noting if each event is signal or background. An optimum cut value on the BDT response is then calculated by taking the significance at each point. In this way, the BDT combines many cut variables, all with various correlations, into a single variable with greatly improved signal selection compared to the previously described cut based analyses.

For this analysis, the events are initially passed though the weights based approach as described in Section 5.5 up to the lepton veto. Therefore each event has a W_i^{total} associated. As a BDT is considerably more CPU intensive than previous methods it is not feasible to train using the total number of events. Therefore a manually selected threshold for each signal and background sample on W^{total} is applied. It was found that it is possible to reduce the number of final states by 90% with only a 0.06% reduction in the integral of final-state weights. Additionally only the signal and background events satisfying $120 < m_{\gamma\gamma} < 130\text{GeV}$ were used for the training, subsequently $m_{\gamma\gamma}$ was not used as a training variable. All the remaining events are then equally and randomly separated into two sets, with one set used to train the BDT as described above and the other half used to test the BDT. The events in the test sample are passed through the trained BDT and the final BDT response is given by $S_i \cdot W_i^{total}$. The BDT response distribution for the test sample is then used to find the optimal cut. Splitting the sample considerably reduces the potential for *overtraining*, which can occur when a decision tree trains on a particular aspect of the data set which is not a true representation. All the BDTs in this thesis use the TMVA package [122] to perform a multivariate analysis.

Due to the increasingly complex environments in high energy physics experiments BDTs have become ubiquitous in physics analyses in recent years. The mv2c10 b-tagging algorithm [124] for example is derived from a BDT. The findings of [26] were based on an overtrained version of the mv2c10 b-tagging algorithm making the

Table 5.2: Summary of kinematic variables used when training the boosted decision tree

Variable	Description
$\Delta R_{b\bar{b}\gamma\gamma}$	Separation between Higgs candidates
$p_{Tb\bar{b}\gamma\gamma}$	p_T of Di-Higgs candidate
$\Delta R_{b\bar{b}}$	Separation between b-jets
$p_{Tb\bar{b}}$	p_T of $b\bar{b}$ Higgs candidate
$m_{b\bar{b}}$	Invariant mass of $b\bar{b}$ Higgs candidate
$\Delta R_{\gamma\gamma}$	Separation between photons
$p_{T\gamma\gamma}$	p_T of $\gamma\gamma$ Higgs candidate
$\eta_{\gamma\gamma}$	η of $\gamma\gamma$ Higgs candidate
p_{Tb1}	p_T of leading b-jet
p_{Tb2}	p_T of sub-leading b-jet
$p_{T\gamma1}$	p_T of leading photon
$p_{T\gamma2}$	p_T of subleading photon
$\cos(\theta^*)_{b\bar{b}}$	Opening angle in $b\bar{b}$ frame
$\cos(\theta^*)_{\gamma\gamma}$	Opening angle in $\gamma\gamma$ frame
$\cos(\theta^*)_{(bb)(\gamma\gamma)}$	Opening angle in $bb\gamma\gamma$ frame
HT_{30}	Scalar sum of p_T for all jets (before selections) with $p_T > 30\text{GeV}$
$HT_{Central}$	Scalar sum of p_T for all jets (before selections) with $|\eta| < 2.37$
MHT_{30}	$\sqrt{\sum p_x^2 + \sum p_y^2}$ of all final state objects with $p_T > 30\text{GeV}$
$massAllJets$	Invariant mass of all jets in final state combination
n_j	Number of jets with $p_T > 20\text{GeV}$ and $|\eta| < 4.9$
n_b	Number of b-jets with $p_T > 20\text{GeV}$ and $|\eta| < 4.9$

results biased, this was described in detail in Section 2.5.6. Also, two aspects of the pre-selection of events for this study were optimised with respect to the previously detailed cuts of Table 5.1. Firstly, a p_T requirement for the leading photon was introduced, $p_{T\gamma1} > 43\text{GeV}$ (previously 30GeV). Secondly, both leading and sub-leading b-tagged jets were subject to the same p_T cut, $p_{Tb} > 35\text{GeV}$ (previously 40/30GeV leading/subleading). The BDT used for this study was trained using new variables, summarised in Table 5.2, which were not considered in the previous methods. The importance rankings of these variables is shown in Figure 5.16. A BDT was also trained using only variables from previous methods to show the improvement possible from just the more advanced technique alone and is presented in Chapter 6.
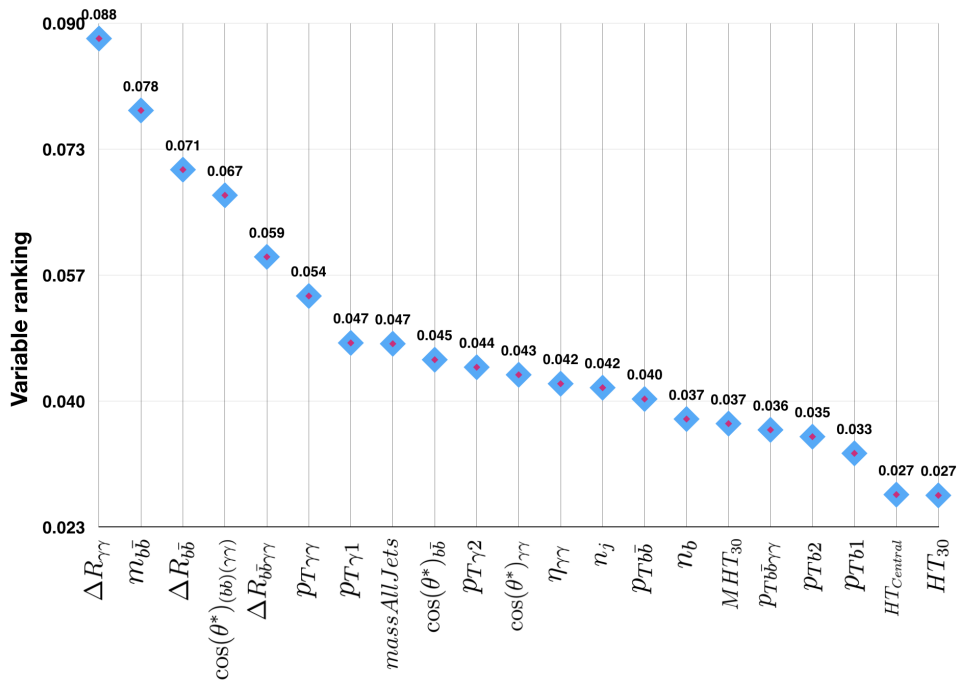
Figure 5.16: Ranking of kinematic variables used when training the boosted decision tree. Normalised such that the sum of all variable rankings equals 1. Section A.8 Figure A.27 shows the signal and background correlation matrices for these variables. It can be seen that, although some of the variables are correlated, each one has a sufficient contribution to signal/background discrimination to be kept

Chapter 6 shows results based on these three analysis methods, numerically showing the improvement each method provides for the prospects for observing the $HH \to b\bar{b}\gamma\gamma$ channel at the HL-LHC.

CHAPTER 6

RESULTS

𝕿his chapter details the results from the three analysis methods discussed in Chapter 5. It is made clear which method was implemented to produce each result.

6.1 Legacy Method and A Weighted Cuts Based Approach

The results of [97], summarised below, were the first to be published on the prospects of measuring $H \rightarrow HH \rightarrow b\bar{b}\gamma\gamma$ at the HL-LHC. The Legacy method was implemented for all background and signal samples with the exception of the $b\bar{b}jj$ sample. The $b\bar{b}jj$ sample used a weighted approach as it would have required too many iterations with the Legacy method due to the large rejection rates. Since these results have been published there have been improved signal estimates leading to refined theoretical predictions for cross sections. These refined cross sections have been applied to the previously published results, as summarised in Table 6.1 for comparison

to later results. The events are split into two categories depending on the photon pseudorapidites, if both photons are located in the barrel region of the EMCal ($|\eta| <$ 1.37) then the event is flagged as *Barrel-barrel*, otherwise it is labelled as *Other*. The significance is then calculated independently for the two regions before they are combined to increase overall performance. All results are normalised to 3000fb^{-1} and are shown with statistical uncertainty. The statistical uncertainty is calculated from the spread on the final number of expected events produced by multiple seeds applied to the smearing functions (see Section 5.3)♠. Every case of 0.00±0.00 expected events is the result of rounding to two decimal places and is not exactly zero. There are many variations and enhancements considered each with their own results, therefore a box diagram summarising each step is shown in Appendix A.5 to aid the reader.

As shown in Table 6.1 the effect of the more realistic sample estimates reduces the overall significance from 1.05±0.02 to 1.00±0.01. All of the following expected events are calculated using the *Updated* cross-sections shown in the last column of Table 6.1.

Since the results of [97] there has been a large collective effort put into the UPFs to improve the performance and realism of the simulated detector responses. Most notably (for this channel) was the development of the mv2c10 *b*-tagging algorithm which used multivariate techniques to capture the signature of jets originating from *b* quarks. This tagging algorithm has been previously discussed in detail in Section 2.5.6. A version of the mv2c10 algorithm was applied to this analysis and results show an increase in significance to 1.29±0.02 [119]. Table 6.2 shows the improvement achieved by adopting the mv2c10 tagging algorithm and the weights based method described in Section 5.5, these result in an increase in significance from the initial 1.00±0.01 to 1.40±0.04.

The weights based method was initially optimised by focusing on the p_T cuts applied to the two photon and two *b*-tagged jet systems fixed at $p_T^{\gamma\gamma/b\bar{b}} > 80$GeV. This

---

♠ This method gives a slightly larger uncertainty than the uncertainty from limited MC statistics as shown in Appendix A.4. The later is therefore not shown for the following results

Table 6.1: Expected number of signal and background events acquired using the Legacy method [97]. Also the same results updated to account for improved signal estimates and the resulting refined cross sections (see text) taken from AMI(ATLAS Metadata Interface) [125]. $All\ bkgs$[sum total of all backgrounds], $SingleH[ZH,\ t\bar{t}H,\ b\bar{b}H,\ ggH]$, $Reducibles[b\bar{b}\gamma\gamma,\ b\bar{b}j\gamma,\ b\bar{b}jj,\ c\bar{c}\gamma\gamma,\ c\bar{c}j\gamma,\ jj\gamma\gamma]$, $Others[\gamma\gamma Z(\to b\bar{b}),\ t\bar{t}\gamma,\ t\bar{t}]$

	PUB note [97]		Improved Signal estimates		Cross section [fb]	
	Barrel-barrel	Other	Barrel-barrel	Other	PUB [97]	Updated [125]
$HH \to bb\gamma\gamma$	7.31±0.03	2.23±0.02	6.98±0.02	2.13±0.02	0.11	0.105
$bb\gamma\gamma$	12.4±0.4	9.4±0.5	12.57±0.41	9.53±0.51	140	141.93
$bbj\gamma$	11.79±0.8	10.8±0.8	11.81±0.80	10.82±0.80	380000	380590
$bbjj$	3.3±0.7	2.05±0.33	3.35±0.71	2.08±0.33	460000000	466940000
$c\bar{c}\gamma\gamma$	5.7±0.31	2.77±0.34	5.87±0.32	2.85±0.35	1100	1132.4
$c\bar{c}j\gamma$	2.5±0.7	0.7±0.4	2.48±0.70	0.70±0.40	1100000	1093100
$jj\gamma\gamma$	2.2±0.5	1.84±0.32	2.21±0.5	1.85±0.32	16000	16052
$ZH(\to \gamma\gamma)$	3.42±0.17	1.56±0.06	3.42±0.17	1.56±0.06		2.24
$t\bar{t}H(\to \gamma\gamma)$	5.89±0.13	1.98±0.08	5.89±0.13	1.98±0.08		1.4
$bbH(\to \gamma\gamma)$	0.11±0.01	0.04±0.01	0.11±0.01	0.04±0.01		1.26
$ggH(\to \gamma\gamma)$	1.96±0.29	0.78±0.19	1.64±0.24	0.65±0.16	120	100.14
$Z(\to bb)\gamma\gamma$	1.21±0.1	0.85±0.1	1.21±0.10	0.85±0.10	5.07	5.0682
$t\bar{t}\gamma$	3.8±0.34	1.36±0.14	3.80±0.34	1.36±0.14	5000	5000
$t\bar{t}$	0.80±0.28	1.60±0.40	0.80±0.28	1.60±0.40	530000	530000

Totals

	Barrel-barrel	Other	Barrel-barrel	Other
All bkgs	55.1±1.6	35.7±1.3	55.2±1.6	35.9±1.3
Single H	11.4±0.4	4.4±0.2	11.1±0.3	4.2±0.2
Reducibles	37.9±1.5	27.6±1.2	38.3±1.5	27.8±1.2
Other	5.8±0.5	3.8±0.4	5.8±0.5	3.8±0.4
$S/\sqrt{B}$	0.98±0.01	0.37±0.01	0.94±0.01	0.36±0.01
Combined	**1.05±0.02**		**1.00±0.01**	

Table 6.2: Expected number of signal and background events acquired using a weights based method (see text). *All bkgs*[sum total of all backgrounds], *SingleH*[ZH, $t\bar{t}H$, $b\bar{b}H$, ggH], *Reducibles*[$b\bar{b}\gamma\gamma$, $b\bar{b}j\gamma$, $b\bar{b}jj$, $c\bar{c}\gamma\gamma$, $c\bar{c}j\gamma$, $jj\gamma\gamma$], *Others*[$\gamma\gamma Z(\to b\bar{b})$, $t\bar{t}\gamma$, $t\bar{t}$]

	PUB note Improved sample estimates		Updated functions Weighted approach	
	Barrel-barrel	Other	Barrel-barrel	Other
$HH \to bb\gamma\gamma$	6.98±0.02	2.13±0.02	8.27±0.25	2.41±0.14
$b\bar{b}\gamma\gamma$	12.57±0.41	9.53±0.51	11.41±0.27	9.12±0.25
$b\bar{b}j\gamma$	11.81±0.8	10.82±0.8	13.99±0.97	10.27±0.55
$b\bar{b}jj$	3.35±0.71	2.08±0.33	2.82±0.44	3.40±0.53
$c\bar{c}\gamma\gamma$	5.87±0.32	2.85±0.35	0.35±0.02	0.19±0.02
$c\bar{c}j\gamma$	2.48±0.7	0.7±0.4	0.29±0.03	0.25±0.02
$jj\gamma\gamma$	2.21±0.5	1.85±0.32	0.21±0.03	0.21±0.3
$ZH(\to \gamma\gamma)$	3.42±0.17	1.56±0.06	1.62±0.11	0.77±0.05
$t\bar{t}H(\to \gamma\gamma)$	5.89±0.13	1.98±0.08	4.28±0.21	1.38±0.09
$b\bar{b}H(\to \gamma\gamma)$	0.11±0.01	0.04±0.01	0.11±0.01	0.04±0.00
$ggH(\to \gamma\gamma)$	1.64±0.24	0.65±0.16	1.64±0.10	0.59±0.06
$Z(\to b\bar{b})\gamma\gamma$	1.21±0.1	0.85±0.1	0.63±0.05	0.50±0.06
$t\bar{t}\gamma$	3.80±0.34	1.36±0.14	1.77±0.86	0.24±0.07
$t\bar{t}$	0.80±0.28	1.60±0.40	0.12±0.03	0.19±0.04
Totals				
All bkgs	55.2±1.6	35.9±1.3	39.2±1.4	27.1±0.8
Single H	11.1±0.3	4.2±0.2	7.7±0.3	2.8±0.1
Reducibles	38.3±1.5	27.8±1.2	29.1±1.1	23.4±0.8
Other	5.8±0.5	3.8±0.4	2.5±0.9	0.9±0.1
S/$\sqrt{B}$	0.94±0.01	0.36±0.01	1.32±0.05	0.46±0.03
Combined	**1.00±0.01**		**1.40±0.04**	
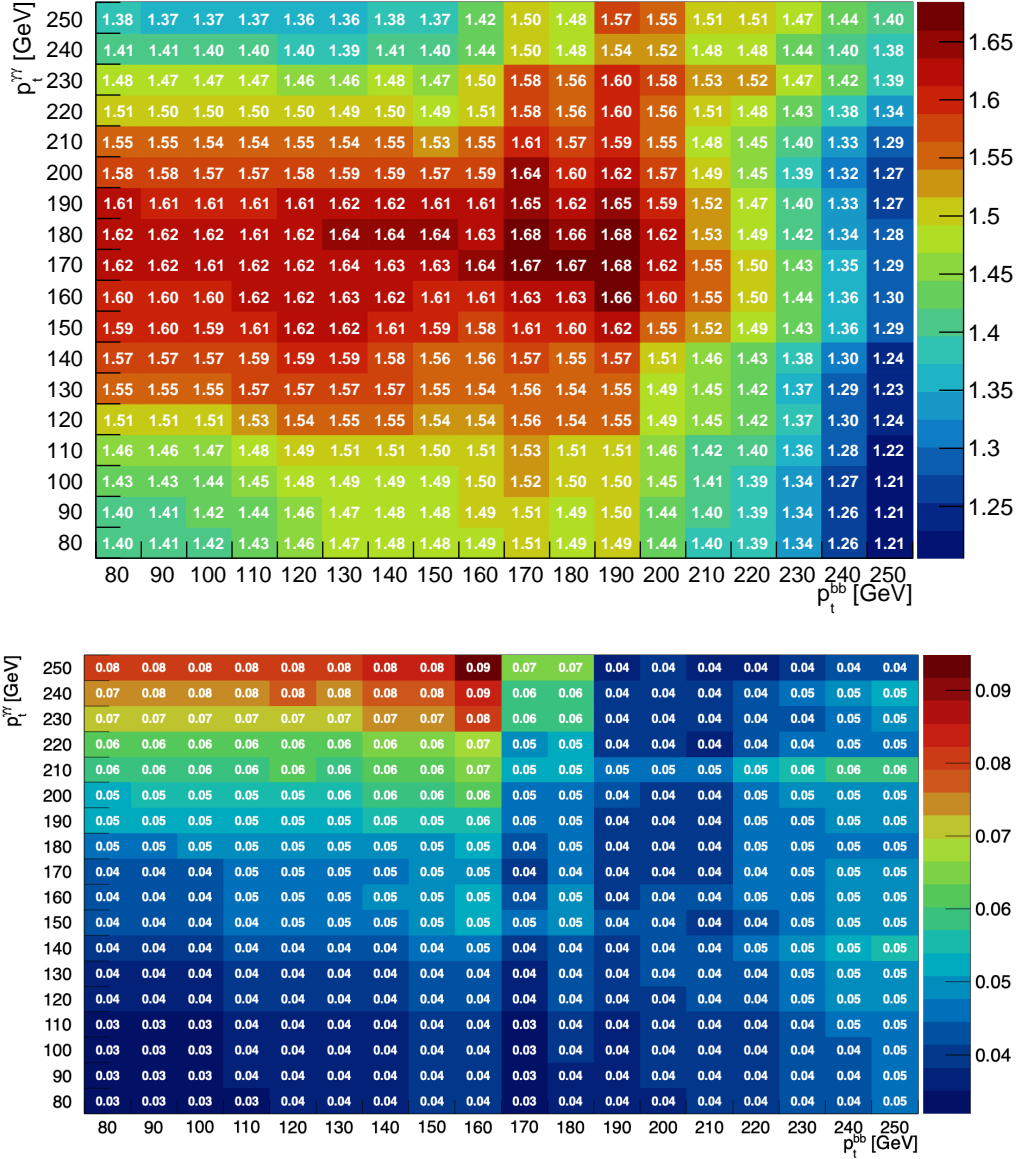
Figure 6.1: Expected significance (top) and error (bottom) acquired using a weights based method for an increase in p_T cuts applied to both the two photon and two b-tagged jet systems. The functions used for these results are based on an overly optimistic material budget

cut was then increased incrementally by 10GeV on both systems in turn up to a maximum of 250GeV, above which the majority of the signal sample was cut (as shown in Figures 5.13 and 5.14). Figure 6.1 shows the significance (top) and associated error (bottom) for each of these 10GeV steps, a clear improvement is seen

Table 6.3: Expected number of signal and background events acquired using a weights based method and increasing the p_T cuts applied to both the two photon and two b-tagged jet systems. Shown is the case for $p_T^{\gamma\gamma} > 180\text{GeV}$ and $p_T^{b\bar{b}} > 170\text{GeV}$. *All bkgs*[sum total of all backgrounds], *SingleH*[ZH, $t\bar{t}H$, $b\bar{b}H$, ggH], *Reducibles*[$b\bar{b}\gamma\gamma$, $b\bar{b}j\gamma$, $b\bar{b}jj$, $c\bar{c}\gamma\gamma$, $c\bar{c}j\gamma$, $jj\gamma\gamma$], *Others*[$\gamma\gamma Z(\to b\bar{b})$, $t\bar{t}\gamma$, $t\bar{t}$]

	Weighted approach		$p_T^{\gamma\gamma} > 180\text{GeV}$, $p_T^{b\bar{b}} > 170\text{GeV}$	
	Barrel-barrel	Other	Barrel-barrel	Other
$HH \to b\bar{b}\gamma\gamma$	8.27±0.25	2.41±0.14	4.20±0.08	1.03±0.04
$b\bar{b}\gamma\gamma$	11.41±0.27	9.12±0.25	2.51±0.20	1.94±0.09
$b\bar{b}j\gamma$	13.99±0.97	10.27±0.55	1.53±0.36	0.83±0.22
$b\bar{b}jj$	2.82±0.44	3.40±0.53	0.07±0.07	0.00±0.00
$c\bar{c}\gamma\gamma$	0.35±0.02	0.19±0.02	0.03±0.00	0.03±0.00
$c\bar{c}j\gamma$	0.29±0.03	0.25±0.02	0.02±0.01	0.03±0.01
$jj\gamma\gamma$	0.21±0.03	0.21±0.03	0.02±0.01	0.01±0.01
$ZH(\to \gamma\gamma)$	1.62±0.11	0.77±0.05	0.75±0.05	0.35±0.03
$t\bar{t}H(\to \gamma\gamma)$	4.28±0.21	1.38±0.09	0.94±0.03	0.18±0.01
$b\bar{b}H(\to \gamma\gamma)$	0.11±0.01	0.04±0.00	0.02±0.00	0.00±0.00
$ggH(\to \gamma\gamma)$	1.64±0.10	0.59±0.06	0.77±0.07	0.27±0.04
$Z(\to b\bar{b})\gamma\gamma$	0.63±0.05	0.50±0.06	0.20±0.03	0.19±0.02
$t\bar{t}\gamma$	1.77±0.86	0.24±0.07	0.01±0.00	0.01±0.00
$t\bar{t}$	0.12±0.03	0.19±0.04	0.02±0.02	0.00±0.00
Totals				
All bkgs	39.2±1.4	27.1±0.8	6.9±0.4	3.8±0.2
Single H	7.7±0.3	2.8±0.1	2.5±0.1	0.8±0.1
Reducibles	29.1±1.1	23.4±0.8	4.2±0.4	2.9±0.2
Other	2.5±0.9	0.9±0.1	0.2±0.0	0.2±0.0
$S/\sqrt{B}$	1.32±0.05	0.46±0.03	1.60±0.06	0.52±0.03
Combined	**1.40±0.04**		**1.68±0.04**	

by increasing the cut on $p_T^{\gamma\gamma}$ peaking around 180GeV. A smaller improvement can also be seen by increasing the cut on $p_T^{b\bar{b}}$, combining both cuts results in an increase in significance from 1.40±0.04, with the original cut $p_T^{\gamma\gamma/b\bar{b}} > 80\text{GeV}$, to a maximum of 1.68±0.04 with cuts of $p_T^{\gamma\gamma} > 180\text{GeV}$ and $p_T^{b\bar{b}} > 170\text{GeV}$. Table 6.3 shows the number of expected events for each sample with these increased $p_T^{\gamma\gamma/b\bar{b}}$ cuts. Using these increased cuts results in a decrease in $HH \to b\bar{b}\gamma\gamma$ events kept by 51% but also reduces the total number of expected background events selected by 84% which results in an increase in significance of 20%.

However, the results of Figure 6.1 (and Table 6.3) are based on a version of the

Table 6.4: Expected number of signal and background events acquired using a weights based method with $p_T^{b\bar{b}/\gamma\gamma} > 80$GeV comparing the performance before (*Previous Layout*) and after (*Layout* 3.0). *All bkgs*[sum total of all backgrounds], *SingleH*[ZH, $t\bar{t}H$, $b\bar{b}H$, ggH], *Reducibles*[$b\bar{b}\gamma\gamma$, $b\bar{b}j\gamma$, $b\bar{b}jj$, $c\bar{c}\gamma\gamma$, $c\bar{c}j\gamma$, $jj\gamma\gamma$], *Others*[$\gamma\gamma Z(\to b\bar{b})$, $t\bar{t}\gamma$, $t\bar{t}$]

	Previous Layout		Layout 3.0	
	Barrel-barrel	Other	Barrel-barrel	Other
$HH \to b\bar{b}\gamma\gamma$	8.27±0.25	2.41±0.14	8.18±0.25	2.41±0.14
$b\bar{b}\gamma\gamma$	11.41±0.27	9.12±0.25	11.47±0.29	9.16±0.24
$b\bar{b}j\gamma$	13.99±0.97	10.27±0.55	14.42±1.12	10.10±0.54
$b\bar{b}jj$	2.82±0.44	3.40±0.53	1.92±0.35	3.04±0.60
$c\bar{c}\gamma\gamma$	0.35±0.02	0.19±0.02	0.85±0.05	0.43±0.04
$c\bar{c}j\gamma$	0.29±0.03	0.25±0.02	0.82±0.06	0.51±0.06
$jj\gamma\gamma$	0.21±0.03	0.21±0.03	0.81±0.07	0.68±0.03
$ZH(\to \gamma\gamma)$	1.62±0.11	0.77±0.05	1.63±0.11	0.79±0.05
$t\bar{t}H(\to \gamma\gamma)$	4.28±0.21	1.38±0.09	4.43±0.21	1.45±0.10
$bbH(\to \gamma\gamma)$	0.11±0.01	0.04±0.00	0.11±0.01	0.04±0.01
$ggH(\to \gamma\gamma)$	1.64±0.10	0.59±0.06	1.80±0.10	0.64±0.07
$Z(\to b\bar{b})\gamma\gamma$	0.63±0.05	0.50±0.06	0.64±0.05	0.50±0.06
$t\bar{t}\gamma$	1.77±0.86	0.24±0.07	2.12±0.84	0.26±0.07
$t\bar{t}$	0.12±0.03	0.19±0.04	0.12±0.03	0.20±0.04
Totals				
All bkgs	39.2±1.4	27.1±0.8	41.1±1.5	27.8±0.9
Single H	7.7±0.3	2.8±0.1	8.0±0.3	2.9±0.1
Reducibles	29.1±1.1	23.4±0.8	30.3±1.2	23.9±0.9
Other	2.5±0.9	0.9±0.1	2.9±0.8	1.0±0.1
S/$\sqrt{B}$	1.32±0.05	0.46±0.03	1.28±0.05	0.46±0.03
Combined	**1.40±0.04**		**1.35±0.03**	

mv2c10 algorithm which showed evidence of overtraining, it was also derived from a simulated detector with an optimistic material budget, discussed in detail in Section 2.5.6. These two factors both result in an overestimate of the *b*-tagging performance. The mv2c10 algorithm has since been thoroughly tested for overtraining and developed using Layout 3.0 of the detector which has a significantly more realistic material budget. Table 6.4 shows how the change to the updated mv2c10 algorithm affects the number of expected events and resulting significances for $p_T^{b\bar{b}/\gamma\gamma} > 80$GeV, this will be used as the new reference value of significance. Figure 6.2 and Table 6.5 show the effects of this change with the $p_T^{b\bar{b}/\gamma\gamma}$ cuts optimised.

Table 6.5: Expected number of signal and background events acquired using a weights based method comparing the performance before (*Previous Layout*) and after (*Layout* 3.0). The more realistic material budget is accounted for and increasing the p_T cuts applied to both the two photon and two b-tagged jet systems. Shown is the case for $p_T^{\gamma\gamma} > 180$GeV and $p_T^{b\bar{b}} > 170$GeV. *All bkgs*[sum total of all backgrounds], *SingleH*[ZH, $t\bar{t}H$, $b\bar{b}H$, ggH], *Reducibles*[$b\bar{b}\gamma\gamma$, $b\bar{b}j\gamma$, $b\bar{b}jj$, $c\bar{c}\gamma\gamma$, $c\bar{c}j\gamma$, $jj\gamma\gamma$], *Others*[$\gamma\gamma Z(\to b\bar{b})$, $t\bar{t}\gamma$, $t\bar{t}$]

|	Previous Layout		Layout 3.0	
	Barrel-barrel	Other	Barrel-barrel	Other
$HH \to b\bar{b}\gamma\gamma$	4.20±0.08	1.03±0.04	4.16±0.08	1.02±0.04
$b\bar{b}\gamma\gamma$	2.51±0.20	1.94±0.09	2.57±0.19	1.94±0.09
$b\bar{b}j\gamma$	1.53±0.36	0.83±0.22	1.50±0.39	1.07±0.20
$b\bar{b}jj$	0.07±0.07	0.00±0.00	0.07±0.07	0.01±0.01
$c\bar{c}\gamma\gamma$	0.03±0.00	0.03±0.00	0.07±0.01	0.08±0.01
$c\bar{c}j\gamma$	0.02±0.01	0.03±0.01	0.08±0.02	0.01±0.01
$jj\gamma\gamma$	0.02±0.01	0.01±0.01	0.10±0.01	0.06±0.01
$ZH(\to \gamma\gamma)$	0.75±0.05	0.35±0.03	0.75±0.05	0.35±0.03
$t\bar{t}H(\to \gamma\gamma)$	0.94±0.03	0.18±0.01	0.99±0.03	0.19±0.01
$bbH(\to \gamma\gamma)$	0.02±0.00	0.00±0.00	0.02±0.00	0.00±0.00
$ggH(\to \gamma\gamma)$	0.77±0.07	0.27±0.04	0.83±0.07	0.29±0.04
$Z(\to bb)\gamma\gamma$	0.20±0.03	0.19±0.02	0.20±0.03	0.18±0.02
$t\bar{t}\gamma$	0.01±0.00	0.01±0.00	0.01±0.00	0.01±0.01
$t\bar{t}$	0.02±0.02	0.00±0.00	0.02±0.02	0.01±0.00
Totals				
All bkgs	6.9±0.4	3.8±0.2	7.2±0.5	4.2±0.2
Single H	2.5±0.1	0.8±0.1	2.6±0.1	0.8±0.1
Reducibles	4.2±0.4	2.9±0.2	4.4±0.4	3.2±0.2
Other	0.2±0.0	0.2±0.0	0.2±0.0	0.2±0.0
S/$\sqrt{B}$	1.60±0.06	0.52±0.03	1.55±0.06	0.50±0.03
Combined	**1.68±0.04**		**1.63±0.04**	
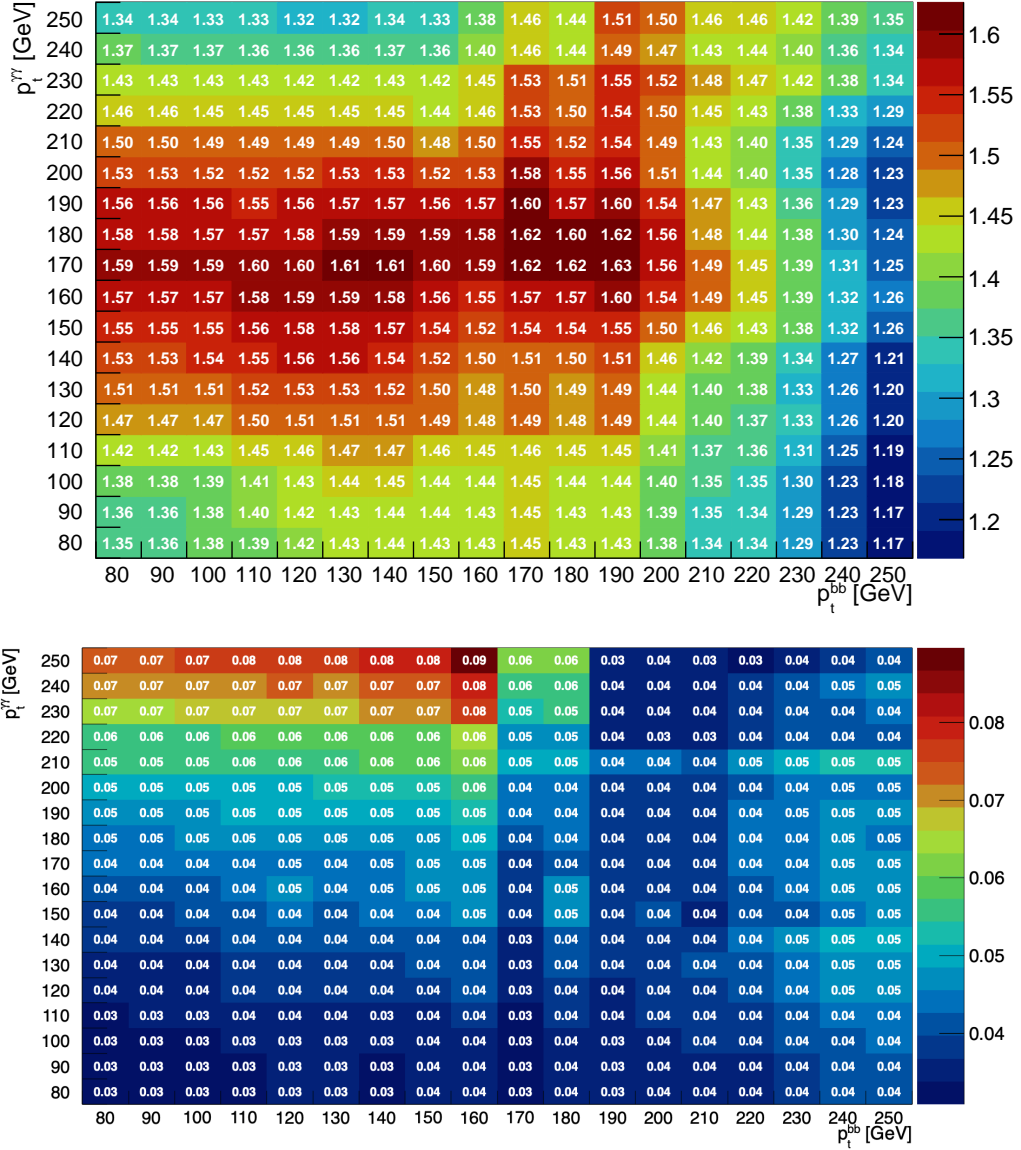
Figure 6.2: Expected significance (top) and error (bottom) acquired using a weights based method for an increase in p_T cuts applied to both the two photon and two b-tagged jet systems. The functions used for these results are based on a more realistic material budget

There is a small decrease to the central significance value, due to a slightly reduced simulated performance in the barrel region, however the results are unchanged within errors. The following results investigate several potential improvements after adopting the updated (and more realistic) mv2c10 algorithm. Initially increasing

the η range of accepted jets to 4.0 (previously 2.5) to maximise the ITk's potential b-tagging range. Figure 6.3 shows the two dimensional η distribution of the two selected b-jets for $HH \rightarrow b\bar{b}\gamma\gamma$ events (left) and for all backgrounds (right) ♠ at various stages of the cut flow described in Table 5.1. The signal is shown to be predominately in the central region with small η differences between b_1 and b_2, whereas, after all cuts have been applied, the backgrounds are evenly distributed throughout the detector. The ΔR cut is η dependant, as shown in Equation 2.2, and it can be shown that with a cut of $\Delta R < 2.0$, any two objects separated by more than two units of η are removed. This focuses on the signal that produces the b jets close in η due to the boost from the decaying Higgs. Increasing the η range of accepted jets to 4.0 is not expected to greatly improve the significance as the signal is concentrated in the region $|\eta| < 2.5$. This is due to the relatively large amount of energy required to create a $H \rightarrow HH$ event which results in the two Higgs bosons being produced at small $|\eta|$ values.

Many of the following results are initially shown before $p_T^{b\bar{b}/\gamma\gamma}$ optimisation so that the effects of different strategies and exploiting different detector capabilities can be clearly seen. Table 6.6 shows that the effect of increasing the range of accepted jets to $|\eta| < 4.0$ has a negligible effect on the total significance. Samples $b\bar{b}\gamma\gamma$, $c\bar{c}\gamma\gamma$, $jj\gamma\gamma$, $ZH(\rightarrow \gamma\gamma)$, $b\bar{b}H(\rightarrow \gamma\gamma)$, $ggH(\rightarrow \gamma\gamma)$ and $Z(\rightarrow b\bar{b})\gamma\gamma$ show an increased number of events as expected however samples $HH \rightarrow b\bar{b}\gamma\gamma$, $b\bar{b}j\gamma$, $b\bar{b}jj$, $c\bar{c}j\gamma$, $t\bar{t}H(\rightarrow \gamma\gamma)$, $t\bar{t}\gamma$ and $t\bar{t}$ show a decrease. This decrease can be explained by examining the cut on the number of total jets per event in more detail. Figure 6.4 shows how the distributions of the number of truth jets per event for each background category ($b\bar{b}\gamma\gamma$ included in *Reducibles*) before and after (those marked -4.0) the η range is increased. In each case it can be seen that the distribution of the number of jets per event is shifted to higher values as expected. A closer investigation into individual backgrounds is shown in Figure 6.5, here it can be seen that for backgrounds with a small number of jets per event, $jj\gamma\gamma$ for example, increasing the η range results in more events with a number of jets between $2 \leq n_{jets} < 6$ which results in more final

---

♠ The two dimensional η distribution of the two selected photons and two selected b-tagged jets for each individual background is shown in Appendix 2 before any cuts are applied
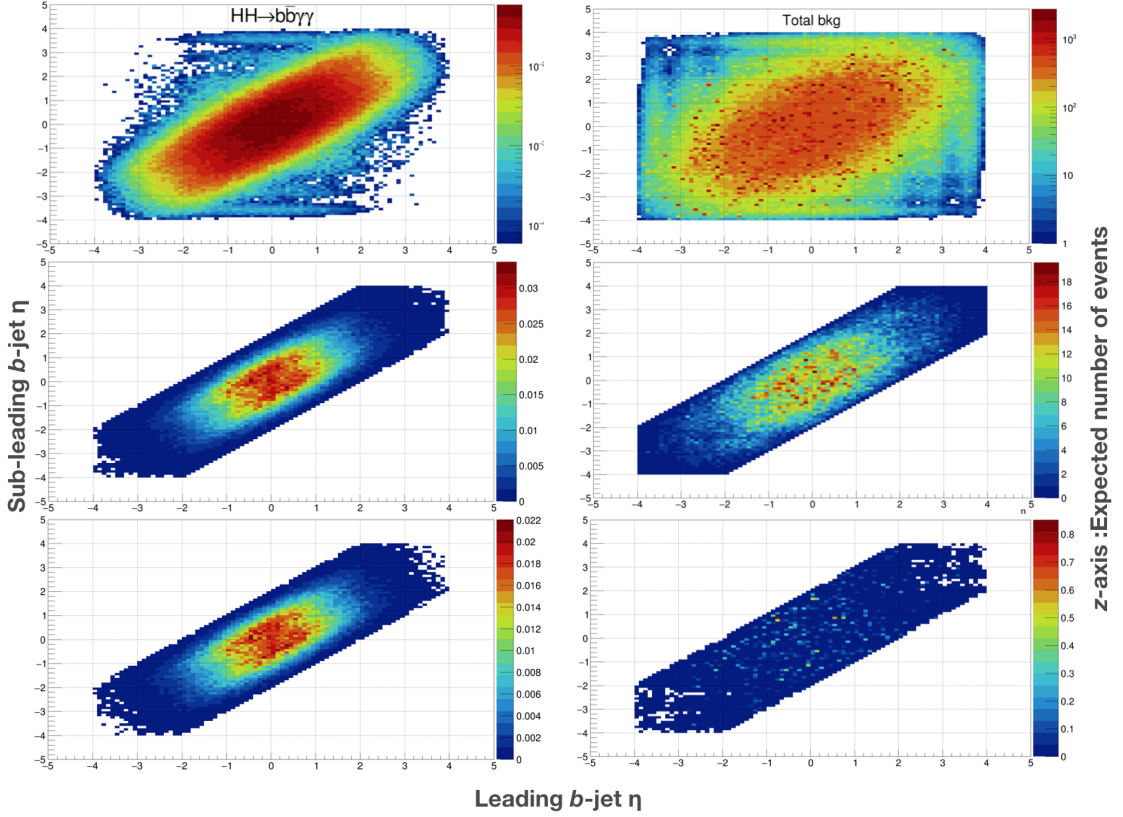
Figure 6.3: η distribution of the two b-tagged jets using a weighted analysis before cuts (top), after the ΔR cut (middle) and after all cuts (bottom). Both signal (left) and the sum of all background samples (right) are shown

events. The converse is true for backgrounds with a large number of jets per event, $t\bar{t}$ for example, where the additional region of accepted jets results in more events with $n_{jets} > 5$ which are then cut. The $HH \rightarrow b\bar{b}\gamma\gamma$ events are subject to these two effects in approximately equally amounts, which results in only a small decrease in final events with an increased $|\eta|$ range.

Table 6.6 shows that to fully exploit the total b-tagging capabilities of the ITk up to $|\eta| < 4.0$ the cut of $2 \leq n_{jets} < 6$ is no longer optimal. Two alternatives to this cut were considered, firstly the limit on the total number of jets was removed entirely. Secondly, the total number of jets cut of $2 \leq n_{jets} < 6$ was only applied to jets within the central $|\eta| < 2.5$ region and jets in the region $2.5 < |\eta| < 4.0$ were considered for reconstruction but not counted in n_{jets}. The three variations of the n_{jets} cut are

Table 6.6: Expected number of signal and background events acquired using a weights based method, comparing the performance if the accepted η range for jets is increased from 2.5 to 4.0 for $p_T^{b\bar{b}/\gamma\gamma} > 80$GeV. Here *jet $\eta < 2.5$* is the same as *Layout*3.0 in Table 6.4. *All bkgs*[sum total of all backgrounds], *SingleH*[ZH, $t\bar{t}H$, $b\bar{b}H$, ggH], *Reducibles*[$b\bar{b}\gamma\gamma$, $b\bar{b}j\gamma$, $b\bar{b}jj$, $c\bar{c}\gamma\gamma$, $c\bar{c}j\gamma$, $jj\gamma\gamma$], *Others*[$\gamma\gamma Z(\to b\bar{b})$, $t\bar{t}\gamma$, $t\bar{t}$]

	jet $\eta < 2.5$		jet $\eta < 4.0$	
	Barrel-barrel	Other	Barrel-barrel	Other
$HH \to b\bar{b}\gamma\gamma$	8.18±0.25	2.41±0.14	7.65±0.24	2.39±0.14
$b\bar{b}\gamma\gamma$	11.47±0.29	9.16±0.24	11.24±0.32	9.42±0.25
$b\bar{b}j\gamma$	14.42±1.12	10.10±0.54	11.87±1.36	9.19±0.42
$b\bar{b}jj$	1.92±0.35	3.04±0.60	1.30±0.45	2.06±0.73
$c\bar{c}\gamma\gamma$	0.85±0.05	0.43±0.04	0.87±0.04	0.51±0.04
$c\bar{c}j\gamma$	0.82±0.06	0.51±0.06	0.68±0.07	0.47±0.03
$jj\gamma\gamma$	0.81±0.07	0.68±0.03	0.84±0.06	0.72±0.05
$ZH(\to \gamma\gamma)$	1.63±0.11	0.79±0.05	1.62±0.10	0.87±0.06
$t\bar{t}H(\to \gamma\gamma)$	4.43±0.21	1.45±0.10	3.51±0.16	1.17±0.08
$bbH(\to \gamma\gamma)$	0.11±0.01	0.04±0.01	0.11±0.01	0.05±0.01
$ggH(\to \gamma\gamma)$	1.80±0.10	0.64±0.07	1.77±0.08	0.71±0.08
$Z(\to b\bar{b})\gamma\gamma$	0.64±0.05	0.50±0.06	0.63±0.04	0.53±0.05
$t\bar{t}\gamma$	2.12±0.84	0.26±0.07	2.02±0.84	0.22±0.07
$t\bar{t}$	0.12±0.03	0.20±0.04	0.10±0.03	0.18±0.04
Totals				
All bkgs	41.1±1.5	27.8±0.9	36.6±1.7	26.1±0.9
Single H	8.0±0.3	2.9±0.1	7.0±0.2	2.8±0.1
Reducibles	30.3±1.2	24.0±0.9	26.8±1.5	22.4±0.9
Other	2.9±0.8	1.0±0.1	2.8±0.8	0.9±0.1
S/$\sqrt{B}$	1.28±0.05	0.46±0.03	1.26±0.05	0.47±0.03
Combined	**1.35±0.03**		**1.35±0.04**	
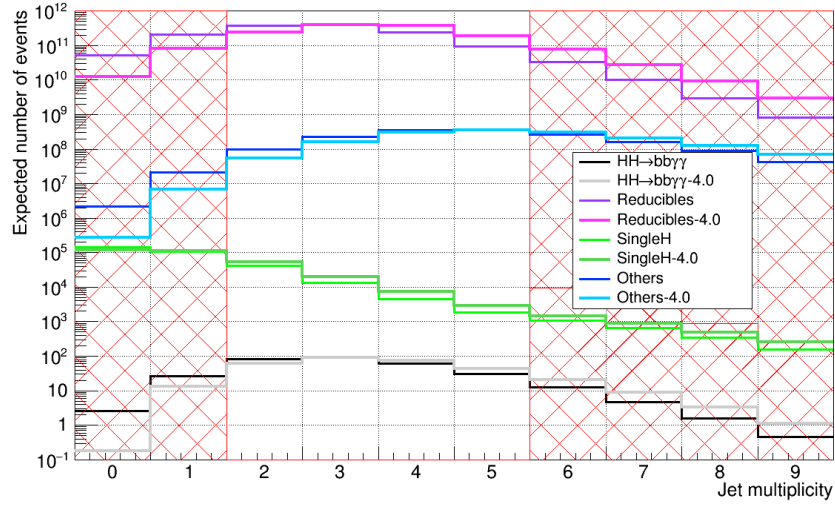
Figure 6.4: Expected number of events for signal and collective background samples showing how the distribution of the number of jets per event is affected by increasing the accepted η range of all jets from 2.5 to 4.0
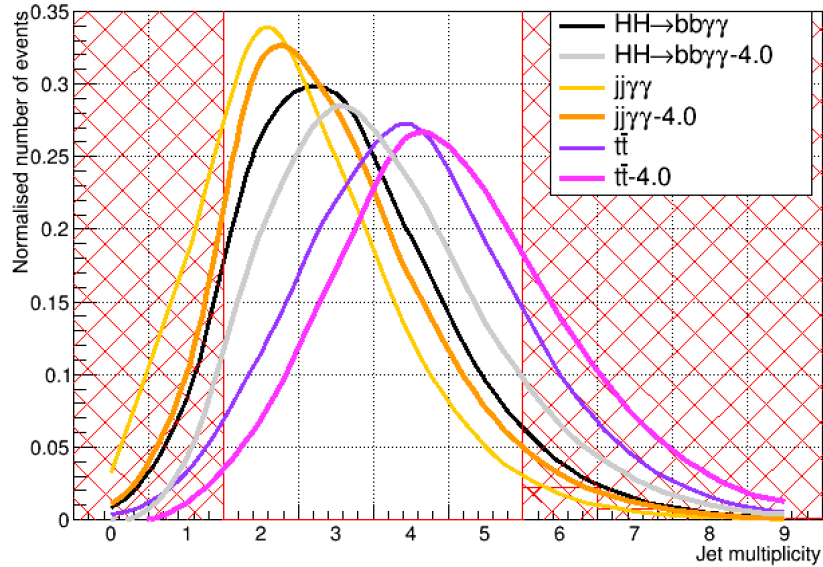
Figure 6.5: Normalised number of events for selected samples showing how the distribution of the number of jets per event is affected by increasing the accepted η range of all jets from 2.5 to 4.0. Each central bin value has been connected for each distribution to better show this affect

compared in Table 6.7 where $6jcut$ represents the $2 \leq n_{jets} < 6$ cut. Where the limit on n_{jets} is removed ($6jcutOFF$) there is a large increase in the final number of signal events however there is also a significant increase in background events resulting in decreased overall performance. If the 6j cut is applied to the central $|\eta| < 2.5$ region

only ($6j2.5$) there is a small increase in the central significance value, however there is no significant difference within errors. The small increase is because the signal integrity is maintained in this region and the additional η range gives a sizeable contribution to the signal relative to the backgrounds.

As shown with previous results it is also possible to increase performance by increasing the $p_T^{b\bar{b}/\gamma\gamma}$ cut. Figure 6.6 shows the 2D significance for different $p_T^{b\bar{b}/\gamma\gamma}$ cuts when the η range of accepted jets is increased to 4.0 and the $2 \leq n_{jets} < 6$ cut is applied to all jets, it also shows that a performance gain from 1.35±0.03 to 1.60±0.04 is possible by applying the cuts $p_T^{b\bar{b}} > 170\text{GeV}$ and $p_T^{\gamma\gamma} > 180\text{GeV}$. Figure 6.7 shows the same distribution but with no limit applied to the number of jets per event. The increase in background events is significantly larger than the increase in signal events, resulting in a decreased performance compared to the results of Figure 6.6, a maximum of only 1.53±0.03 is achievable. However, as shown in Figure 6.8, if the requirement on the number of jets is limited to the central $\eta < 2.5$ region only, then a significance of 1.67±0.04 is achieved by applying the cuts $p_T^{b\bar{b}} > 170\text{GeV}$ and $p_T^{\gamma\gamma} > 180\text{GeV}$. As this final variant on the n_{jets} cut gives the greatest performance it is implemented in all further studies whenever the full $\eta < 4.0$ range of accepted jets is considered.

To optimise the background rejection♠, a two dimensional Gaussian curve can be applied to the η distributions of the two b-tagged jets which is described by the following:

$$\frac{(x - \overline{x})^2}{n_x^2 \sigma_x^2} + \frac{(y - \overline{y})^2}{n_y^2 \sigma_y^2} - \frac{2\rho(x - \overline{x})(y - \overline{y})}{n_x \sigma_x n_y \sigma_y} + \rho^2 \quad = \quad 1 \qquad (6.1)$$

where $\overline{x}$ and $\overline{y}$ are the means and σ_x and σ_y are the standard deviations of the x and y data sets respectively, n_x and n_y are factors applied post-fit which can be varied to adjust the shape of the 2D Gaussian and ρ is the correlation coefficient between

---

♠ Note that many of the background samples are only LO in QCD and there are a limited number of events with high $p_T^{b\bar{b}/\gamma\gamma}$, therefore small changes in background estimates could change significance values

Table 6.7: Expected number of signal and background events acquired using a weights based method comparing different implementations of the 6 jet cut for $p_T^{b\bar{b}/\gamma\gamma} > 80$GeV. Where $6jcutON$ is the same as $jet\ \eta < 4.0$ in Table 6.6. *All bkgs*[sum total of all backgrounds], $SingleH[ZH, t\bar{t}H, b\bar{b}H, ggH]$, $Reducibles[b\bar{b}\gamma\gamma, b\bar{b}j\gamma, b\bar{b}jj, c\bar{c}\gamma\gamma, c\bar{c}j\gamma, jj\gamma\gamma]$, $Others[\gamma\gamma Z(\to b\bar{b}), t\bar{t}\gamma, t\bar{t}]$

	6jcutON		6jcutOFF		6j2.5	
	Barrel-barrel	Other	Barrel-barrel	Other	Barrel-barrel	Other
$HH \to bb\gamma\gamma$	7.65±0.24	2.39±0.14	9.36±0.29	2.85±0.17	8.42±0.26	2.61±0.15
$bb\gamma\gamma$	11.24±0.32	9.42±0.25	13.84±0.27	11.54±0.26	12.30±0.33	10.34±0.23
$bbj\gamma$	11.87±1.36	9.19±0.42	20.80±1.48	15.92±2.00	14.42±1.54	11.30±0.52
$bbjj$	1.30±0.45	2.06±0.73	1.83±0.52	3.85±1.06	1.65±0.46	2.49±0.86
$c\bar{c}\gamma\gamma$	0.87±0.04	0.51±0.04	1.30±0.06	0.60±0.05	1.01±0.05	0.55±0.04
$c\bar{c}j\gamma$	0.68±0.07	0.47±0.03	1.09±0.09	0.78±0.09	0.80±0.08	0.61±0.06
$jj\gamma\gamma$	0.84±0.06	0.72±0.05	1.13±0.09	0.89±0.07	0.95±0.07	0.77±0.05
$ZH(\to \gamma\gamma)$	1.62±0.10	0.87±0.06	1.74±0.11	0.91±0.07	1.68±0.11	0.90±0.07
$t\bar{t}H(\to \gamma\gamma)$	3.51±0.16	1.17±0.08	11.99±0.49	3.64±0.25	4.52±0.21	1.60±0.11
$bbH(\to \gamma\gamma)$	0.11±0.01	0.05±0.01	0.12±0.01	0.05±0.01	0.12±0.01	0.05±0.01
$ggH(\to \gamma\gamma)$	1.77±0.08	0.71±0.08	2.13±0.10	0.78±0.07	1.98±0.10	0.77±0.07
$Z(\to bb)\gamma\gamma$	0.63±0.04	0.53±0.05	0.81±0.04	0.57±0.06	0.71±0.04	0.55±0.06
$t\bar{t}\gamma$	2.02±0.84	0.22±0.07	5.72±1.37	0.34±0.08	2.10±0.84	0.27±0.07
$t\bar{t}$	0.10±0.03	0.18±0.04	0.21±0.05	0.25±0.04	0.12±0.03	0.20±0.05
Totals						
All bkgs	36.6±1.7	26.1±0.9	62.7±2.2	40.1±2.3	42.4±1.9	30.4±1.1
Single H	7.0±0.2	2.8±0.1	16.0±0.5	5.4±0.3	8.3±0.3	3.3±0.2
Reducibles	26.8±1.5	22.4±0.9	40.0±1.6	33.6±2.3	31.1±1.6	26.1±1.0
Other	2.8±0.8	0.9±0.1	6.7±1.4	1.2±0.1	2.9±0.9	1.0±0.1
$S/\sqrt{B}$	1.26±0.05	0.47±0.03	1.18±0.04	0.45±0.03	1.29±0.05	0.47±0.03
Combined	**1.35±0.03**		**1.26±0.03**		**1.38±0.04**	
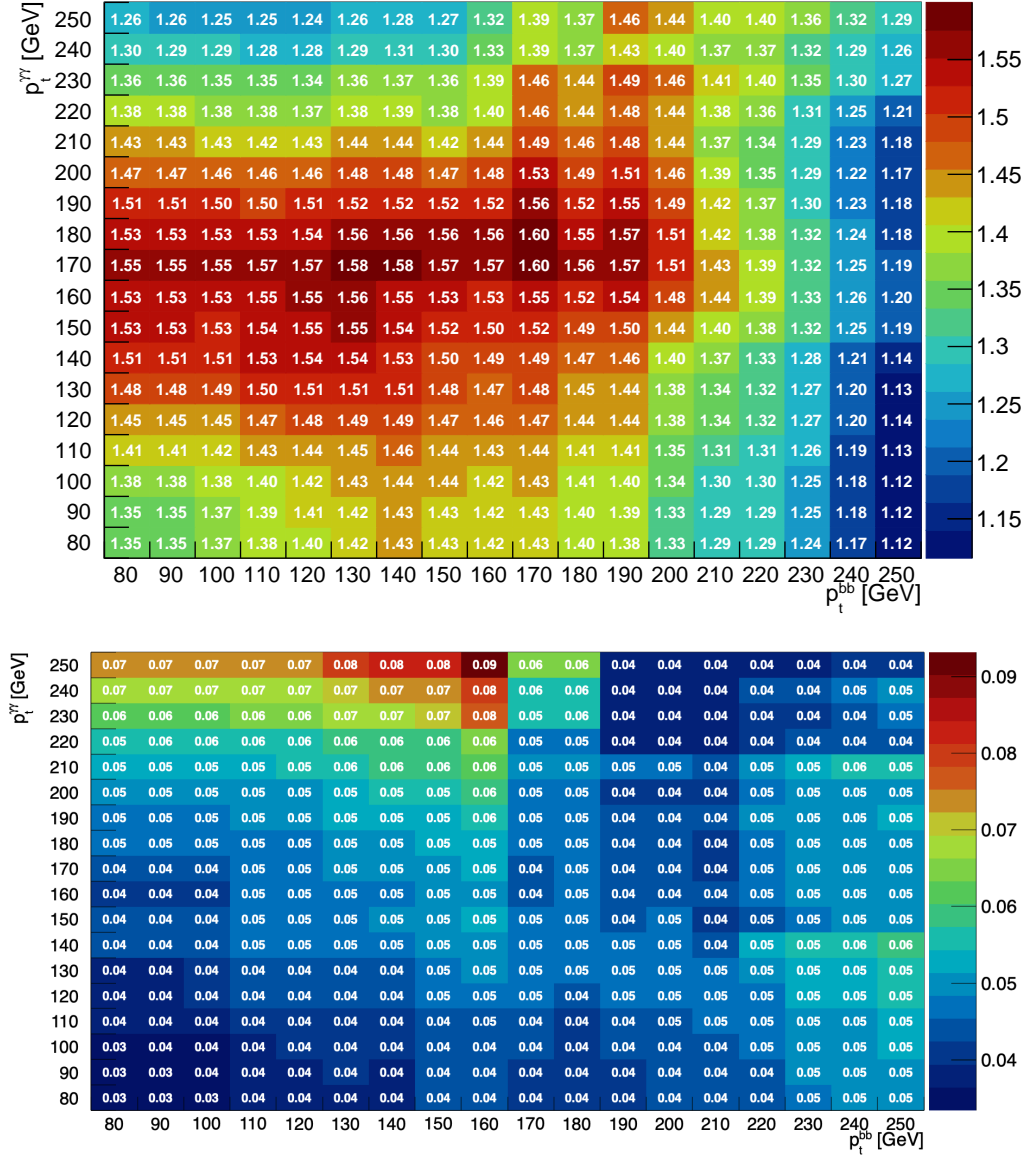
Figure 6.6: Expected significance (top) and error (bottom) acquired using a weights based method for an increase in p_T cuts applied to both the two photon and two b-tagged jet systems. Also with an increased accepted jet η from 2.5 to 4.0

the two data sets. Once the fit to the signal events is complete and the parameters found, n_x and n_y are scanned over and events resulting in Equation 6.1 returning ≤ 1 are cut. The same equation and parameters are applied to the background events and then an optimum set of parameters can be found which gives the greatest $S/\sqrt{B}$. It was found that the 2D fit gives the greatest performance when only applied to
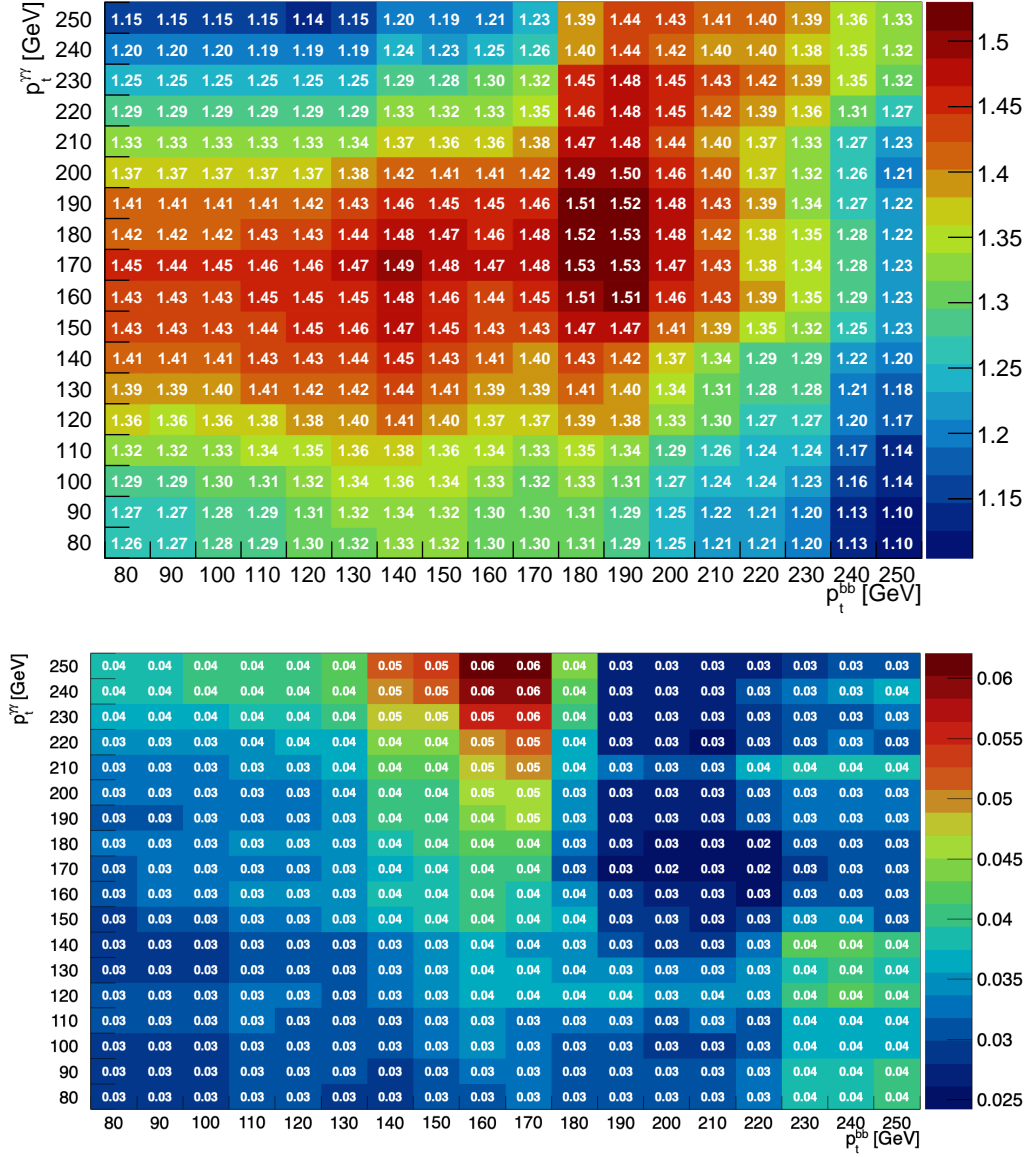
Figure 6.7: Expected significance (top) and error (bottom) acquired using a weights based method for an increase in p_T cuts applied to both the two photon and two b-tagged jet systems. Also with an increased accepted jet η from 2.5 to 4.0 and with no cuts applied to the maximum number of jets per event

the events that have both photons in the barrel region (those marked *barrel-barrel*) and when the events marked *Other* are not subject to further cuts. Figure 6.9 shows the results of this technique applied to increasing cuts on $p_T^{b\bar{b}/\gamma\gamma}$, which gives a maximum significance of 1.83±0.08. Table 6.8 shows the expected number of signal
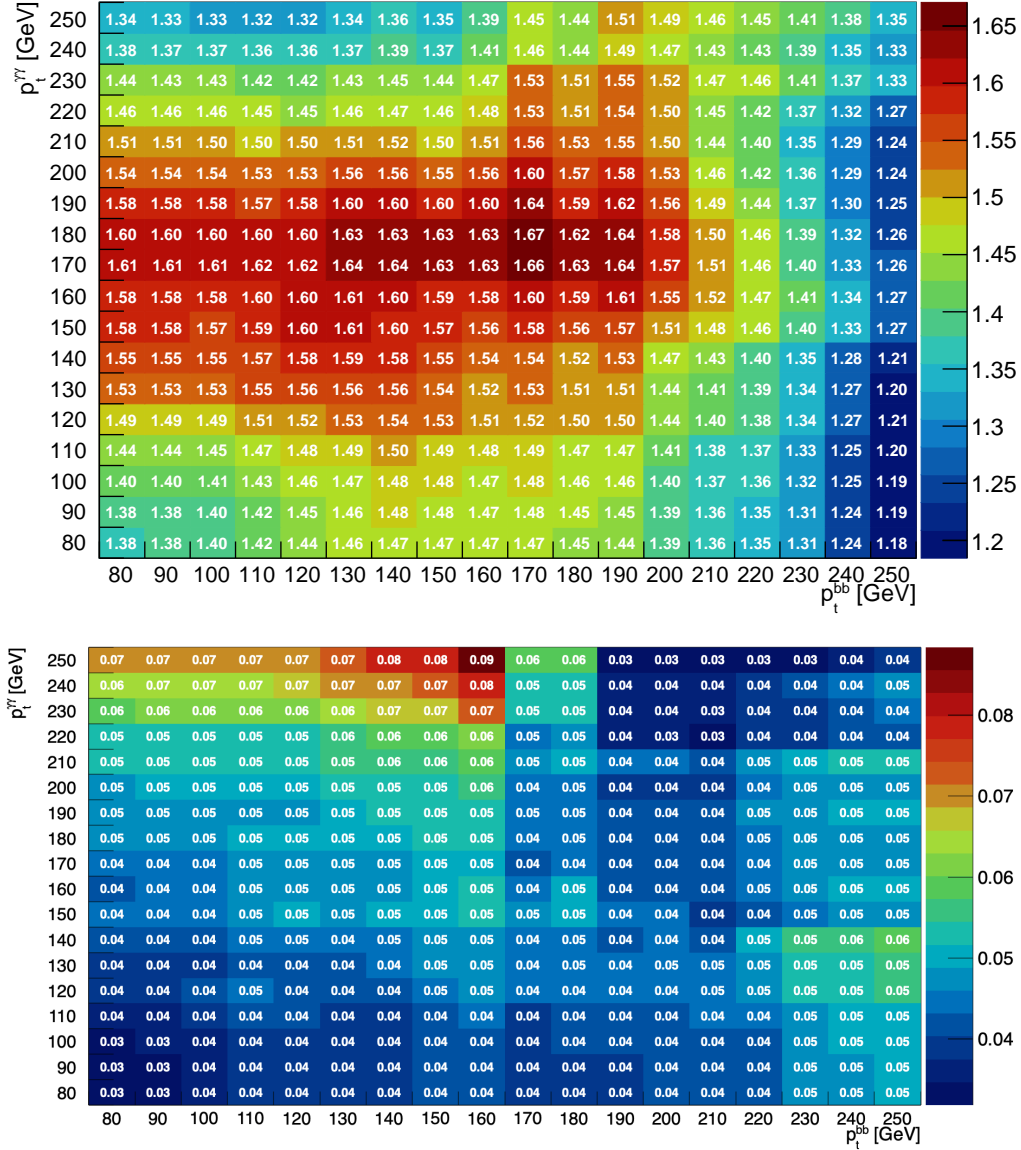
Figure 6.8: Expected significance (top) and error (bottom) acquired using a weights based method for an increase in p_T cuts applied to both the two photon and two b-tagged jet systems. Also with an increased accepted jet η from 2.5 to 4.0 but with less than six jets in the central $|\eta| < 2.5$ region only

and background events which can result from the best performing $p_T^{b\bar{b}/\gamma\gamma}$ cuts when the $6j2.5$ cut is applied (left) and also when the 2D Gaussian cuts are included (right). The increase in the number of events in some of the samples is due to the best performing $p_T^{b\bar{b}/\gamma\gamma}$ cuts being different for the two scenarios shown.

Table 6.8: Expected number of signal and background events acquired using a weights based method including elliptical cuts on the η distribution of jets. *All bkgs*[sum total of all backgrounds], *SingleH*[ZH, $t\bar{t}H$, $b\bar{b}H$, ggH], *Reducibles*[$b\bar{b}\gamma\gamma$, $b\bar{b}j\gamma$, $b\bar{b}jj$, $c\bar{c}\gamma\gamma$, $c\bar{c}j\gamma$, $jj\gamma\gamma$], *Others*[$\gamma\gamma Z(\to b\bar{b})$, $t\bar{t}\gamma$, $t\bar{t}$]

|	$p_T^{bb/\gamma\gamma} < 80$GeV		$p_T^{bb/\gamma\gamma}$ optimised		$p_T^{bb/\gamma\gamma}$ Elliptical cuts	
	Barrel-barrel	Other	Barrel-barrel	Other	Barrel-barrel	Other
$HH \to bb\gamma\gamma$	8.18±0.25	2.41±0.14	4.59±0.10	1.19±0.05	4.97±0.23	1.66±0.09
$bb\gamma\gamma$	11.47±0.29	9.16±0.24	2.87±0.12	2.10±0.13	2.37±0.28	3.64±0.20
$bbj\gamma$	14.42±1.12	10.10±0.54	1.66±0.43	0.91±0.18	1.98±0.69	2.54±0.62
$bbjj$	1.92±0.35	3.04±0.60	0.07±0.07	0.00±0.00	0.07±0.07	0.20±0.20
$c\bar{c}\gamma\gamma$	0.85±0.05	0.43±0.04	0.12±0.02	0.11±0.02	0.11±0.02	0.17±0.02
$c\bar{c}j\gamma$	0.82±0.06	0.51±0.06	0.07±0.02	0.03±0.02	0.09±0.03	0.10±0.03
$jj\gamma\gamma$	0.81±0.07	0.68±0.03	0.11±0.02	0.06±0.01	0.09±0.02	0.15±0.02
$ZH(\to \gamma\gamma)$	1.63±0.11	0.79±0.05	0.77±0.06	0.36±0.03	0.76±0.04	0.44±0.04
$t\bar{t}H(\to \gamma\gamma)$	4.43±0.21	1.45±0.10	1.17±0.05	0.29±0.02	1.62±0.12	0.68±0.05
$bbH(\to \gamma\gamma)$	0.11±0.01	0.04±0.01	0.02±0.00	0.00±0.00	0.03±0.00	0.01±0.00
$ggH(\to \gamma\gamma)$	1.80±0.10	0.64±0.07	1.01±0.07	0.33±0.05	0.80±0.10	0.50±0.06
$Z(\to bb)\gamma\gamma$	0.64±0.05	0.50±0.06	0.21±0.02	0.19±0.02	0.16±0.03	0.23±0.03
$t\bar{t}\gamma$	2.12±0.84	0.26±0.07	0.45±0.41	0.00±0.00	0.03±0.02	0.01±0.00
$t\bar{t}$	0.12±0.03	0.20±0.04	0.00±0.00	0.00±0.00	0.02±0.02	0.00±0.00
Totals						
All bkgs	41.1±1.5	27.8±0.9	8.5±0.6	4.4±0.2	8.2±0.8	8.7±0.7
Single H	8.0±0.3	2.9±0.1	3.0±0.1	1.0±0.1	3.2±0.2	1.6±0.1
Reducibles	30.3±1.2	23.1±0.9	4.9±0.5	3.2±0.2	4.7±0.8	6.8±0.7
Other	2.9±0.8	1.0±0.1	0.7±0.4	0.2±0.0	0.2±0.0	0.3±0.0
$S/\sqrt{B}$	1.28±0.05	0.46±0.03	1.57±0.07	0.57±0.03	1.74±0.12	0.56±0.04
Combined	**1.35±0.03**		**1.67±0.04**		**1.83±0.08**	
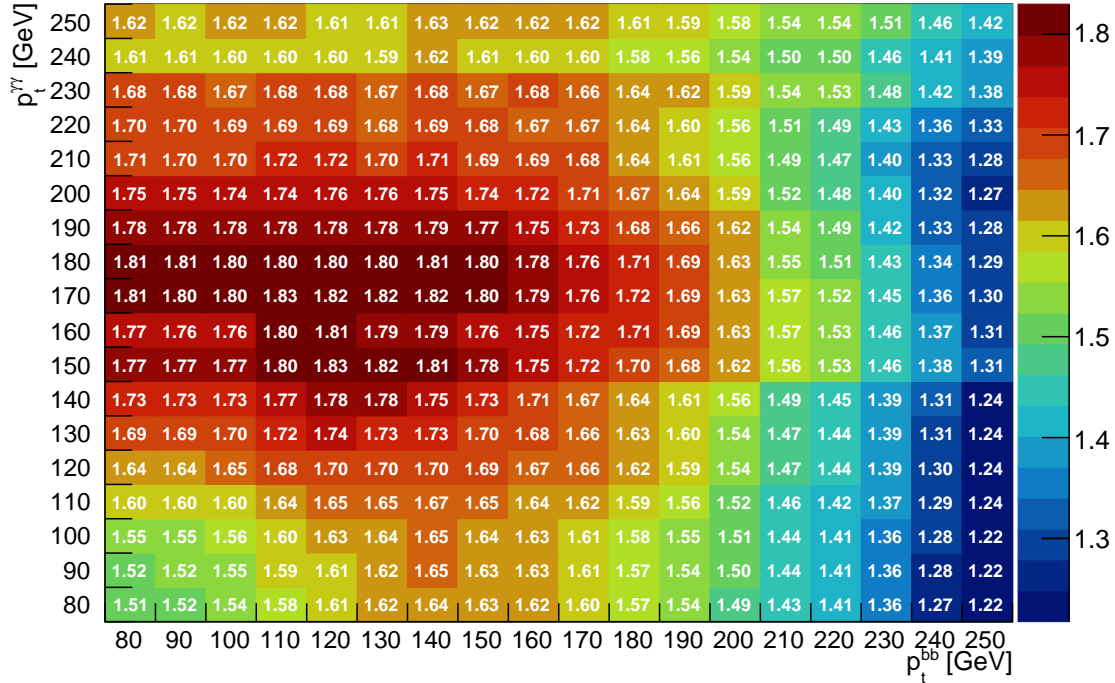
Figure 6.9: Expected significance acquired using a weights based method for an increase in p_T cuts applied to both the two photon and two b-tagged jet systems and with an increased accepted jet η from 2.5 to 4.0 but also with less than six jets in the central $|\eta| < 2.5$ region. Additional cuts are also applied based on a 2D Gaussian fit to the η distributions of the two b-tagged jets

6.2   Studies including the High Granularity Timing Detector

By increasing the η range of accepted jets to 4.0 the effects of the High Granularity Timing Detector (HGTD) can also be considered. The latest version of the mv2c10 b-tagging algorithm however does not include parametrisation for the HGTD, instead a different algorithm, named $ip3dsv1$ [77] (discussed in Section 2.5.6), has been utilised for Layout 3.0 to account for the HGTD. Figure 6.10 shows the relative b-tagging performance of this algorithm with and without the effects of the HGTD. Note the two z-axis scales where the greyscale is negative, i.e. performance in these areas decreases when the HGTD is included. The decrease is due to the early stage of development for including the HGTD in tagging algorithms, several improvements are

currently being considered including dedicated MC samples. However the ip3dsv1 tagger is considered sufficient to compare the effects of including the HGTD.
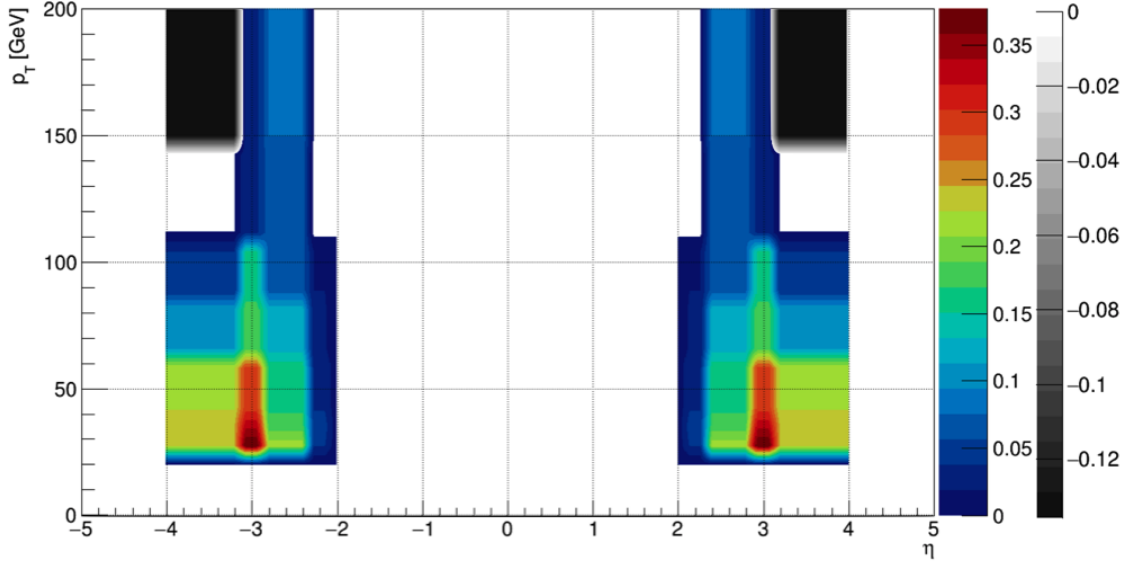
Figure 6.10: Difference in ip3dsv1 b-tagging performance between scenarios including the HGTD and without as a function of p_T and η

To see the effects of including the HGTD the previously shown results were repeated using the ip3dsv1 algorithm and are shown in Table 6.9, where all results are shown with cuts of $p_T^{\gamma\gamma} > 170\text{GeV}$ and $p_T^{b\bar{b}} > 180\text{GeV}$ applied which gives the greatest performance for each case. Table 6.9 shows improved performance when increasing the accepted jet η range from 2.5 to 4.0 while maintaining the n_{jets} cut to only jets within the central $\eta < 2.5$ region with the ip3dsv1 tagging algorithm (as also seen with the mv2c10 algorithm). The HGTD however is seen to have no effect within errors on any sample resulting in no change to performance. This as expected due to the majority of $HH \rightarrow b\bar{b}\gamma\gamma$ events being produced in the central region where the HGTD does not provide any additional information and the number of events at high η being too few to make a difference to performance. As previously discussed in Section 6.1 and shown in Figure 6.3, the two selected b-tagged jets are favourably produced in the central region of the detector. The same is also true for the two selected photons as shown in Figure 6.11 which shows the two dimensional η distribution of these two photons for $HH \rightarrow b\bar{b}\gamma\gamma$ events (left) and for all backgrounds (right) at various stages of the cut flow as described in Table

5.1.
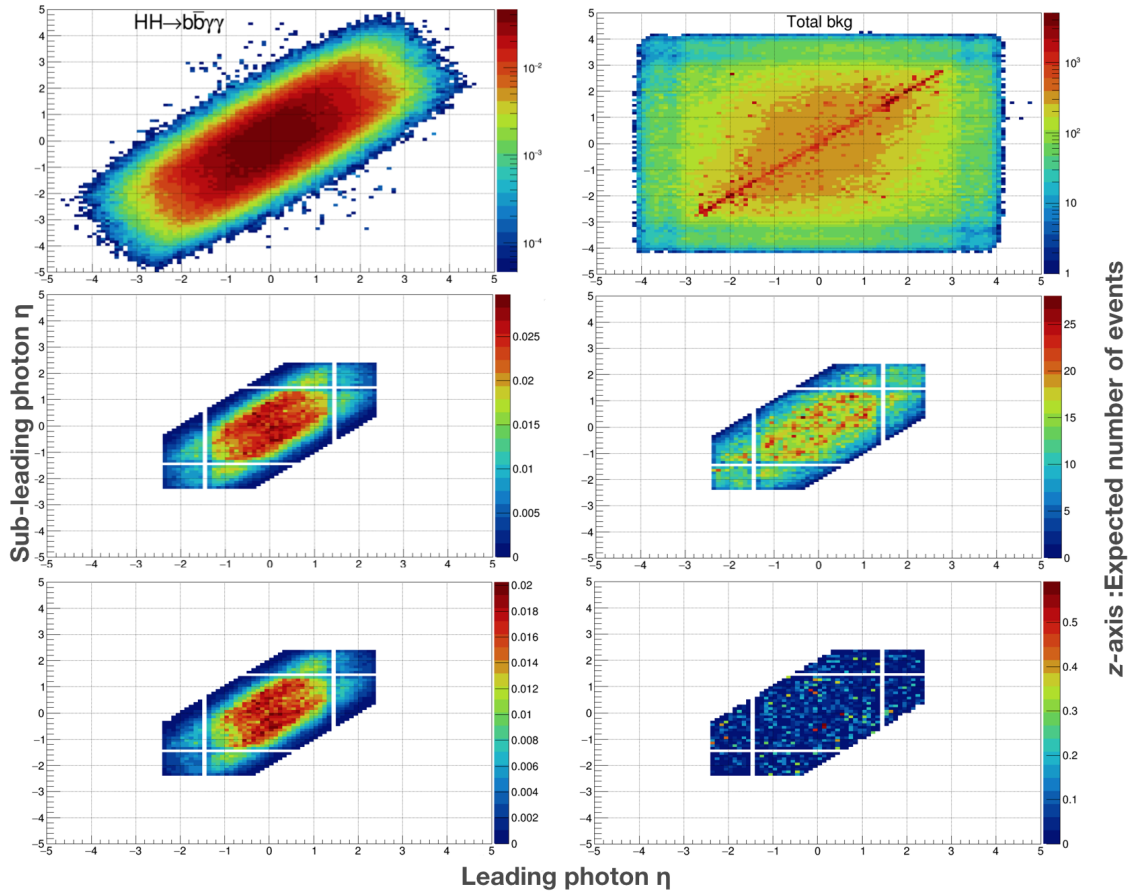
Figure 6.11: η distribution of the two selected photons using a weighted analysis before cuts (top), after the ΔR cut (middle) and after all cuts (bottom). Both signal (left) and the sum of all background samples (right) are shown

Table 6.9: Expected number of signal and background events acquired using the IP3DSV1 b-tagging algorithms and a weights based method comparing different implementations of the 6 jet cut and the effects of the HGTD. Shown is the case of $p_T^{\gamma\gamma} > 180$GeV and $p_T^{b\bar{b}} > 170$GeV which gives the greatest significance across all three scenarios. $All\ bkgs$[sum total of all backgrounds], $SingleH$[ZH, $t\bar{t}H$, bbH, ggH], $Reducibles$[$b\bar{b}\gamma\gamma$, $b\bar{b}j\gamma$, $b\bar{b}jj$, $c\bar{c}\gamma\gamma$, $c\bar{c}j\gamma$, $jj\gamma\gamma$], $Others$[$\gamma\gamma Z(\to b\bar{b})$, $t\bar{t}\gamma$, $t\bar{t}$]

	jet $\eta < 2.5$ 6jON		jet $\eta < 4.0$ 6j2.5		jet $\eta < 4.0$ 6j2.5 HGTD	
	Barrel-barrel	Other	Barrel-barrel	Other	Barrel-barrel	Other
$HH \to bb\gamma\gamma$	4.10±0.08	1.10±0.05	4.21±0.09	1.18±0.05	4.19±0.09	1.18±0.05
$bb\gamma\gamma$	2.51±0.16	1.94±0.05	2.64±0.16	2.14±0.08	2.64±0.16	2.10±0.08
$bbj\gamma$	1.99±0.32	0.79±0.18	1.56±0.31	0.78±0.21	1.56±0.31	0.79±0.21
$bbjj$	0.17±0.16	0.00±0.00	0.16±0.16	0.00±0.00	0.16±0.16	0.00±0.00
$c\bar{c}\gamma\gamma$	0.49±0.04	0.50±0.07	0.57±0.06	0.57±0.08	0.56±0.05	0.55±0.07
$c\bar{c}j\gamma$	0.23±0.06	0.49±0.16	0.24±0.06	0.52±0.14	0.24±0.06	0.52±0.14
$jj\gamma\gamma$	0.37±0.09	0.22±0.05	0.38±0.12	0.37±0.08	0.47±0.11	0.36±0.07
$ZH(\to \gamma\gamma)$	0.83±0.05	0.36±0.03	0.87±0.06	0.39±0.03	0.86±0.06	0.39±0.03
$t\bar{t}H(\to \gamma\gamma)$	1.37±0.05	0.35±0.02	1.37±0.06	0.36±0.02	1.36±0.06	0.36±0.02
$bbH(\to \gamma\gamma)$	0.02±0.00	0.00±0.00	0.02±0.00	0.01±0.00	0.02±0.00	0.01±0.00
$ggH(\to \gamma\gamma)$	1.24±0.07	0.37±0.04	1.31±0.08	0.45±0.05	1.32±0.07	0.45±0.05
$Z(\to bb)\gamma\gamma$	0.19±0.02	0.15±0.02	0.21±0.02	0.16±0.02	0.21±0.02	0.16±0.02
$t\bar{t}\gamma$	0.51±0.46	0.03±0.01	0.52±0.47	0.01±0.01	0.51±0.47	0.01±0.01
$t\bar{t}$	0.01±0.00	0.00±0.00	0.00±0.00	0.00±0.00	0.00±0.00	0.00±0.00
Totals						
All bkgs	9.9±0.6	5.2±0.3	9.9±0.6	5.8±0.3	9.9±0.6	5.7±0.3
Single H	3.5±0.1	1.1±0.1	3.6±0.1	1.2±0.1	3.6±0.1	1.2±0.1
Reducibles	5.8±0.4	3.9±0.3	5.6±0.4	4.4±0.3	5.6±0.4	4.3±0.3
Other	0.7±0.5	0.2±0.0	0.7±0.5	0.2±0.0	0.7±0.5	0.2±0.0
$S/\sqrt{B}$	1.30±0.05	0.48±0.02	1.34±0.05	0.49±0.03	1.33±0.05	0.49±0.03
Combined	**1.39±0.04**		**1.43±0.04**		**1.42±0.04**	

6.3   Boosted Decision Tree

Various additional optimisations are possible with a weights based approach to the $HH \rightarrow b\bar{b}\gamma\gamma$ due to its distinctive topology. However a cuts based approach will often make sub-optimal use of all the available information so the multivariate approach is instead adopted to achieve the maximal significance.

The results of [26] are the first to show the effect of a BDT on the prospects of the $HH \rightarrow b\bar{b}\gamma\gamma$ channel. The results are summarised in Table 6.10 where a different approximation of the significance has been adopted as the $S/\sqrt{B}$ approximation is only valid for $S << B$. This approximation (detailed in [126]) provides the median significance Z_0 in the hypothesis of S signal and B background events:

$$median[Z_0|S+B] = \sqrt{q_0, A} \quad \approx \sqrt{2\left((S+B)ln\left(1 + \frac{S}{B}\right) - S\right)} \qquad (6.2)$$

Both approximations are included in Table 6.10 to show the extent the $S/\sqrt{B}$ approximation becomes an overestimate when $S \simeq B$, subsequently all BDT results will adopt the $\sqrt{q_0, A}$ approximation of the significance.

Table 6.10 shows a significance of 1.98 is possible, however this was achieved using both a different set of variables to previous methods (shown in Table 5.2) and also the overtrained version of the mv2c10 tagging algorithm. Additionally events were not separated based on the two selected photon pseudorapidites. Therefore in this section the effects of a BDT on the $HH \rightarrow b\bar{b}\gamma\gamma$ channel are updated to include the latest available b-tagging algorithms and previously shown techniques. Also results of studies into the potential improvements possible with different pixel sensor geometries and a reduced radius of the innermost layer are investigated.

All the following results are shown after the pre-selection (detailed in Section 5.6); the BDT response cut; an additional cut of $m_{\gamma\gamma}$ of $123 < m_{\gamma\gamma} < 127\text{GeV}$ and after events are split into *Barrel-barrel* and *Other* to improve performance as discussed

Table 6.10: Expected number of signal and background events acquired using a BDT. Showing a summary of the published results, with an unrealistic material budget [26]. Results are after the BDT response cut of 0.54 and an additional $123 < m_{\gamma\gamma} < 127$GeV cut. The BDT response distribution is shown in Appendix A.6 . *All bkgs*[sum total of all backgrounds], *SingleH*[ZH, $t\bar{t}H$, $b\bar{b}H$, ggH], *Reducibles*[$b\bar{b}\gamma\gamma$, $b\bar{b}j\gamma$, $b\bar{b}jj$, $c\bar{c}\gamma\gamma$, $c\bar{c}j\gamma$, $jj\gamma\gamma$], *Others*[$\gamma\gamma Z(\rightarrow b\bar{b})$, $t\bar{t}\gamma$, $t\bar{t}$]

	First BDT results
$HH \rightarrow b\bar{b}\gamma\gamma$	6.46
$bb\gamma\gamma$	1.9
$b\bar{b}j\gamma$	1.16
$b\bar{b}jj$	0.16
$c\bar{c}\gamma\gamma$	0.06
$c\bar{c}j\gamma$	0.021
$jj\gamma\gamma$	0.12
$ZH(\rightarrow \gamma\gamma)$	0.93
$t\bar{t}H(\rightarrow \gamma\gamma)$	1.51
$b\bar{b}H(\rightarrow \gamma\gamma)$	0.025
$ggH(\rightarrow \gamma\gamma)$	0.68
$Z(\rightarrow b\bar{b})\gamma\gamma$	0.10
$t\bar{t}\gamma$	0.07
$t\bar{t}$	0.05
Totals	
All bkgs	6.8
Single H	3.1
Reducibles	3.4
Other	0.2
S/$\sqrt{B}$	**2.48**
$\sqrt{q_0}, \bar{A}$	**1.98**

above. Compared to the results of Table 6.10, the following results utilise different pre-selection cuts on $m_{\gamma\gamma}$, a different BDT response cut and use the updated Layout 3.0 mv2c10 b-tagging functions♠.

Table 6.11 shows the effects of updating to the more realistic Layout 3.0 mv2c10 b-tagging functions. These results are based on the BDT response distribution shown in Figure 6.12, where the maximum $\sqrt{q_0, A}$ significance is achieved with a BDT response cut of 0.57. As previously shown, when the updated functions were applied to the weighted cuts based approach a reduction to the central significance value of 3.6% was observed. Compared to the results of Table A.4, a reduction in total performance of 1.6% was found for the BDT approach. This shows the ability of a BDT to focus on the areas of p_T-η space which perform best in each Layout (as shown in Figure 2.28).
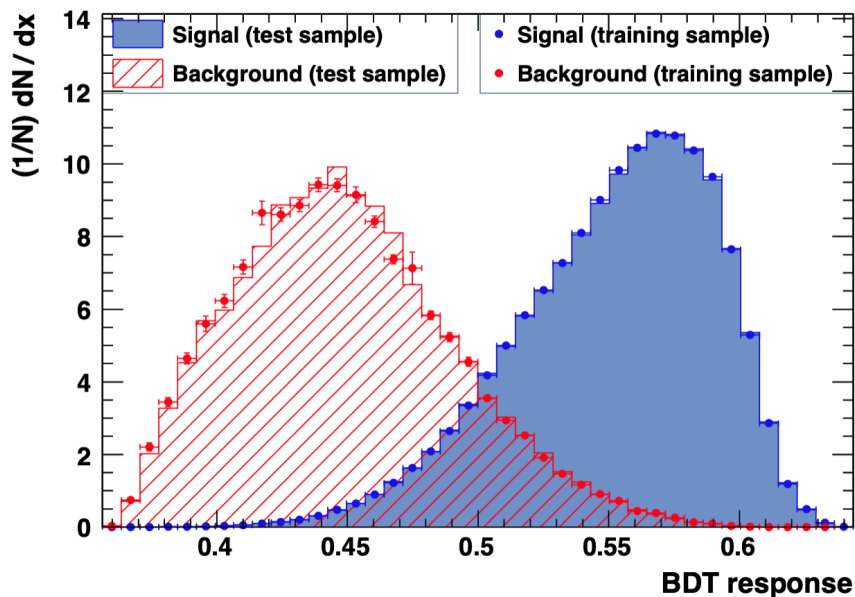
Figure 6.12: The BDT response distributions for signal and background for both training and testing samples (bottom). Utilising the variables used in the published paper for a $50\times50\mu\text{m}^2$ pixel sensor geometry

The results of Table 6.11 are based on a BDT trained using the variables shown in Table 5.2 where many variables were not considered for the weighted cuts based

---

♠ To show the improvement from different pre-selection cuts on $m_{\gamma\gamma}$ and a different BDT response cut only, a BDT was also trained using the same upgrade performance functions as 6.10 [26]. These results are shown in Appendix A.7

Table 6.11: Expected number of events acquired using a BDT method trained with the Layout 3.0 mv2c10 b-tagging algorithm. Additional training and testing plots are shown in Appendix A.8. *All bkgs*[sum total of all backgrounds], *SingleH*[ZH, $t\bar{t}H$, $b\bar{b}H$, ggH], *Reducibles*[$b\bar{b}\gamma\gamma$, $b\bar{b}j\gamma$, $b\bar{b}jj$, $c\bar{c}\gamma\gamma$, $c\bar{c}j\gamma$, $jj\gamma\gamma$], *Others*[$\gamma\gamma Z(\to b\bar{b})$, $t\bar{t}\gamma$, $t\bar{t}$]

	Events after pre-selection		Events passing BDT response		Events passing BDT response $123 < m_{\gamma\gamma} < 127$GeV	
	Barrel-barrel	Other	Barrel-barrel	Other	Barrel-barrel	Other
$HH \to bb\gamma\gamma$	28.69±0.01	10.56±0.01	11.19±0.01	2.43±0.01	9.17±0.01	1.77±0.01
$bb\gamma\gamma$	1001.96±4.63	702.75±2.86	4.47±0.33	1.83±0.22	1.43±0.21	0.53±0.17
$bbj\gamma$	795.94±5.19	619.79±4.74	3.13±0.29	0.71±0.08	1.34±0.23	0.17±0.05
$bbjj$	167.69±2.03	155.87±1.62	0.42±0.09	0.05±0.03	0.19±0.08	0.03±0.03
$c\bar{c}\gamma\gamma$	109.10±0.95	54.53±0.49	0.40±0.07	0.04±0.01	0.26±0.06	0.02±0.01
$c\bar{c}j\gamma$	44.77±0.29	30.93±0.39	0.07±0.01	0.03±0.01	0.02±0.01	0.01±0.00
$jj\gamma\gamma$	67.74±1.53	71.99±2.27	0.09±0.02	0.04±0.02	0.03±0.01	0.00±0.00
$ZH(\to\gamma\gamma)$	32.22±0.14	18.43±0.15	1.74±0.08	0.41±0.04	1.45±0.07	0.35±0.04
$t\bar{t}H(\to\gamma\gamma)$	154.24±0.36	60.96±0.22	2.11±0.03	0.29±0.02	1.73±0.03	0.20±0.01
$b\bar{b}H(\to\gamma\gamma)$	5.61±0.02	2.10±0.01	0.05±0.00	0.01±0.00	0.04±0.00	0.01±0.00
$ggH(\to\gamma\gamma)$	36.67±0.47	20.79±0.34	1.23±0.11	0.25±0.02	0.98±0.10	0.24±0.02
$Z(\to bb)\gamma\gamma$	22.71±0.15	15.87±0.26	0.45±0.04	0.09±0.03	0.19±0.03	0.07±0.02
$t\bar{t}\gamma$	383.51±9.29	179.00±3.80	0.16±0.04	0.00±0.00	0.02±0.00	0.00±0.00
$t\bar{t}$	125.89±5.35	185.83±9.46	0.20±0.09	0.02±0.01	0.03±0.00	0.00±0.00
Totals						
All bkgs	2948±13	2119±12	14.5±0.5	3.8±0.2	7.7±0.4	1.6±0.2
Single H	228.8±0.6	102.3±0.4	5.1±0.1	1.0±0.1	4.2±0.1	0.8±0.1
Continuum	2187±7	1636±6	8.6±0.5	2.7±0.2	3.3±0.3	0.8±0.2
Other	532±11	381±10	0.8±0.1	0.1±0.0	0.2±0.0	0.1±0.0
$S/\sqrt{B}$	0.53±0.00	0.23±0.00	2.94±0.05	1.26±0.04	3.31±0.08	1.39±0.08
Combined	**0.58±0.00**		**3.19±0.04**		**3.59±0.06**	
$\sqrt{q_0}, A$	0.53±0.34	0.23±0.37	2.65±0.18	1.15±0.17	2.85±0.18	1.21±0.20
Combined	**0.58±0.25**		**2.88±0.13**		**3.10±0.13**	

approach. To directly see the improvement from a BDT method only, and not from additional variables, a BDT was trained using only the variables considered in the weighted cuts based method and is shown in Table 6.12. This shows an increase in significance from 1.83±0.08 (with the Elliptical cuts on the weights based approach) to 2.91±0.11, roughly a 60% increase.

The results of 6.12 however show a small decreased performance compared to the results of 6.11 which proves the variables in Table 5.2 better capture the topology of $HH \rightarrow b\bar{b}\gamma\gamma$ events. As previously shown in Section 6.1, an increase in performance was possible by increasing the η range of accepted jets to 4.0 and adapting the cut on the number of jets. These two changes were applied to two separate BDTs; one trained using the variables from the weighted cuts based method only and the other trained using the variables in Table 5.2. Both are considered, as the extra information from the increased η range can affect the decisions made during training, resulting in either set of variables performing better. Table 6.13 shows the effects of increasing the η range of accepted jets to 4.0 and restricting the number of jets in the central $|\eta| < 2.5$ region to six for a BDT trained using variables from 5.2. Table 6.14 shows the effects resulting from the same changes but for a BDT trained only on the variables considered in the weighted cuts based method. In both cases a small reduction in total performance was observed. This is due to each BDT being unable to efficiently categorise all the additional information per event. If the BDTs were trained with more trees and an increased depth, the performance would be expected to increase, however this was not possible using the CPU power available. Therefore for all the following results, the best performing scenario of the two variable sets with the η range of accepted jets kept at 2.5 has been adopted, i.e. the variables from Table 5.2.

As discussed in Section 2.5.5, changing the geometry of the pixel sensors within the ITk from $50 \times 50 \mu m^2$ to $25 \times 100 \mu m^2$ changes performance. The extent of these changes are shown in Table 6.15. These results are based on the BDT response distribution shown in Figure 6.13, where the maximum $\sqrt{q_0, A}$ significance is achieved with a BDT response cut of 0.58. A small increase of $\simeq 2\%$ to the central signifi-

Table 6.12: Expected number of events acquired using a BDT method trained with the Layout 3.0 mv2c10 b-tagging algorithm and variables only considered in the weighted cuts based approach. Additional training and testing plots are shown in Appendix A.9. All $bkgs$[sum total of all backgrounds], $SingleH$[ZH, ttH, bbH, ggH], $Reducibles$[$b\bar{b}\gamma\gamma$, $b\bar{b}j\gamma$, $b\bar{b}jj$, $c\bar{c}\gamma\gamma$, $c\bar{c}j\gamma$, $jj\gamma\gamma$], $Others$[$\gamma\gamma Z(\to b\bar{b})$, $t\bar{t}\gamma$, $t\bar{t}$]

	Events after pre-selection		Events passing BDT response		Events passing BDT response 123 < $m_{\gamma\gamma}$ < 127GeV	
	Barrel-barrel	Other	Barrel-barrel	Other	Barrel-barrel	Other
$HH \to bb\gamma\gamma$	28.70±0.01	10.57±0.01	10.09±0.01	1.51±0.00	8.29±0.01	1.09±0.00
$b\bar{b}\gamma\gamma$	1008.28±4.56	732.16±2.81	3.99±0.47	0.74±0.11	1.19±0.22	0.29±0.07
$b\bar{b}j\gamma$	806.44±5.17	667.02±4.46	2.24±0.21	0.30±0.10	0.98±0.12	0.04±0.04
$b\bar{b}jj$	171.10±2.06	171.13±1.92	0.36±0.08	0.00±0.00	0.17±0.07	0.00±0.00
$c\bar{c}\gamma\gamma$	109.86±0.93	57.16±0.48	0.31±0.06	0.01±0.00	0.21±0.06	0.01±0.00
$c\bar{c}j\gamma$	45.33±0.28	33.53±0.45	0.08±0.02	0.01±0.00	0.02±0.01	0.00±0.00
$jj\gamma\gamma$	68.07±1.51	74.65±2.08	0.05±0.01	0.05±0.02	0.02±0.01	0.01±0.01
$ZH(\to \gamma\gamma)$	32.24±0.14	18.54±0.15	1.40±0.04	0.15±0.01	1.19±0.05	0.13±0.02
$ttH(\to \gamma\gamma)$	154.45±0.36	61.49±0.23	2.68±0.05	0.24±0.02	2.22±0.06	0.16±0.02
$bbH(\to \gamma\gamma)$	5.62±0.02	2.12±0.01	0.04±0.01	0.00±0.00	0.03±0.00	0.00±0.00
$ggH(\to \gamma\gamma)$	36.67±0.47	20.82±0.34	0.78±0.07	0.20±0.02	0.58±0.05	0.19±0.02
$Z(\to bb)\gamma\gamma$	22.82±0.15	16.25±0.26	0.39±0.04	0.03±0.02	0.17±0.03	0.03±0.02
$t\bar{t}\gamma$	384.39±9.29	192.68±4.50	0.07±0.01	0.00±0.00	0.02±0.00	0.00±0.00
$t\bar{t}$	126.98±5.34	195.54±9.48	0.13±0.06	0.01±0.00	0.03±0.00	0.00±0.00
Totals						
All bkgs	2972±13	2243±12	12.5±0.5	1.7±0.2	6.8±0.3	0.9±0.1
Single H	229.0±0.6	103.0±0.4	4.9±0.1	0.6±0.0	4.0±0.1	0.5±0.0
Continuum	2209±7	1736±6	7.0±0.5	1.1±0.2	2.6±0.3	0.4±0.1
Other	534±11	404±11	0.6±0.1	0.0±0.0	0.2±0.0	0.0±0.0
$S/\sqrt{B}$	0.53±0.00	0.22±0.00	2.85±0.06	1.15±0.05	3.17±0.07	1.18±0.06
Combined	**0.57±0.00**		**3.07±0.04**		**3.38±0.05**	
$\sqrt{q_0}, A$	0.53±0.34	0.22±0.36	2.56±0.21	1.02±0.17	2.73±0.15	1.01±0.14
Combined	**0.57±0.24**		**2.76±0.14**		**2.91±0.11**	

Table 6.13: Expected number of events acquired using a BDT method trained with the Layout 3.0 mv2c10 b-tagging algorithm and variables in Table 5.2. Also with an increased η range of accepted jets to 4.0 and restricted number of jets in the central $|\eta| < 2.5$ region to six. Additional training and testing plots are shown in Appendix A.10. *All bkgs*[sum total of all backgrounds], *SingleH*[ZH, $t\bar{t}H$, $b\bar{b}H$, ggH], *Reducibles*[$b\bar{b}\gamma\gamma$, $b\bar{b}j\gamma$, $b\bar{b}jj$, $c\bar{c}\gamma\gamma$, $c\bar{c}j\gamma$, $jj\gamma\gamma$], *Others*[$\gamma\gamma Z(\to b\bar{b})$, $t\bar{t}\gamma$, $t\bar{t}$]

	Events after pre-selection		Events passing BDT response		Events passing BDT response $123 < m_{\gamma\gamma} < 127$GeV	
	Barrel-barrel	Other	Barrel-barrel	Other	Barrel-barrel	Other
$HH \to bb\gamma\gamma$	30.07±0.01	11.81±0.01	10.96±0.01	2.42±0.01	9.00±0.01	1.76±0.01
$bb\gamma\gamma$	1168.91±4.55	913.96±2.79	4.61±0.47	1.96±0.21	1.32±0.19	0.60±0.12
$bbj\gamma$	949.85±5.51	782.76±5.33	2.94±0.28	0.84±0.10	1.38±0.25	0.25±0.11
$bbjj$	216.62±2.81	196.25±2.29	0.41±0.08	0.03±0.02	0.17±0.07	0.00±0.00
$c\bar{c}\gamma\gamma$	132.26±1.11	76.54±0.37	0.41±0.05	0.03±0.00	0.28±0.03	0.02±0.00
$c\bar{c}j\gamma$	57.12±0.54	41.66±0.63	0.06±0.01	0.03±0.01	0.02±0.00	0.00±0.00
$jj\gamma\gamma$	87.99±1.92	106.04±3.05	0.08±0.01	0.05±0.02	0.03±0.01	0.01±0.00
$ZH(\to \gamma\gamma)$	33.52±0.15	22.72±0.16	1.72±0.07	0.41±0.02	1.42±0.08	0.34±0.03
$ttH(\to \gamma\gamma)$	163.07±0.40	70.48±0.25	2.20±0.04	0.32±0.03	1.80±0.05	0.21±0.02
$bbH(\to \gamma\gamma)$	7.48±0.03	3.48±0.03	0.05±0.00	0.01±0.00	0.04±0.00	0.01±0.00
$ggH(\to \gamma\gamma)$	43.12±0.61	24.82±0.44	1.09±0.08	0.27±0.03	0.86±0.09	0.26±0.03
$Z(\to bb)\gamma\gamma$	26.53±0.21	21.13±0.27	0.45±0.04	0.05±0.03	0.18±0.03	0.04±0.02
$t\bar{t}\gamma$	401.60±9.51	214.63±4.24	0.09±0.03	0.01±0.00	0.01±0.00	0.00±0.00
$t\bar{t}$	131.27±5.46	213.04±9.86	0.20±0.09	0.01±0.00	0.03±0.00	0.01±0.00
Totals						
All bkgs	3419±14	2688±13	14.3±0.6	4.0±0.2	7.5±0.4	1.7±0.2
Single H	247.2±0.8	121.5±0.5	5.1±0.1	1.0±0.1	4.1±0.1	0.8±0.1
Continuum	2613±8	2117±7	8.5±0.6	2.9±0.2	3.2±0.3	0.9±0.2
Other	559±11	449±11	0.7±0.1	0.1±0.0	0.2±0.0	0.0±0.0
$S/\sqrt{B}$	0.51±0.00	0.23±0.00	2.90±0.06	1.21±0.04	3.28±0.08	1.34±0.07
Combined	**0.56±0.00**		**3.14±0.04**		**3.54±0.06**	
$\sqrt{q_0}, A$	0.56±0.33	0.23±0.36	2.61±0.21	1.11±0.16	2.83±0.18	1.17±0.18
Combined	**0.56±0.23**		**2.84±0.15**		**3.06±0.13**	

Table 6.14: Expected number of events acquired using a BDT method trained with the Layout 3.0 mv2c10 b-tagging algorithm and variables only considered in the weighted cuts based approach. Also with an increased η range of accepted jets to 4.0 and restricted number of jets in the central $|\eta| < 2.5$ region to six. Additional training and testing plots are shown in Appendix A.11. *All bkgs*[sum total of all backgrounds], *SingleH*[ZH, $t\bar{t}H$, $b\bar{b}H$, ggH], *Reducibles*[$b\bar{b}\gamma\gamma$, $b\bar{b}j\gamma$, $b\bar{b}jj$, $c\bar{c}\gamma\gamma$, $c\bar{c}j\gamma$, $jj\gamma\gamma$], *Others*[$\gamma\gamma Z(\to b\bar{b})$, $t\bar{t}\gamma$, $t\bar{t}$]

	Events after pre-selection		Events passing BDT response		Events passing BDT response $123 < m_{\gamma\gamma} < 127$GeV	
	Barrel-barrel	Other	Barrel-barrel	Other	Barrel-barrel	Other
$HH \to bb\gamma\gamma$	30.08±0.01	11.83±0.01	13.45±0.01	2.91±0.01	10.99±0.01	2.11±0.00
$b\bar{b}\gamma\gamma$	1176.41±4.55	950.03±2.71	8.34±0.47	3.06±0.30	3.03±0.28	1.17±0.11
$b\bar{b}j\gamma$	962.62±5.45	841.67±5.07	4.98±0.41	1.71±0.22	1.93±0.34	0.64±0.14
$b\bar{b}jj$	220.91±2.90	215.80±2.63	0.85±0.14	0.19±0.05	0.39±0.09	0.07±0.03
$c\bar{c}\gamma\gamma$	133.19±1.08	80.07±0.39	0.66±0.10	0.04±0.01	0.37±0.07	0.02±0.01
$c\bar{c}j\gamma$	57.81±0.52	45.20±0.68	0.16±0.02	0.03±0.01	0.05±0.01	0.01±0.00
$jj\gamma\gamma$	88.42±1.88	109.48±2.78	0.14±0.04	0.09±0.03	0.06±0.01	0.03±0.01
$ZH(\to \gamma\gamma)$	33.54±0.15	22.85±0.16	2.59±0.08	0.50±0.04	2.15±0.08	0.42±0.05
$t\bar{t}H(\to \gamma\gamma)$	163.28±0.40	71.04±0.25	4.80±0.07	0.72±0.02	3.95±0.09	0.50±0.03
$b\bar{b}H(\to \gamma\gamma)$	7.49±0.03	3.52±0.03	0.07±0.00	0.01±0.00	0.06±0.00	0.00±0.00
$ggH(\to \gamma\gamma)$	43.12±0.61	24.85±0.44	1.75±0.09	0.48±0.06	1.44±0.12	0.40±0.06
$Z(\to b\bar{b})\gamma\gamma$	26.64±0.21	21.67±0.27	0.86±0.04	0.17±0.04	0.41±0.06	0.11±0.04
$t\bar{t}\gamma$	402.59±9.52	230.09±5.49	0.36±0.05	0.06±0.02	0.05±0.01	0.01±0.01
$t\bar{t}$	132.40±5.43	223.26±9.84	0.22±0.06	0.02±0.00	0.06±0.01	0.01±0.00
Totals						
All bkgs	3448±14	2840±13	25.8±0.7	7.1±0.4	14.0±0.5	3.4±0.2
Single H	247.4±0.8	122.3±0.5	9.2±0.1	1.7±0.1	7.6±0.2	1.3±0.1
Continuum	2639±8	2242±7	15.1±0.7	5.1±0.4	5.8±0.5	1.9±0.2
Other	562±11	475±11	1.4±0.1	0.3±0.0	0.5±0.1	0.1±0.0
$S/\sqrt{B}$	0.51±0.00	0.22±0.00	2.65±0.03	1.09±0.03	2.94±0.05	1.15±0.03
Combined	**0.56±0.00**		**2.87±0.02**		**3.16±0.04**	
$\sqrt{q_0}, A$	0.51±0.33	0.22±0.35	2.46±0.18	1.03±0.20	2.65±0.18	1.05±0.15
Combined	**0.56±0.23**		**2.66±0.13**		**2.85±0.13**	

cance value was observed from 3.10±0.13 to 3.17±0.11♠, this was expected due to the relative *b*-tagging performance differences shown in Section 2.5.6 and a BDTs ability to focus on the best performing regions. However, within errors, there is no performance difference between the two pixel sensor geometries.
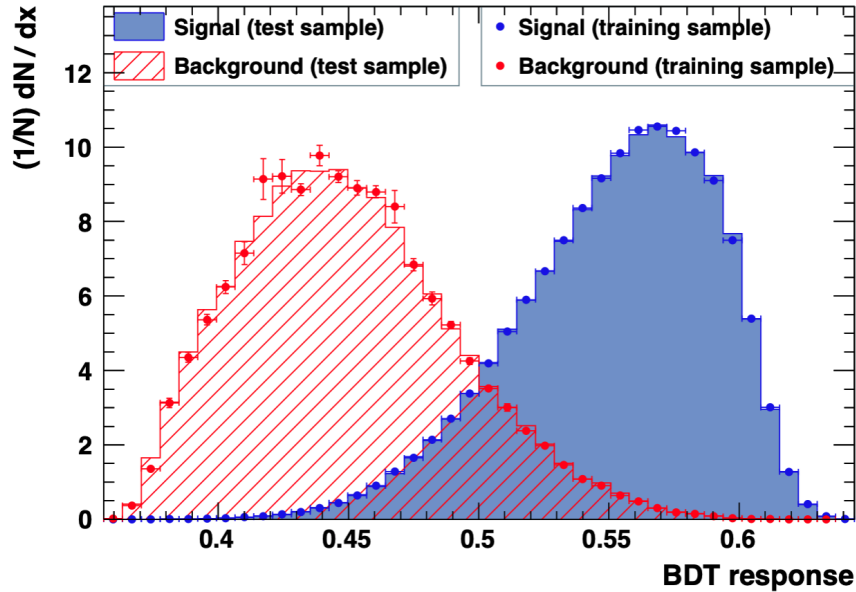
Figure 6.13: The BDT response distributions for signal and background for both training and testing samples (bottom). Utilising the variables used in the published paper for a $25\times100\mu m^2$ pixel sensor geometry

Figures 6.14 and 6.15 show the M_{HH} distribution at the three stages of the BDT method for $50\times50\mu m^2$ and $25\times100\mu m^2$ pixel sensor geometry respectively.

♠ Systematic errors were not fully considered for this analysis. However as shown in [26] the effects of systematics previously on this channel reduced the overall significance by 4.8%. This method is expected to be overstating the effects of systematics

Table 6.15: Expected number of events acquired using a BDT method trained with the Layout 3.0, $25\times100\mu m^2$ pixel geometry, mv2c10 b-tagging algorithm and variables in Table 5.2. Additional training and testing plots are shown in Appendix A.12. *All bkgs*[sum total of all backgrounds], *SingleH*[ZH, $t\bar{t}H$, $b\bar{b}H$, ggH], *Reducibles*[$b\bar{b}\gamma\gamma$, $b\bar{b}j\gamma$, $b\bar{b}jj$, $c\bar{c}\gamma\gamma$, $c\bar{c}j\gamma$, $jj\gamma\gamma$], *Others*[$\gamma\gamma Z(\to b\bar{b})$, $t\bar{t}\gamma$, $t\bar{t}$]

	Events after pre-selection		Events passing BDT response		Events passing BDT response $123 < m_{\gamma\gamma} < 127$GeV	
	Barrel-barrel	Other	Barrel-barrel	Other	Barrel-barrel	Other
$HH \to bb\gamma\gamma$	28.72±0.01	10.57±0.01	9.44±0.01	1.80±0.01	7.77±0.01	1.31±0.01
$b\bar{b}\gamma\gamma$	1001.96±4.63	702.67±2.86	2.76±0.31	0.86±0.12	0.78±0.15	0.21±0.10
$b\bar{b}j\gamma$	795.75±5.18	619.55±4.74	1.83±0.27	0.44±0.11	0.74±0.13	0.07±0.03
$b\bar{b}jj$	167.53±2.03	155.73±1.62	0.29±0.07	0.00±0.00	0.16±0.07	0.00±0.00
$c\bar{c}\gamma\gamma$	115.70±1.01	56.71±0.51	0.30±0.07	0.02±0.00	0.19±0.05	0.01±0.00
$c\bar{c}j\gamma$	47.15±0.31	32.33±0.42	0.04±0.00	0.01±0.00	0.01±0.00	0.00±0.00
$jj\gamma\gamma$	65.33±1.50	68.69±2.27	0.04±0.01	0.04±0.02	0.02±0.01	0.00±0.00
$ZH(\to \gamma\gamma)$	32.25±0.14	18.44±0.15	1.21±0.05	0.26±0.02	1.02±0.05	0.21±0.02
$t\bar{t}H(\to \gamma\gamma)$	154.42±0.36	61.01±0.22	1.35±0.04	0.12±0.01	1.13±0.05	0.09±0.01
$b\bar{b}H(\to \gamma\gamma)$	5.61±0.02	2.09±0.01	0.04±0.00	0.00±0.00	0.03±0.00	0.00±0.00
$ggH(\to \gamma\gamma)$	36.65±0.47	20.80±0.34	0.71±0.09	0.23±0.02	0.56±0.07	0.23±0.02
$Z(\to b\bar{b})\gamma\gamma$	22.71±0.15	15.86±0.26	0.33±0.04	0.01±0.01	0.12±0.02	0.00±0.00
$t\bar{t}\gamma$	383.65±9.30	179.04±3.80	0.04±0.00	0.00±0.00	0.00±0.00	0.00±0.00
$t\bar{t}$	126.00±5.35	185.80±9.46	0.05±0.01	0.01±0.00	0.02±0.00	0.00±0.00
Totals						
All bkgs	2955±13	2119±12	9.0±0.4	2.0±0.2	4.8±0.2	0.8±0.1
Single H	228.9±0.6	102.3±0.4	3.3±0.1	0.6±0.0	2.8±0.1	0.5±0.0
Continuum	2193±7	1636±6	5.3±0.4	1.4±0.2	1.9±0.2	0.3±0.1
Other	532±11	381±10	0.4±0.0	0.0±0.0	0.1±0.0	0.0±0.0
$S/\sqrt{B}$	0.53±0.00	0.23±0.00	3.15±0.08	1.27±0.05	3.55±0.09	1.43±0.09
Combined	**0.58±0.00**		**3.39±0.05**		**3.82±0.06**	
$\sqrt{q_0}, A$	0.53±0.34	0.23±0.37	2.75±0.20	1.13±0.17	2.94±0.16	1.19±0.16
Combined	**0.58±0.25**		**2.97±0.14**		**3.17±0.11**	

Figure 6.14: M_{HH} distribution for the $50 \times 50 \mu m^2$ pixel geometry at various stages of the BDT method. Pre-training (left), post-BDT response (right) and post-BDT response and additional $123 < m_{\gamma\gamma} < 127$GeV cut (bottom)
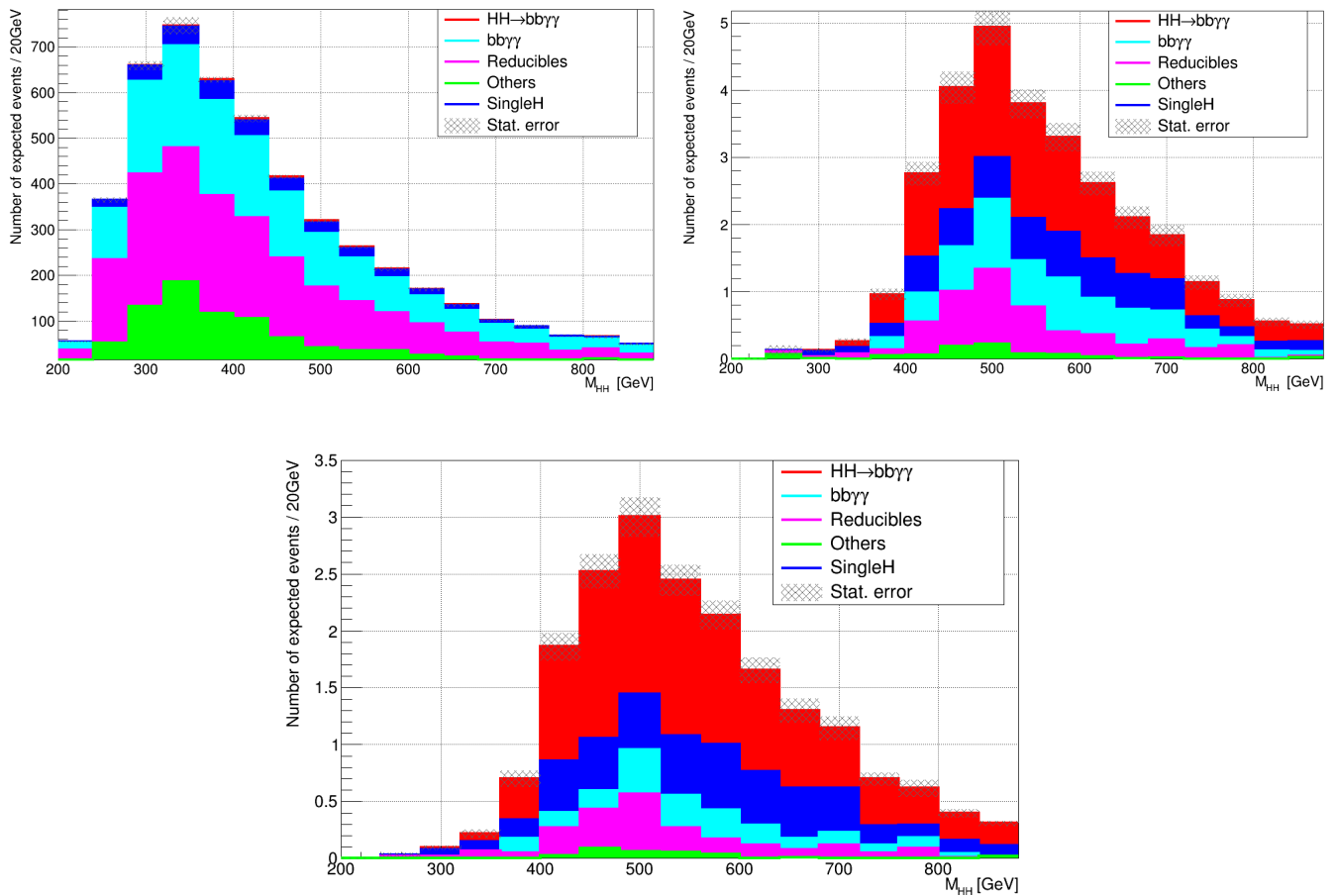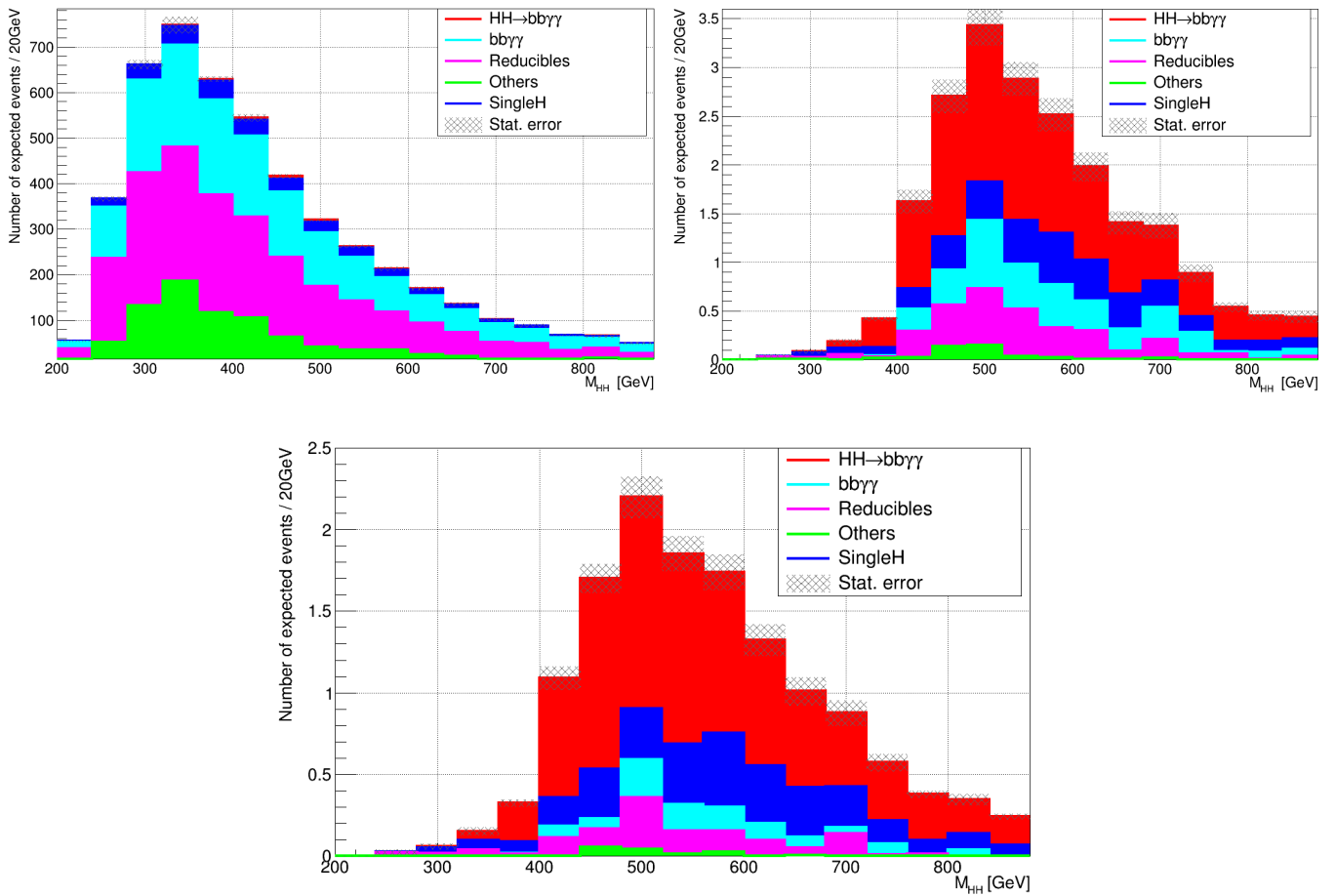
Figure 6.15: M_{HH} distribution for the $25\times100\mu\mathrm{m}^2$ pixel geometry at various stages of the BDT method. Pre-training (left), post-BDT response (right) and post-BDT response and additional $123 < m_{\gamma\gamma} < 127\mathrm{GeV}$ cut (bottom)

6.4   Radius of innermost pixel layer studies

As also discussed in Section 2.5.5, performance changes are also possible by varying the radius of the innermost layer of the ITk. At the time of this thesis, dedicated upgrade performance functions were not available for these different radii. However, as shown in Figures 2.36 and 2.37 the expected light jet rejection factors for radii of 39mm, 36mm and 33mm in different η and p_T ranges can be extracted. To roughly estimate the effects of reducing the radius, the same relative performance difference seen in the l-jet rejection was also applied to the c-jet and PU-jet rejection. The six scenarios ($50{\times}50\mu m^2$ vs $25{\times}100\mu m^2$ and 39mm vs 36mm vs 33mm) were investigated with the weighted cuts based method. These results are summarised in Tables 6.16 where an increased η range on accepted jets up to 4.0 but with less than six jets in the central $|\eta| < 2.5$ region only was included♠. All results show the expected behaviour of improving performance with decreased radii. An improvement of approximately 3% to overall performance is seen when adopting a reduced innermost radius of 33mm compared to 39mm. However, this study is not based on dedicated b-tagging functions and it was not applied to the BDT method. Therefore once the upgrade performance functions utilising 33mm as the innermost ITk layer become available, it is expected to further increase the expected significance of the $HH \rightarrow b\bar{b}\gamma\gamma$ channel.

♠ The full background breakdown for the reduced radii studies are shown in Appendix A.13

Table 6.16: Summary of weighted cut based results for different pixel geometries and radii of the innermost pixel layer. The different radii are simulated by applying the relative performance of l-jets to c and PU-jets also. Considering a cut of $p_T^{b\bar{b}/\gamma\gamma} > 80$GeV. Also with an increased accepted jet η from 2.5 to 4.0 but with less than six jets in the central $|\eta| < 2.5$ region only

	Signal	Background	Significance
$50{\times}50\mu$m^2, 39mm	12.04	72.21	**1.55**
$50{\times}50\mu$m^2, 36mm	12.00	69.38	**1.57**
$50{\times}50\mu$m^2, 33mm	11.96	67.34	**1.60**
$25{\times}100\mu$m^2, 39mm	11.92	71.20	**1.54**
$25{\times}100\mu$m^2, 36mm	11.89	69.56	**1.55**
$25{\times}100\mu$m^2, 33mm	11.87	67.57	**1.57**

6.5 Summary of results

From an initial significance of 1.00±0.01 a weights based approach (and more advanced UPFs) was able to increase performance to 1.40±0.04. Further optimisations of the $p_T^{b\bar{b}/\gamma\gamma}$ cuts increase this further to 1.68±0.04, however this was reduced to 1.63±0.04 after a more realistic material budget was accounted for. Increasing the accepted η range for jets and adapting the cut on n_{jets} recovered some of this lost performance and resulted in a significance of 1.67±0.04. The addition of the HGTD was shown to have no effect on this channel due to the centrality of the $HH \rightarrow b\bar{b}\gamma\gamma$ events, however this was exploited by including additional cuts based on a 2D Gaussian fit to the η distributions of the two selected b-tagged jets in each event. This combined with the optimised $p_T^{b\bar{b}/\gamma\gamma}$ and n_{jets} cuts results in a significance of 1.83±0.08.

To make superior use of all the available information a BDT method was adopted. Using only training variables from the previous methods a large significance increase to 2.91±0.11 was achieved. This was further improved to 3.10±0.13 by using additional variables, introduced in [26], to train the BDT. By considering alternative pixel sensor geometries it was found that $25{\times}100\mu$m^2 and $50{\times}50\mu$m^2 sensors give comparable results. The $25{\times}100\mu$m^2 pixel sensor geometry gives a small increase to

the central significance value up to 3.17±0.11.

Reducing the radius of the innermost ITk layer from 39mm to 36mm and to 33mm was found to result in an increase to total significance of around 3% for both pixel sensor geometries when using the weighted cuts based method. However the study on different radii was overly simplified and will likely produce further improved results with dedicated b-tagging functions for each radii.

Therefore, 9.08±0.01 $HH \rightarrow b\bar{b}\gamma\gamma$ events and 5.64±0.27 background events from 3000fb^{-1} of data are expected with a pixel sensor geometry of $25{\times}100\mu\mathrm{m}^2$ producing an overall significance of 3.17±0.11. However with comparable results from a sensor geometry of $50{\times}50\mu\mathrm{m}^2$ and only small differences between the performance at different radii of the innermost ITk layer, the $HH \rightarrow b\bar{b}\gamma\gamma$ channel shows no heavy dependence on the detector design.

CHAPTER 7

CONCLUSION

$\mathfrak{B}$y the end of the HL-LHC era before 2040 the ATLAS experiment aims to increase the size of the dataset from $\sim$300fb^{-1}, acquired at the end of LHC running, up to $\sim$3000fb^{-1}. The HL-LHC will produce considerably higher radiation levels and therefore the ATLAS Inner Detector will be replaced by an all silicon Inner Tracker(ITk) capable of providing higher precision measurements. All aspects of the ITk need to be tested to ensure they can maintain a sufficient performance over the lifetime of the HL-LHC. The University of Birmingham Medical Physics Cyclotron is capable of delivering the expected doses over the full HL-LHC operation. Also the University of Birmingham is able to test the performance of sensors before and after irradiation using the AliBaVA system. The available prototype readout chips at the time showed a sufficient performance after HL-LHC doses which is explained in detail in Chapter 3.

The large dataset expected after HL-LHC operation increases the likelihood of seeing

rare processes such as di-Higgs production. Through measurements of di-Higgs it is possible to measure the Higgs boson self-coupling which gives a direct probe of the Higgs potential. The $H \rightarrow HH \rightarrow b\bar{b}\gamma\gamma$ decay channel is one of the most promising channels to measure the Higgs boson self-coupling with an expected number of events of 315 over the entire HL-LHC era. This is because the channel benefits from both the large branching fraction of the $H \rightarrow b\bar{b}$ decay and the narrow mass peak from the $H \rightarrow \gamma\gamma$ decay resulting in a clear di-Higgs signal.

To determine the prospects for observing this channel, upgrade performance functions are developed to mimic the expected detector response to various physics objects. As the design of the HL-LHC ATLAS detector changes or more advanced techniques are explored or modelling errors are corrected the upgrade performance functions also change. Chapter 6 details how some of the most recent changes effect the prospects for measuring the $H \rightarrow HH \rightarrow b\bar{b}\gamma\gamma$ channel across several analysis methods.

From an initial significance of 1.00±0.01 a weights based approach (and more advanced UPFs) was able to increase performance to 1.40±0.04. However this was an overestimate and was reduced after a more realistic material budget was considered. The weights based method was then optimised by considering different cuts on the $p_T^{b\bar{b}/\gamma\gamma}$, number of jets and additional cuts based on a 2D Gaussian fit to the η distributions of the two selected b-tagged jets in each event which all results in a significance of 1.83±0.08.

The addition of the HGTD was shown to have no effect on this channel due to the centrality of the $HH \rightarrow b\bar{b}\gamma\gamma$ events. Reducing the radius of the innermost ITk layer from 39mm to 36mm and to 33mm was also considered. As an approximation of the possible expected improvements the relative performance of the l-jet rejection at the reduced radii was applied to c and pile-up jets. This resulted in an increase in total significance of around 3% between adopting 39mm and 33mm for both pixel sensor geometries. However once dedicated functions utilising 33mm as the innermost ITk layer become available, it is expected to further increase the expected significance

of this channel.

A cuts based analysis often makes suboptimal use of the available information, therefore a multivariate technique was adopted, a Boosted Decision Tree method. Using the same variables as in the previous cuts based method the significance increases to 2.91±0.11. This was further improved to 3.10±0.13 by using additional variables, introduced in [26], to train the BDT and further still to 3.17±0.11 if a pixel sensor geometry of $25\times100\mu\mathrm{m}^2$ is adopted (over a $50\times50\mu\mathrm{m}^2$ geometry). With comparable results between a sensor geometry of $50\times50\mu\mathrm{m}^2$ and $25\times100\mu\mathrm{m}^2$ and only small differences between the performance at different radii of the innermost ITk layer, the $HH \to b\bar{b}\gamma\gamma$ channel does not show a considerable dependence on the detector design.

As shown in this study, even with a dataset from the entire HL-LHC era, measuring the $H \to HH \to b\bar{b}\gamma\gamma$ channel will be very challenging.

REFERENCES

[1] M. Gell-Mann, "A schematic model of baryons and mesons," *Physics Letters*, vol. 8, pp. 214–215, Feb. 1964.

[2] G. Zweig, "An SU$_3$ model for strong interaction symmetry and its breaking; Version 1," Tech. Rep. CERN-TH-401, CERN, Geneva, Jan 1964.

[3] G. Zweig, "An SU$_3$ model for strong interaction symmetry and its breaking; Version 2," p. 80 p, Feb 1964.

[4] S. L. Glashow, "Partial-symmetries of weak interactions," *Nuclear Physics*, vol. 22, no. 4, pp. 579 – 588, 1961.

[5] A. Salam, "Weak and Electromagnetic Interactions," *Conf. Proc.*, vol. C680519, pp. 367–377, 1968.

[6] S. Weinberg, "A Model of Leptons," *Phys. Rev. Lett.*, vol. 19, pp. 1264–1266, 1967.

[7] ATLAS Collaboration, "Observation of a new particle in the search for the Standard Model Higgs boson with the ATLAS detector at the LHC," *Phys. Lett. B*, 2012.

[8] CMS Collaboration, "Observation of a New Boson at a Mass of 125 GeV with the CMS Experiment at the LHC," *Phys. Lett.*, vol. B716, pp. 30–61, 2012.

[9] Particle Data Group, "Review of particle physics," *Phys. Rev. D*, vol. 98, p. 030001, Aug 2018.

[10] Plank Collaboration, "Planck 2018 results. VI. Cosmological parameters," 2018. arXiv:1807.06209 astro-ph.CO.

[11] LHCb Collaboration, "Observation of *CP* violation in charm decays," *Phys. Rev. Lett.*, vol. 122, p. 211803. 12 p, Mar 2019.

[12] M. Cacciari, G. P. Salam, and G. Soyez, "The anti-ktjet clustering algorithm," *Journal of High Energy Physics*, vol. 2008, p. 063063, Apr 2008.

[13] A. Grozin, "Asymptotic freedom: history and interpretation," 2008. arXiv:0803.2589 physics.hist-ph.

[14] DESY, "Weighty insights from heavy quarks." `www.desy.de/news/news_search/index_eng.html?openDirectAnchor=1420`, 2018/06/16.

[15] P. W. Higgs, "Broken Symmetries and the Masses of Gauge Bosons," *Phys. Rev. Lett.*, vol. 13, pp. 508–509, 1964. [,160(1964)].

[16] F. Englert and R. Brout, "Broken Symmetry and the Mass of Gauge Vector Mesons," *Phys. Rev. Lett.*, vol. 13, pp. 321–323, 1964. [,157(1964)].

[17] G. S. Guralnik, C. R. Hagen, and T. W. B. Kibble, "Global Conservation Laws and Massless Particles," *Phys. Rev. Lett.*, vol. 13, pp. 585–587, 1964. [,162(1964)].

[18] M. Hussein, "Higgs boson production at the lhc," *Nuclear Physics B - Proceedings Supplements*, vol. 207-208, pp. 110 – 113, 2010. Proceedings of the QCD 10: 15th High-Energy Physics International Conference on Quantum Chromodynamics.

[19] ATLAS Collaboration, "The ATLAS Experiment at the CERN Large Hadron Collider," *JINST*, vol. 3, p. S08003, 2008.

[20] ATLAS Collaboration, "Combined measurement of differential and total cross sections in the $H \to \gamma\gamma$ and the $H \to ZZ^* \to 4\ell$ decay channels at $\sqrt{s} = 13$ TeV with the ATLAS detector," *Phys. Lett.*, vol. B786, pp. 114–133, 2018.

[21] ATLAS Collaboration, "Measurement of the Higgs boson mass in the $H \to ZZ^* \to 4\ell$ and $H \to \gamma\gamma$ channels with $\sqrt{s} = 13$ TeV pp collisions using the ATLAS detector," *Phys. Lett.*, vol. B784, pp. 345–366, 2018.

[22] CMS Collaboration, "Measurements of properties of the Higgs boson in the four-lepton final state at $\sqrt{s} = 13$ TeV," 2018.

[23] CMS Collaboration, "Measurements of Higgs boson properties in the diphoton decay channel in proton-proton collisions at $\sqrt{s} = 13$ TeV," *JHEP*, vol. 11, p. 185, 2018.

[24] ATLAS and CMS Collaboration, "Combined Measurement of the Higgs Boson Mass in pp Collisions at $\sqrt{s} = 7$ and 8 TeV with the ATLAS and CMS Experiments," *Phys. Rev. Lett.*, vol. 114, p. 191803, 2015.

[25] D. de Florian *et al.*, "Handbook of LHC Higgs Cross Sections: 4. Deciphering the Nature of the Higgs Sector," 2016.

[26] ATLAS Collaboration, "Measurement prospects of the pair production and self-coupling of the Higgs boson with the ATLAS experiment at the HL-LHC," Tech. Rep. ATL-PHYS-PUB-2018-053, CERN, Geneva, Dec 2018.

[27] ATLAS Collaboration, "Prospects for Observing $t\bar{t}HH$ Production with the ATLAS Experiment at the HL-LHC," Tech. Rep. ATL-PHYS-PUB-2016-023, CERN, Geneva, Oct 2016.

[28] "Restarting the LHC: Why 13TeV?." `https://cds.cern.ch/record/1998739`. 2020-03-12.

[29] "Imagine owned and produced by cern." 2011.

[30] "Pileup interactions and data taking efficiency." `https://twiki.cern.ch/twiki/bin/view/AtlasPublic/LuminosityPublicResultsRun2`. 2019-03-17.

[31] E. Mobs, "The CERN accelerator complex. Complexe des acclrateurs du CERN," Jul 2016. General Photo.

[32] "Physics at the LHC and sLHC," *Nuclear Instruments and Methods in Physics Research Section A: Accelerators, Spectrometers, Detectors and Associated Equipment*, vol. 636, no. 1, Supplement, pp. S1 – S7, 2011. 7th International.

[33] "Longer term LHC schedule." `https://lhc-commissioning.web.cern.ch/lhc-commissioning/schedule/LHC-long-term.htm`. 2020-02-09.

[34] CMS Collaboration, "The CMS experiment at the CERN LHC," *Journal of Instrumentation*, vol. 3, pp. S08004–S08004, aug 2008.

[35] LHCb Collaboration, "The LHCb Detector at the LHC," *JINST*, vol. 3, p. S08005, 2008.

[36] "LHCb." `https://home.cern/science/experiments/lhcb`. 2020-02-08.

[37] The ALICE Collaboration, "The ALICE experiment at the CERN LHC," *Journal of Instrumentation*, vol. 3, pp. S08002–S08002, aug 2008.

[38] "ALICE." `https://home.cern/science/experiments/alice`. 2020-02-08.

[39] ATLAS Collaboration, "The ATLAS experiment at the CERN large hadron collider," *Journal of Instrumentation*, vol. 3, pp. S08003–S08003, aug 2008.

[40] J. Pequenao and P. Schaffner, "An computer generated image representing how ATLAS detects particles." Jan 2013.

[41] ATLAS Collaboration, *ATLAS inner detector: Technical Design Report, 1.* Technical Design Report ATLAS, Geneva: CERN, 1997.

[42] K. Potamianos, "The upgraded Pixel detector and the commissioning of the Inner Detector tracking of the ATLAS experiment for Run-2 at the Large Hadron Collider," Tech. Rep. ATL-PHYS-PROC-2016-104, CERN, Geneva, Aug 2016. 15 pages, EPS-HEP 2015 Proceedings.

[43] M. Capeans, G. Darbo, K. Einsweiller, M. Elsing, T. Flick, M. Garcia-Sciveres, C. Gemme, H. Pernegger, O. Rohne, and R. Vuillermet, "ATLAS Insertable B-Layer Technical Design Report," Tech. Rep. CERN-LHCC-2010-013. ATLAS-TDR-19, Sep 2010.

[44] ATLAS Collaboration, "The ATLAS experiment at the CERN large hadron collider," *Journal of Instrumentation*, vol. 3, pp. S08003–S08003, aug 2008.

[45] A. Andronic and J. Wessels, "Transition radiation detectors," *Nuclear Instruments and Methods in Physics Research Section A: Accelerators, Spectrometers, Detectors and Associated Equipment*, vol. 666, p. 130147, Feb 2012.

[46] M. Tanabashi *et al.*, "Review of Particle Physics," *Phys. Rev.*, vol. D98, no. 3, p. 030001, 2018.

[47] "Electron and photon identification in ATLAS," in *Hadron Collider Physics 2005* (X. Wu, A. Clark, and M. Campanelli, eds.), (Berlin, Heidelberg), pp. 107–111, Springer Berlin Heidelberg, 2006.

[48] ATLAS Collaboration, *ATLAS liquid-argon calorimeter: Technical Design Report.* Technical Design Report ATLAS, Geneva: CERN, 1996.

[49] ATLAS Collaboration, *ATLAS muon spectrometer: Technical Design Report.* Technical Design Report ATLAS, Geneva: CERN, 1997.

[50] R. Ruber, Y. Makida, G. Cipolla, L. Deront, Y. Doi, T. Haruyama, F. Haug, T. Kanahara, M. Kawai, T. Kondo, Y. Kondo, N. Kopeykin, S. Mizumaki, J. Metselaar, A. Park, O. Pavlov, M. Pezzetti, O. Pirotte, S. Ravat, and A. Yamamoto, "On-surface integration and test of the atlas central solenoid and its proximity cryogenics," *Applied Superconductivity, IEEE Transactions on*, vol. 14, pp. 500 – 503, 07 2004.

[51] H. Ten Kate, "The ATLAS superconducting magnet system at the large hadron collider," *Physica C Superconductivity*, vol. 468, pp. 2137–2142, 09 2008.

[52] ATLAS Collaboration, "The Run-2 ATLAS Trigger System," Tech. Rep. ATL-DAQ-PROC-2016-003, CERN, Geneva, Feb 2016.

[53] R. E. Owen, "The ATLAS Trigger System," Feb 2018. ATL-DAQ-SLIDE-2018-074, https://cds.cern.ch/record/2302730.

[54] P. Vankov, "Atlas upgrade for the hl-lhc: meeting the challenges of a five-fold increase in collision rate," *EPJ Web of Conferences*, vol. 28:12069, 2012.

[55] ATLAS Collaboration, "Technical Design Report for the ATLAS Inner Tracker Pixel Detector," Tech. Rep. CERN-LHCC-2017-021. ATLAS-TDR-030, CERN, Geneva, Sep 2017.

[56] ATLAS Collaboration, "Technical Design Report for the ATLAS Inner Tracker Strip Detector," Tech. Rep. CERN-LHCC-2017-005. ATLAS-TDR-025, CERN, Geneva, Apr 2017.

[57] ATLAS Collaboration, "Expected Tracking Performance of the ATLAS Inner Tracker at the HL-LHC," Tech. Rep. ATL-COM-INDET-2019-013, CERN, Geneva, Mar 2019.

[58] W. Lu, F. Anghinolfi, L. Cheng, J. D. Witt, J. Kaplon, P. Keener, A. Narayan, M. Newcomer, and K. Swientek, "Development of the ABCStar front-end chip for the ATLAS silicon strip upgrade," *Journal of Instrumentation*, vol. 12, pp. C04017–C04017, apr 2017.

[59] K. Mahboubi, A. Greenall, P. P. Allport, A. A. Affolder, M. Wormald, A. Smith, J. Carroll, S. Wonsak, C. L. Llacer, J. Bernabeu, R. Marco-Hernandez, C. Garcia, D. S. Munoz, I. M. Gregor, M. Stanitzki, D. Ariza, I. Bloch, C. Friedric, L. Poley, L. Rehnisch, R. Mori, M. M. Hauser, S. Kuehn, K. Jakobs, and U. Parzefall, "The front-end hybrid for the ATLAS HL-LHC silicon strip tracker," *Journal of Instrumentation*, vol. 9, pp. C02027–C02027, feb 2014.

[60] N. Lehmann, "Tracking with self-seeded Trigger for High Luminosity LHC," *Section of Electrical and Electrical Engineering, Masters thesis*, 2014.

[61] F. Hgging, "Front-end electronics and integration of ATLAS pixel modules," *Nuclear Instruments and Methods in Physics Research Section A: Accelerators, Spectrometers, Detectors and Associated Equipment*, vol. 549, no. 1, pp. 157 – 164, 2005. VERTEX 2003.

[62] ATLAS Collaboration, "Expected performance of the ATLAS detector at the High-Luminosity LHC," Tech. Rep. ATL-PHYS-PUB-2019-005, CERN, Geneva, Jan 2019.

[63] ATLAS Collaboration, "Technical Design Report: A High-Granularity Timing Detector for the ATLAS Phase-II Upgrade," Tech. Rep. ATL-COM-UPGRADE-2019-003, CERN, Geneva, Mar 2019.

[64] G. Pellegrini, P. Fernndez-Martnez, M. Baselga, C. Fleta,D. Flores, V. Greco, S. Hidalgo, I. Mandi, G. Kramberger, D. Quirion and M. Ullan, "Technology developments and first measurements of Low Gain Avalanche Detectors (LGAD) for high energy physics applications," *Nuclear Instruments and Methods in Physics Research Section A: Accelerators, Spectrometers, Detectors and Associated Equipment*, vol. 765, pp. 12 – 16, 2014. HSTD-9 2013 - Proceedings of the 9th International.

[65] ATLAS Collaboration, "Technical Design Report for the Phase-II Upgrade of the ATLAS LAr Calorimeter," Tech. Rep. CERN-LHCC-2017-018. ATLAS-TDR-027, CERN, Geneva, Sep 2017.

[66] ATLAS Collaboration, "Technical Design Report for the Phase-II Upgrade of the ATLAS Tile Calorimeter," Tech. Rep. CERN-LHCC-2017-019. ATLAS-TDR-028, CERN, Geneva, Sep 2017.

[67] ATLAS Collaboration, "Technical Design Report for the Phase-II Upgrade of the ATLAS Muon Spectrometer," Tech. Rep. CERN-LHCC-2017-017. ATLAS-TDR-026, CERN, Geneva, Sep 2017.

[68] ATLAS Collaboration, "Technical Design Report for the Phase-II Upgrade of the ATLAS TDAQ System," Tech. Rep. CERN-LHCC-2017-020. ATLAS-TDR-029, CERN, Geneva, Sep 2017.

[69] A. Salzburger, "Track Simulation and Reconstruction in the ATLAS Experiment," *PhD Thesis*, 2008.

[70] ATLAS Collaboration, "ATLAS Insertable B-Layer Technical Design Report," Tech. Rep. CERN-LHCC-2010-013. ATLAS-TDR-19, Sep 2010.

[71] ATLAS Collaboration, "Forward Jet Vertex Tagging: A new technique for the identification and rejection of forward pileup jets," Tech. Rep. ATL-PHYS-PUB-2015-034, CERN, Geneva, Aug 2015.

[72] ATLAS Collaboration, "Tagging and suppression of pileup jets with the ATLAS detector," Tech. Rep. ATLAS-CONF-2014-018, CERN, Geneva, May 2014.

[73] M. Elsing et al., "Final Report of the second ITk Pixel Layout Task Force," Tech. Rep. ATL-COM-ITK-2018-053, CERN, Geneva, Dec 2018.

[74] J.Nielsen, "ATLAS restricted - Upgrade Performance Functions." `https://twiki.cern.ch/twiki/bin/viewauth/AtlasProtected/UpgradePerformanceFunctions`, 2019-10-23.

[75] ATLAS Collaboration, "Expected performance for an upgraded ATLAS detector at High-Luminosity LHC," Tech. Rep. ATL-PHYS-PUB-2016-026, CERN, Geneva, Oct 2016.

[76] ATLAS Collaboration, "Expected Tracking Performance of the ATLAS Inner Tracker at the HL-LHC," Tech. Rep. ATL-PHYS-PUB-2019-014, CERN, Geneva, Mar 2019.

[77] ATLAS Collaboration, "Optimisation of the ATLAS b-tagging performance for the 2016 LHC Run," Tech. Rep. ATL-PHYS-PUB-2016-012, CERN, Geneva, Jun 2016.

[78] ATLAS Collaboration, "Commissioning of the ATLAS high-performance b-tagging algorithms in the 7 TeV collision data," Tech. Rep. ATLAS-CONF-2011-102, CERN, Geneva, Jul 2011.

[79] G. Piacquadio and C. Weiser, "A new inclusive secondary vertex algorithm for b-jet tagging in ATLAS," *Journal of Physics: Conference Series*, vol. 119, p. 032032, jul 2008.

[80] ATLAS Collaboration, "Expected performance of the ATLAS *b*-tagging algorithms in Run-2," Tech. Rep. ATL-PHYS-PUB-2015-022, CERN, Geneva, Jul 2015.

[81] P. Dervan, R. French, P. Hodgson, H. Marin-Reyes, and J. Wilson, "The birmingham irradiation facility," *Nuclear Instruments and Methods in Physics Research Section A: Accelerators, Spectrometers, Detectors and Associated Equipment*, vol. 730, pp. 101 – 104, 2013. Proceedings of the 9th International Conference on Radiation Effects on Semiconductor Materials Detectors and Devices.

[82] M. Moll, "Displacement damage in silicon detectors for high energy physics. Displacement Damage in Silicon Detectors for High Energy Physics," *IEEE Trans. Nucl. Sci.*, vol. 65, no. 8, pp. 1561–1582. 22 p, 2018.

[83] H. E. Boesch and F. B. McLean, "Hole transport and trapping in field oxides," *IEEE Transactions on Nuclear Science*, vol. 32, pp. 3940–3945, Dec 1985.

[84] A. Paccagnella, A. Cester, and G. Cellere, "Ionizing radiation effects on mosfet thin and ultra-thin gate oxides," in *IEDM Technical Digest. IEEE International Electron Devices Meeting, 2004.*, pp. 473–476, Dec 2004.

[85] D. Forshaw, "Development of radiation hard planar silicon tracking detectors for the ATLAS experiment at the HL-LHC," *PhD Thesis*, 2014.

[86] A.Morningstar and R.Teuscher, "Total Ionizing Dose Testing of the ABC130 ASIC for the ATLAS Phase-II Semiconductor Tracker Upgrade ," *IPP CERN summer student*.

[87] F.Faccio, "Radiation-Induced Edge Effects in Deep Submicron CMOS Transistors," *IEEE Transaction on Nuclear Science*, vol. 52, No. 6.

[88] T. R. Oldham, F. B. McLean, H. E. Boesch, and J. M. McGarrity, "An overview of radiation-induced interface traps in MOS structures," *Semiconductor Science and Technology*, vol. 4, pp. 986–999, dec 1989.

[89] P. Allport, M. Baca, D. Briglin, J. Broughton, R. Canavan, A. Chisholm, L. Gonella, P. Knights, K. Nikolopoulos, D. Parker, T. Price, J. Thomas, J. Wilson, A. Affolder, G. Casse, P. Dervan, A. Greenall, I. Tsurin, S. Wonsak, S. Dixon, S. Edwards, R. French, P. Hodgson, P. Kemp-Russell, E. Kourlitis, H. Marin-Reyes, and K. Parker, "Recent results and experience with the

birmingham MC40 irradiation facility," *Journal of Instrumentation*, vol. 12, pp. C03075–C03075, mar 2017.

[90] "UoB AIDA-2020 Transnational Access." `https://www.youtube.com/watch?v=8JIY4VdmXvY&list=WL&index=11&t=105s`, 2020-02-08.

[91] "SRIM - The Stopping and Range of Ions in Matter." `http://www.srim.org/`. James F. Ziegler,2020-03-13.

[92] J. H. Broughton, "Searches for rare exclusivHiggs boson decays to mesoanssociated photon with the ATLAS detector," *PhD Thesis*, 2018.

[93] "Data courtesy of Sven Wonsak, University of Liverpool." 2015-08-09.

[94] M.Moll, "Radiation Damage in Silicon Particle Detectors," *PhD Thesis*, 1999.

[95] K. Hara, A. Chilingarov, and H. Fox, "Charge collection and field profile studies of heavily irradiated strip sensors for the atlas inner tracker upgrade," *Nuclear Instruments and Methods in Physics Research Section A: Accelerators, Spectrometers, Detectors and Associated Equipment*, vol. 831, pp. 181–188, 9 2016.

[96] M. E. Geyik, "Connectivity Implementation for ITk-DAQ-Software," Sep 2018. Presented 12 Sep 2018.

[97] ATLAS Collaboration, "Study of the double Higgs production channel $H(\to b\bar{b})H(\to \gamma\gamma)$ with the ATLAS experiment at the HL-LHC," Tech. Rep. ATL-PHYS-PUB-2017-001, CERN, Geneva, Jan 2017.

[98] J.Alwall et al, "The automated computation of tree-level and next-to-leading order differential cross sections, and their matching to parton shower simulations," *JHEP*, vol. 07, p. 079, 2014.

[99] S. Frixione and B. R. Webber, "Matching NLO QCD computations and parton shower simulations," *JHEP*, vol. 06, p. 029, 2002.

[100] S. Frixione, P. Nason, and B. R. Webber, "Matching NLO QCD and parton showers in heavy flavor production," *JHEP*, vol. 08, p. 007, 2003.

[101] T. Sjostrand, S. Mrenna, and P. Z. Skands, "A Brief Introduction to PYTHIA 8.1," *Comput. Phys. Commun.*, vol. 178, pp. 852–867, 2008.

[102] ATLAS Collaboration, "ATLAS Run 1 Pythia8 tunes," Tech. Rep. ATL-PHYS-PUB-2014-021, CERN, Geneva, Nov 2014.

[103] R. D. Ball *et al.*, "Parton distributions for the LHC Run II," *JHEP*, vol. 04, p. 040, 2015.

[104] D. de Florian and J. Mazzitelli, "Higgs Boson Pair Production at Next-to-Next-to-Leading Order in QCD," *Phys. Rev. Lett.*, vol. 111, p. 201801, 2013.

[105] J. Grigo, K. Melnikov, and M. Steinhauser, "Virtual corrections to Higgs boson pair production in the large top quark mass limit," *Nucl. Phys.*, vol. B888, pp. 17–29, 2014.

[106] S. Alioli, P. Nason, C. Oleari, and E. Re, "A general framework for implementing NLO calculations in shower Monte Carlo programs: the POWHEG BOX," *JHEP*, vol. 06, p. 043, 2010.

[107] H.-L. Lai, M. Guzzi, J. Huston, Z. Li, P. M. Nadolsky, J. Pumplin, and C. P. Yuan, "New parton distributions for collider physics," *Phys. Rev.*, vol. D82, p. 074024, 2010.

[108] T. Sjostrand, S. Mrenna, and P. Z. Skands, "PYTHIA 6.4 Physics and Manual," *JHEP*, vol. 05, p. 026, 2006.

[109] O. Brein, A. Djouadi, and R. Harlander, "NNLO QCD corrections to the Higgs-strahlung processes at hadron colliders," *Phys. Lett.*, vol. B579, pp. 149–156, 2004.

[110] M. L. Ciccolini, S. Dittmaier, and M. Kramer, "Electroweak radiative corrections to associated WH and ZH production at hadron colliders," *Phys. Rev.*, vol. D68, p. 073003, 2003.

[111] W. Beenakker, S. Dittmaier, M. Kramer, B. Plumper, M. Spira, and P. M. Zerwas, "Higgs radiation off top quarks at the Tevatron and the LHC," *Phys. Rev. Lett.*, vol. 87, p. 201805, 2001.

[112] W. Beenakker, S. Dittmaier, M. Kramer, B. Plumper, M. Spira, and P. M. Zerwas, "NLO QCD corrections to t anti-t H production in hadron collisions," *Nucl. Phys.*, vol. B653, pp. 151–203, 2003.

[113] S. Dawson, L. H. Orr, L. Reina, and D. Wackeroth, "Associated top quark Higgs boson production at the LHC," *Phys. Rev.*, vol. D67, p. 071503, 2003.

[114] S. Dawson, C. Jackson, L. H. Orr, L. Reina, and D. Wackeroth, "Associated Higgs production with top quarks at the large hadron collider: NLO QCD corrections," *Phys. Rev.*, vol. D68, p. 034022, 2003.

[115] M. Wiesemann, R. Frederix, S. Frixione, V. Hirschi, F. Maltoni, and P. Torrielli, "Higgs production in association with bottom quarks," *JHEP*, vol. 02, p. 132, 2015.

[116] J. Pumplin, D. R. Stump, J. Huston, H. L. Lai, P. M. Nadolsky, and W. K. Tung, "New generation of parton distributions with uncertainties from global QCD analysis," *JHEP*, vol. 07, p. 012, 2002.

[117] M. Czakon and A. Mitov, "Top++: A Program for the Calculation of the Top-Pair Cross-Section at Hadron Colliders," *Comput. Phys. Commun.*, vol. 185, p. 2930, 2014.

[118] K. Melnikov, M. Schulze, and A. Scharf, "QCD corrections to top quark pair production in association with a photon at hadron colliders," *Phys. Rev.*, vol. D83, p. 074013, 2011.

[119] ATLAS Collaboration, "Technical Design Report for the Phase-II Upgrade of the ATLAS LAr Calorimeter," Tech. Rep. Sec4.3.2 CERN-LHCC-2017-018. ATLAS-TDR-027, CERN, Geneva, Sep 2017.

[120] ATLAS Collaboration, "Prospects for measuring Higgs pair production in the channel $H(\to \gamma\gamma)H(\to b\bar{b})$ using the ATLAS detector at the HL-LHC," Tech. Rep. ATL-PHYS-PUB-2014-019, CERN, Geneva, Oct 2014.

[121] U. Baur, T. Plehn, and D. Rainwater, "Probing the higgs self-coupling at hadron colliders using rare decays," *Physical Review D*, vol. 69, Mar 2004.

[122] A. Hoecker, P. Speckmayer, J. Stelzer, J. Therhaag, E. von Toerne, H. Voss, M. Backes, T. Carli, O. Cohen, A. Christov, D. Dannheim, K. Danielowski, S. Henrot-Versille, M. Jachowski, K. Kraszewski, A. K. Jr., M. Kruk, Y. Mahalalel, R. Ospanov, X. Prudent, A. Robert, D. Schouten, F. Tegenfeldt, A. Voigt, K. Voss, M. Wolter, and A. Zemla, "Tmva - toolkit for multivariate data analysis," 2007.

[123] Y. Freund and R. E. Schapire, "A short introduction to boosting," in *In Proceedings of the Sixteenth International Joint Conference on Artificial Intelligence*, pp. 1401–1406, Morgan Kaufmann, 1999.

[124] ATLAS Collaboration, "Optimisation and performance studies of the ATLAS b-tagging algorithms for the 2017-18 LHC run," Tech. Rep. ATL-PHYS-PUB-2017-013, CERN, Geneva, Jul 2017.

[125] "AMI(ATLAS Metadata Interface)." `https://ami.in2p3.fr/`. created 01-26-2016.

[126] G. Cowan, K. Cranmer, E. Gross, and O. Vitells, "Asymptotic formulae for likelihood-based tests of new physics," *The European Physical Journal C*, vol. 71, Feb 2011.

APPENDIX A

A.1 IP3DSV1 b-tagging algorithm

The impact parameter is an essential input to flavour tagging algorithms. The IP3D tagger is a Run-2 b-tagging algorithm used in ATLAS based on multivariate techniques and has been adapted for HL-LHC operation also [124]. It is based on track impact parameters and combines the single-track level information in $r - \phi$ and $r - z$. Figure A.1 shows the expected light-jet rejection possible with the IP3D tagger as a function of the b-jets efficiency for $t\bar{t}$ events at $\langle\mu\rangle$=200 for different $|\eta|$ regions. As shown in Figure A.1 (left) the $25\times100\mu$m^2 pixel pitch is expected to noticeably improve performance due to the improved resolution in the transverse impact parameter. The light-jet rejection degreases with increasing $|\eta|$ due to the increase in the impact resolution of both z_0 and d_0 as shown in Figure 2.22. Comparing the performance for $|\eta| < 2.5$ to the Run-2 detector, a clear improvement in the light-jet rejection capability for the standard efficiency operating points used during Run-2 is expected for the ITk with a $25\times100\mu$m^2 pixel pitch.

Figure A.2 shows the b-tagging performance for the IP3D+SV1 tagging algorithm (top left), with the HGTD included (top right) and the relative performance (bottom) (performance of HGTD included - performance with no HGTD) in p_T-η space. As well as the IP3D+SV1 algorithm giving the probability a b-jet is correctly b-tagged, it also provides the likelihood of other physics objects being mistakenly b-tagged. Figures 2.29, 2.30 and 2.31 show the performance differences with and without the HGTD included for a c-jet, l-jet and a pileup jet to be reconstructed as a b-jet respectively.
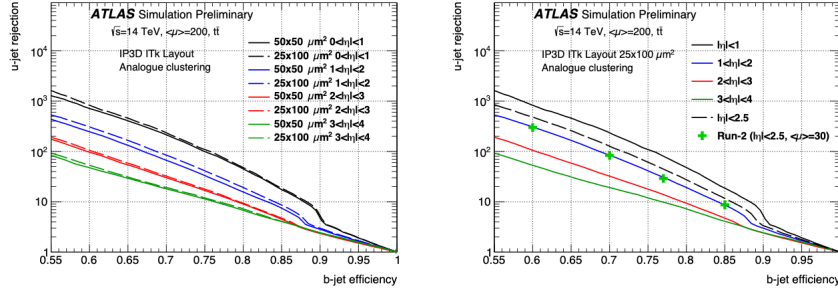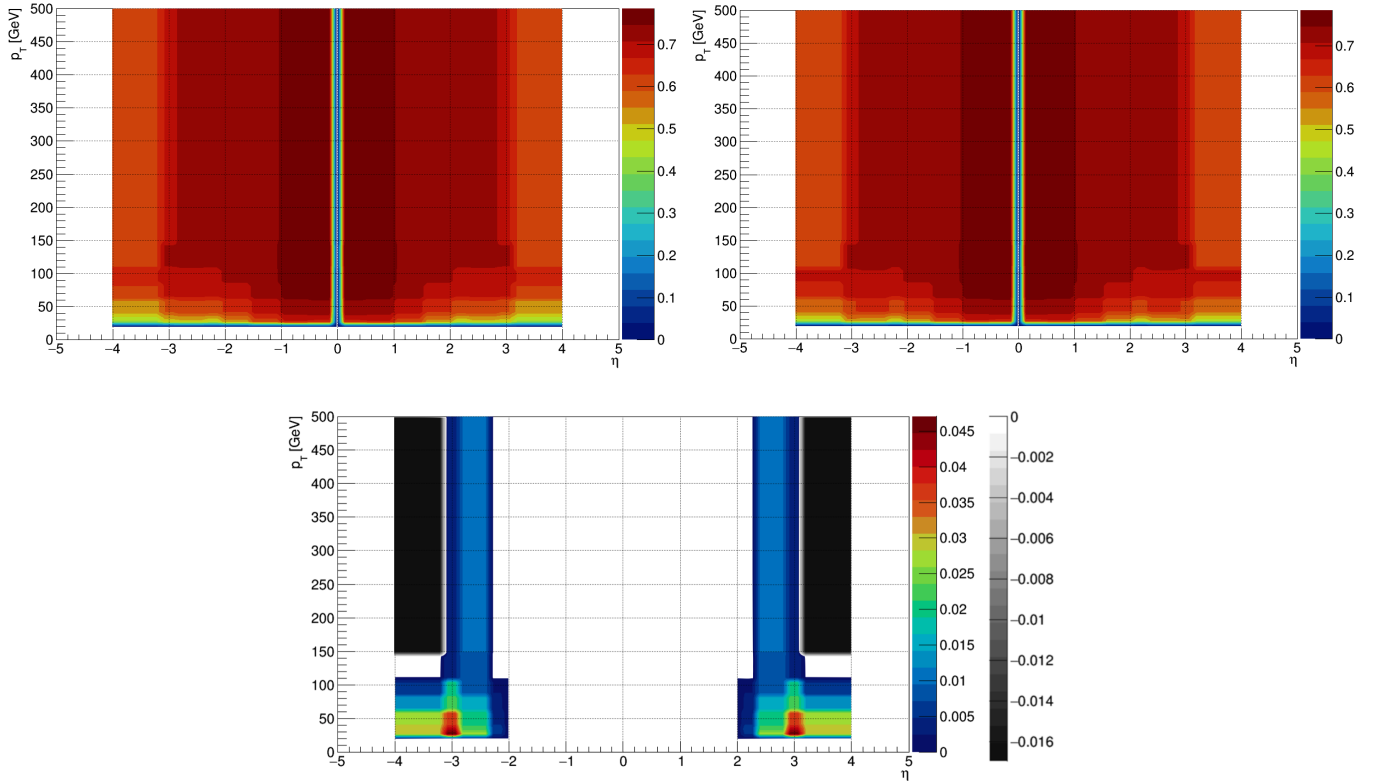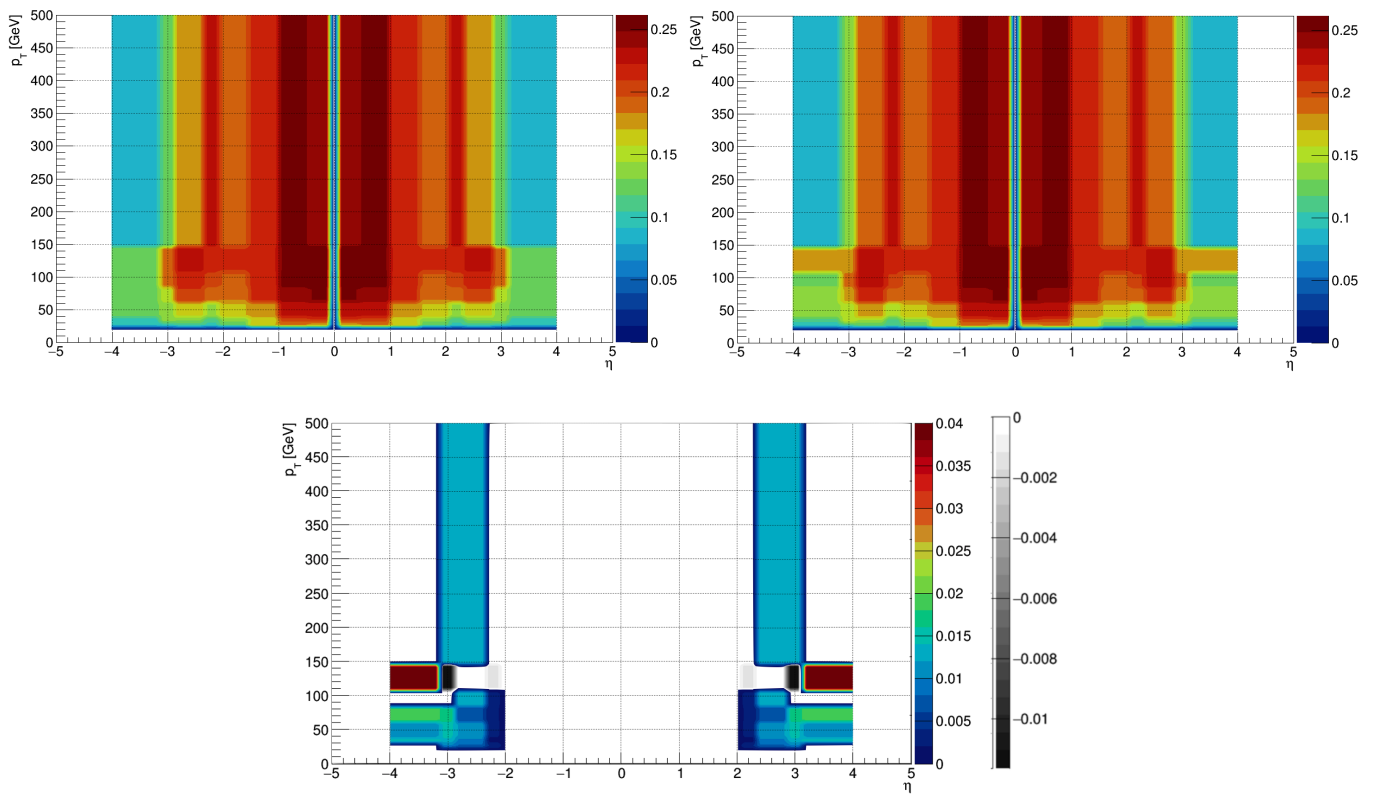
Figure A.1: Performance of the IP3D b-tagging algorithm in $t\bar{t}$ events with $\langle\mu\rangle =$ 200. The rejection of light jets is shown as a function of b-jet efficiency for different η regions. Results are shown for $50\times50\mu$m^2 (lines) and $25\times100\mu$m^2 (dashed lines) pixels (left) and results for $25\times100\mu$m^2 pixels are compared with the performance of the b-tagging working points corresponding to the current Run-2 Inner Detector with an average pileup of 30 (green crosses)(right) [57]
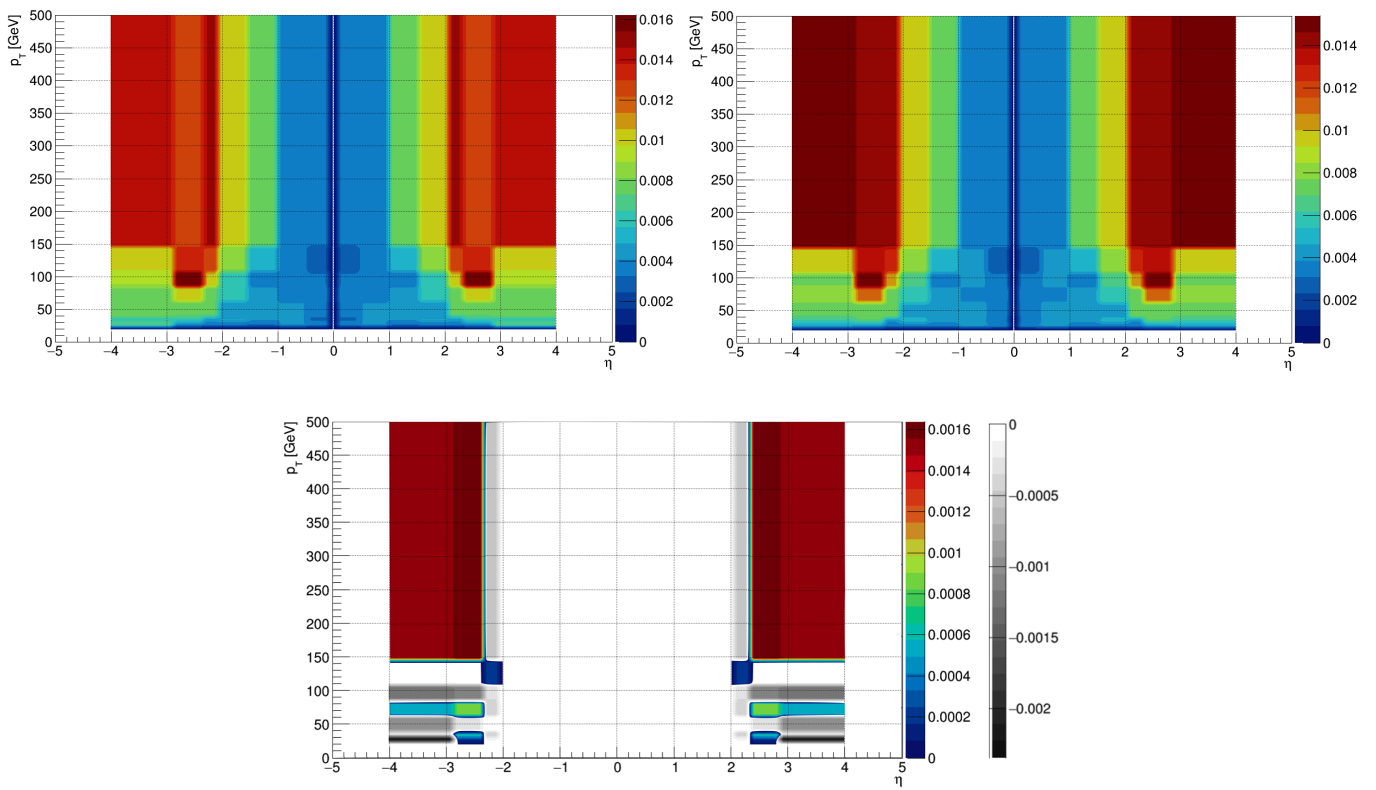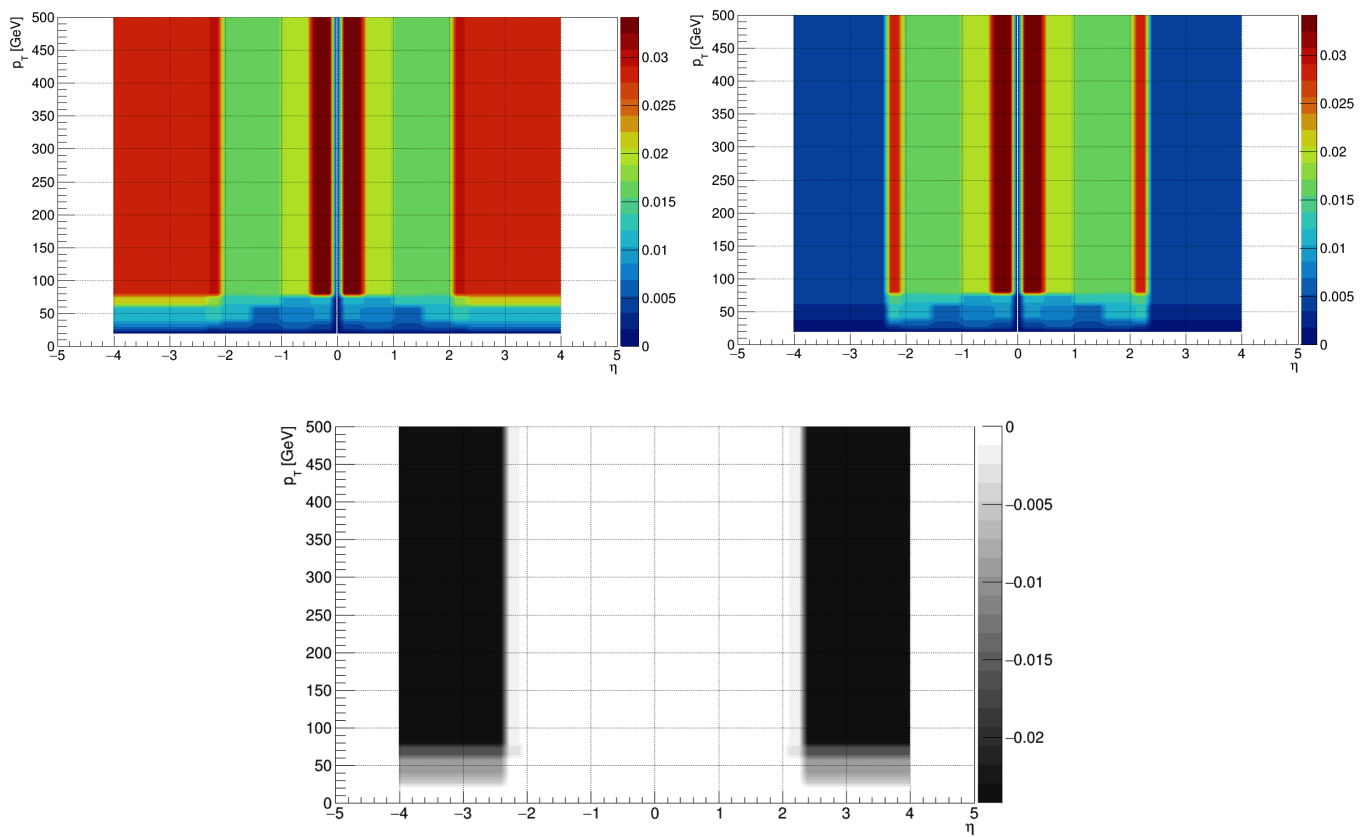

Figure A.2: b-tagging efficiency for the ip3dsv1 tagging algorithm (top left), the algorithm with the HGTD included (top right) and the relative performance (bottom) in p_T-η space

Figure A.3: *c*-tagging efficiency for the ip3dsv1 tagging algorithm (top left), the algorithm with the HGTD included (top right) and the relative performance (bottom) in p_T-η space

Figure A.4: *l*-tagging efficiency for the ip3dsv1 tagging algorithm (top left), the algorithm with the HGTD included (top right) and the relative performance (bottom) in p_T-η space

Figure A.5: Pileup-tagging efficiency for the ip3dsv1 tagging algorithm (top left), the algorithm with the HGTD included (top right) and the relative performance (bottom) in p_T-η space
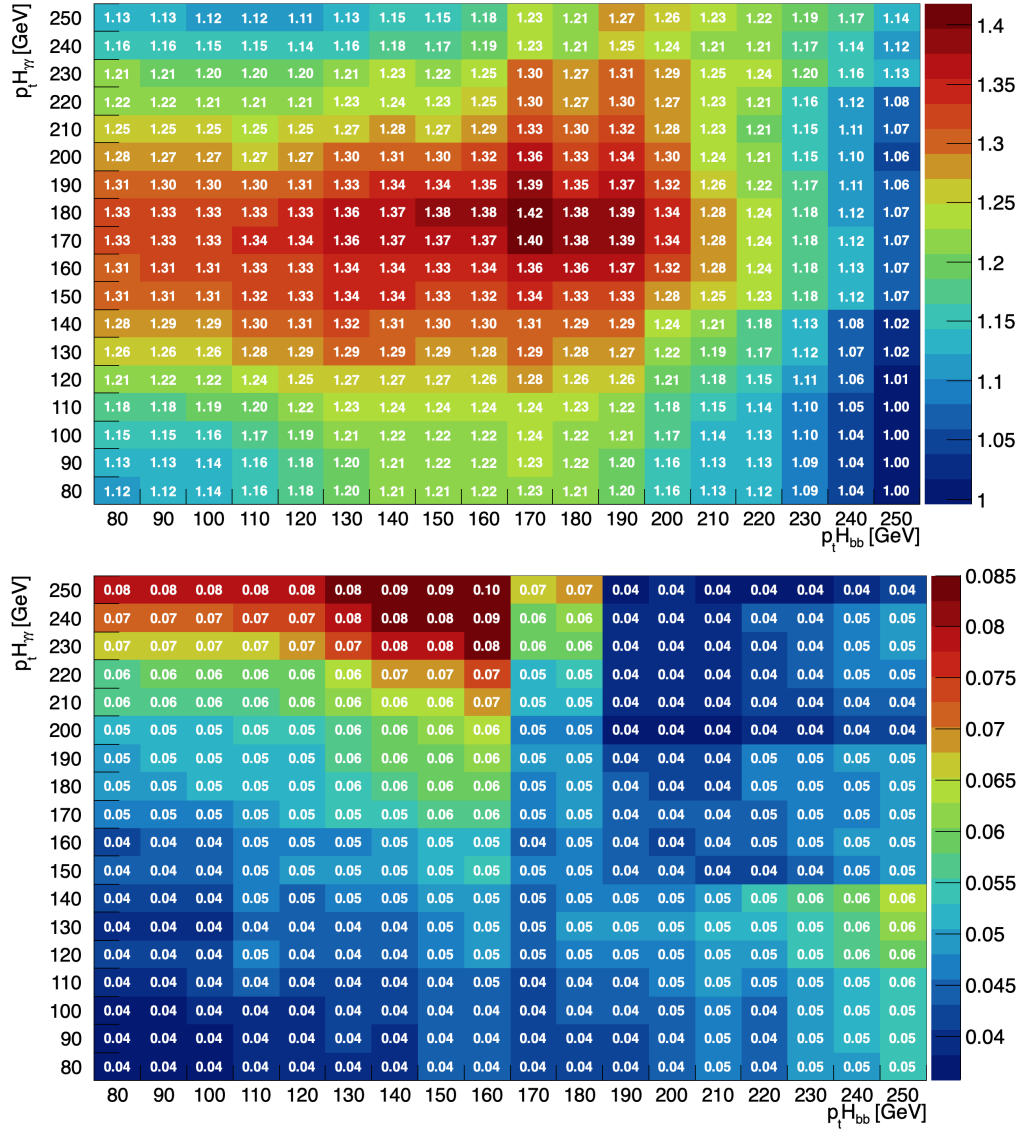
Figure A.6: Expected significance (top) and error (bottom) acquired using a weights based method, including the HGTD, for an increase in p_T cuts applied to both reconstructed Higgs boson candidates. Also with an increased accepted jet η from 2.5 to 4.0 but with less than six jets in the central $|\eta| < 2.5$ region only.

A.2   2D η distributions
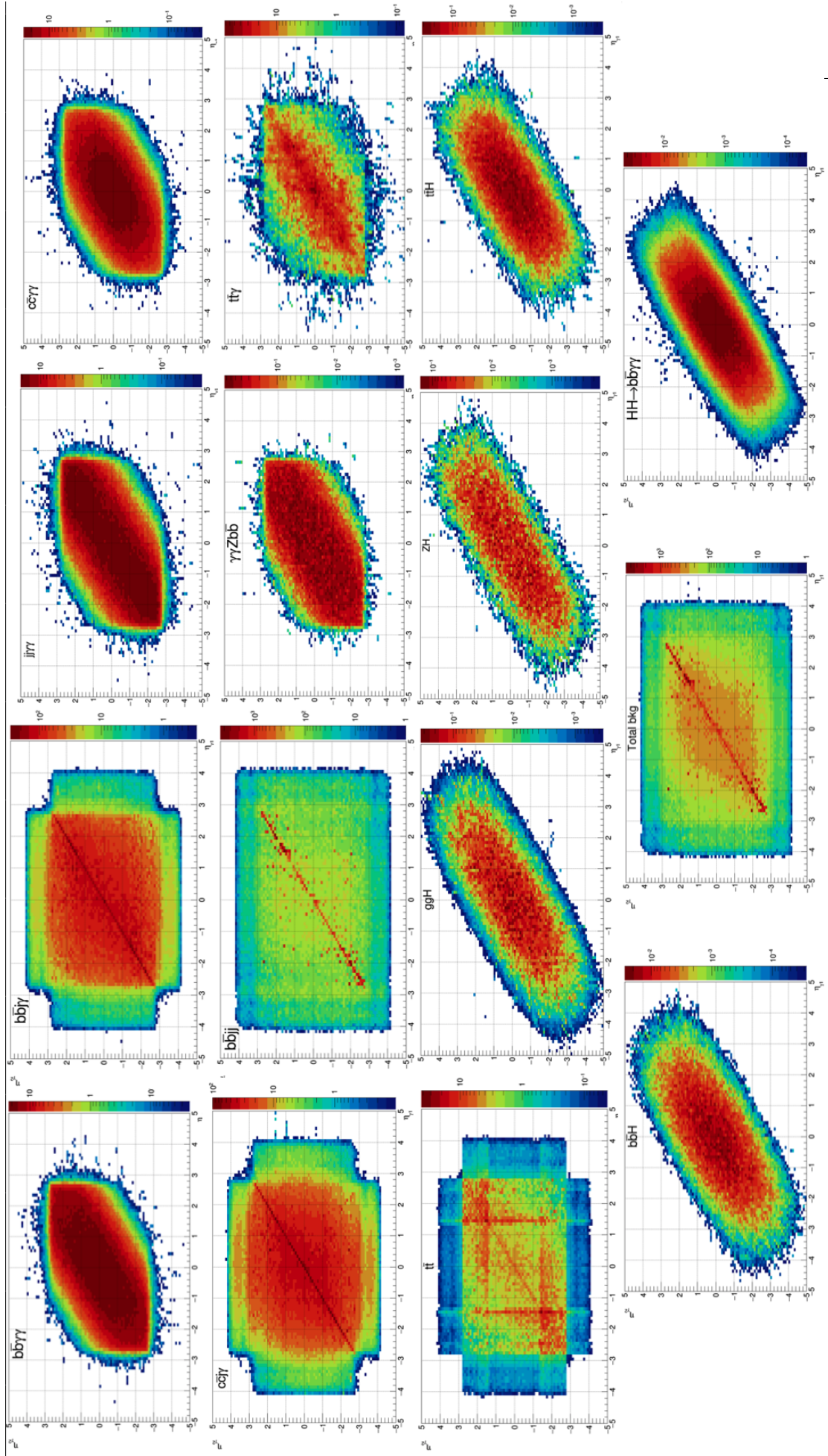
Figure A.7: η distribution of the two selected photons before ΔR cuts are applied

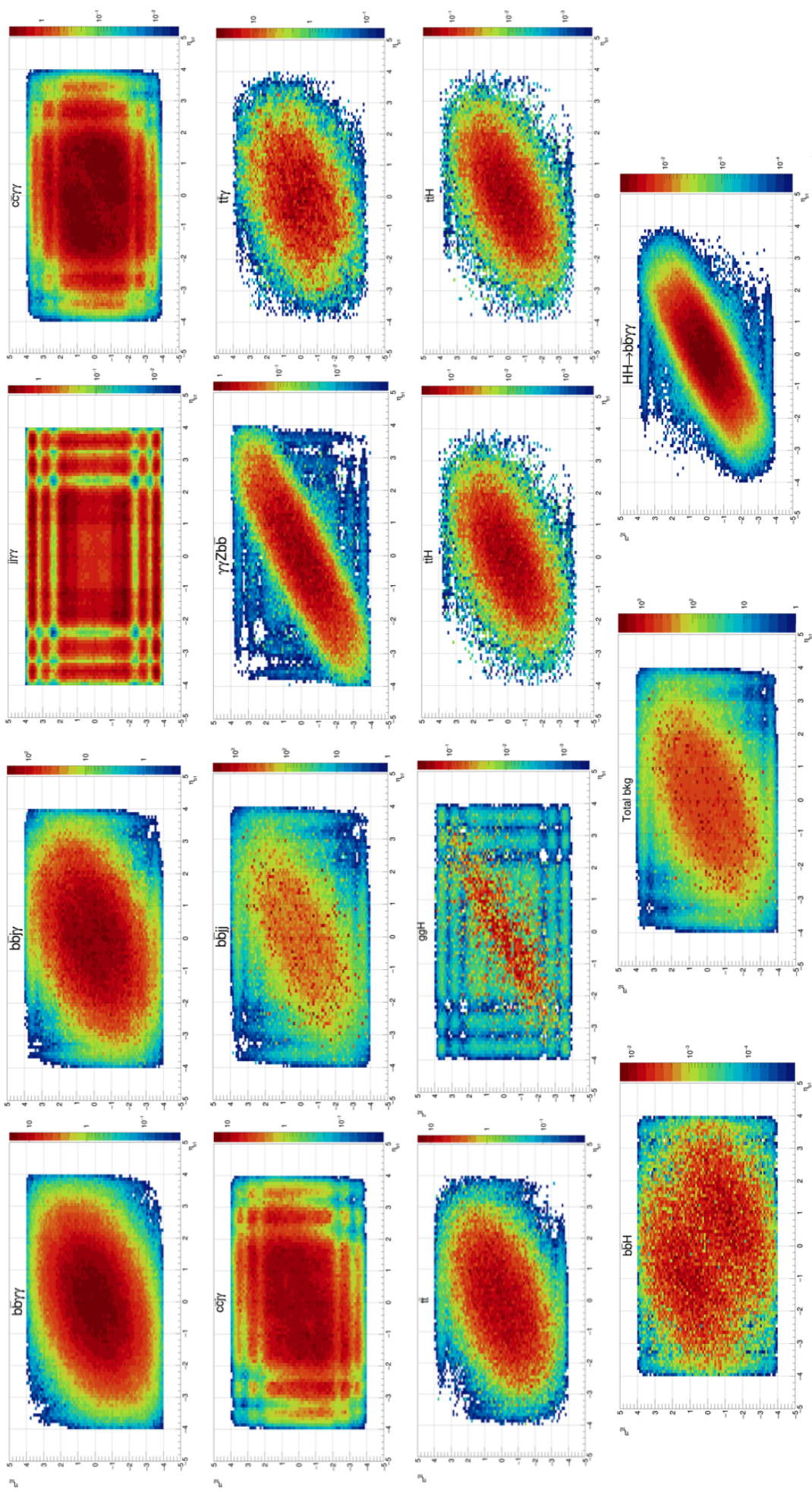Figure A.8: η distribution of the two selected b-tagged jets before ΔR cuts are applied
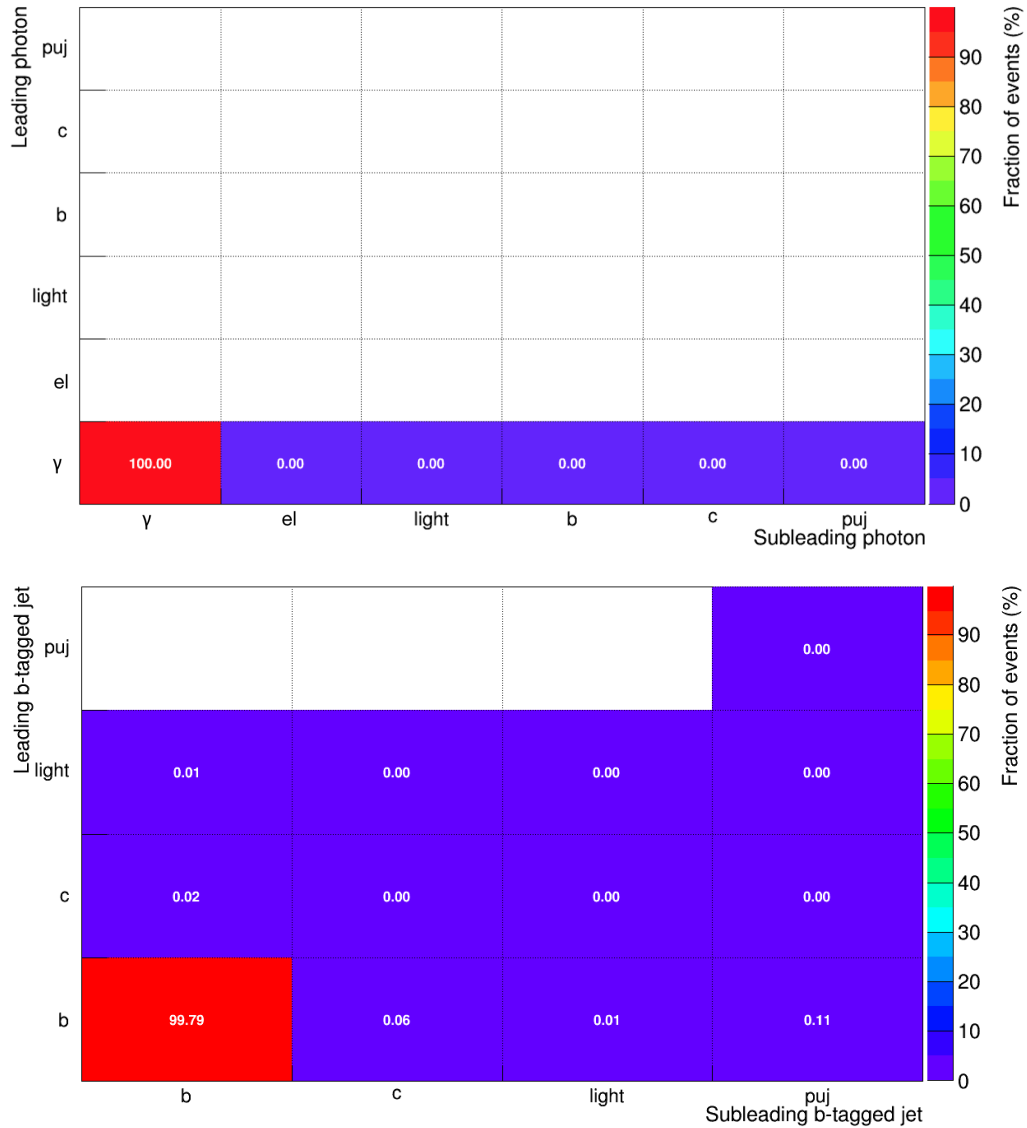
A.3   Signal source

Figure A.9: Source of photons (top) and *b*-tagged jets (bottom) for the signal sample. The sources considered are *b*-jets (b), *c*-jets (c), jets arising from light quarks (light) or from pileup jets (puj). Photon fakes can arise from fake jets and misidentified electrons (el)

A.4   Statistical uncertainties

Table A.1: Expected number of events for a weighted cuts based method using the latest available flavour tagging functions for the scenario using $50{\times}50\mu\text{m}^2$ pixel geometry and $p_T^{b\bar{b}/\gamma\gamma} > 80\text{GeV}$. Also with an increased accepted jet η from 2.5 to 4.0 but with less than six jets in the central $|\eta| < 2.5$ region only. Showing two types of statistical error and the result of adding them in quadrature (*Comb.*). *All bkgs*[sum total of all backgrounds], *SingleH*[*ZH*, *t\bar{t}H*, *b\bar{b}H*, *ggH*], *Reducibles*[$b\bar{b}\gamma\gamma$, $b\bar{b}j\gamma$, $b\bar{b}jj$, $c\bar{c}\gamma\gamma$, $c\bar{c}j\gamma$, $jj\gamma\gamma$], *Others*[$\gamma\gamma Z(\to b\bar{b})$, $t\bar{t}\gamma$, $t\bar{t}$]

	Barrel-barrel				Other			
	Expected events	Seed error	Stat. error	Comb.	Expected events	Seed error	Stat. error	Comb.
$HH \to b\bar{b}\gamma\gamma$	8.42	0.26	0.01	0.26	2.61	0.15	0.01	0.15
$b\bar{b}\gamma\gamma$	12.30	0.33	0.44	0.55	10.34	0.23	0.38	0.45
$b\bar{b}j\gamma$	14.42	1.54	1.48	2.13	11.30	0.52	1.15	1.26
$b\bar{b}jj$	1.65	0.46	0.50	0.68	2.49	0.86	0.67	1.09
$c\bar{c}\gamma\gamma$	1.01	0.05	0.06	0.07	0.55	0.04	0.04	0.06
$c\bar{c}j\gamma$	0.80	0.08	0.09	0.12	0.61	0.06	0.09	0.10
$jj\gamma\gamma$	0.95	0.07	0.07	0.10	0.77	0.05	0.05	0.08
$ZH(\to \gamma\gamma)$	1.68	0.11	0.07	0.13	0.90	0.07	0.05	0.08
$t\bar{t}H(\to \gamma\gamma)$	4.52	0.21	0.08	0.23	1.60	0.11	0.05	0.12
$bbH(\to \gamma\gamma)$	0.12	0.01	0.01	0.01	0.05	0.01	0.00	0.01
$ggH(\to \gamma\gamma)$	1.98	0.10	0.14	0.17	0.77	0.07	0.09	0.11
$Z(\to b\bar{b})\gamma\gamma$	0.71	0.04	0.06	0.07	0.55	0.06	0.05	0.08
$t\bar{t}\gamma$	2.10	0.84	0.75	1.13	0.27	0.07	0.07	0.10
$t\bar{t}$	0.12	0.03	0.02	0.04	0.20	0.05	0.04	0.06
Totals								
All bkgs	42.37	1.87	1.80	2.59	30.40	1.05	1.40	1.75
Single H	8.30	0.26	0.17	0.31	3.31	0.15	0.11	0.18
Reducibles	31.13	1.64	1.63	2.31	26.06	1.04	1.39	1.73
Other	2.93	0.85	0.75	1.13	1.03	0.10	0.10	0.14
$S/\sqrt{B}$	1.29	0.05	0.03	0.06	0.47	0.03	0.01	0.03

	$S/\sqrt{B}$	Seed error	Stat error	Comb
Total events	**1.38**	**0.05**	**0.03**	**0.05**

Table A.2: Expected number of events for a weighted cuts based method using the latest available flavour tagging functions for the scenario using $50 \times 50 \mu \mathrm{m}^2$ pixel geometry and $p_T^{b\bar{b}/\gamma\gamma} > 170/180 \mathrm{GeV}$. Also with an increased accepted jet η from 2.5 to 4.0 but with less than six jets in the central $|\eta| < 2.5$ region only. Showing two types of statistical error and the result of adding them in quadrature ($Comb.$). *All bkgs*[sum total of all backgrounds], $SingleH[ZH, t\bar{t}H, b\bar{b}H, ggH]$, $Reducibles[b\bar{b}\gamma\gamma, b\bar{b}j\gamma, b\bar{b}jj, c\bar{c}\gamma\gamma, c\bar{c}j\gamma, jj\gamma\gamma]$, $Others[\gamma\gamma Z(\to b\bar{b}), t\bar{t}\gamma, t\bar{t}]$

	Barrel-barrel				Other			
	Expected events	Seed error	Stat. error	Comb.	Expected events	Seed error	Stat. error	Comb.
$HH \to b\bar{b}\gamma\gamma$	4.59	0.10	0.01	0.10	1.19	0.05	0.01	0.05
$b\bar{b}\gamma\gamma$	2.87	0.12	0.22	0.25	2.10	0.13	0.19	0.23
$b\bar{b}j\gamma$	1.66	0.43	0.43	0.61	0.91	0.18	0.30	0.35
$b\bar{b}jj$	0.07	0.07	0.07	0.10	0.00	0.00	0.00	0.00
$c\bar{c}\gamma\gamma$	0.12	0.02	0.02	0.03	0.11	0.02	0.02	0.02
$c\bar{c}j\gamma$	0.07	0.02	0.02	0.03	0.03	0.02	0.02	0.02
$jj\gamma\gamma$	0.11	0.02	0.02	0.02	0.06	0.01	0.01	0.01
$ZH(\to \gamma\gamma)$	0.77	0.06	0.05	0.07	0.36	0.03	0.03	0.04
$t\bar{t}H(\to \gamma\gamma)$	1.17	0.05	0.04	0.06	0.29	0.02	0.02	0.03
$bbH(\to \gamma\gamma)$	0.02	0.00	0.00	0.00	0.00	0.00	0.00	0.00
$ggH(\to \gamma\gamma)$	1.01	0.07	0.11	0.13	0.33	0.05	0.06	0.08
$Z(\to b\bar{b})\gamma\gamma$	0.21	0.02	0.03	0.04	0.19	0.02	0.03	0.04
$t\bar{t}\gamma$	0.45	0.41	0.42	0.59	0.00	0.00	0.00	0.00
$t\bar{t}$	0.00	0.00	0.00	0.00	0.00	0.00	0.00	0.00
Totals								
All bkgs	8.54	0.62	0.66	0.90	4.39	0.23	0.36	0.43
Single H	2.98	0.10	0.12	0.16	0.98	0.06	0.07	0.09
Reducibles	4.89	0.45	0.49	0.67	3.20	0.22	0.35	0.42
Other	0.67	0.41	0.42	0.59	0.20	0.02	0.03	0.04
$S/\sqrt{B}$	1.57	0.07	0.06	0.09	0.57	0.03	0.02	0.04

	$S/\sqrt{B}$	Seed error	Stat error	Comb
Total events	**1.67**	**0.06**	**0.06**	**0.08**

Table A.3: Expected number of events for a BDT method using the latest available flavour tagging functions for the scenario using $50\times50\mu\mathrm{m}^2$ pixel geometry. Showing two types of statistical error and the result of adding them in quadrature ($Comb.$) All $bkgs$[sum total of all backgrounds], $SingleH[ZH, t\bar{t}H, b\bar{b}H, ggH]$, $Reducibles[b\bar{b}\gamma\gamma,$ $b\bar{b}j\gamma, b\bar{b}jj, c\bar{c}\gamma\gamma, c\bar{c}j\gamma, jj\gamma\gamma]$, $Others[\gamma\gamma Z(\to b\bar{b}), t\bar{t}\gamma, t\bar{t}]$

	Barrel-barrel				Other			
	Expected events	Seed error	Stat. error	Comb.	Expected events	Seed error	Stat. error	Comb.
$HH \to b\bar{b}\gamma\gamma$	9.17	0.01	0.02	0.02	1.77	0.01	0.01	0.01
$b\bar{b}\gamma\gamma$	1.43	0.21	0.20	0.29	0.53	0.17	0.13	0.21
$b\bar{b}j\gamma$	1.34	0.23	0.21	0.31	0.17	0.05	0.06	0.08
$b\bar{b}jj$	0.19	0.08	0.06	0.09	0.03	0.03	0.03	0.04
$c\bar{c}\gamma\gamma$	0.26	0.06	0.07	0.09	0.02	0.01	0.01	0.01
$c\bar{c}j\gamma$	0.02	0.01	0.00	0.01	0.01	0.00	0.00	0.00
$jj\gamma\gamma$	0.03	0.01	0.01	0.01	0.00	0.00	0.00	0.00
$ZH(\to \gamma\gamma)$	1.45	0.07	0.08	0.11	0.35	0.04	0.04	0.06
$t\bar{t}H(\to \gamma\gamma)$	1.73	0.03	0.06	0.07	0.20	0.01	0.02	0.02
$b\bar{b}H(\to \gamma\gamma)$	0.04	0.00	0.00	0.01	0.01	0.00	0.00	0.00
$ggH(\to \gamma\gamma)$	0.98	0.10	0.13	0.16	0.24	0.02	0.07	0.08
$Z(\to b\bar{b})\gamma\gamma$	0.19	0.03	0.04	0.05	0.07	0.02	0.03	0.04
$t\bar{t}\gamma$	0.02	0.00	0.00	0.01	0.00	0.00	0.00	0.00
$t\bar{t}$	0.03	0.00	0.00	0.00	0.00	0.00	0.00	0.00
Totals								
All bkgs	7.69	0.35	0.35	0.49	1.62	0.19	0.17	0.25
Single H	4.20	0.13	0.16	0.21	0.79	0.05	0.09	0.10
Reducibles	3.26	0.33	0.30	0.45	0.75	0.18	0.15	0.23
Other	0.23	0.03	0.04	0.05	0.08	0.02	0.03	0.04
$S/\sqrt{B}$	3.31	0.08	0.07	0.11	1.39	0.08	0.07	0.11

	$S/\sqrt{B}$	Seed error	Stat error	Comb
Total events	**3.59**	**0.08**	**0.07**	**0.11**

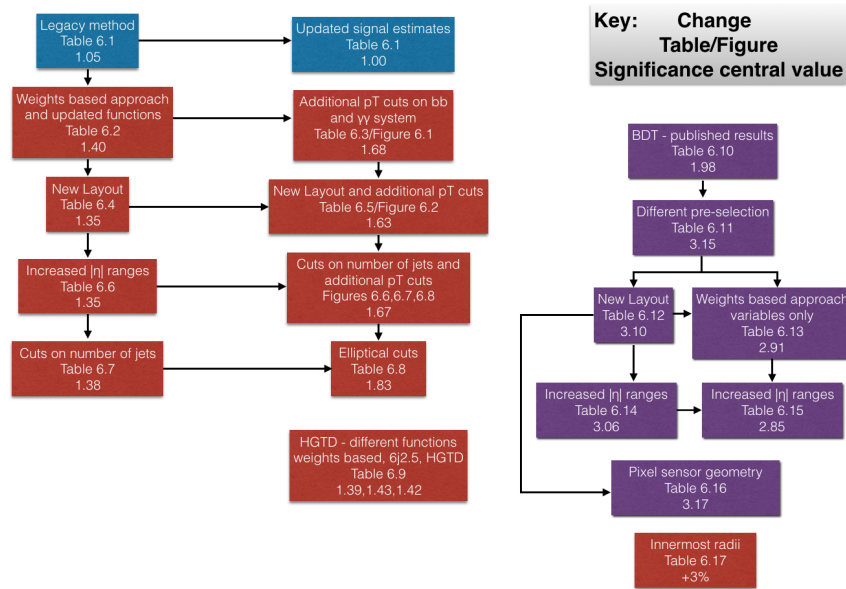## A.5   Diagram of results flow

Figure A.10: Box diagram of the results flow. Showing the various changes, corresponding tables/figures and resulting significance for the Legacy (blue), weighted cuts based (red) and BDT (purple) methods

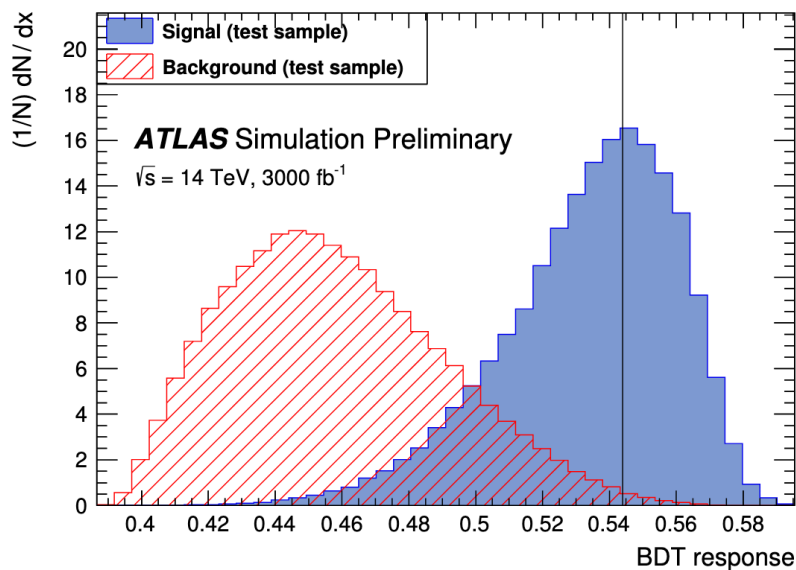## A.6   Published BDT response distribution

Figure A.11: BDT response for signal and background test samples. The vertical line denotes the optimal cut on the BDT response that maximises the significance [26]
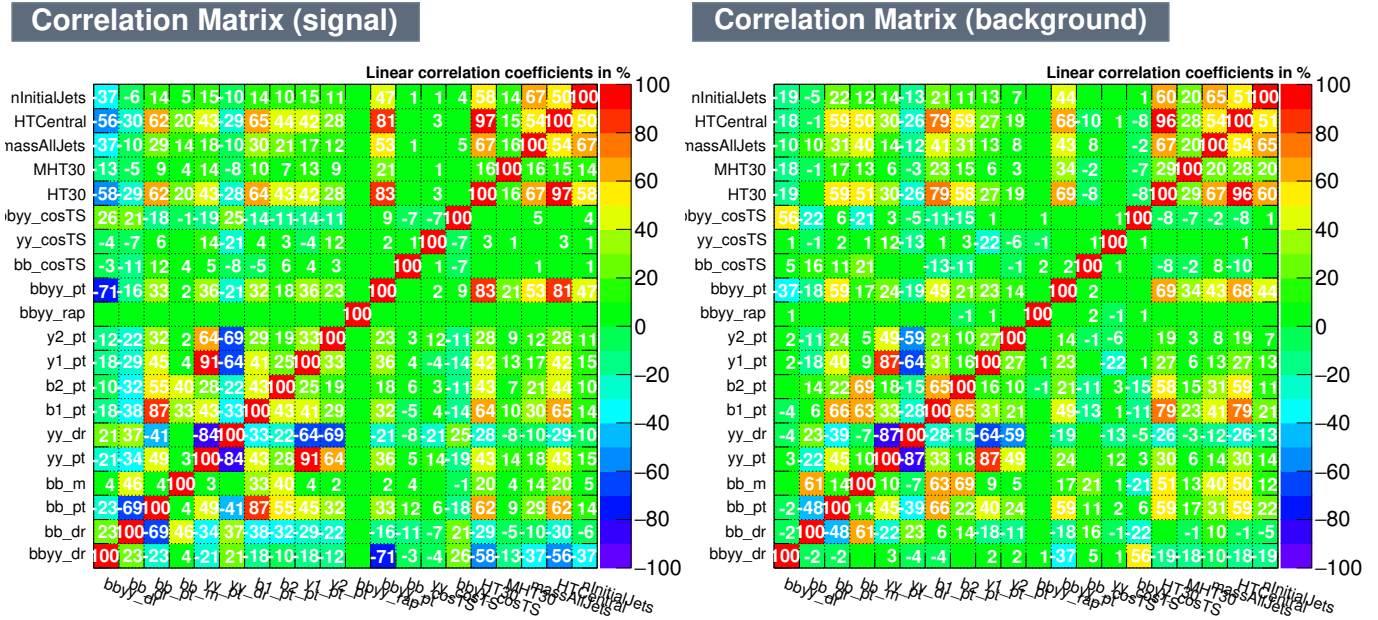
A.7   BDT training and testing plots: Overtrained mv2c10

Figure A.12: Correlation plots for signal (left) and background (right) between the variables used in the published paper for an innermost pixel layer radius of 39mm and adopting the $50{\times}50\mu\mathrm{m}^2$ pixel sensor geometry. The *b*-tagging functions are based on the overtrained mv2c10 with the overoptimistic material budget

Table A.4: Expected number of events acquired using a BDT method trained with the overtrained mv2c10 *b*-tagging algorithm similar to 6.10. However multiple seeds for the smearing functions, different pre-selection cuts on $m_{\gamma\gamma}$ and a different BDT response cut have been considered, hence the improved performance compared to 6.10. Additional training and testing plots are shown in this Appendix section. *All bkgs*[sum total of all backgrounds], *SingleH*[ZH, $t\bar{t}H$, $b\bar{b}H$, ggH], *Reducibles*[$b\bar{b}\gamma\gamma$, $b\bar{b}j\gamma$, $b\bar{b}jj$, $c\bar{c}\gamma\gamma$, $c\bar{c}j\gamma$, $jj\gamma\gamma$], *Others*[$\gamma\gamma Z(\to b\bar{b})$, $t\bar{t}\gamma$, $t\bar{t}$]

|	Events after pre-selection		Events passing BDT response		Events passing BDT response $123 < m_{\gamma\gamma} < 127$ GeV	
	Barrel-barrel	Other	Barrel-barrel	Other	Barrel-barrel	Other
$HH \to b\bar{b}\gamma\gamma$	28.67±0.01	10.54±0.01	8.13±0.01	1.42±0.00	6.72±0.01	1.04±0.00
$b\bar{b}\gamma\gamma$	997.60±4.62	699.79±2.84	2.16±0.21	0.44±0.05	0.63±0.09	0.10±0.05
$b\bar{b}j\gamma$	786.39±5.20	612.66±4.73	1.33±0.21	0.18±0.05	0.56±0.12	0.06±0.04
$bbjj$	164.92±2.05	153.76±1.59	0.19±0.06	0.00±0.00	0.13±0.06	0.00±0.00
$c\bar{c}\gamma\gamma$	42.79±0.50	20.73±0.28	0.16±0.04	0.00±0.00	0.12±0.03	0.00±0.00
$c\bar{c}j\gamma$	18.68±0.18	12.46±0.23	0.01±0.00	0.00±0.00	0.00±0.00	0.00±0.00
$jj\gamma\gamma$	37.28±0.91	39.63±1.23	0.01±0.00	0.02±0.01	0.01±0.00	0.00±0.00
$ZH(\to \gamma\gamma)$	31.92±0.14	18.27±0.15	0.87±0.04	0.17±0.03	0.70±0.04	0.15±0.02
$t\bar{t}H(\to \gamma\gamma)$	151.70±0.35	59.77±0.22	1.04±0.03	0.10±0.01	0.86±0.04	0.07±0.01
$b\bar{b}H(\to \gamma\gamma)$	5.60±0.02	2.09±0.01	0.03±0.00	0.00±0.00	0.02±0.00	0.00±0.00
$ggH(\to \gamma\gamma)$	35.65±0.48	20.35±0.34	0.51±0.07	0.02±0.02	0.39±0.06	0.02±0.02
$Z(\to bb)\gamma\gamma$	22.53±0.15	15.76±0.26	0.23±0.02	0.04±0.03	0.10±0.02	0.02±0.02
$t\bar{t}\gamma$	379.94±9.28	177.15±3.81	0.03±0.00	0.00±0.00	0.00±0.00	0.00±0.00
$t\bar{t}$	123.96±5.39	184.36±9.47	0.03±0.01	0.00±0.00	0.01±0.00	0.00±0.00
Totals						
All bkgs	2799±13	2017±12	6.6±0.3	1.0±0.1	3.5±0.2	0.4±0.1
Single H	224.9±0.6	100.5±0.4	2.5±0.1	0.3±0.1	2.0±0.1	0.2±0.0
Reducibles	2048±7	1539±6	3.9±0.3	0.6±0.1	1.5±0.2	0.2±0.1
Other	526±11	377±10	0.3±0.0	0.0±0.0	0.1±0.0	0.0±0.0
$S/\sqrt{B}$	0.54±0.00	0.23±0.00	3.17±0.08	1.44±0.06	3.57±0.10	1.58±0.12
Combined	**0.59±0.00**		**3.48±0.06**		**3.91±0.07**	
$\sqrt{q_0}, A$	0.54±0.35	0.23±0.37	2.72±0.17	1.21±0.12	2.90±0.14	1.24±0.15
Combined	**0.59±0.25**		**2.98±0.12**		**3.15±0.10**	
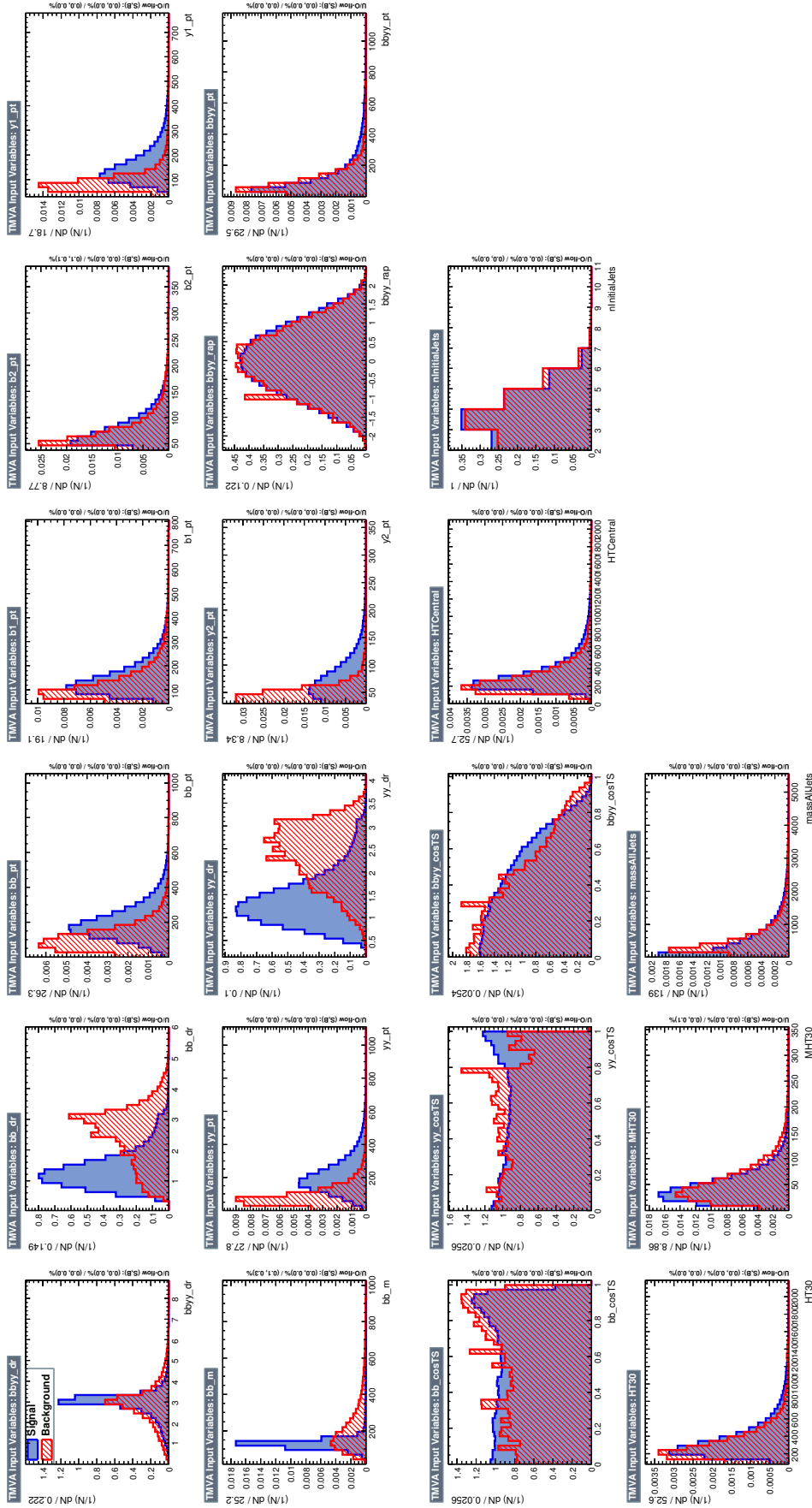
Figure A.13: Distributions of signal and background for each of the variables used in the published paper for an innermost pixel layer radius of 39mm and adopting the $50 \times 50 \mu m^2$ pixel sensor geometry. The b-tagging functions are based on the overtrained mv2c10 with the overoptimistic material budget
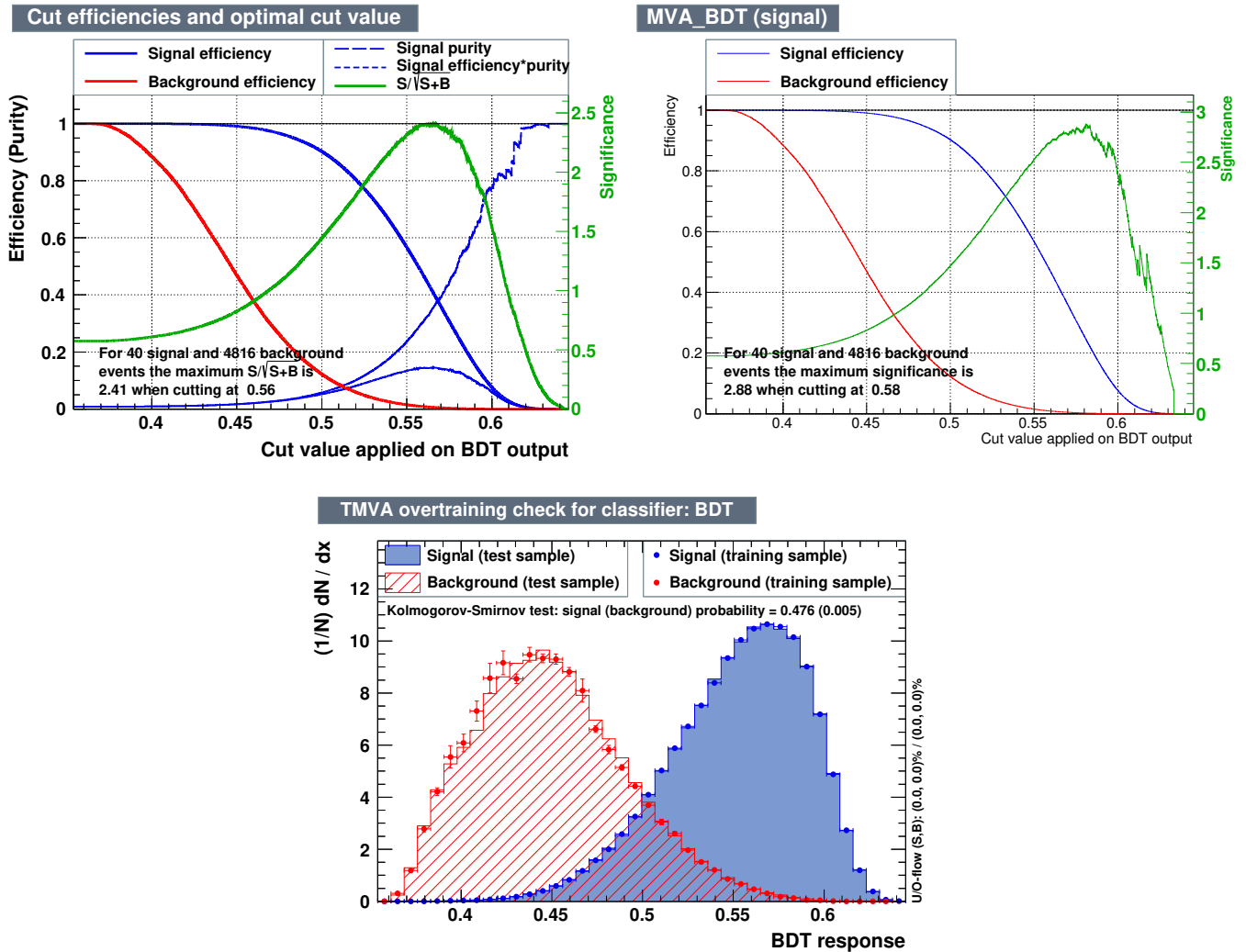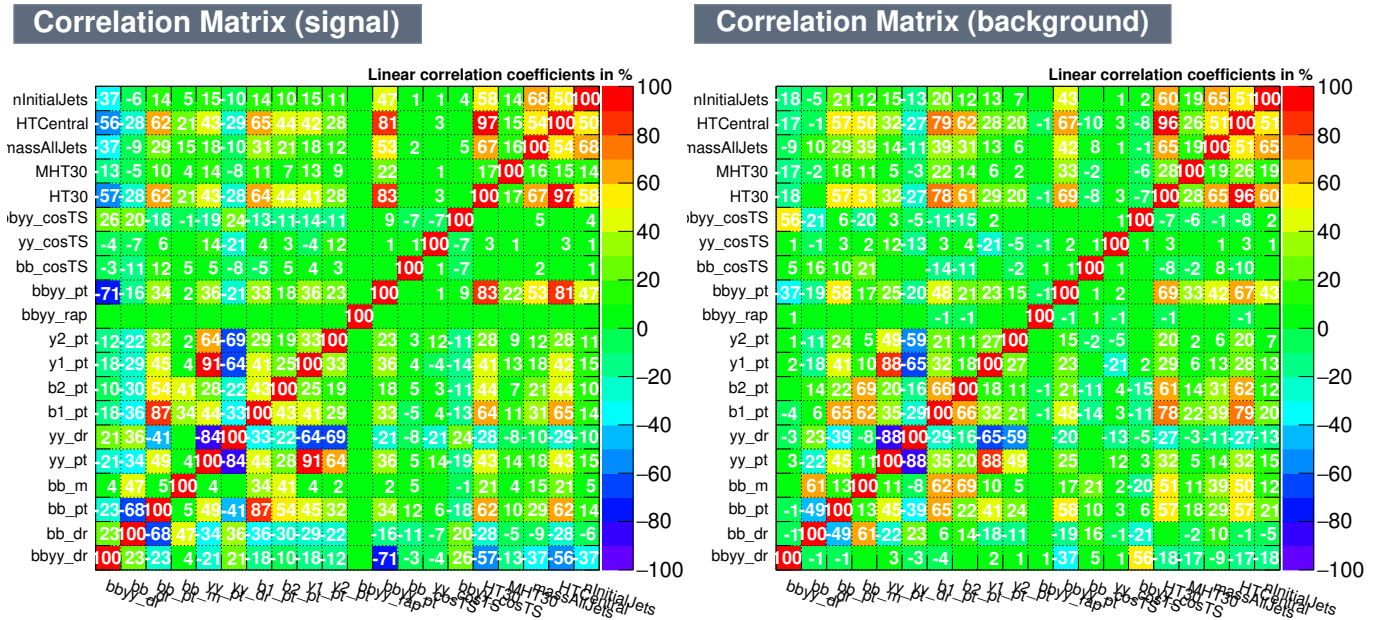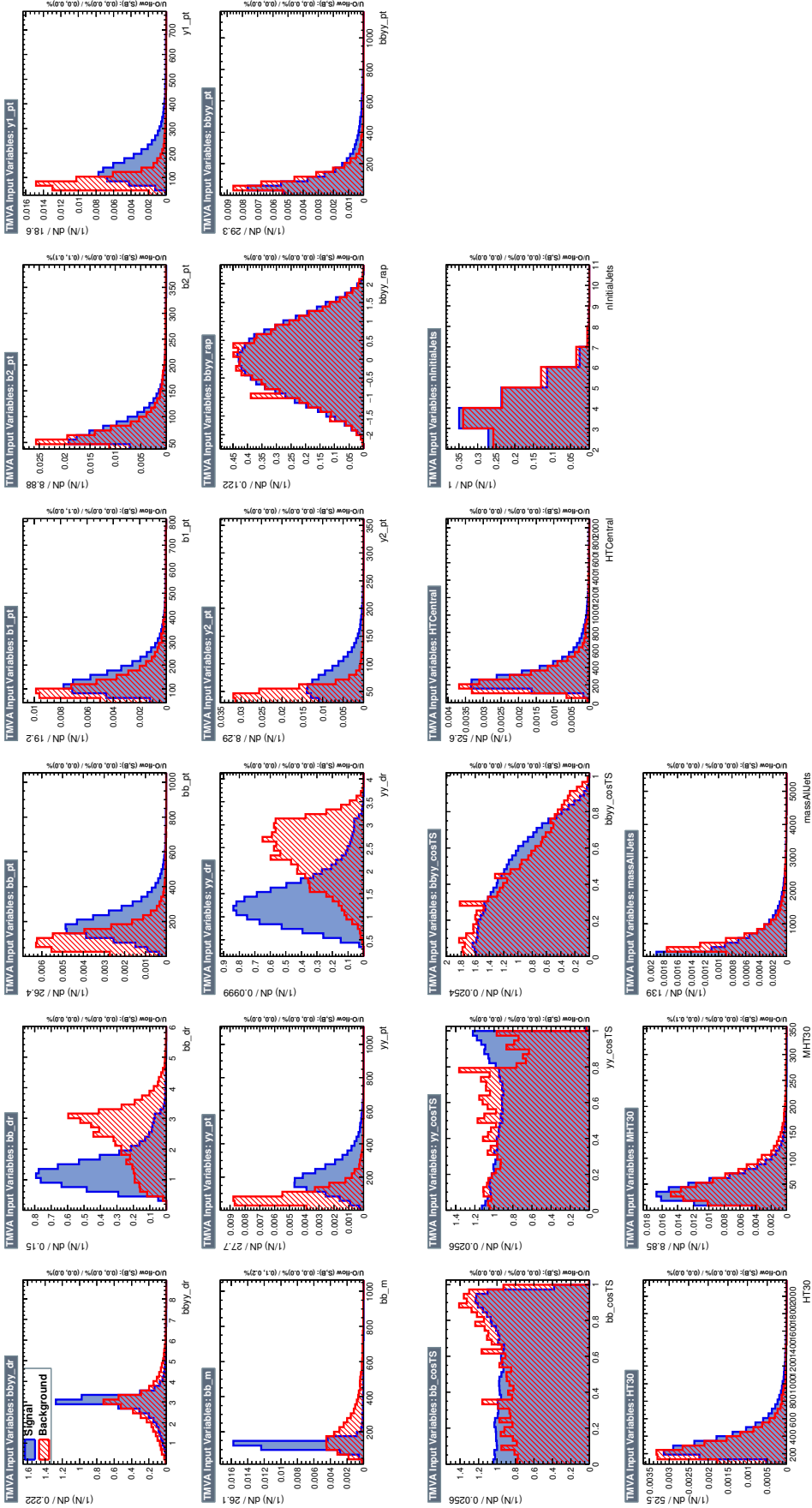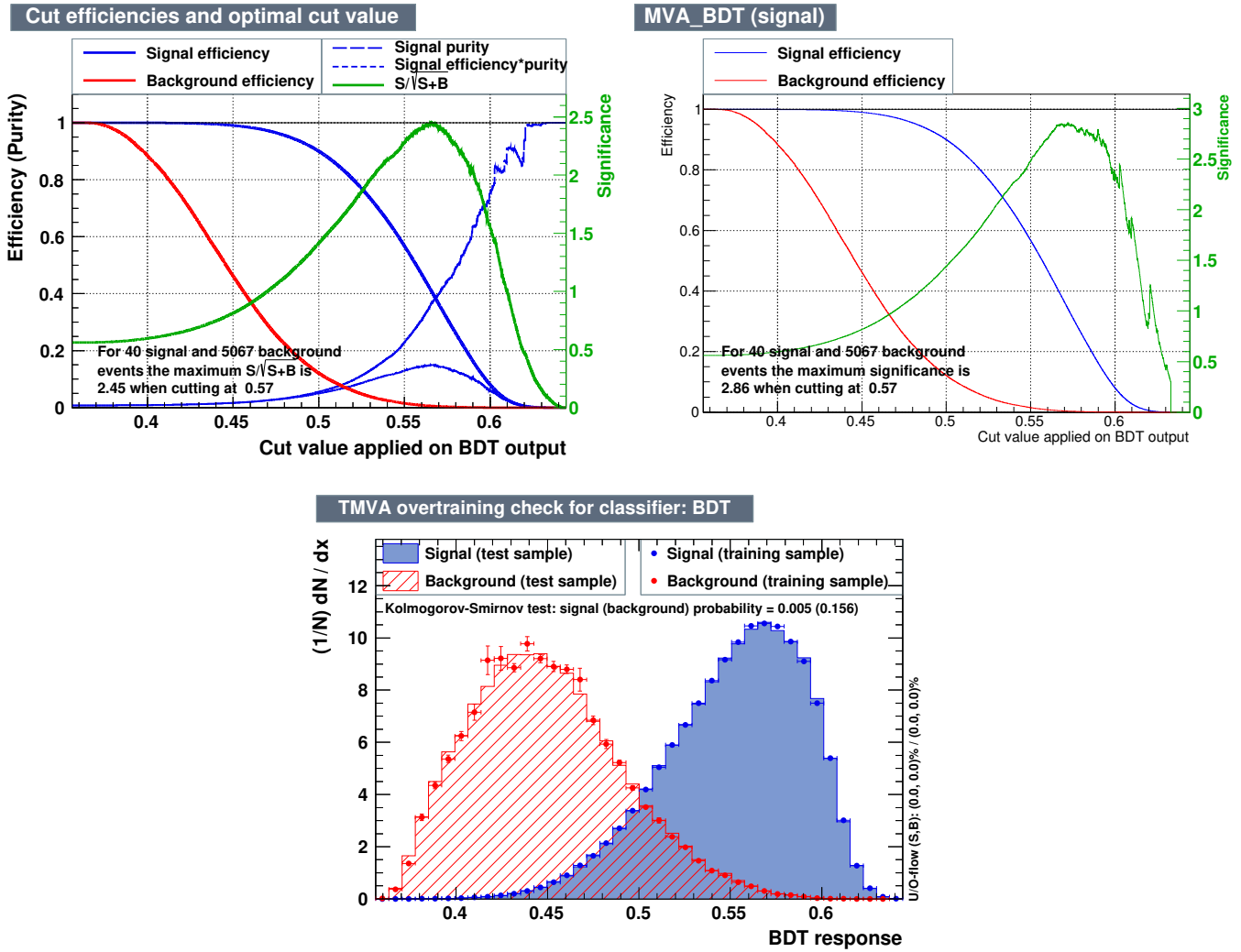
Figure A.14: Signal and background efficiency plots showing purity and $S/\sqrt{S+B}$ (left) and $\sqrt{q_0, A}$ significance (right). Also the BDT response distributions for signal and background for both training and testing samples (bottom). All figures utilise the variables used in the published paper for an innermost pixel layer radius of 39mm and adopting the $50{\times}50\mu\text{m}^2$ pixel sensor geometry. The b-tagging functions are based on the overtrained mv2c10 with the overoptimistic material budget

A.8   BDT training and testing plots: New layout
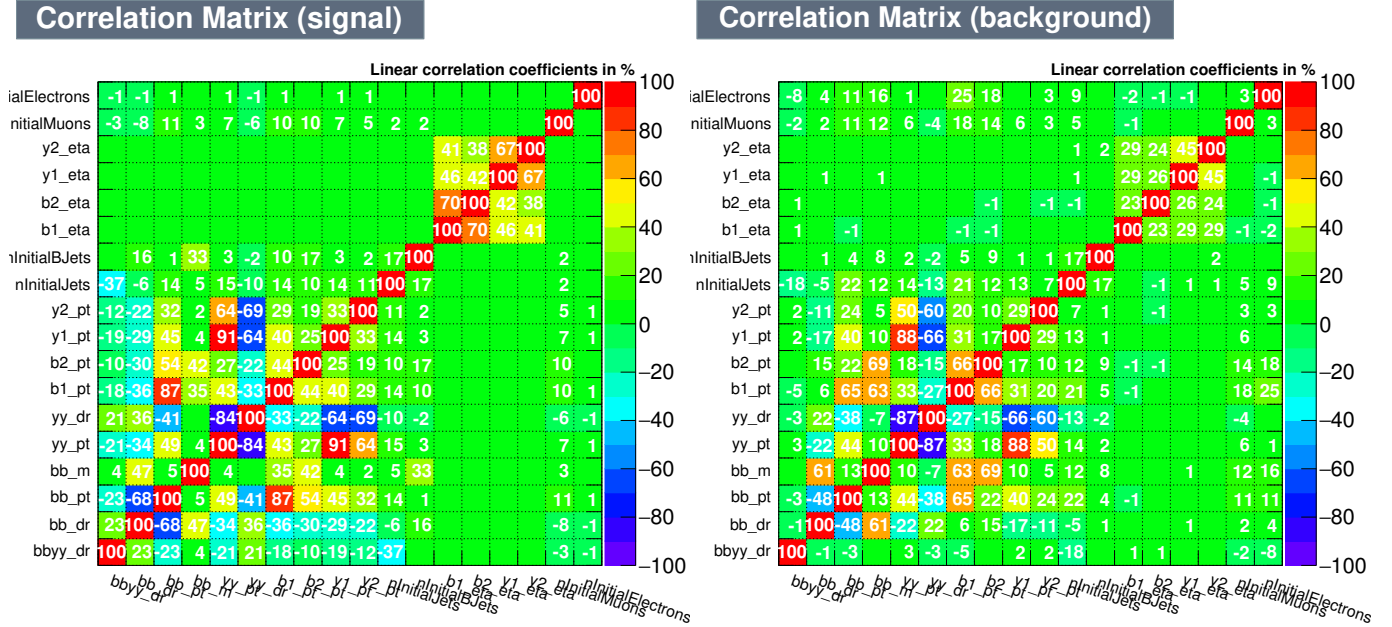

Figure A.15: Correlation plots for signal (left) and background (right) between the variables used in the published paper for an innermost pixel layer radius of 39mm and adopting the $50{\times}50\mu\mathrm{m}^2$ pixel sensor geometry

Figure A.16: Distributions of signal and background for each of the variables used in the published paper for an innermost pixel layer radius of 39mm and adopting the $50 \times 50 \mu m^2$ pixel sensor geometry

Figure A.17: Signal and background efficiency plots showing purity and $S/\sqrt{S+B}$ (left) and $\sqrt{q_0, A}$ significance (right). Also the BDT response distributions for signal and background for both training and testing samples (bottom). All figures utilise the variables used in the published paper for an innermost pixel layer radius of 39mm and adopting the $50{\times}50\mu\mathrm{m}^2$ pixel sensor geometry

A.9 BDT training and testing plots: Weights based variables

Figure A.18: Correlation plots for signal (left) and background (right) between the variables used in the weighted cuts based method for an innermost pixel layer radius of 39mm and adopting the $50 \times 50 \mu m^2$ pixel sensor geometry
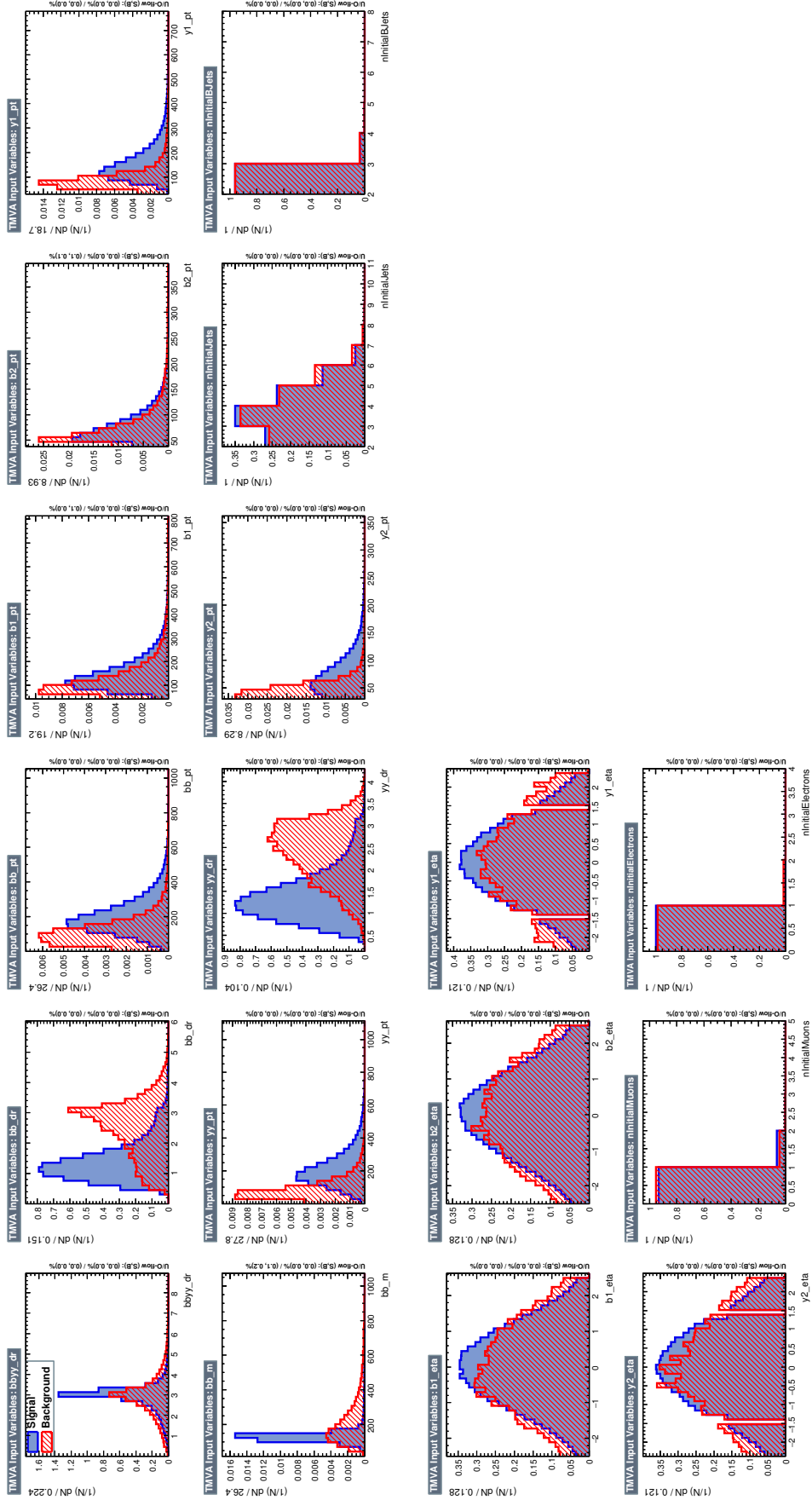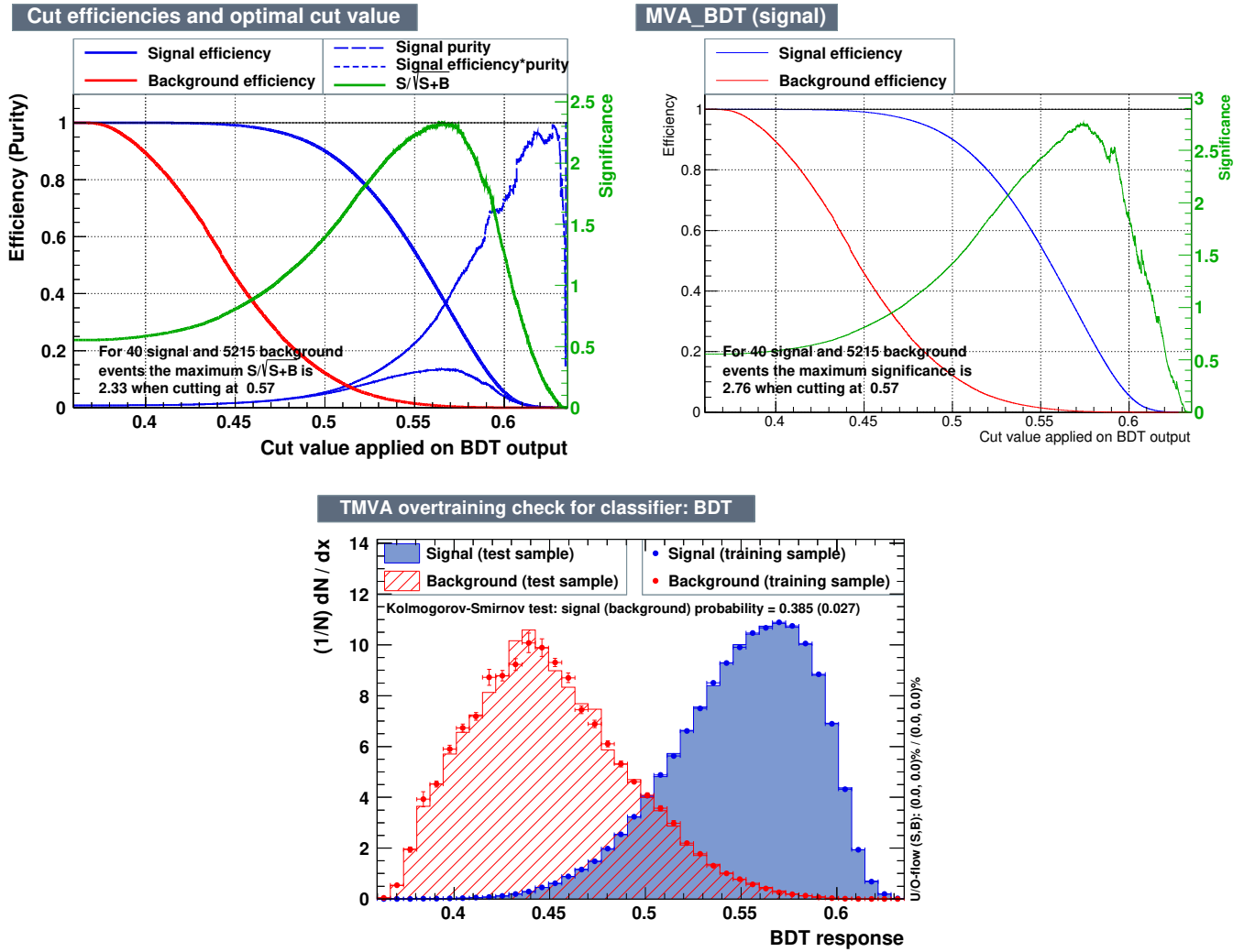
Figure A.19: Distributions of signal and background for each of the variables used in the weighted cuts based method for an innermost pixel layer radius of 39mm and adopting the 50×50μm² pixel sensor geometry

Figure A.20: Signal and background efficiency plots showing purity and $S/\sqrt{S+B}$ (left) and $\sqrt{q_0, A}$ significance (right). Also the BDT response distributions for signal and background for both training and testing samples (bottom). All figures utilise the variables used in the weighted cuts based method for an innermost pixel layer radius of 39mm and adopting the $50{\times}50\mu m^2$ pixel sensor geometry

A.10   BDT training and testing plots: New layout and increased η range
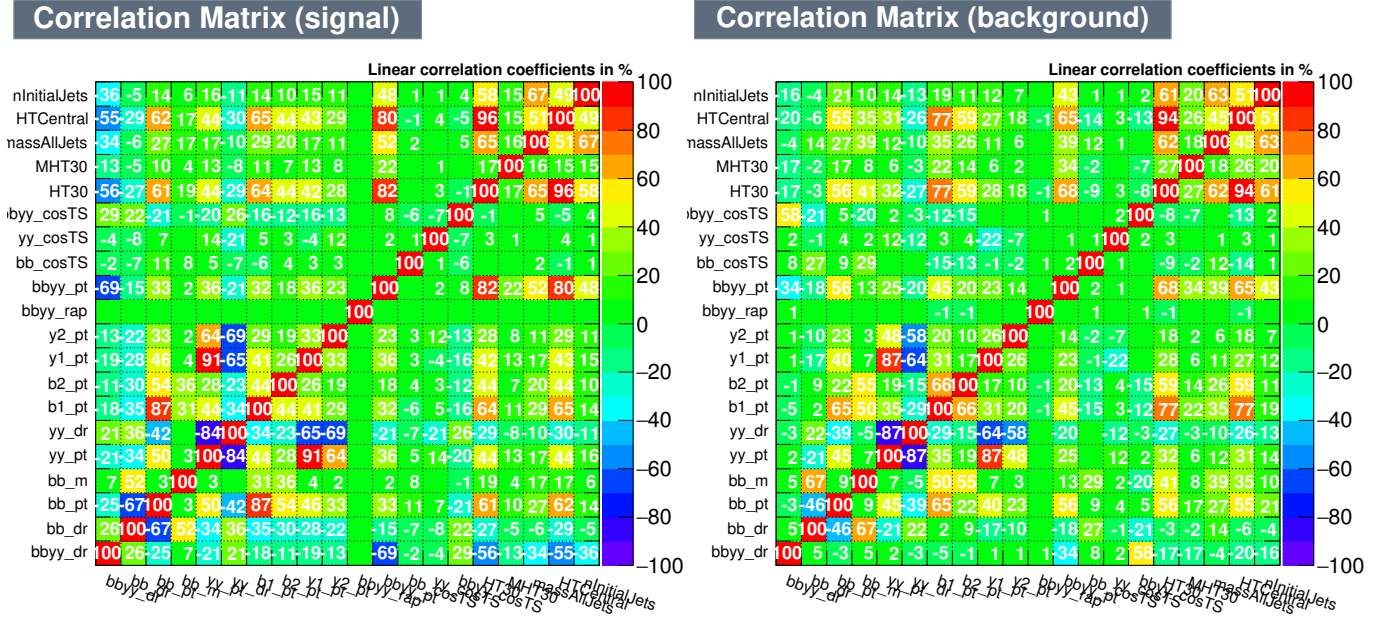

Figure A.21: Correlation plots for signal (left) and background (right) between the variables used in the published paper for an innermost pixel layer radius of 39mm and adopting the $50{\times}50\mu m^2$ pixel sensor geometry. Also with an increased η range for accepted jets up to 4.0, while the number of jets per event is limited to the central $|\eta| < 2.5$ region
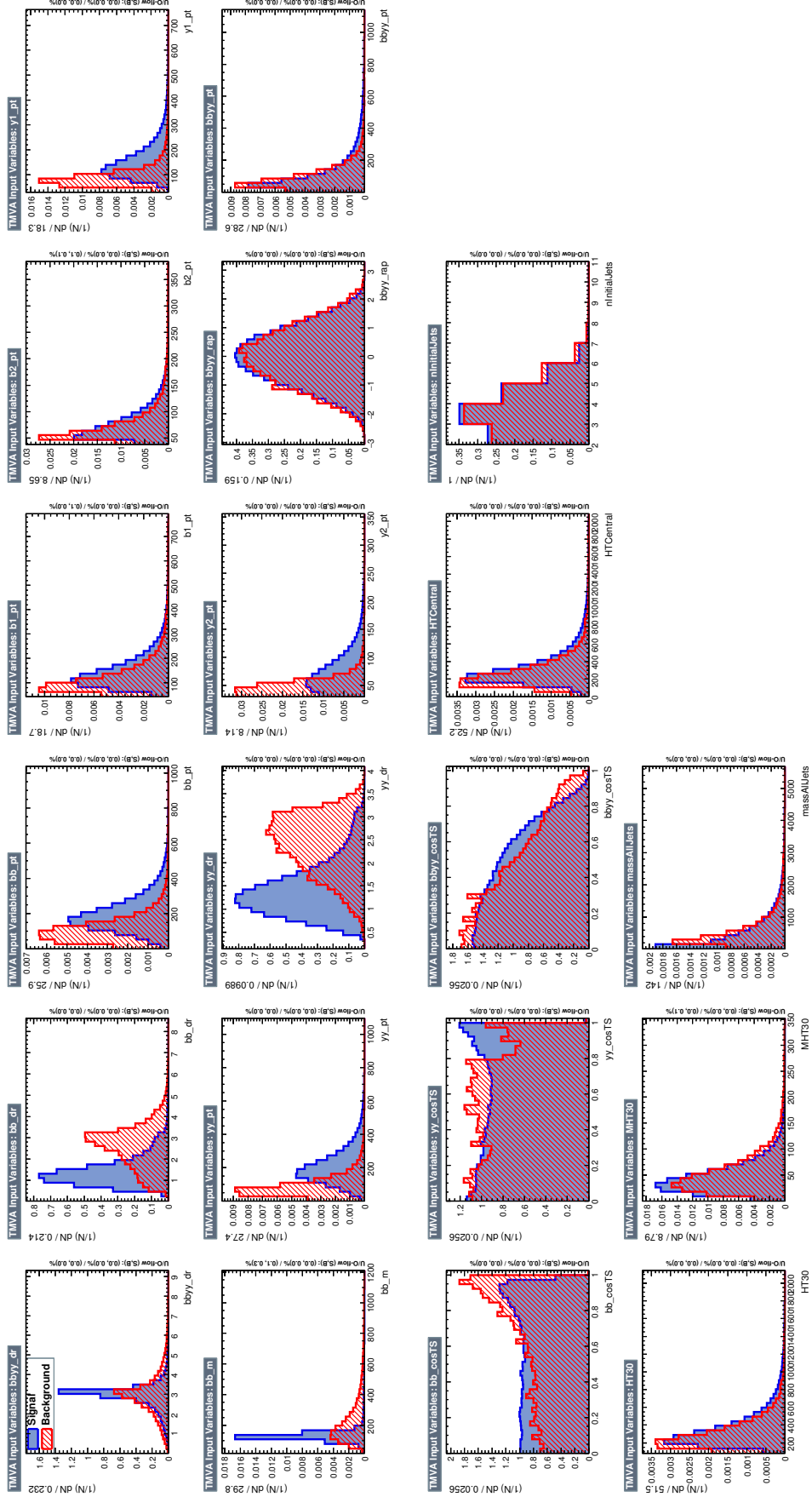
Figure A.22: Distributions of signal and background for each of the variables used in the published paper for an innermost pixel layer radius of 39mm and adopting the $50\times50\mu m^2$ pixel sensor geometry. Also with an increased η range for accepted jets up to 4.0, while the number of jets per event is limited to the central $|\eta| < 2.5$ region
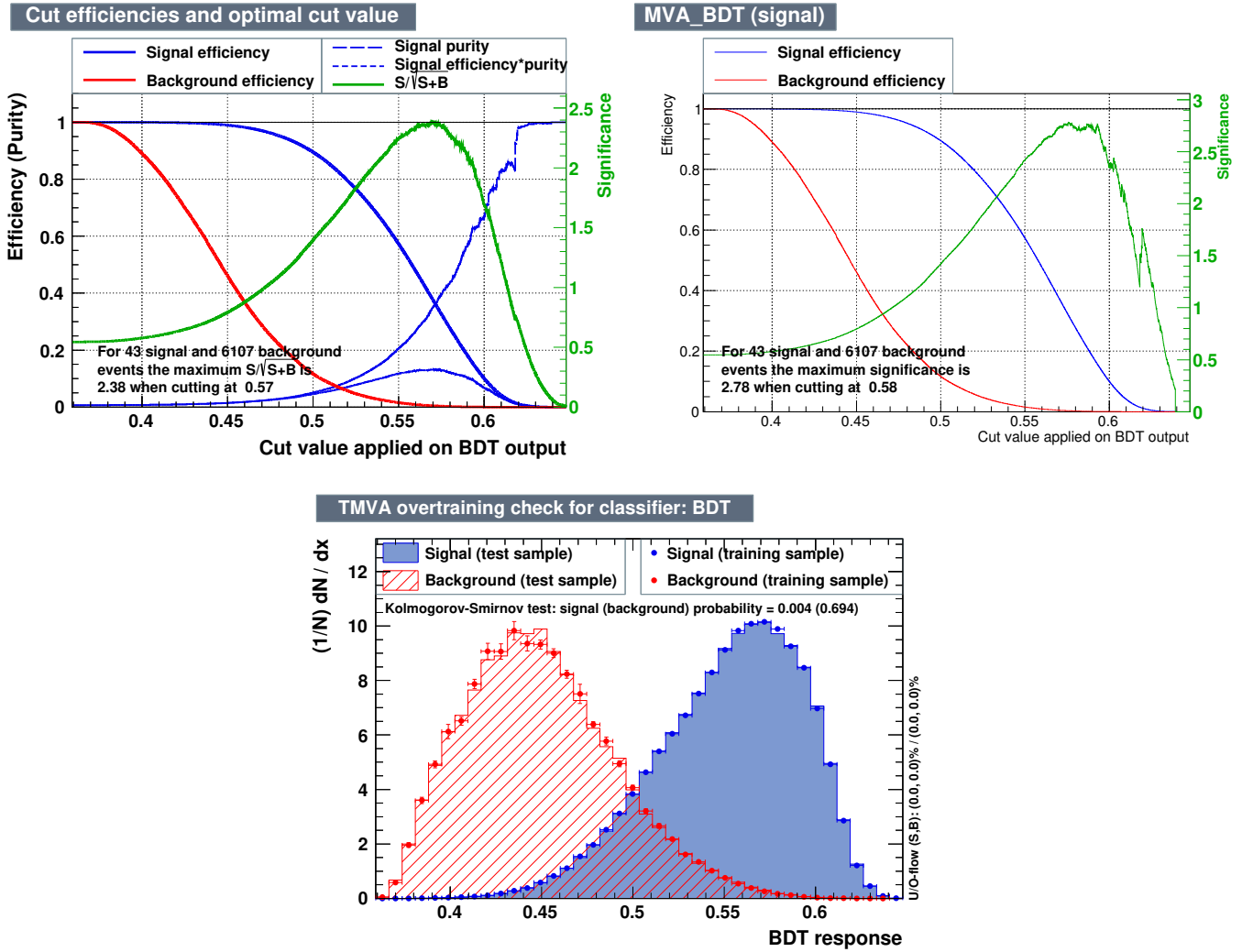
Figure A.23: Signal and background efficiency plots showing purity and $S/\sqrt{S+B}$ (left) and $\sqrt{q_0, A}$ significance (right). Also the BDT response distributions for signal and background for both training and testing samples (bottom). All figures utilise the variables used in the published paper for an innermost pixel layer radius of 39mm and adopting the $50{\times}50\mu\mathrm{m}^2$ pixel sensor geometry. Also with an increased η range for accepted jets up to 4.0, while the number of jets per event is limited to the central $|\eta| < 2.5$ region

A.11 BDT training and testing plots: Weights based cut variables and increased η range
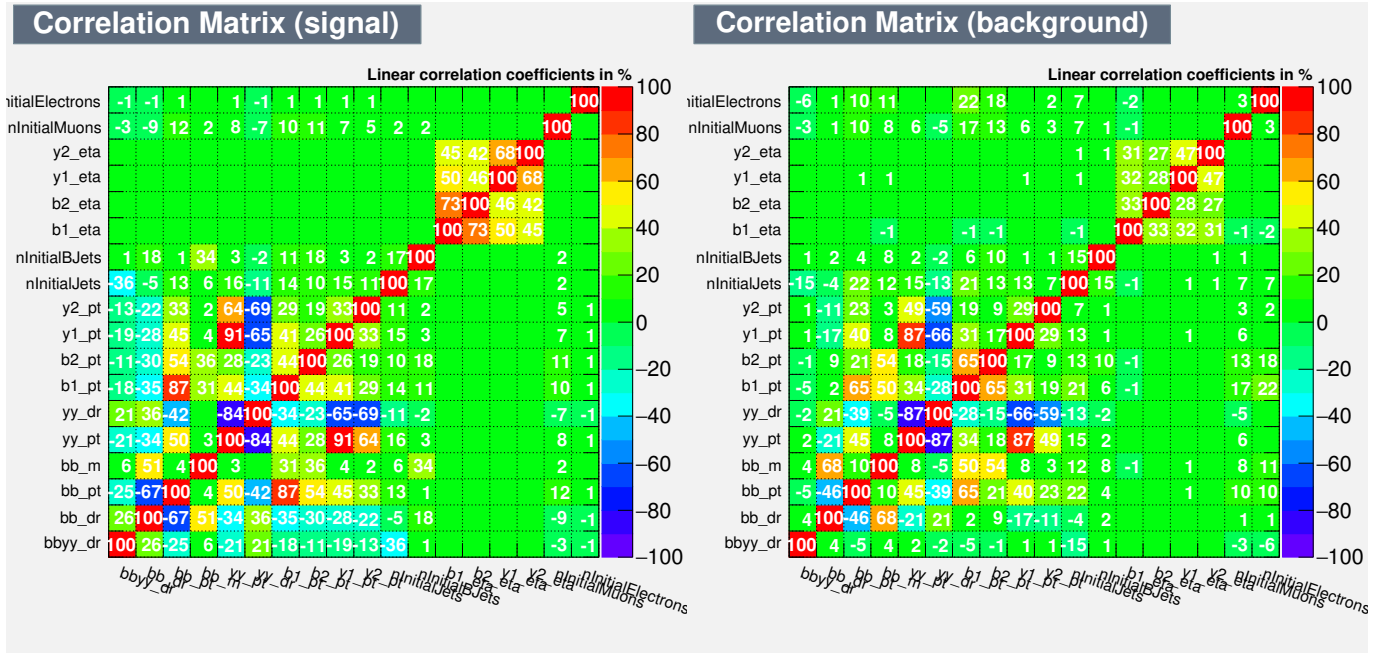

Figure A.24: Correlation plots for signal (left) and background (right) between the variables used in the weighted cuts based method for an innermost pixel layer radius of 39mm and adopting the $50 \times 50 \mu m^2$ pixel sensor geometry. Also with an increased η range for accepted jets up to 4.0, while the number of jets per event is limited to the central $|\eta| < 2.5$ region
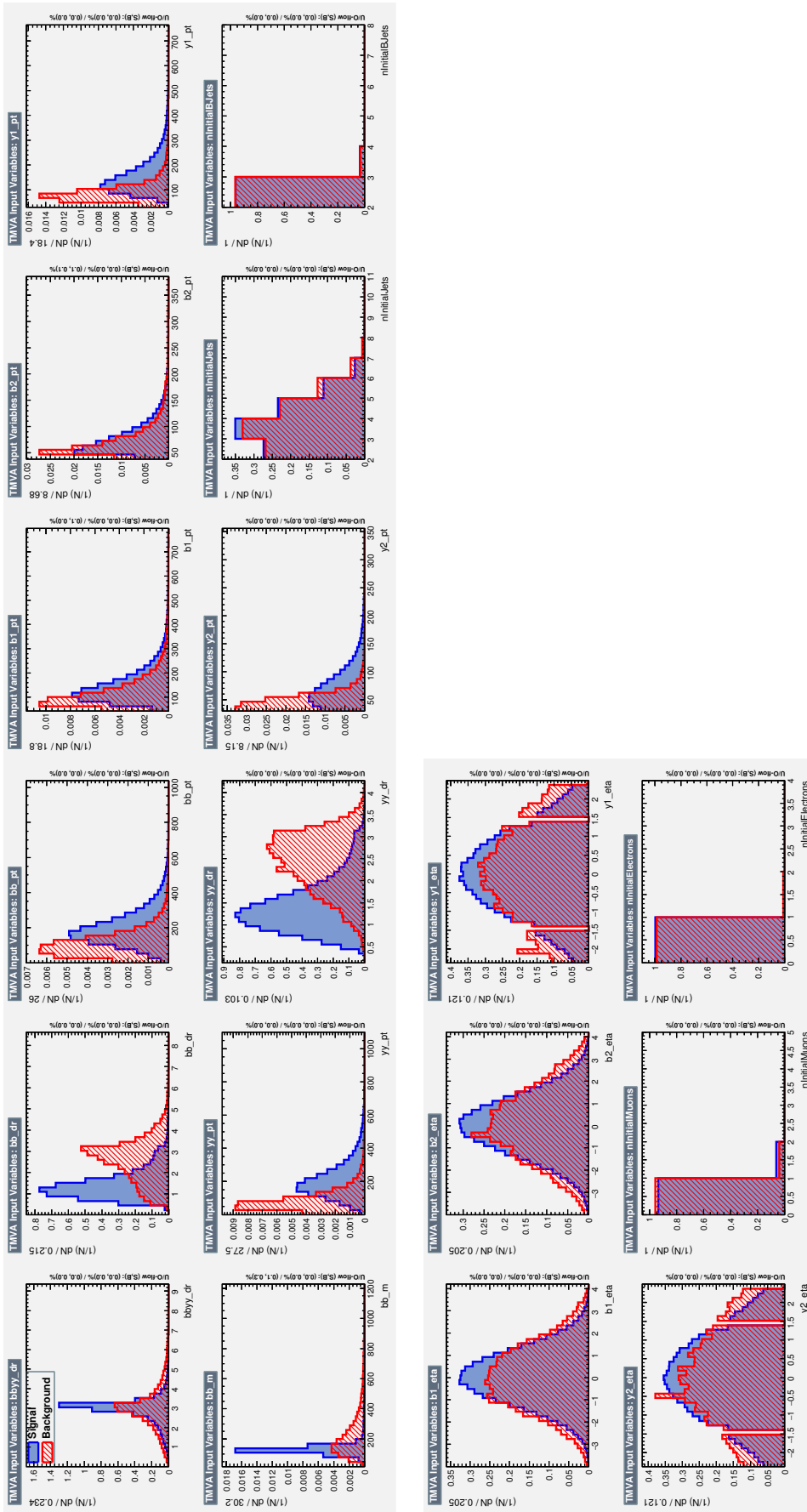
Figure A.25: Distributions of signal and background for each of the variables used in the weighted cuts based method for an innermost pixel layer radius of 39mm and adopting the $50{\times}50\mu m^2$ pixel sensor geometry. Also with an increased η range for accepted jets up to 4.0, while the number of jets per event is limited to the central $|\eta| < 2.5$ region
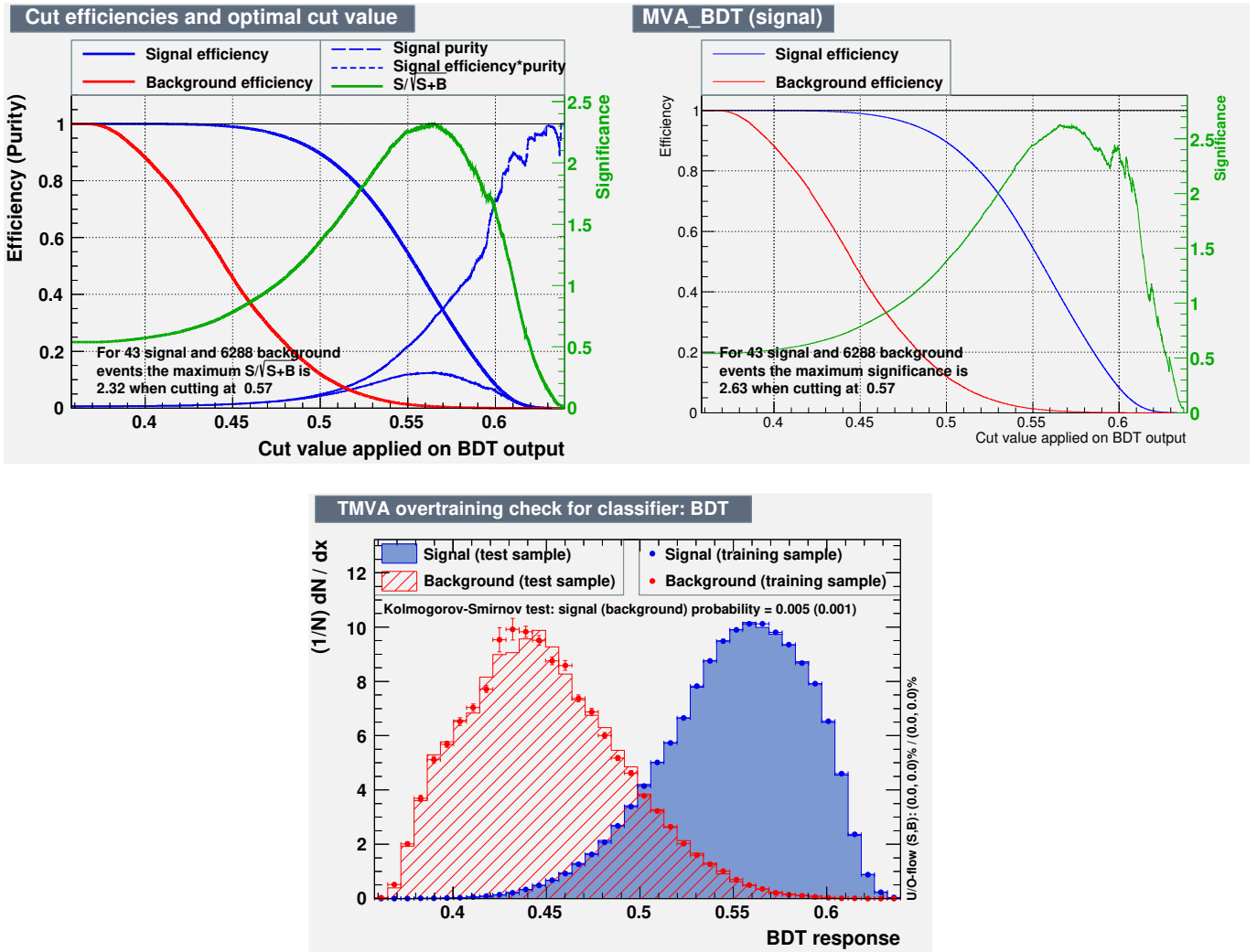
Figure A.26: Signal and background efficiency plots showing purity and $S/\sqrt{S+B}$ (left) and $\sqrt{q_0, A}$ significance (right). Also the BDT response distributions for signal and background for both training and testing samples (bottom). All figures utilise the variables used in the weighted cuts based method for an innermost pixel layer radius of 39mm and adopting the $50{\times}50\mu\mathrm{m}^2$ pixel sensor geometry. Also with an increased η range for accepted jets up to 4.0, while the number of jets per event is limited to the central $|\eta| < 2.5$ region

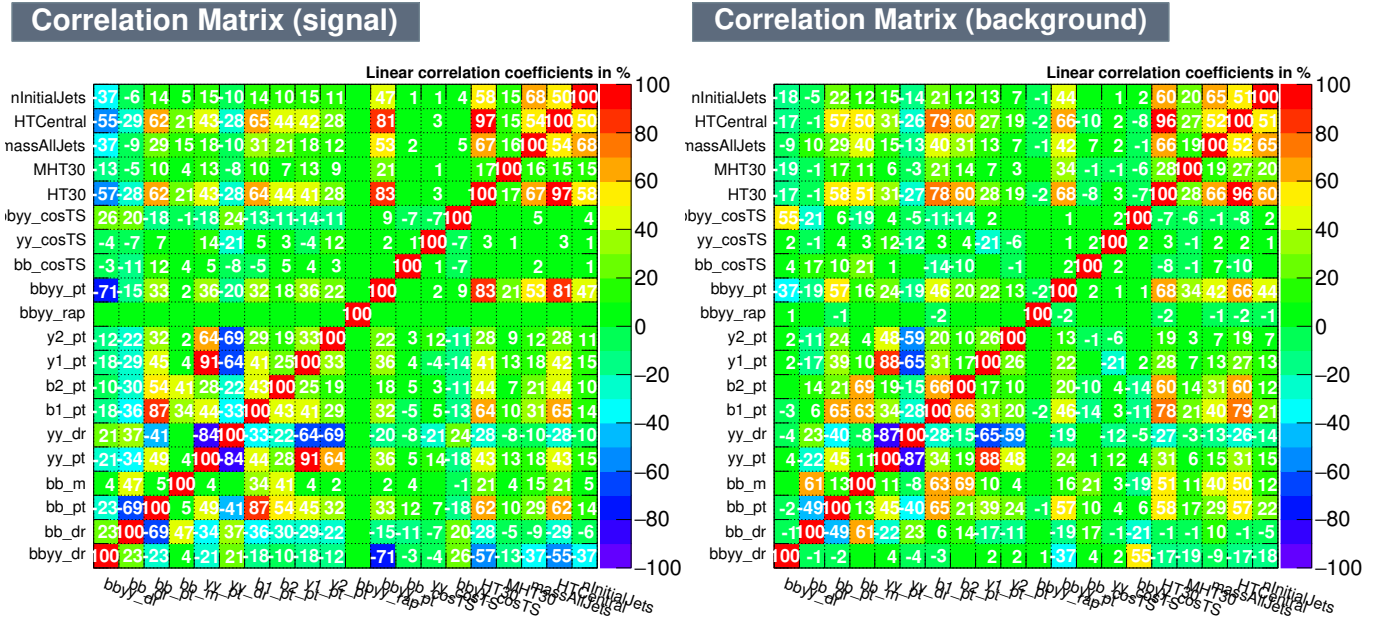## A.12   BDT training and testing plots: Pixel geometries

Figure A.27: Correlation plots for signal (left) and background (right) between the variables used in the published paper for an innermost pixel layer radius of 39mm and adopting the $25 \times 100 \mu\text{m}^2$ pixel sensor geometry
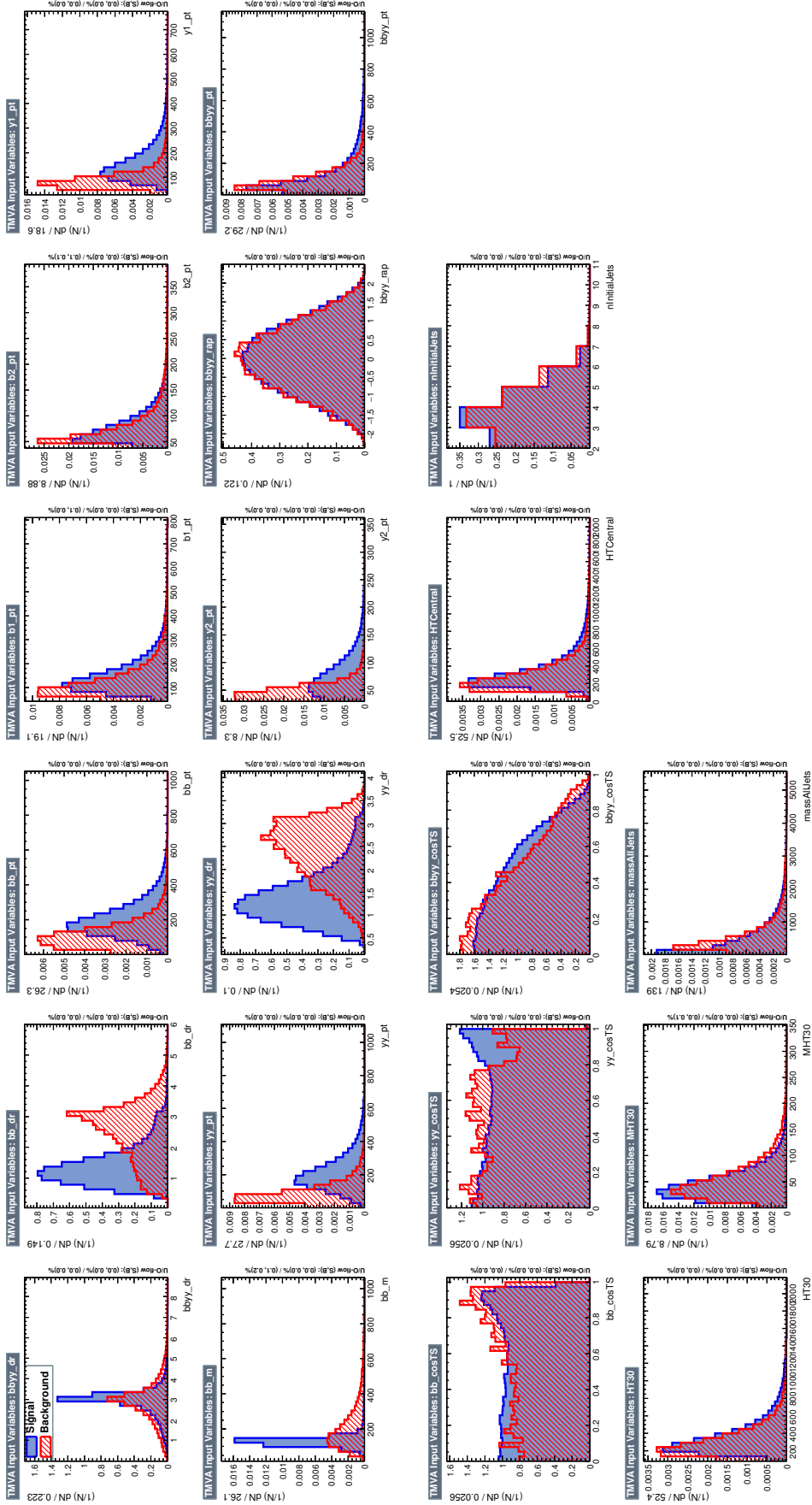
Figure A.28: Distributions of signal and background for each of the variables used in the published paper for an innermost pixel layer radius of 39mm and adopting the $25\times100\mu m^2$ pixel sensor geometry

Figure A.29: Signal and background efficiency plots showing purity and $S/\sqrt{S+B}$ (left) and $\sqrt{q_0, A}$ significance (right). Also the BDT response distributions for signal and background for both training and testing samples (bottom). All figures utilise the variables used in the published paper for an innermost pixel layer radius of 39mm and adopting the $25{\times}100\mu\text{m}^2$ pixel sensor geometry
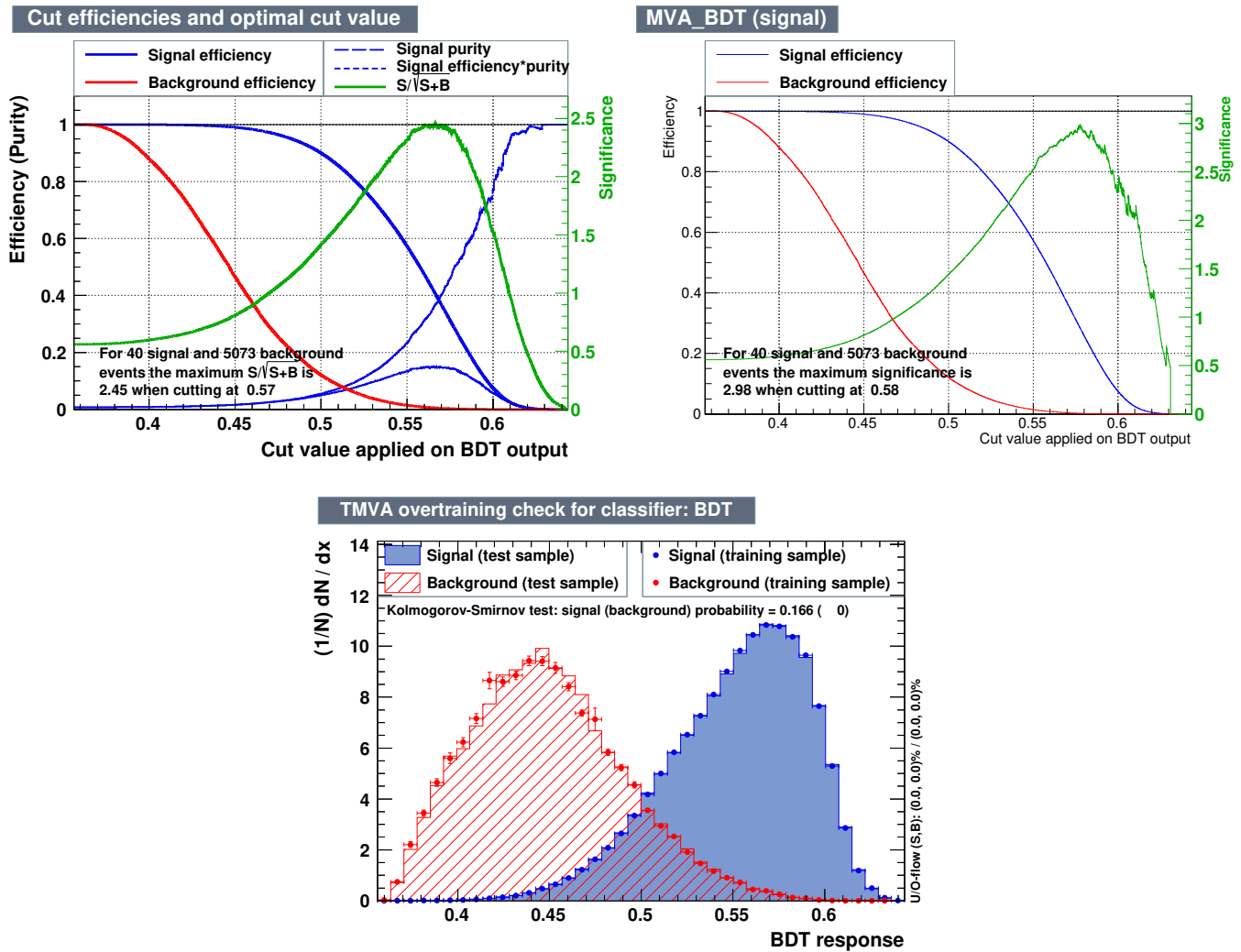
A.13   Weighted cuts based method: Reduced radii

Table A.5: Expected number of events for a weighted cuts based method using the latest available flavour tagging functions for the scenario using $50\times50\mu m^2$ pixel geometry at different innermost layer radii and $p_T^{b\bar{b}/\gamma\gamma} > 80$GeV. Also with an increased accepted jet η from 2.5 to 4.0 but with less than six jets in the central $|\eta| < 2.5$ region only. *All bkgs*[sum total of all backgrounds], *SingleH*[ZH, $t\bar{t}H$, $b\bar{b}H$, ggH], *Reducibles*[$b\bar{b}\gamma\gamma$, $b\bar{b}j\gamma$, $b\bar{b}jj$, $c\bar{c}\gamma\gamma$, $c\bar{c}j\gamma$, $jj\gamma\gamma$], *Others*[$\gamma\gamma Z(\to b\bar{b})$, $t\bar{t}\gamma$, $t\bar{t}$]

| | 39mm | | 36mm | | 33mm | |
	Barrel-barrel	Other	Barrel-barrel	Other	Barrel-barrel	Other
$HH \to bb\gamma\gamma$	8.88±0.04	3.16±0.02	8.85±0.04	3.15±0.02	8.83±0.04	3.14±0.02
$b\bar{b}\gamma\gamma$	12.36±1.22	10.26±1.11	12.28±1.22	10.19±1.10	12.22±1.21	10.14±1.10
$b\bar{b}j\gamma$	10.85±3.66	14.06±4.04	10.70±3.63	13.99±4.03	9.99±3.55	13.93±4.01
$b\bar{b}jj$	0.64±0.49	2.90±1.53	0.64±0.49	2.88±1.53	0.64±0.49	2.87±1.52
$c\bar{c}\gamma\gamma$	0.88±0.14	0.61±0.12	0.53±0.09	0.40±0.08	0.33±0.06	0.21±0.04
$c\bar{c}j\gamma$	0.08±0.05	0.87±0.32	0.05±0.03	0.54±0.20	0.06±0.03	0.40±0.14
$jj\gamma\gamma$	0.76±0.16	0.84±0.16	0.48±0.10	0.45±0.09	0.34±0.07	0.34±0.06
$ZH(\to \gamma\gamma)$	1.91±0.20	1.10±0.14	1.88±0.20	1.08±0.14	1.87±0.20	1.07±0.14
$t\bar{t}H(\to \gamma\gamma)$	4.87±0.23	2.02±0.14	4.72±0.23	1.96±0.14	4.65±0.23	1.93±0.14
$b\bar{b}H(\to \gamma\gamma)$	0.13±0.02	0.06±0.01	0.13±0.02	0.06±0.01	0.13±0.02	0.06±0.01
$ggH(\to \gamma\gamma)$	2.09±0.42	0.74±0.24	1.97±0.41	0.70±0.24	1.89±0.41	0.69±0.24
$Z(\to bb)\gamma\gamma$	1.03±0.20	0.50±0.15	1.03±0.20	0.50±0.15	1.02±0.20	0.49±0.15
$t\bar{t}\gamma$	1.85±1.23	0.56±0.36	1.44±0.93	0.55±0.35	1.28±0.76	0.55±0.35
$t\bar{t}$	0.11±0.03	0.13±0.05	0.11±0.03	0.12±0.05	0.10±0.03	0.12±0.05
Totals						
All bkgs	37.6±4.1	34.7±4.5	36.0±4.0	33.4±4.5	34.5±3.9	32.8±4.5
Single H	9.0±0.5	3.9±0.3	8.7±0.5	3.8±0.3	8.5±0.5	3.8±0.3
Reducibles	25.6±3.9	30.0±4.5	24.7±3.9	28.5±4.5	23.6±3.8	28.0±4.4
Other	3.0±1.3	1.2±0.4	2.6±1.0	1.2±0.4	2.4±0.8	1.2±0.4
$S/\sqrt{B}$	1.45±0.08	0.54±0.04	1.48±0.08	0.54±0.04	1.50±0.08	0.55±0.04
Combined	**1.55±0.08**		**1.57±0.08**		**1.60±0.08**	

Table A.6: Expected number of events for a weighted cuts based method using the latest available flavour tagging functions for the scenario using 25×100μm² pixel geometry at different innermost layer radii and $p_T^{b\bar{b}/\gamma\gamma} > 80$GeV. Also with an increased accepted jet η from 2.5 to 4.0 but with less than six jets in the central $|\eta| < 2.5$ region only. *All bkgs*[sum total of all backgrounds], *SingleH*[ZH, $t\bar{t}H$, $b\bar{b}H$, ggH], *Reducibles*[$b\bar{b}\gamma\gamma$, $b\bar{b}j\gamma$, $b\bar{b}jj$, $c\bar{c}\gamma\gamma$, $c\bar{c}j\gamma$, $jj\gamma\gamma$], *Others*[$\gamma\gamma Z(\to b\bar{b})$, $t\bar{t}\gamma$, $t\bar{t}$]

|	39mm		36mm		33mm	
	Barrel-barrel	Other	Barrel-barrel	Other	Barrel-barrel	Other
$HH \to bb\gamma\gamma$	8.79±0.04	3.13±0.02	8.77±0.04	3.12±0.02	8.75±0.04	3.12±0.02
$bb\gamma\gamma$	12.22±1.21	10.36±1.11	12.16±1.21	10.31±1.11	12.12±1.20	10.27±1.11
$bbj\gamma$	10.73±3.72	13.60±3.99	10.62±3.70	13.55±3.97	10.54±3.68	13.50±3.96
$bbjj$	0.63±0.48	2.85±1.50	0.63±0.48	2.84±1.50	0.63±0.48	2.83±1.50
$c\bar{c}\gamma\gamma$	0.98±0.17	0.55±0.11	0.72±0.13	0.39±0.07	0.41±0.07	0.26±0.05
$c\bar{c}j\gamma$	0.16±0.07	0.82±0.31	0.16±0.06	0.81±0.31	0.09±0.04	0.40±0.15
$jj\gamma\gamma$	0.68±0.12	0.60±0.12	0.49±0.09	0.40±0.09	0.33±0.06	0.28±0.06
$ZH(\to \gamma\gamma)$	1.89±0.20	1.09±0.14	1.87±0.20	1.08±0.14	1.86±0.20	1.06±0.14
$ttH(\to \gamma\gamma)$	4.82±0.23	2.00±0.14	4.74±0.23	1.97±0.14	4.65±0.23	1.93±0.14
$bbH(\to \gamma\gamma)$	0.13±0.02	0.06±0.01	0.13±0.02	0.06±0.01	0.13±0.02	0.06±0.01
$ggH(\to \gamma\gamma)$	2.02±0.41	0.72±0.24	1.92±0.41	0.69±0.24	1.87±0.41	0.68±0.24
$Z(\to bb)\gamma\gamma$	1.02±0.20	0.49±0.15	1.02±0.20	0.49±0.15	1.02±0.20	0.49±0.15
$t\bar{t}\gamma$	1.97±1.27	0.55±0.36	1.71±1.07	0.55±0.35	1.39±0.84	0.54±0.35
$t\bar{t}$	0.11±0.03	0.13±0.05	0.10±0.03	0.13±0.05	0.10±0.03	0.12±0.05
Totals						
All bkgs	37.4±4.2	33.8±4.5	36.3±4.1	33.3±4.4	35.1±4.0	32.4±4.4
Single H	8.9±0.5	3.9±0.3	8.7±0.5	3.8±0.3	8.5±0.5	3.7±0.3
Reducibles	25.4±4.0	28.8±4.4	24.8±3.9	28.3±4.4	24.1±3.9	27.5±4.4
Other	3.1±1.3	1.2±0.4	2.8±1.1	1.2±0.4	2.5±0.9	1.2±0.4
$S/\sqrt{B}$	1.44±0.08	0.54±0.04	1.46±0.08	0.54±0.04	1.48±0.08	0.55±0.04
Combined	1.54±0.08		1.55±0.08		1.57±0.08	

A.14   The weighted cuts based method
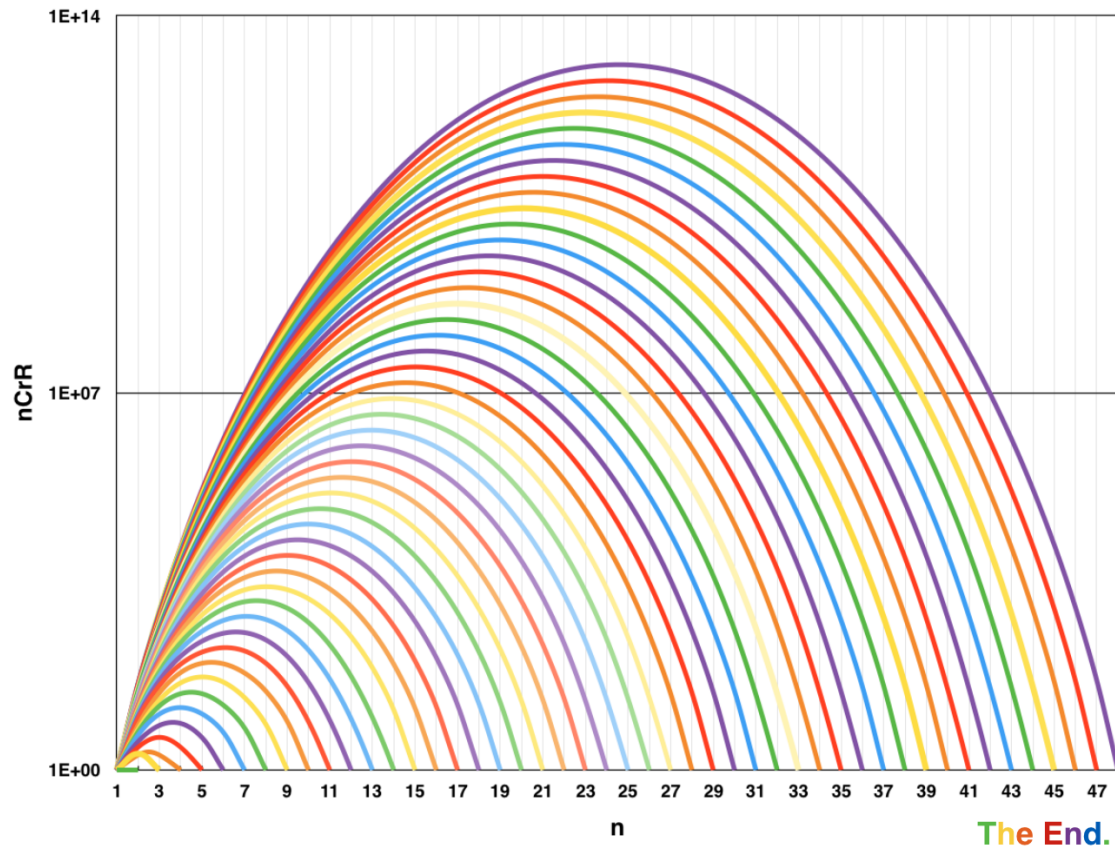
Figure A.30: A diagram showing the number of ways n objects can be combined. e.g. given 27 objects there are 7,696,444 combinations to select 14 objects. This is used extensively during the weighted cuts based method